

TECHNICAL REPORT

EARLY DETECTION MONITORING IMAGE OF BEARING FAULT THERMAL IMAGE IN INDUCTION MOTOR

KAMARUL HAWARI BIN GHAZALI
SABIRA KHATUN
IZZELDIN IBRAHIM MOHAMED ABDELAZIZ
MOHD SHAWAL BIN JADIN
ROHANA BINTI ABDUL KARIM
FTKEE
kamarul@ump.edu.my

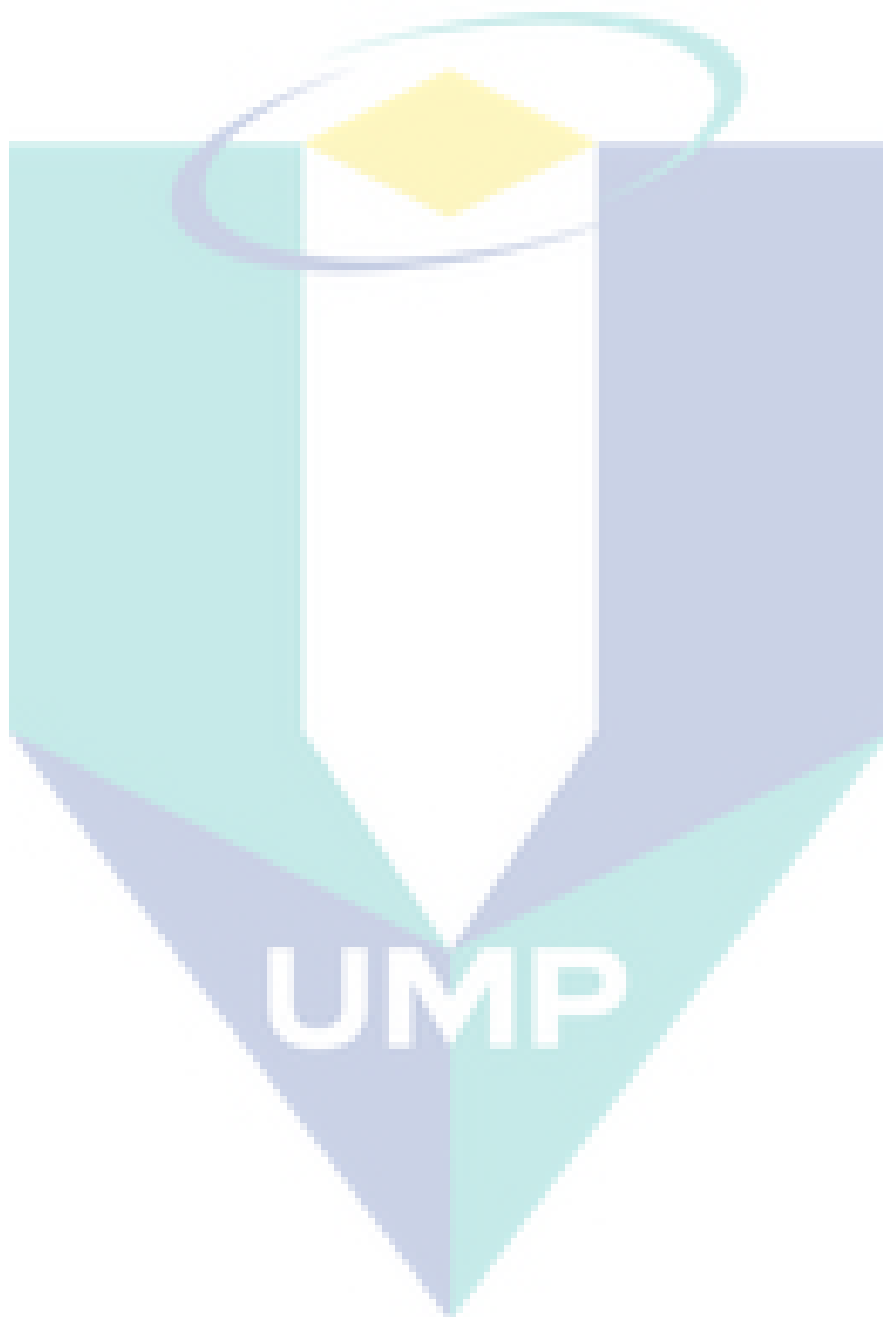
UMP

TABLE OF CONTENT

TITLE PAGE	ii
CHAPTER 1 INTRODUCTION	1
1.1 Background of Study	1
1.2 Problem Statement (buat semula)	5
1.3 Objectives of the Study	8
1.4 Scopes of the study (perbaiki)	9
1.5 Research Significance (Perbaiki)	11
1.6 Thesis Organization (Perbaiki)	12
CHAPTER 2 LITERATURE REVIEW	14
2.1 Introduction	14
2.1.1 Machinery system	15
2.1.2 Motor for industrial machine	20
2.1.3 Diagnosis and Monitoring System for Bearing	20
2.2 State of Arts method for the Feature Extraction Process in Thermal Motor Bearing Image	23
2.2.1 Color-based feature extraction methods	23
2.2.2 Transformation-based feature extraction method	24
2.3 Feature Selection	26
2.3.1 ANOVA	29
2.4 Classification	30
2.4.1 K-Fold Cross Validation in Multi-layer Artificial Neural Networks (MLANNs)	30
2.4.2 Linear Thresholding	32

CHAPTER 3 METHODOLOGY	34
3.1 Introduction	34
3.2 Data Acquisition	35
3.3 Pre-Processing and Segmentation	37
3.4 Feature Extraction	41
3.4.1 Algorithm for the Original Gabor Wavelet Transform (GWT)- based Feature Extraction Method	42
3.4.2 Algorithm for the Proposed an Enhanced Gabor Features (EGF) - based Feature Extraction Method	47
3.4.3 Algorithm for the Proposed an Enhanced GWSMH -based Feature Extraction Method	53
3.4.4 Algorithm for the Proposed an Enhanced GWCLAHE -based Feature Extraction Method	58
3.4.5 Algorithm for the HSV color-based Feature Extraction Method	63
3.4.6 Algorithm for the L*a*b color- based Feature Extraction Method	66
3.5 Feature selection based-Fisher score technique	68
3.5.1 Fisher Score Algorithm in the Original Gabor Wavelet Transform (GWT)-based Feature Extraction Method	70
3.5.2 Fisher Score Algorithm in the Proposed an Enhanced Gabor Features (EGF) -based Feature Extraction Method	74
3.5.3 Fisher Score Algorithm in the Proposed an Enhanced GWSMH- based Feature Extraction Method	78
3.5.4 Fisher Score Algorithm in the Proposed an Enhanced GWCLAHE -based Feature Extraction Method	81
3.5.5 Fisher Score Algorithm for Color based Feature Extraction Method	84
3.6 A one-way ANOVA test	87
3.7 Classification	89

3.7.1	Multi-Layer Artificial neural Networks (MLANNs) Algorithm for solving Classification Tasks	90
3.7.2	Linear Thresholding (LT)	112
CHAPTER 4 RESULT & DISCUSSION		113
4.1	Introduction	113
4.2	Image Acquisition and Image segmentation	113
4.2.1	Image Acquisition	113
4.2.2	Data analysis	114
4.3	Original Gabor Wavelet Transform (GWT)-based Feature Extraction Method	115
4.3.1	Feature selection	122
4.3.2	Classification	129
4.4	Proposed an Enhanced Gabor Features (EGF) -based Feature Extraction Method	136
4.4.1	Feature Selection	144
4.4.2	Classification	152
4.5	Proposed Other Enhanced Methods based on GWT Feature Extraction	159
4.5.1	Propose an Enhanced GWSMH-based Feature Extraction Method	159
4.5.2	Propose an Enhanced GWCLAHE-based Feature Extraction Method	181
4.6	Color based feature extraction for comparison purpose	202
4.6.1	HSV color-based feature extraction algorithm	202
4.6.2	Lab color	209
4.7	Summary	216
4.7.1	Testing and Validation	217



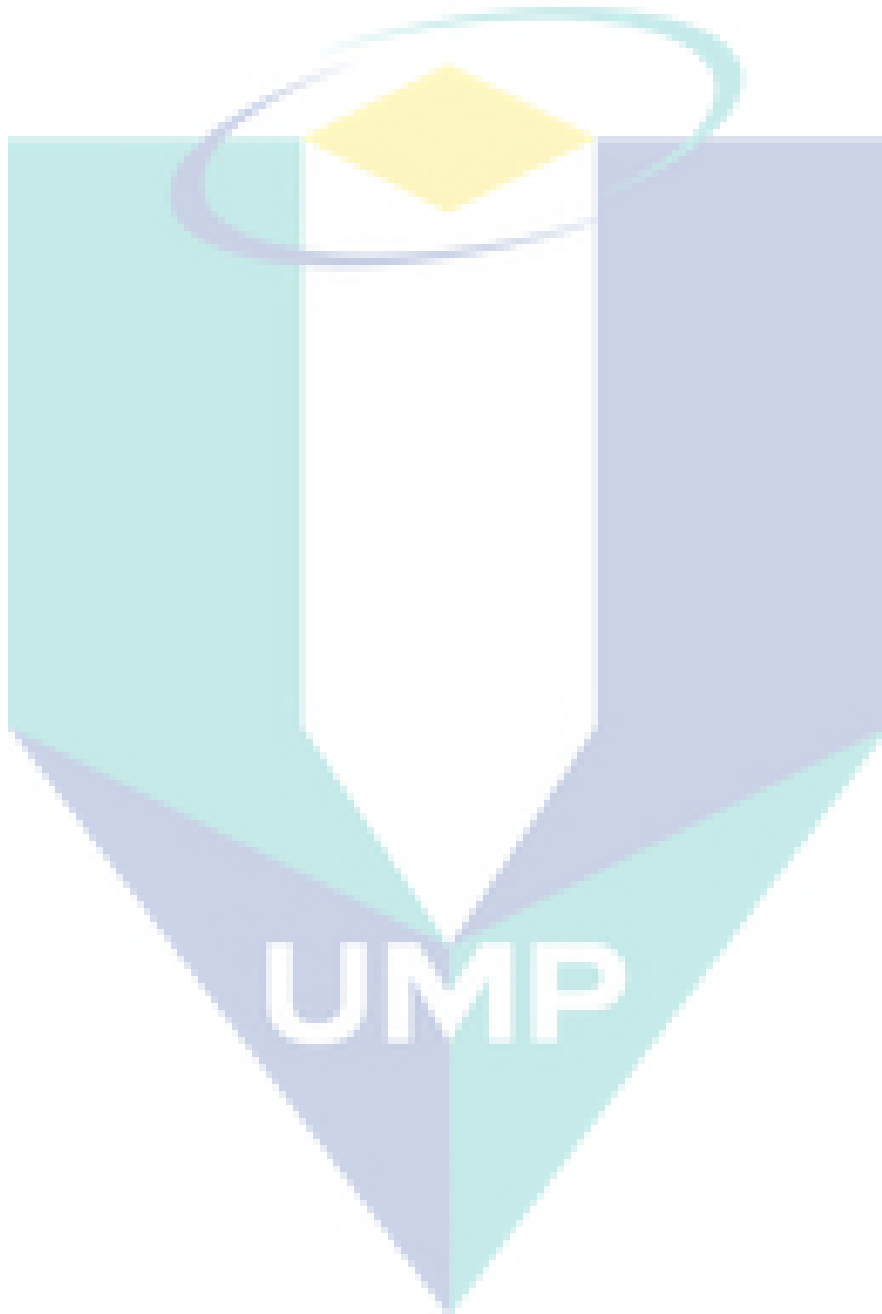
LIST OF TABLES

Table 1.1	Specification of thermal camera	9
Table 1.2	Specification of Squirrel cage Induction Motor (SE2663-1K)	10
Table 1.3	Load torque , stator current acquired and thermal image bearing conditions	10
Table 3.4	Description of ' <i>trainlm</i> ' and ' <i>trainbr</i> ' training algorithms	31
Table 3.2	Gabor filter parameters (number of scales)	43
Table 3.3	A one-way ANOVA table	88
Table 4.1	Distribution of training, validation and testing	114
Table 4.2	Three conditions of thermal motor bearing images before and after convolution of Gabor filter with scale 15x15 at orientation 90°	118
Table 4.3	Overall Local energy features for multi-scales and multi-orientations in GWT based feature extraction method	120
Table 4.4	Overall Mean Amplitude features for multi-scales and multi-orientations in GWT based feature extraction method	121
Table 4.5	Descriptive statistics value for Local Energy feature	127
Table 4.6	ANOVA for local energy feature	128
Table 4.7	Training and validation performance results using TRAINLM, TRAINBR, TRAINSCG using 5-fold and 10-fold cross-validations in MLANNs model for LE and MA features	130
Table 4.8	Best validation performance for TRAINBR in MLANNs model for Local Energy and Mean Amplitude features	133
Table 4.9	Validation performance results using TRAINBR in MLANNs model for Local Energy and Mean Amplitude features	134
Table 4.10	Testing performance results using TRAINBR in MLANNs model for Local Energy and Mean Amplitude features	134
Table 4.11	Classification performances using Linear Thresholding model for GWT based feature extraction's features	136
Table 4.12	Feature Extraction based on proposed EGF filter for 1 sample from 3 groups of thermal motor bearing images with scale 15x15 at orientation 0°	141
Table 4.13	Fisher scoring for each Enhanced Gabor filter's scale for Local Energy	145
Table 4.14	Fisher scoring for each Enhanced Gabor filter's scale for Mean Amplitude	146
Table 4.15	Descriptive statistics value for new Local Energy feature	150
Table 4.16	Descriptive statistics value for new Mean Amplitude feature	150

Table 4.17	Training and validation performance results using TRAINLM, TRAINBR, TRAINSCG using 5-fold and 10-fold cross-validations in MLANNs model for Local Energy and Mean Amplitude features	152
Table 4.18	Best validation performance for TRAINSCG in MLANNs model for Local Energy and Mean Amplitude features	156
Table 4.19	Training performance results using TRAINSCG in MLANNs model for Local Energy and Mean Amplitude features	157
Table 4.20	Testing performance results using TRAINSCG in MLANNs model for Local Energy and Mean Amplitude features	157
Table 4.21	Classification performances using Linear Thresholding model for EGF based feature extraction's features	159
Table 4.22	Three conditions of thermal motor bearing images before and after convolution of GWSMH-based filter with scale 15x15 at orientation 0°	163
Table 4.23	Fisher scoring for each Enhanced Gabor filter's scale for Local Energy	167
Table 4.24	Fisher scoring for each Enhanced Gabor filter's scale for Mean Amplitude	168
Table 4.25	Descriptive statistics value for new Local Energy feature	172
Table 4.26	Descriptive statistics value for new Mean Amplitude feature	172
Table 4.27	ANOVA for Local Energy features	173
Table 4.28	Training and validation performance results using TRAINLM, TRAINBR, TRAINSCG using 5-fold and 10-fold cross-validations in MLANNs model for Local Energy and Mean Amplitude feature	174
Table 4.29	Best validation performance for TRAINBR in MLANNs model for Local Energy and Mean Amplitude features	178
Table 4.30	Validation performance results using TRAINBR in MLANNs model for Local Energy and Mean Amplitude features	179
Table 4.31	Testing performance results using TRAINBR in MLANNs model for Local Energy and Mean Amplitude features	179
Table 4.32	Classification performances using Linear Thresholding model for GWSMH based feature extraction's features	181
Table 4.33	Three conditions of thermal motor bearing images before and after convolution of Gabor filter with scale 9x9 at orientation 90°	184
Table 4.34	Fisher scoring for each Enhanced Gabor filter's scale for Local Energy	188
Table 4.35	Fisher scoring for each Enhanced Gabor filter's scale for Mean Amplitude	189
Table 4.36	Descriptive statistics value for new Local Energy feature	193
Table 4.37	Descriptive statistics value for new Mean Amplitude feature	193
Table 4.38	ANOVA for new Local Energy feature	194

Table 4.39	Training and validation performance results using TRAINLM, TRAINBR, TRAINSCG using 5- fold and10-fold cross-validations in MLANNs model for Local Energy and Mean Amplitude feature	195
Table 4.40	Best validation performance for TRAINBR in MLANNs model for Local Energy and Mean Amplitude features	199
Table 4.41	Validation performance results using TRAINBR in MLANNs model for Local Energy and Mean Amplitude features	200
Table 4.42	Testing performance results using TRAINBR in MLANNs model for Local Energy and Mean Amplitude features	200
Table 4.43	Classification performances using Linear Thresholding model for GWCLAHE based feature extraction's features	202
Table 4.44	Data selection for HSV color fetatures	203
Table 4.45	Training and validation performance results using TRAINLM, TRAINBR, TRAINSCG using 5- fold and10-fold cross-validations in MLANNs model for Local Energy and Mean Amplitude feature	205
Table 4.46	Validation performance results using TRAINLM in MLANNs model for Local Energy and Mean Amplitude features	207
Table 4.47	Best validation performance for TRAINLM in MLANNs model for Local Energy and Mean Amplitude features	207
Table 4.48	Testing performance results using TRAINLM in MLANNs model for Local Energy and Mean Amplitude features	207
Table 4.49	Classification performances using Linear Thresholding model for HSV color features	208
Table 4.50	Sample table	210
Table 4.51	Training and validation performance results using TRAINLM, TRAINBR, TRAINSCG using 5- fold and10-fold cross-validations in MLANNs model for L*a*b based feature extraction algorithm	212
Table 4.52	Validation performance results using TRAINLM in MLANNs model for Local Energy and Mean Amplitude features	214
Table 4.53	Best validation performance for TRAINLM in MLANNs model for Local Energy and Mean Amplitude features	214
Table 4.54	Testing performance results using TRAINLM in MLANNs model for Local Energy and Mean Amplitude features	215
Table 4.55	Classification performances using Linear Thresholding model for l*a*b color features	216
Table 4.56	Comparison performance results in MLANNs model for all enhancement based feature extraction methods	217
Table 4.57	Comparison performance results in MLANNs model for all methods	218
Table 4.58	Comparison classification performance results in Linear Thresholding model for all enhancement based feature extraction methods	219

Table 4.59 Comparison classification performance results in Linear Thresholding model for all enhancement based feature extraction methods 220



LIST OF FIGURES

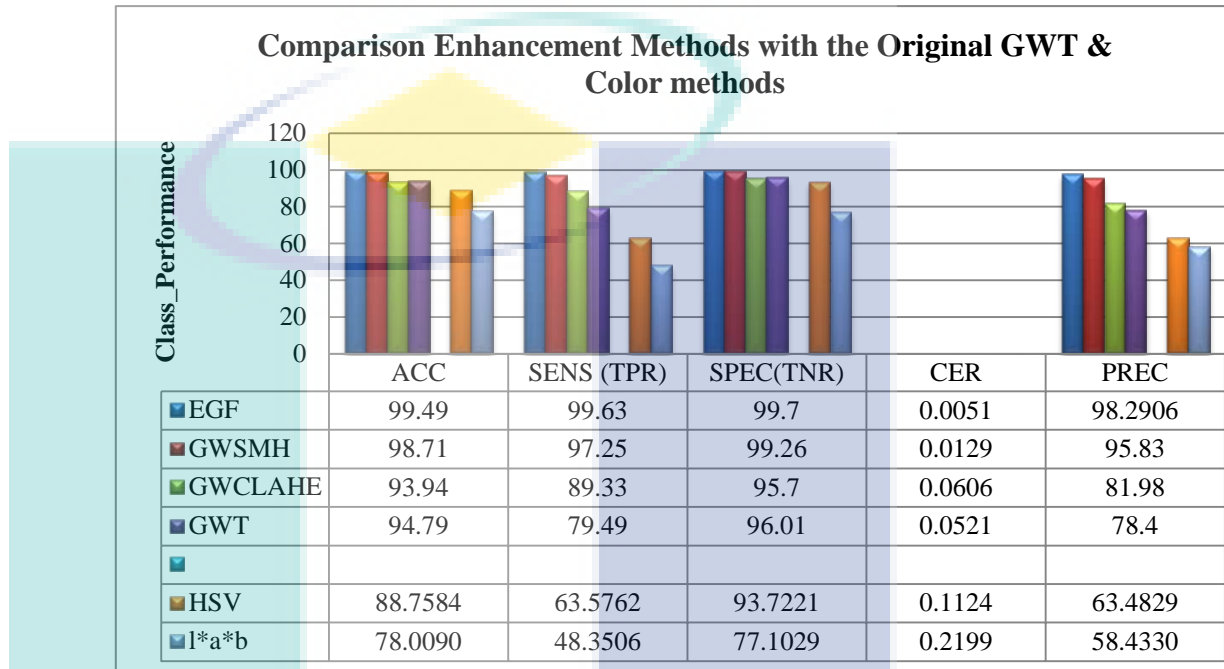
Figure 3.1	Block diagram of overall image processing in thermal motor bearing images	35
Figure 3.2	Experiment setup using thermal camera.	36
Figure 3.3	Surface bearing part of induction motor	37
Figure 3.4	Flowchart of Active Contour-based segmentation technique	40
Figure 3.5	Flowchart of Gabor Wavelet Transform based feature extraction technique	46
Figure 3.6	Flowchart of Enhanced Gabor Features (EGF) based feature extraction technique	52
Figure 3.7	Flowchart of HSV Color-based feature extraction technique	65
Figure 3.8	Flowchart of L*a*b Color based feature extraction technique	68
Figure 3.9	Gabor filter selection based on Fisher Score technique	73
Figure 3.10	EGF filter selection based on Fisher Score technique	77
Figure 3.11	GWSMH filter selection based on Fisher Score technique	80
Figure 3.12	GWCLAHE filter selection based on Fisher Score technique	83
Figure 3.13	HSV color selection based on Fisher Score technique	85
Figure 3.14	l*a*b color selection based on Fisher Score technique	87
Figure 3.15	A general framework for classification process	89
Figure 3.17	Single hidden layer architecture Artificial Neural Network	90
Figure 3.18	Cross Validation procedure	93
Figure 3.19	Flowchart for the proposed MLANNs for Gabor Wavelet Transform (GWT)	96
Figure 3.20	Flowchart for the proposed MLANNs for Enhanced Gabor Features (EGF)- based feature extraction	99
Figure 3.21	Flowchart for the proposed MLANNs for Enhanced GWHSM - based feature extraction	102
Figure 3.22	Flowchart for the proposed MLANNs for Enhanced GWHSM - based feature extraction.	105
Figure 3.23	Flowchart MLANNs-based classification for HSV color-based feature extraction methods.	108
Figure 3.24	Flowchart MLANNs-based classification for l*a*b color-based feature extraction methods.	111
Figure 4.1	Motor bearing image	113
Figure 4.2	Cropped the segmented bearing image	115

Figure 4.3	Sample of the 2D-Gabor function in the spatial domain (new Real (cosine) component and new Imaginary(sine) component) for normal thermal image condition	116
Figure 4.4	A new real componnets of EGF filters in spatial domain rotates at 5 scales and 8 orientations in normal conditon image	117
Figure 4.5	The oriented output sample of response matrices (features) for normal condition image when pass through individual Gabor filter with five scales and eight orientations	118
Figure 4.6	Variation of non consistent local energy vector for thermal motor bearing image groups in scale 15x15 at teta 5	122
Figure 4.7	Variation of Fisher score value for local energy between normal, warning and abnormal thermal motor bearing images	124
Figure 4.8	Variation of Fisher score value for Mean Amplitude between normal, warning and abnormal thermal motor bearing images	124
Figure 4.9	Variation Local Energy feature of condition thermal motor bearing images with 8 orientations for SCALE 15x15 in GWT	125
Figure 4.10	Variation Mean Amplitude feature of thermal motor bearing image conditions with 8 orientations for SCALE 15x15 in GWT	125
Figure 4.11	The optimal selection Local Energy feature for GWT is at SCALE 15x15 (orientation 90°)	126
Figure 4.12	The optimal selection Mean Amplitude feature for GWT is at SCALE 15x15 (orientation 157.5°)	126
Figure 4.13	Descriptive statistics value for Mean Amplitude feature	127
Figure 4.14	ANOVA for Mean Amplitude features	128
Figure 4.15	Validation performance for TRAINLM based on Kfold-5 and Kfold-10	131
Figure 4.16	Validation performance for TRAINBR based on Kfold-5 and Kfold-10	132
Figure 4.17	Validation performance for TRAINSCG based on Kfold-5 and Kfold-10	132
Figure 4.18	Best validation performances among all training algorithm types	133
Figure 4.19	Comparison bar graph between training and testing performance using GWT based feature extraction algorithm	135
Figure 4.20	(a)Original Image and Original Image Histogram for group normal, warning and abnormal (b) Equalized Image and Equalized Image Histogram for group normal, warning and abnormal	138
Figure 4.21	Sample of the 2D-EGF function in the spatial domain (new Real (cosine) component and new Imaginary(sine) component) for normal thermal image condition	138
Figure 4.22	A new real componnets of EGF filters in spatial domain rotates at 5 scales and 8 orientations in normal conditon image	139

Figure 4.23	A new EGF magnitude response of the convolution of normal thermal motor bearing image with five scales and eight orientations	140
Figure 4.24	The oriented output sample of response matrices (features) for normal condition image when pass through individual EGF-based filter with five scales and eight orientations	141
Figure 4.25	Variation of Fisher score value for local energy between normal, warning and abnormal thermal motor bearing images	146
Figure 4.26	Variation of Fisher score value for Mean Amplitude between normal, warning and abnormal thermal motor bearing images	147
Figure 4.27	Variation Local Energy feature of condition thermal motor bearing images with 8 orientations for SCALE 15x15 in EGF	148
Figure 4.28	Variation Mean Amplitude feature of condition thermal motor bearing images with 8 orientations for SCALE 13x13	148
Figure 4.29	The optimal selection Local Energy feature for EGF is at SCALE 15x15 (teta 1)	149
Figure 4.30	The optimal Mean Amplitude feature for EGF is at SCALE 13x13 (Orientation 0°)	149
Figure 4.31	Validation performance for TRAINLM based on Kfold-5 and Kfold-10	154
Figure 4.32	Validation performance for TRAINBR based on Kfold-5 and Kfold-10	154
Figure 4.33	Validation performance for TRAINSCG based on Kfold-5 and Kfold-10	155
Figure 4.34	Best validation performances among all training algorithm types	156
Figure 4.35	Comparison bar graph between training and testing performance using EGF based feature extraction algorithm	158
Figure 4.36	Noise removed in each input grayscale thermal images group by using Unsharp filter and Median filter (a) Input grayscale thermal image (b) Unsharp filter image (c) Median filter image	161
Figure 4.37	(a) A sample of Magnitude response for 5 scales at orientation 0° (b) A Sample of Real GWSMH-based filter with five scales and eight orientations	163
Figure 4.38	Variation of Fisher score value for local energy between normal, warning and abnormal thermal motor bearing images	169
Figure 4.39	Variation of Fisher score value for Mean Amplitude between normal, warning and abnormal thermal motor bearing images	169
Figure 4.40	Variation Local Energy feature of condition thermal motor bearing images with 8 orientations for SCALE 15x15	170
Figure 4.41	Variation Mean Amplitude feature of condition thermal motor bearing images with 8 orientations for SCALE 15x15	170
Figure 4.42	The optimal selection Local Energy feature for GWSMH is at SCALE 15x15 (orientation 0°)	171

Figure 4.43	The optimal selection Mean Amplitude feature for GWSMH is at SCALE 15x15 (orientation 0°)	171
Figure 4.44	Validation performance for TRAINLM based on Kfold-5 and Kfold-10	176
Figure 4.45	Validation performance for TRAINBR based on Kfold-5 and Kfold-10	176
Figure 4.46	Validation performance for TRAINSCG based on Kfold-5 and Kfold-10	177
Figure 4.47	Best validation performances among all training algorithm types	178
Figure 4.48	Comparison bar graph between training and testing performance using GWSMH based feature extraction algorithm	180
Figure 4.49	Image enhancement method using CLAHE (a) Input grayscale thermal image (b) Enhanced CLAHE image	182
Figure 4.50	(a) A Sample of Real GWCLAHE-based filter with five scales and eight orientations (b) A sample of Magnitude response for 5 scales at orientation 0°	184
Figure 4.51	Variation of Fisher score value for local energy between normal, warning and abnormal thermal motor bearing images	189
Figure 4.52	Variation of Fisher score value for Mean Amplitude between normal, warning and abnormal thermal motor bearing images	190
Figure 4.53	Variation Local Energy feature of condition thermal motor bearing images with 8 orientations for SCALE 9x9	191
Figure 4.54	Variation Mean Amplitude feature of condition thermal motor bearing images with 8 orientations for SCALE 15x15	191
Figure 4.55	The optimal selection Local Energy feature for GWCLAHE is at SCALE 9x9 (orientation 90°)	192
Figure 4.56	The optimal selection Mean Amplitude feature for GWCLAHE is at SCALE 15x15 (orientation 157.5°)	192
Figure 4.57	Validation performance for TRAINLM based on Kfold-5 and Kfold-10	197
Figure 4.58	Validation performance for TRAINBR based on Kfold-5 and Kfold-10	198
Figure 4.59	Validation performance for TRAINSCG based on Kfold-5 and Kfold-10	198
Figure 4.60	Best validation performances among all training algorithm types	199
Figure 4.61	Comparison bar graph between training and testing performance using GWCLAHE based feature extraction algorithm	201
Figure 4.62	Variation of Fisher score value for HSV color method between normal, warning and abnormal thermal motor bearing images	203
Figure 4.63	The optimal selection for HSV	204

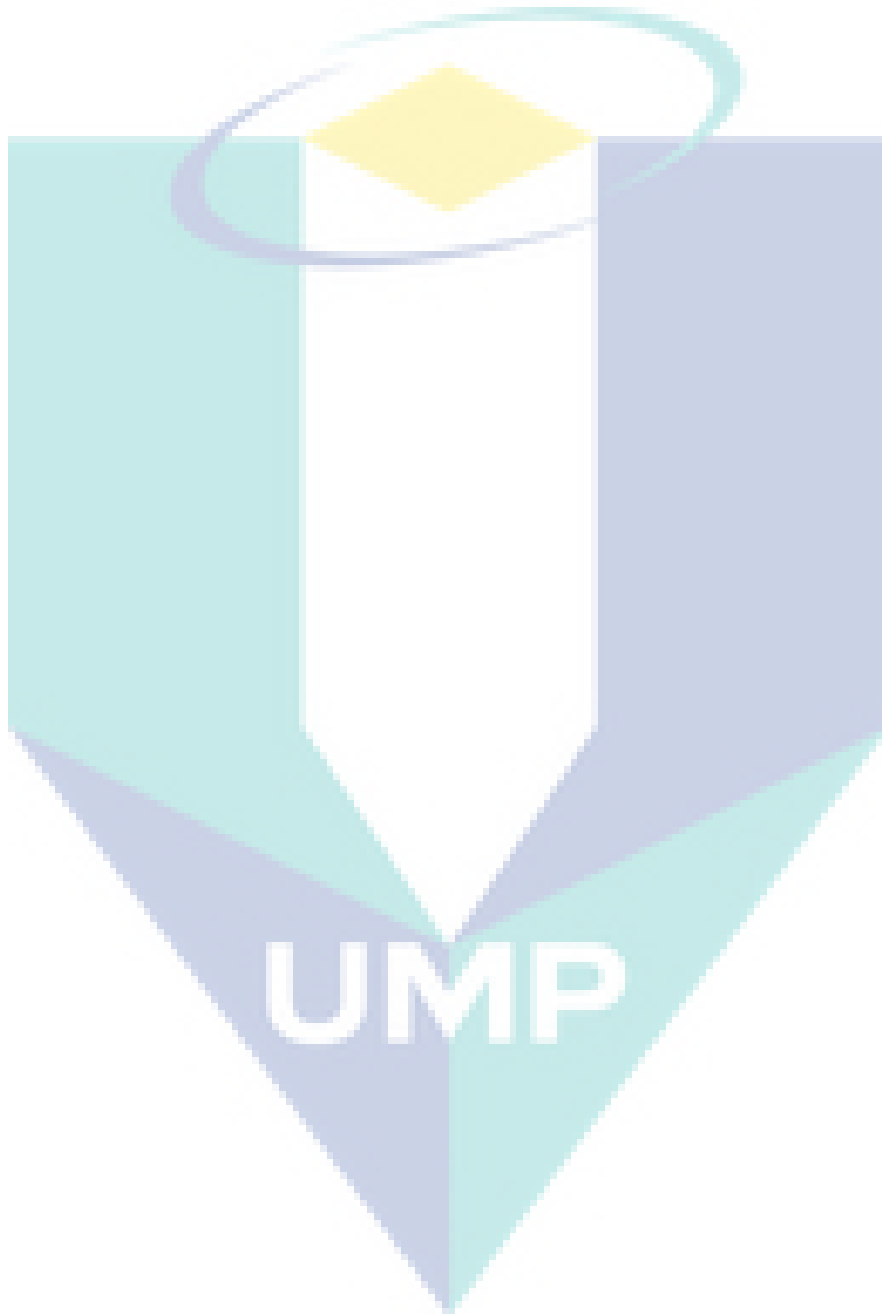
- Figure 4.64 Variation of Fisher score value for l*a*b color method between normal, warning and abnormal thermal motor bearing images 210
- Figure 4.65 The optimal selection for l*a*b* 211
- Figure 4.66 Distribution of comparison classification performance enhancement method with the original GWT based feature extraction method using MLANNs 218



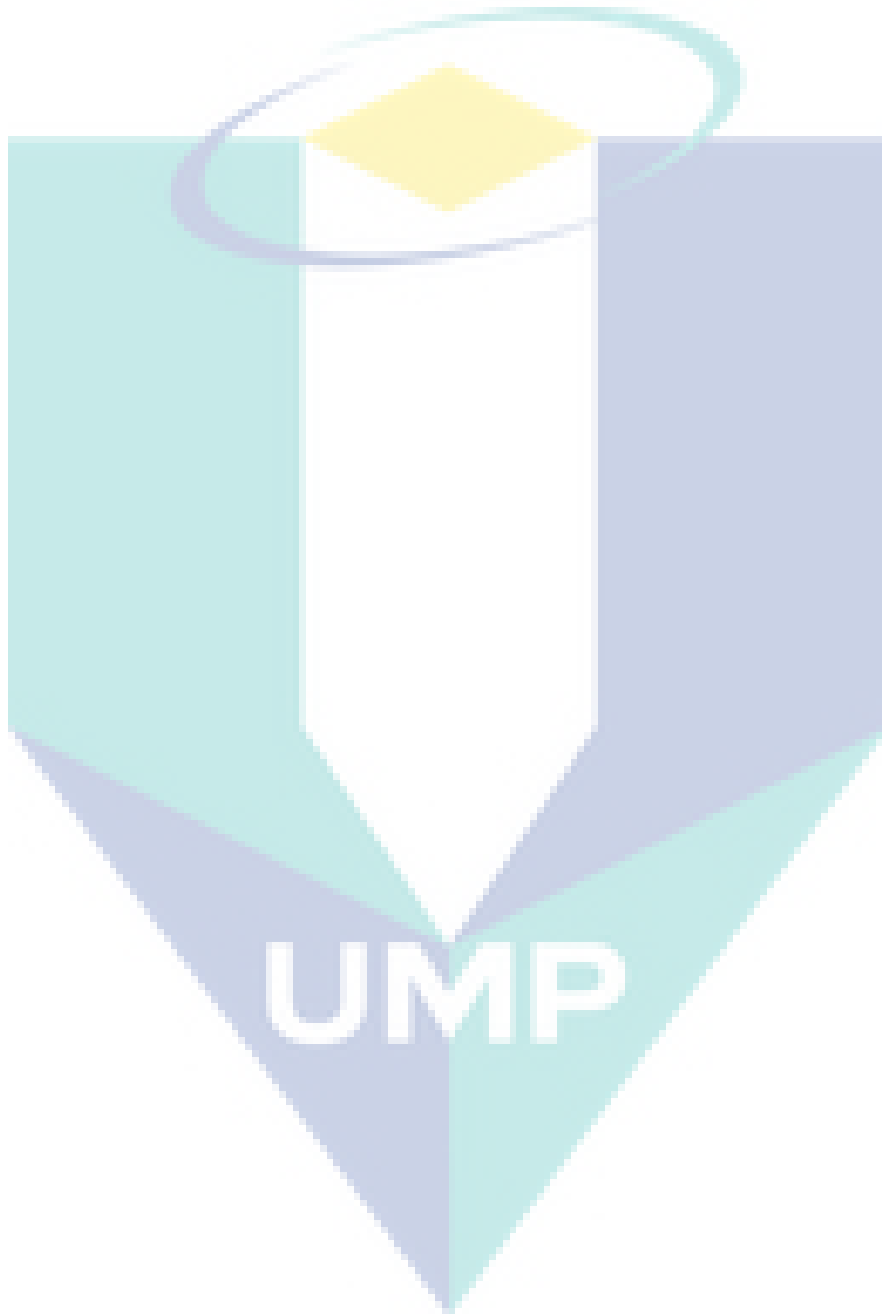
- Figure 4.67 Distribution of comparison classification performance using MLANNs for all methods 219
- Figure 4.68 Distribution of comparison classification performance using Linear Thresholding for all methods 220
- Figure 4.69 Distribution of comparison classification performance using Linear Thresholding for all methods 221

UMP

LIST OF SYMBOLS



LIST OF ABBREVIATION



CHAPTER 1

INTRODUCTION

1.1 Background of Study

AC Squirrel cage induction motors are the most important alternating current (ac) machine in industries due to their advantages of reliability, rugged construction, easy maintenance, and cost-effective pricing. More than 90% of all motors used in industry worldwide are ac induction motors (M.Peltola, 2002). Based on studies, the most common fault occurrences of induction motor are relate on bearing faults (Albrecht, Appiarius, McCoy, Owen, & Sharma, 1986; "IEEE Recommended Practice for the Design of Reliable Industrial and Commercial Power Systems," 1988; Thomson & Fenger, 2001). Yet, (Hashemian, 2011; Nandi, Toliyat, & Li, 2005; Schoen, Habetler, Kamran, & Bartfield, 1995) have identified that, up to 40%-50% of machinery defects are related to bearing faults. This has reveals that bearings are the primary cause and most severe and common fault in the motor system.

Bearing is an important component and are used extensively in most rotating machines including electrical and mechanical system to support static and dynamic loads. Their performance is of the utmost importance in automotive industries, aerospace turbo machinery, chemical plants, power stations, and process industries that require precise and efficient performance. Any bearing in operation will unavoidably fail at some point. If one of the bearings fails, not only the machine, but also the assembly line stops and the deriving costs may be extremely high. In machinery system, they are many root causes that can lead to bearing failure such as improper lubricant, high temperatures, contamination, misalignment, corrosion, overheating, excessive load, thermal overload, fatigue and improper mounting (Austin H Bonnett, 1992; A. H. Bonnett, 1993; "Chapter 3 - Machinery Component Failure Analysis," 1999; Huang, Yang, Zhou, & Litak, 2019; Vencl & Rac, 2014).

This research is focuses on thermal overload as a root cause that lead to bearing failure. Thermal overload situation is occurred when high load torque values is produced in the motor, then it generates current on the motor beyond the nameplate rated value (draw more current) causes an abnormal temperature (Karmakar, 2016; M & Ushakumari, 2011; Rowlett, 2019 ; Schatz, 1971; Siddique, Yadava, & Singh, 2005) and subsequently produces excessive heating on induction motor (Gonzalez-Cordoba, Osornio-Rios, Granados-Lieberman, Romero-Troncoso, & Valtierra-Rodriguez, 2018). In addition, this excessive heating also will accelerate the process of bearing failure (Russell Wanhill, 2019; Schoen, Habetler, Kamran, & Bartheld, 1994; Siddiqui, Sahay, & Giri, 2015). According to the standards on Squirrel-Cage induction motor provided by the norms National Electrical Manufacturers Association (NEMA) Guide [MG 1-2011] , variation from nameplate amperes for alternating-current motors is operated at rated voltage, rated frequency, and rated horsepower output, the input in amperes shall not vary from the nameplate value by more than 10 percent [MG 1-12.47] ("Information Guide for General Purpose Industrial AC SmallandMedium Squirrel-Cage Induction Motor Standards," 2014). In other work, over current flowing will potentially generate negative effects such as thermal stress (Sengupta, 2016), where it consequences cause the failure of motor parts such as stator, locked rotor, shaft frame and bearing part (Banerjee, Tiwari, Vico, & Wester, 2008; Ojaghi, Sabouri, & Faiz, 2014) and may lead to induction motors failure (Gonzalez-Cordoba, Osornio-Rios, Granados-Lieberman, Romero-Troncoso, & Valtierra-Rodriguez, 2017; Gonzalez-Cordoba et al., 2018; Mike Eby, 2011). Therefore, if these potential problems are not identified and analysed promptly, sooner or later it will lead to a bearing problem that can affect the motor performance such as fatal breakdown of motor to freeze up and burn out. Thus, predicting the degradation process of bearings before they reach the failure is extremely important. To prevent potential problem occurred, early condition monitoring detection of such incipient faults is required as prevention for bearing component and many unexpected mechanical machinery performance degradation and malfunctions, to avoid sudden breakdown, minimize down-time, reduce maintenance cost, and extend the lifetime of machines. Thus, by monitoring the condition or health of the bearing component, failure can be predicted at an early stage and the appropriate maintenance can be scheduled or other actions can be taken to avoid the failure occurs.

Nowadays, there are a few current conditions monitoring technologies that been used in industry as a preventive maintenance including vibration, sound, lumped parameter based thermal and acoustic emission monitoring analysis but all these monitoring methods require specialized expertise to identify the health of the bearing condition. The use of these sensor-based methods become difficult and led to long time consumption in determining the exact bearing failure due to data acquisition from the bearing through vibration signal induces a large amount of signal noise during machine operation, this make difficult to identify the signal obtained that usually drowned out in other noise emanating from the machine which will challenge the later fault diagnosis. Additionally, sensor-based method also sometimes invasive since it is often requires the installation of additional sensors and probes to obtain the vibration data. Besides, by using lumped parameter thermal monitoring, its function is to tune the parameters of a thermal model for overload protection, however, when the temperature rises in the region of the fault, this sensor is too slow to detect the incipient fault before it progresses into a more severe faults (Mehala, October 2010). Therefore, infrared thermal imaging-based monitoring approaches has been successfully proposed and utilized recently as an interesting complementary technique for several condition monitoring applications as one of the method to detect fault at the earlier stage including in rotating machinery application (Glowacz & Glowacz, 2017; Olivier Janssens et al., 2015; Osornio-Rios, Antonino-Daviu, & Romero-Troncoso, 2019; Resendiz-Ochoa, Osornio-Rios, Benitez-Rangel, Romero-Troncoso, & Morales-Hernandez, 2018; Singh, Anil Kumar, & Naikan, 2016). This infrared thermography also has been established as an effective tool in many different applications (Bortoni, Siniscalchi, & Jardini, 2010; Cetingul & Herman, 2008; Duberstein et al., 2012; Jadin, Ghazali, & Taib, 2014; Jadin, Ghazali, Taib, & Huda, 2012; Kamaruddin, Sunard, Ghazali, & Hamid; Zin, Hawari, & Khamisan, 2016). It is a non-destructive testing (NDT) method that measures the temperature and can discern the thermal profiles of a body remotely and provides the thermal image of the entire component or machinery that allows quick detection of potential problem/ defects before failure. Other than that, this tool also very quick monitoring system and non-contact technique which can monitor the induction motor without any interference physical contacts to the whole system. Due to all of these advantages, it makes this technique a very interesting option to at least complement the diagnosis provided by other well-known techniques, such as acoustic emission signal, motor current analysis or vibration analysis. This has been

motivated to use this infrared thermograph monitoring tool in this study. By capture the infrared (IR) energy transfer (thermal radiation pattern) from bearing motor component to its environment, it records the surface temperature distribution in the form of thermogram and produces a real-time image in a colour palette where hotter objects appear brighter and cooler objects appear darker. Discoloration observed from the infrared image is one of the failure pattern which should be considered as a key indicator in order to diagnose the failure of motor bearing (Austin H Bonnett, 1992). According to (Rolf Hopple, 2007), it has described that early indications for potential bearing problems are an increased temperature (discoloration), higher vibration levels or higher noise levels of the motor. Thus, predicting the degradation process of bearings before they reach the failure is extremely important. **To be accurately, an image processing approach using computer vision technology is required to process the thermogram obtained could be analysed and predicted the failure of the infrared image bearing machine at earlier stage with more easily.**

Over the last decades, the arrival of computer assisted data acquisition by video cameras has made it easy for further image processing and analysis. Currently, an increasing number of research works are concentrating on the use of image processing and computational intelligence techniques. There are a few researchers have taken their interest in image processing technique incorporated with an IRT system for diagnosing the condition of induction machine due to different mechanical faulty (misalignment faulty, mass-unbalance faulty, bearing faulty, fan faulty, cooling system faulty, inter turn- faulty, outer-raceway faulty, broken rotor bar faulty) by evaluating the Infrared image (O. Janssens, Loccufier, & Hoecke, 2019; Olivier Janssens et al., 2015; Jia, Liu, Vong, & Pecht, 2019; Karvelis et al., 2014; Resendiz-Ochoa, Osornio-Rios, Benitez-Rangel, Hernandez, & Romero-Troncoso, 2017; Resendiz-Ochoa et al., 2018). In their work, various image processing techniques are employed in the segmentation and feature extraction process to diagnose the condition of induction motor based on thermal image investigation of the failure mode inside the motor. However, this study is focuses on thermal image bearings component. From the literature review, there is no further studies have been found to determine early detection of thermal overloading for bearing failure prediction based on thermal image processing techniques. This has been motivated to focus this research. Therefore, development the new algorithm of an early detection of thermal overloading for bearing failure prediction based thermal image

processing technique has been done. The focus on the developed algorithm is to solve the problem of feature extraction methods which is to retrieve the significant features of the bearing thermal image in order to detect the early bearing failure state due to thermal overloading effect. All extracting the hottest or coldest regions in the bearing thermal images was investigated in this thesis.

1.2 Problem Statement (buat semula)

Early detection of thermal overloading for bearing failure prediction based on thermal image processing techniques is the focuses in this research. Thermal overloading is one of the root causes that can lead to bearing failure which is focuses of this research. It is occurred when high load torque values is produced in the motor and generates current on the motor beyond the nameplate rated value (draw more current). This situation will causes an abnormal temperature and produces excessive heating that will accelerate the process of bearing failure. Subsequently, thermal overload also will potentially generate negative effects such as thermal stress, where it consequences cause the failure of motor parts such as bearing part and can affect the motor performance such as fatal breakdown of motor to freeze up and burn out. In machinery system, bearing is an important component and are used extensively in most rotating machines including electrical and mechanical system. Any bearing in operation will unavoidably fail at some point. If one of the bearings fails, not only the machine, but also the assembly line stops and the deriving costs may be extremely high. Thus, predicting the degradation process of bearings before they reach the failure is extremely important. To prevent potential problem occurred, early condition monitoring detection of such incipient faults is required for solving and as prevention for bearing component and many unexpected mechanical machinery performance degradation and malfunctions, to avoid sudden breakdown, minimize down-time, reduce maintenance cost, and extend the lifetime of machines. Thus, by monitoring the condition or health of the bearing component, failure can be predicted at an early stage.

Nowadays, there are a few current conditions monitoring technologies that been used in industry as a preventive maintenance including lumped parameter based thermal, vibration, sound and acoustic emission monitoring analysis but all these monitoring methods require specialized expertise to identify the health of the motor bearing condition. The use of these sensor-based methods become difficult and led to

long time consumption in determining the exact motor bearing failure due to data acquisition from the bearing through vibration signal induces a large amount of signal noise during machine operation, this make difficult to identify the signal obtained that usually drowned out in other noise emanating from the machine which will challenge the later fault diagnosis. Additionally, sensor-based method also sometimes invasive since it is often requires the installation of additional sensors and probes to obtain the vibration data. Besides, by using lumped parameter thermal monitoring, its function is to tune the parameters of a thermal model for overload protection, however, when the temperature rises in the region of the fault, this sensor is too slow to detect the incipient fault before it progresses into more severe faults. To address these issues, infrared thermal imaging-based monitoring approaches has been successfully proposed and utilized as an interesting complementary technique for condition monitoring of the bearing in this research due to its quick detection of potential problems or defects that will reduce troubleshooting time and preventative maintenance. This approach doesn't require human expert to interpret the thermal images and offer non-contact inspections that are extremely safe, reducing the need for predictive maintenance teams to put themselves in harm's way when performing an inspection. Subsequently, by combining this infrared thermal imaging system with an image processing approach; early detection of motor bearing failure conditions based on thermal imaging techniques are investigated. This thermal image processing approach will be processed by using MATLAB software.

Since there is no previous research focusing on the detection of thermal overload for bearing failure predictions at early stage, this research was motivated to look further for the suitable and efficient feature extraction methods to retrieve the significant features that can distinguish the condition of thermal bearing image failure prediction which further provides a more accurate solution to image processing system performance. From the previous literature, the ability of the Gabor Wavelet Transform (GWT) method for solving the feature extraction method to identify the presence of abnormal tissues in breast thermal images at early stages (Suganthi, 2014), motivated this study to develop the GWT method for extracting features of thermal overload to differentiate the condition of thermal bearing image. However from the experimental that has carried out, the result shows the accuracy performance for this GWT based feature extraction method and classification process is not fulfilled to distinguish the condition of thermal

bearing images in this study. This might be caused by the environmental condition at the time of capture the image which causes the features detected on thermal images is instable which contains noise and less contrast. Consequently, to address this issue, some modification image enhancement for thermal image features in image processing technique along with GWT-based extraction features is needed. From the previous review, the ability of the histogram equalization method for solving image enhancement method in thermal images for object detection and matching (Akçay & Avsar, 2017), motivated this study to employed this histogram equalization and GWT method respectively for solving feature extraction issues. Image enhancement method will adjust the low quality digital thermal images to produce more suitable image for extraction and classification by enhance the contract and remove the image noise involved. This process is carried out to improve the feature extraction and classification performance of thermal image processing system Therefore; this has led to the development of a new algorithm based feature extraction process, named as Enhanced Gabor Features (EGF). All the processing of bearing thermal images condition including data acquisition, feature extraction and classification processing were investigated in this thesis. Generally, the problem statements of this research can be summarized as follow:

(a) Weakness of conventional sensor-based methods such as:

-Lumped parameter based thermal too slow to detect the incipient fault before it progresses into more severe faults.

Vibration, sound and acoustic emission sensor-based difficult and led to long time consumption in determining the signal obtained that usually drowned out in other noise emanating from the machine which will challenge the later fault diagnosis.

(b) The implementation of feature extraction based on GWT algorithm in thermal images bearing has led to inaccurate solution in term of output learning performance for classification due to instability features and generates low quality to thermal images bearing.

(c) The accuracy performance for classification according to utilizing GWT based feature extraction algorithm produce inaccurate solution in order to distinguish the condition of thermal images bearing.

(d) The execution of GWT-based feature extraction algorithm for solving feature extraction in image processing system performance in order to differentiate thermal image bearing conditions is not efficient.

Therefore, the main research questions were set up as follows:

- (i) How thermal overload for a bearing failure prediction database be developed by using infrared thermography (IRT) monitoring technique?
- (ii) How can an Enhanced Gabor features (EGF) method be developed for solving thermal overloading for bearing thermal images failure conditions at early detection?
- (iii) What is the algorithm method based thermal image processing technique to classify the condition of thermal overloading for bearing thermal images failure conditions in early detection?
- (iv) Will the developed algorithm method be the efficient thermal imaging technique to solve image processing system performance for early detection of thermal overloading for bearing failure prediction based thermal image processing technique?

1.3 Objectives of the Study

Based on the research questions, this study embarked on the following research objectives:

- (i) To develop a new thermal imaging algorithm for three phase induction motor bearing failure detection based on the Gabor Wavelet Transform (GWT)-based Feature Extraction method.
- (ii) To identify the performance of a new thermal imaging algorithm by classifying the conditions of thermal induction motor bearing image by

using Multilayer Artificial Neural Networks (MLANNs) and Linear Thresholding (LT) techniques.

- (iii) To validate the performance of a new thermal imaging algorithm as a solution of feature extraction in image processing system performance by comparing the simulated accuracy results with the Gabor Wavelet Transform (GWT) technique. as well as comparing it with two other methods which are feature extraction based on HSV color method and I*a*b color method.

1.4 Scopes of the study (perbaiki)

Firstly, the database is collected in the morning in indoor area Power laboratory in Faculty of Electrical & Electronic Engineering, University Malaysia Pahang (UMP). In this work, the monitoring systems were carried out by using thermography camera FLIR A615 that has IR resolution 640 x 480 pixels at a distance of 0.5m. The sensor used in the experiments for this study is a long-wave IR camera. The details main specification of thermal camera used as indicated in Table 1.1.

Table 1.1 Specification of thermal camera

Thermal Camera	Rated Value
FLIR A615	-IR resolution: 640 x 480 pixels -80°(H) x 64.4°(V) FoV -20°C to +2000°C Object Temp Range -8 Lens Options -16-bit 640 × 480 pixel images at 50 Hz, signal, temperature linear, and radiometric -Thermal sensitivity/NETD: < 0.05°C @ +30°C (+86°F) / 50 mK -Ethernet type: Gigabit Ethernet

Afterwards, the specification of induction motor used in this research is a 1-hp, three phase asynchronous squirrel cage machine industrial version (SE2663-1K). The details main specification of induction motor operated as denoted in Table 1.2.

Table 1.2 Specification of Squirrel cage Induction Motor (SE2663-1K)

Induction Motor	Rated Value
Rated Voltage	400/230 V, 50Hz
Rated Current	1.8 Ampere
Rated Speed	1360 rpm
Cos phi	0.8
Dimension	340x210x210
Weight	9 kg

In this experiment, to obtain a dataset of thermal images for bearing conditions, the thermal load torque effect is applied to the motor. Load torque is proportional to stator current value which is motor current varies in relation to the amount of load torque applied. With increased load, the current also will increase as well. In this study, there are three conditions of thermal image bearing obtained the effect of load torque and stator current imposed on motor; normal, warning and abnormal condition. To obtain the normal state of the thermal bearing image, the need current output generated is under rated current motor which is below 1.8 Ampere. For warning state, thermal overload condition is created manually by increase load torque value cause the stator current also increase beyond the rated current value. However, the value of current in this region is still allowed by NEMA which is an additional 10% after rated value current [MG 1-12.47]. Meanwhile for abnormal condition, it is observed when the stator current generated in the motor beyond the 10% condition allowed by the NEMA. All the experiment data acquired is specified in the Table 1.3 as well as the entire thermal image produced is stored directly to the PC to be processed by MATLAB software.

Table 1.3 Load torque , stator current acquired and thermal image bearing conditions

Load Torque value (N-m)	Current value (Ampere)	Thermal images Bearing
0	0	Normal
0-0.2	0-0.55	Normal
0.2-0.4	0.55-0.8	Normal
0.4-0.8	0.8-1.8	Normal
0.8-2.0	1.8-1.98	Warning
0.8-2.0	1.98-2.0	Abnormal

Secondly, this research was aimed on developing an Enhanced Gabor Features (EGF) algorithm method based on thermal color for early detection of thermal overloading for

bearing thermal images failure conditions. An algorithm was developed to retrieve the significant features in order to prove that the presence of abnormal in the failure bearing thermal image due to thermal overloading effects could be identified in early detection.

Thirdly, the classification approaches was proposed by using Artificial Neural Network (ANN) method and Linear Thresholding (LT) method to classify and distinguish the selected features of bearing thermal images conditions which further provides a more accurate solution to image processing system performance in this research as well as a quantitative verification in this research. The ratio that is used in the classification process is 70% for training, 15% for testing and 15% for validation process.

Lastly, the validation process is done by compare the performance of Enhanced Gabor Features (EGF) algorithm method as a solution in image processing system performance by comparing the simulated accuracy results with the comparative studies with LaB colour method, HSV colour method and Gabor Wavelet Transform method

1.5 Research Significance (Perbaiki)

Based on the Gabor Wavelet Transform's method findings in this study, the presence of noise in an thermal image has reduce thermal image quality and has influence the accuracy performance in digital image processing system. In this work, a successful image feature extraction is essential to provide thermal image processing process accurately. Hence, the proposed Enhanced Gabor features (EGF) based feature extraction method in this work, it was managed to successfully address the low quality digital thermal images in order to produce more suitable images for extraction and classification process. This EGF method have performed to retrieve the significant Gabor features at different scales and orientations in order to identify the presence of normal, warning and abnormal for bearing thermal image due to thermal overloading effects at early stage. The ability the image enhancement process by adjusting the intensities of thermal image pixels in Enhanced Gabor features (EGF) method has enhanced the contrast and removes the image noises which subsequently enhance better features of an image. This result also will help improve the extraction performance of in thermal image processing system.

Second, this research also aims to improve the accuracy of classification performance of thermal image processing technique which is a quantitative verification system by classifying the features of bearing thermal images conditions using the Artificial Neural Network (ANN) and Linear Thresholding (LT) methods. The best classifier is selected which give a better accuracy solutions.

1.6 Thesis Organization (Perbaiki)

This thesis is divided into five main chapters. Below is a brief description of the chapters contained in this thesis.

Chapter 1: This chapter presents an introduction to the whole thesis. It introduces the background of this research and motivation of this study, the problem statements, research objectives, scope of the research as well as its significance.

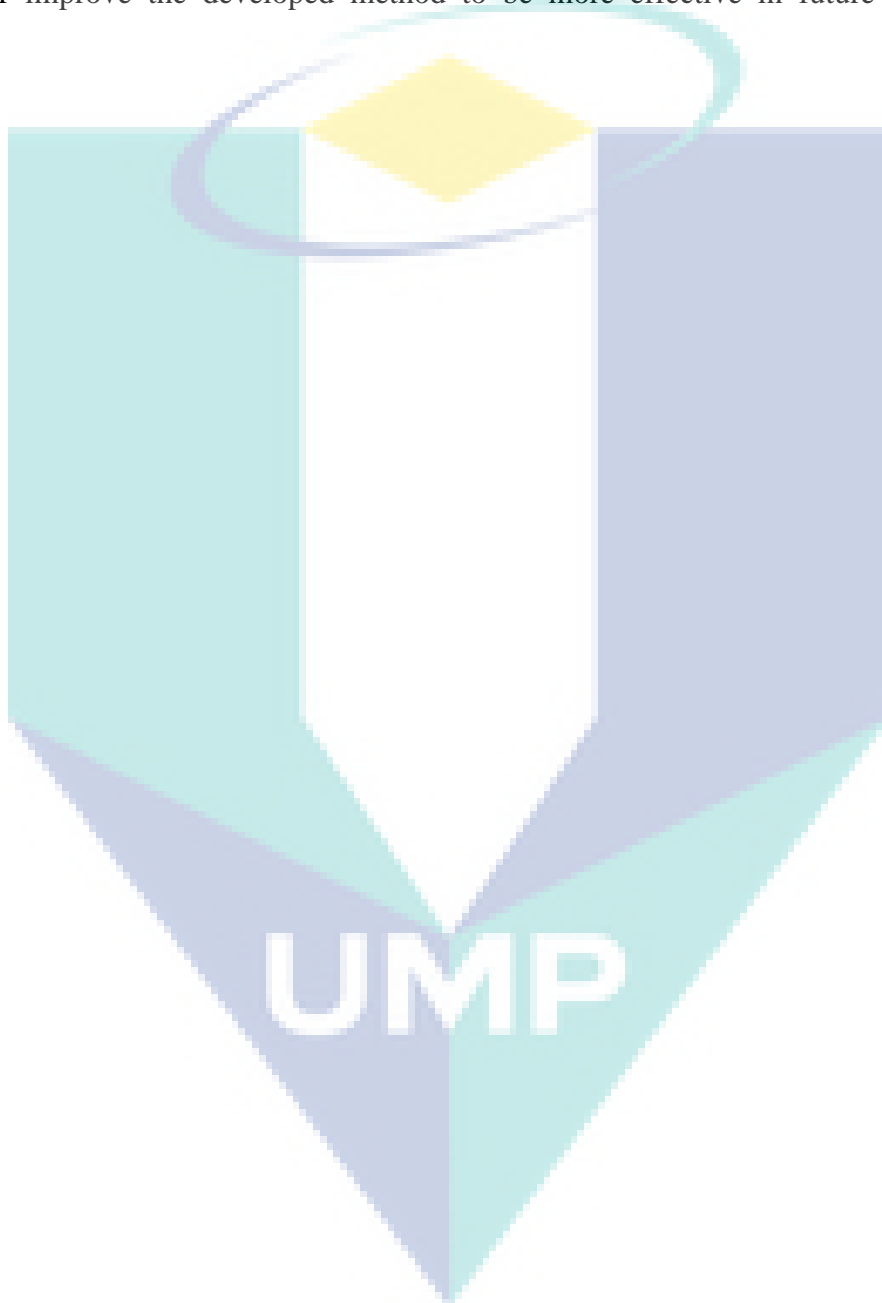
Chapter 2: This chapter describes the literature review of the related studies of this research. All important aspects such as condition monitoring based infrared thermal camera, bearing, and image processing method involved will briefly discussed. This chapter also focuses particularly on feature extraction methods used in thermal **overloading** for thermal bearing image failure predictions such as the HSV method, LaB method, and Gabor Wavelet Transform (GWT), which ultimately are motivated to develop a new feature extraction method namely Enhanced Gabor Features (EGF)

Chapter 3: This chapter discusses the methodology of thermal image processing in development of early detection of thermal overloading for bearing failure prediction using the Enhanced Gabor Features (EGF) feature extraction method. In this section the description of the related hardware and software to carry out the experiment are presented. Other method's methodologies (HSV, LaB and GWT approaches) as a comparison also will be presented in this chapter. All the thermal image processing involved will be thoroughly explained in separate sections in this chapter.

Chapter 4: This chapter presents the findings of thermal image processing of thermal overload for bearing failure prediction using the Enhanced Gabor Features (EGF) feature extraction method. The comparison with findings of other methods is also denoted in this chapter to prove that the performance accuracy obtained for the EGF-based feature extraction method provides a good solution in this thesis. Other

methods involved are HSV, LaB and GWT approaches. All the thermal image processing involved will be thoroughly explained in separate sections in this chapter.

Chapter 5 provides conclusions for the objectives of this research based on the attained findings. This is followed by few suggestions that can be implemented to further improve the developed method to be more effective in future applications.



CHAPTER 2

LITERATURE REVIEW

2.1 Introduction

kegagalan pada bearing motor boleh terjadi dari banyak faktor. salah satu darinya adalah kesan dari overloading dan selalui dijumpai dalam application. daripada literatures yang sedia ada, tiada lagi kajian yang fokus pada kerosakan bearing kesan daripada overloading ini keatas image processing dengan menggunakan thermal camera. ini menyebabkan termotivasi untuk membuat kajian ini.

failure on motor bearing can occur from many factors. one of them is the effect of overloading and being found in the application. of the existing literatures, there is no study focused on bearing damage resulting from this overloading on image processing using a thermal camera. This led to motivation to make this study.

One of it is the effect of overloading and being found in the machinery application. From the existing literatures, there is no research that focused on bearing faulty due to overloading on image processing by using a thermal camera. This led to motivation to make this study.

Bearing is an important component and are used extensively in most rotating machines including electrical and mechanical system to support static and dynamic loads. Their performance is of the utmost importance in automotive industries, aerospace turbo machinery, chemical plants, power stations, and process industries that require precise and efficient performance. Any bearing in operation will unavoidably fail at some point. Based on studies, the most common fault occurrences of induction motor are relate on bearing faults (Albrecht, Appiarius, McCoy, Owen, & Sharma,

1986; "IEEE Recommended Practice for the Design of Reliable Industrial and Commercial Power Systems," 1988; Thomson & Fenger, 2001). Yet, (Hashemian, 2011; Nandi, Toliyat, & Li, 2005; Schoen, Habetler, Kamran, & Bartfield, 1995) have identified that, up to 40%-50% of machinery defects are related to bearing faults. This has reveals that bearings are the primary cause and most severe and common fault in the motor system. In machinery system, they are many root causes that can lead to bearing failure such as lubricant failure, contamination, misalignment, corrosion, overheating, excessive load, fatigue and improper storage (Austin H Bonnett, 1992; A. H. Bonnett, 1993; "Chapter 3 - Machinery Component Failure Analysis," 1999; Huang, Yang, Zhou, & Litak, 2019; Vencl & Rac, 2014). If these potential problems are not identified and analysed promptly, sooner or later it will lead to a bearing problem that can cause the fatal breakdown of motor to freeze up and burn out. Therefore, to prevent these faults occurred, early monitoring detection of such incipient faults is required.

Since the beginning of 1990s, the development of reliable monitoring systems has become one of the most important tasks in a wide array of industries involving rotary machinery. It has become challenging and important task for the identification of different machine condition which can effect productivity, quality and cost for the industry. This condition monitoring is important as a way to avert many unexpected mechanical machinery performance degradation and malfunctions including bearing failure, to avoid sudden breakdown, minimize down-time, reduce maintenance cost, and extend the lifetime of machines. Thus, by monitoring the condition or health of the bearing component, faults can be predicted at an early stage and the appropriate maintenance can be scheduled or other actions can be taken to avoid the failure occurs.

2.1.1 Machinery system

Electrical motor torque is proportional to the product of magnetic flux and the armature current. Mechanical or load torque is proportional to the product of force and distance. Motor current varies in relation to the amount of load torque applied. When a motor is running in steady state, the armature current is constant, and the electrical torque is equal and opposite of the mechanical torque. When a motor is decelerating, the motor torque is less than the load torque. Conversely, when a motor is accelerating, the motor torque is higher than the load torque.

2.4 MOTOR STANDARDS

Worldwide, various standards exist which specify various operating and constructional parameters of a motor. The two most widely used standards are the National Electrical Manufacturers Association (NEMA) and the International Electrotechnical Commission (IEC).

2.4.1 NEMA

NEMA sets standards for a wide range of electrical products, including motors. NEMA is primarily associated with motors used in North America. The standards developed represent the general industry practices and are supported by manufacturers of electrical equipment.

2.4.2 Classification of NEMA Standard

The NEMA standards mainly specify four design types for AC induction motors- Design A, B, C and D. Their typical torque-speed curves are shown in Fig. 2.2.

- Design A has normal starting torque (typically 150-170% of rated) and relatively high starting current. The breakdown torque is the highest of all the NEMA types. It can handle heavy overloads for a short duration. The slip is $< 5\%$. A typical application is the powering of injection molding machines.

- Design B is the most common type of AC induction motor sold. It has a normal starting torque, similar to Design A, but offers low starting current. The locked rotor torque is good enough to start many loads encountered in the industrial applications. The slip is $< 5\%$. The motor efficiency and full-load power factor are comparatively high, contributing to the popularity of the design. The typical applications include pumps, fans and machine tools.

- Design C has high starting torque (greater than the previous two designs, say 200%), useful for driving heavy breakaway loads like conveyors, crushers, stirring machines, agitators, reciprocating pumps, compressors, etc. These motors are intended

for operation near full speed without great overloads. The starting current is low. The slip is $< 5\%$.

- Design D has high starting torque (higher than all the NEMA motor types). The starting current and full-load speed are low. The high slip values (5-13%) make this motor suitable for applications with changing loads and subsequent sharp changes in the motor speed, such as in machinery with energy storage flywheels, punch presses, shears, elevators, extractors, winches, hoists, oil-well pumping, wire-drawing machines, etc. The speed regulation is poor, making the design suitable only for punch presses, cranes, elevators and oil well pumps. This motor type is usually considered a “special order” item. Recently, NEMA has added another design -D in its standard for induction motor. It is similar to design B, but has a higher efficiency.

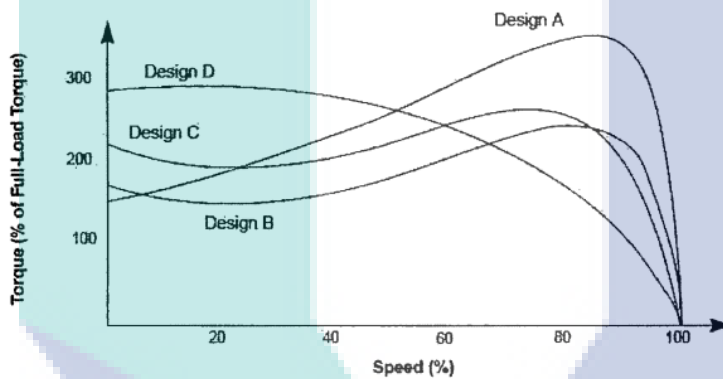


Fig. 2.7 Torque Speed Curve for different NEMA standard

2.43 IEC

IEC is a European-based organization that publishes and promotes worldwide, the mechanical and electrical standards for motors, among other things. In simple terms, it can be said that the EEC is the international counterpart of the NEMA. The IEC standards are associated with motors used in many countries. The EEC torque-speed design ratings are the same as those of NEMA those used in industries. Only the EEC duty cycle ratings are different from those NEMA. This duty cycle is given below. With respect to design criteria, all other things except the duty cycle are same as NEMA.

Locked rotor current (<https://kebblog.com/nema-b-three-phase-squirrel-cage-motors-locked-rotor-current/>)

For NEMA B motors, here is a listing of the maximum allowed locked-rotor current at 230V, as defined by MG 1 12.35.1. For values outside 230V, NEMA states "The locked-rotor current of motors designed for voltages other than 230 volts shall be inversely proportional to the voltages". Which leads us to calculate the other values.

HP	Locked rotor current (A)			
	200	230	460	575
0.5	23	20	10	8
0.75	29	25	13	10
1	35	30	15	12
1.5	46	40	20	16
2	58	50	25	20
3	74	64	32	26
5	106	92	46	37

2.1.1.1 AC Motor and DC Motor

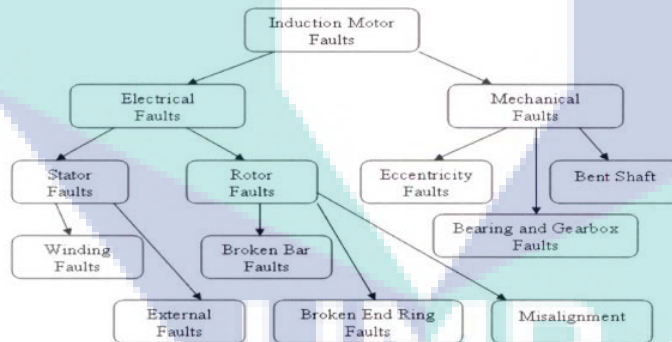
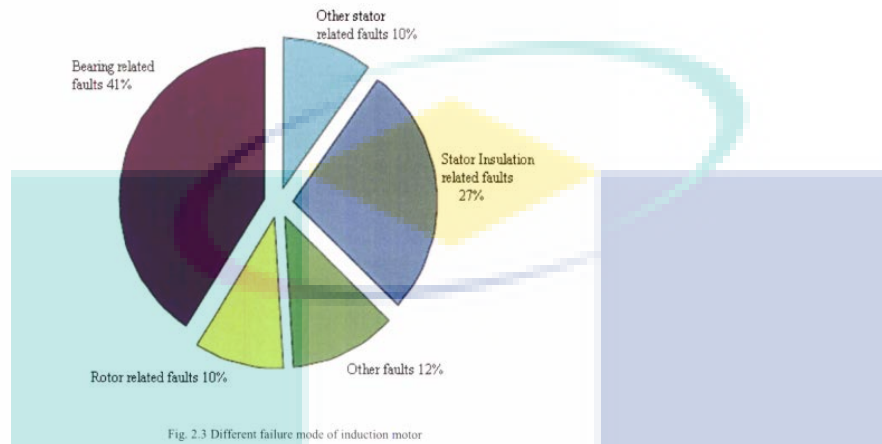


Fig. 2.2 Block diagram of Induction motor fault categories

2.1.1.2 Bearing

2.2.1 Mechanical Failure Mode

An energy research consortium study gives that 53 percent of motors fail due to mechanical reasons [35]. The failure distribution is as follows:



Numerous factors have a profound effect on the actual life of bearing. These factors are as follows [48]

2.2.1.1 Bearing Failure

Bearing problems are the primary cause of motor failure. Almost 40-50% of all motor failure is bearing related. Numerous factors have a profound effect on the actual life of bearing. These factors are as follows [48]

- Contamination = 45% to 55%
- Lubrication = 11% to 17%
- Improper assembly = 11% to 13%
- Misalignment = 10% to 13%
- Overloading (application) = 8% to 10%
- Other = 1% to 6%

Rolling element bearings generally consist of two rings, an inner and an outer, between which a set of balls or rollers rotate in raceways. Under normal operating conditions of balanced load and good alignment, the fatigue failure begins with small value located between the surface of the raceway and the rolling elements will gradually propagate to the surface generating detectable vibrations and increasing noise levels. Continued stress causes fragments of the material to break loose, producing localized fatigue phenomena known as flaking. Once started, the affected area expands rapidly contaminating the lubricant and causing localized overloading over the entire circumference of the raceway. Eventually, the failure results in rough running of the bearing. While this is the normal mode of failure in rolling element bearings, there are many other conditions, which reduce the time to bearing failure. These external sources include contamination, corrosion, improper lubrication,

focussing on bearings of rotating machinery

How Do Motors Fail?

Bearings.....60-70%	Insulation.....30-40%
<ul style="list-style-type: none"> ■ • Over/Under Lubrication ■ • Misalignment/Belt Tension • Contaminants/Compatibility • Vibration • Thrust ■ • High Ambient • Bearing Currents • Fatigue....L10 	<ul style="list-style-type: none"> ■ • Overload ■ • Excessive Number of Starts ■ • Contaminants/Ventilation Failure ■ • Thermal Aging • Voltage spikes from VFD's ■ • System Disturbances ■ • Excessive Load Inertia ■ • Insufficient Torque ■ • Locked Rotor ■ • Single Phasing ■ • High Ambient • Vibration

2.1.1.3 Cause of Faults

2.1.2 Motor for industrial machine

2.1.3 Diagnosis and Monitoring System for Bearing

Acoustic emission monitoring

Current analysis

Many researchers have focused their attention on incipient fault detection and preventive maintenance in recent years. There are invasive and noninvasive methods for machine fault detection. The noninvasive methods are more preferable than the invasive methods because they are based on easily accessible and inexpensive measurements to diagnose the machine conditions without disintegrating the machine structure.

The mechanical fault detection is typically based on vibration signals, a robust and effective technique, that is quite invasive and with high latency.

Early stage fault diagnosis of Induction Machines (IMs) is an important research topic for cost and maintenance savings

It is preferable to find faults before complete motor failure. This is called “incipient fault detection”. Often the motor can run with incipient faults, but eventually it will lead to motor failure causing downtime and large losses

Vibration signals are commonly adopted for mechanical faults detection in IMs and/or related mechanical loads.

Mechanical faults as bearing faults, shaft-load connection faults, gear faults and mechanical imbalances are usually monitored by vibration signals. The vibration monitoring is wide spread and relies on common standards, such as ISO 10816. Vibration signals are obtained by sensor placed on the external part of machine and they are quite reliable and mature.

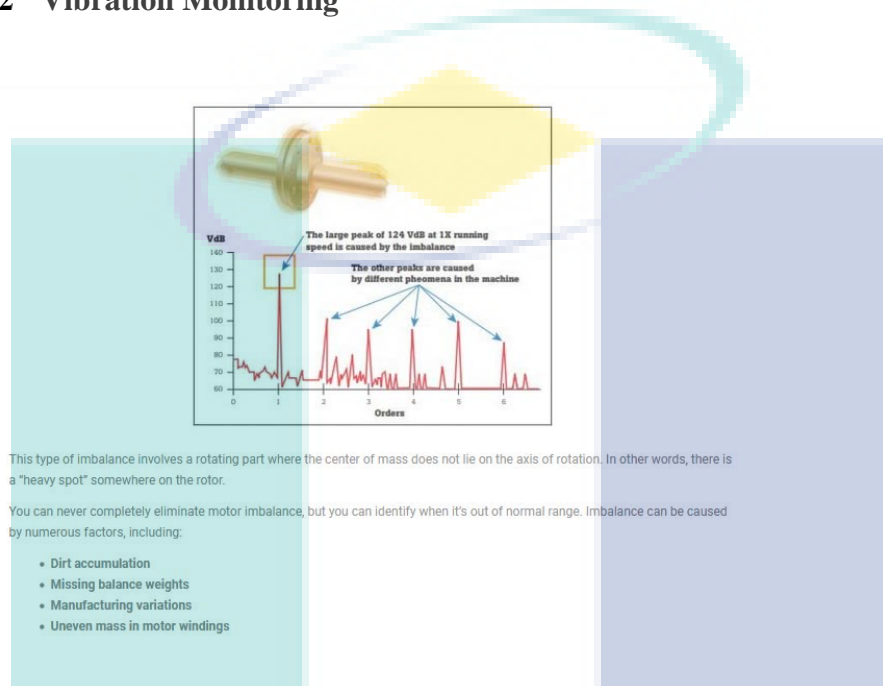
For this reason, early identification of failures is of great importance

The rotating machinery plays a vital role in industrial systems, in which unexpected mechanical faults during operation can lead to severe consequences. For fault prevention, many fault diagnostic methods based on vibration signals are available in the literature. However, the vibration signals are obtained by using different types of sensors, which can cause sensor installation issues and damage the rotating machinery. In addition, this kind of data acquisition through vibration signal induces a large amount of signal noise during machine operation, which will challenge the later fault diagnosis. A recent fault detection method based on infrared thermography (IRT) for rotating machinery avoids these issues. However, the corresponding literature is limited by the fact that the characteristics of the manual design cannot characterize the fault completely so that the diagnostic accuracy cannot exceed the diagnostic method based on the vibration signals. This paper introduces a popular image feature extraction method into the fault diagnosis of rotating machinery based on IRT for the first time. First, capturing the IRT images of the rotating machinery in different states, and then two popular feature extraction methods for IRT images, bag-of-visual-word, and convolutional neural network, are tested in turn. Finally, the extracted features are classified to implement the automatic fault diagnosis. The developed method is applied to analyze the experimental IRT images collected from bearings, and the results demonstrate that the developed method is more effective than the traditional methods based on vibration signals.

2.1.3.1 Ultrasound Emission Monitoring

Vibration techniques are suitable for higher rotating speeds whilst acoustic emission techniques for low rotating speeds

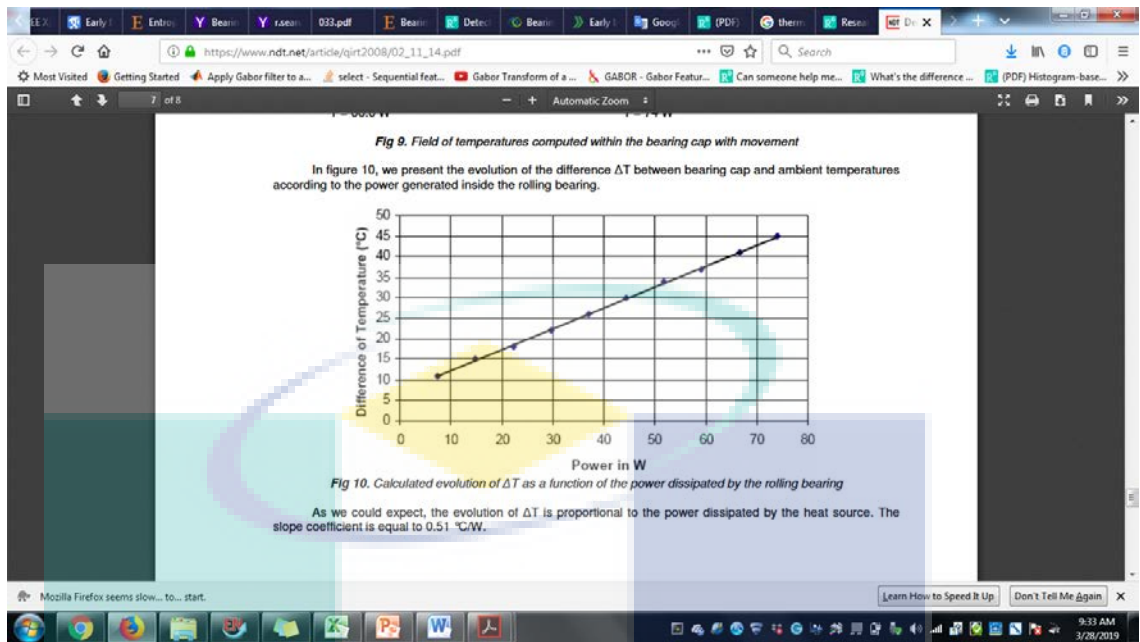
2.1.3.2 Vibration Monitoring



on the one hand the vibratory defect engendered within the rolling bearing leads to a quantifiable heating of the surface (Mazioud, Ibos, Khlaifi, & Durastanti, 2008)

2.1.3.3 Thermal Imaging Monitoring

Thermal intensity is a function of the temperature radiated from an object and the contrast of the object with the background (Duberstein et al., 2012)



2.2 State of Arts method for the Feature Extraction Process in Thermal Motor Bearing Image

2.2.1 Color-based feature extraction methods

2.2.1.1 HSV based-method

2.2.1.2 L*a*b based-method

The color based image feature extraction using L*a*b is proposed in this work as a way to compute and extract a set of features from thermal images. This L*a*b* colour space method includes all perceivable colours which means that its gamut exceeds those of the RGB and CMYK colour models. This method is proposed due to it is one of the most important attributes of the L*a*b* model is the device independency. It means that the colours are defined independent, thus the different colors in image could be analysed.

2.2.2 Transformation-based feature extraction method

Generally, the set of scale channels is configured to capture a specific scale of frequency components from an image. Meanwhile, the set of the orientation channels is utilized to extract the directional of features.

2.2.2.1 Original GWT based feature extraction

The beginning of GWT was invented by a Hungarian-born British physicist, Dennis Gabor in 1946. This technique is a good characteristic of space-frequency localization, effective to all images at different scale's level, and widely worked in various applications for extracting features such as in object detection, content based image retrieval (CBIR), recognition and tracking. This Gabor Wavelet based algorithm such Gabor filter with appropriate scale and orientation angle is proposed in this work as an essential task to compute and extract a set of visual features from the response of the thermal image bearing based on **different illumination** of the database. Features based on Gabor filters have been used in image processing due to their powerful properties. Gabor kernels are characterized as localized, orientation selective, and frequency selective. A family of Gabor kernel is the product of a Gaussian envelope and a plane wave. A 2D Gabor filter is expressed as a Gaussian modulated sinusoid in the spatial domain and as shifted Gaussian in the frequency domain. The Gabor wavelet representation of images allows description of spatial frequency structure in the image while preserving information about spatial relations. The Equation of Gabor is customized as

2.2.2.2 Proposed an Enhanced Gabor Features (EGF) -based Feature Extraction Method

The purpose of this implementation is to improve the classification performance of the image processing system in this study. From the literature, several studies have shown that a resolution-enhanced image gives better classification performance in image processing systems (Ji, Wang, Su, Song, & Xing, 2013; Thangaswamy, Kadarkarai, & Thangaswamy, 2013). Through their studies,

This section discusses the feature enhancements from the original feature extraction method based on GWT as in section 3.5.1. The purpose of this implementation is to improve the classification performance of the image processing system in this study. From the literature, several studies have shown that a resolution-enhanced image gives better classification performance in image processing systems (Ji, Wang, Su, Song, & Xing, 2013; Thangaswamy, Kadarkarai, & Thangaswamy, 2013). Through their studies,

process using the image's histogram in order to enhance the features proposed in this work due to it is simple and ease of use than other conventional methods, a higher performance and output with almost all kind of image. This histogram equalization approach is a spatial domain technique and generates uniform distribution of pixel intensity on the output image. Therefore, by applying this HE method with the manipulation the level of gray based on the distribution probability on the input image (Abdullah-Al-Wadud, Kabir, Dewan, & Chae, 2007), the new grayscale levels intensities from output histogram's image is generated and an image can be improved of the output image. The histogram equalization (HE) method is proposed in this work as a contrast enhancement

Therefore, it has been motivated to use enhancement methods in this study for the purpose of improving the features based on the feature extraction method.

The histogram equalization (HE) method is proposed in this work as a contrast enhancement process using the image's histogram in order to enhance the features images by improving the interpretation of information contained in it. It is also proposed in this work due to it is simple and ease of use than other conventional methods, a higher performance and output with almost all kind of image.

To overcome the problems of variations in brightness and contrast, as well as, the different lighting conditions, histogram equalization [25] was used.

Histogram equalization is a technique for adjusting image intensities to enhance contrast.

It is very important because as in HE process, the image variance is increased and pixel intensity range is stretched to available range of pixel intensity. By this pretreatment, features can be easily segmented and classified

It is very important because as in HE process, the image variance is increased and pixel intensity range is stretched to available range of pixel intensity. By this pretreatment, features can be easily segmented and classified.

No, it only affects the image brightness and improve it.

In general, HE increases the contrast of the image.

(R. C. Gonzalez a& R. E. Woods,(2008) "Digital Image Processing" , Prentice-Hall, 3rd Edition.)

This histogram equalization approach is a spatial domain technique and generates uniform distribution of pixel intensity on the output image. Therefore, by applying this HE method with the manipulation the level of gray based on the distribution probability on the input image (Abdullah-Al-Wadud, Kabir, Dewan, & Chae, 2007), the new grayscale levels intensities from the output histogram's image is generated and an image can be improved of the output image.

2.2.2.3 Proposed an Enhanced GWSMH -based Feature Extraction Method

As in Section 3.5.2, this study proposes an image enhancement process for GWT-based feature extraction methods to improve the visual quality of the original proposed method as in section 3.5.1. According to (da Silva & Mendonça, 2005), by improving the visual quality of the image, it will improve classification performance in the image processing system. Therefore, the studies in this section have been proposed.

2.2.2.4 Proposed an Enhanced GWCLAHE -based Feature Extraction Method

2.3 Feature Selection

From the previous studies, a multi-scale and multi-orientation features at each image points from the feature extraction based on GWT technique will produced [cited]. This high dimensional of the resultant Gabor feature vector that occurs will

cause the computational and memory required for recognition are prohibitively large. To address this problem, feature reduction method will be employed to reduce the dimensionality of the data in order to simplify the calculation analysis and improve learning performances in term of higher learning accuracy for classification in this work. Feature selection is one of the most popular methods due to the preservation of the original meaning of features and it is an important part of machine learning. This feature selection is an approach to seek to capture the most useful subset of the original variables or features for use in the implementation of the machine learning model in order to speed up the training time, enhance the learning interpretability, lowering computational cost and complexity. Furthermore, the current subset generated from these predictive features will improve the robustness of the classification models.

From the previous studies, there are various feature selection techniques that have been implemented in the field of machine learning. According to (Abhishree, Latha, Manikantan, & Ramachandran, 2015), they were proposed a feature selection approach by using binary particle swarm optimization (BPSO) to solve a high dimensional data that occurred from the Gabor filter extraction into face recognition application. It is to find a feature space for the optimal feature subset. However, this BPSO approach is much more computationally intensive and it's reducing the number of features to approximately half only. In (Shen & Bai, 2006), they proposed a feature selection based AdaBoost Algorithm in order to eliminate redundancy among Gabor features. This technique is not ideal as redundancy among AdaBoost selected features. As a result, many classifiers selected by the AdaBoost algorithm might be similar and redundant. They improved their selection technique by developing a mutualBoost algorithm, however this algorithm technique is complex, requires longer training time and much more computational.

Moreover, as explained in (Alelyani, Tang, & Liu, 2018; Panda Suchishree, 2018; Rodriguez-Galiano, Luque-Espinar, Chica-Olmo, & Mendes, 2018; Stańczyk, 2015), feature selection can also categorized into two standard approaches which are filter models and wrapper models which are briefly described as follows. The filter model relies on a proxy measure to select some features in the original variables without any additional learning model on the training dataset. However, the wrapper model requires a specified predictive model for each new subset and uses the error rate of the model to

score, and the subset with best performance is selected out. Since each subset is used to build the predictive model, it is much more computationally intensive, particularly for large feature spaces because each feature set must be evaluated, computation cost and slow down the feature selection process.

In this study, filter-based feature selection model is employed due to this filter method are much simpler to build and faster in process, scalable with high dimensional datasets and also computationally simple compared to wrapper approach. This filter algorithm consists of two steps. First step, features are selected and ranked, evaluated independently of feature space in the univariate scheme and in a batch in multivariate scheme. Second step, the best performance subset are chosen based on highest rankings and selected out in order to induce classification models. Some common filter-based feature selection methods are fisher score (FS), chi-square (CS) and information gain (IG) (Bhattacharya & Goswami, 2017; Sánchez et al., 2018; Sharma, Krishna, & Sahay, 2019; Vora & Yang, 2017; Y. Zhang, Zhou, Zhang, & Song, 2019). These feature selection methods is ranked by ranking, compute and return a score for each feature individually. Previous studies have demonstrated that the fisher score has good general performance in feature selection (Ahmad, Javed, & Hayat, 2017; Ahmed & Nandi, 2017; Aksu, Üstebay, Aydin, & Atmaca, 2018; Cherrington, Thabtah, Lu, & Xu, 2019; Gu, Li, & Han, 2012a; Saqlain et al., 2019; Sharma et al., 2019; Sun et al., 2019).

Over the year, fisher score method have been implemented extensively in various application in image processing field for solving high dimensionality data resulting from feature extraction process(Ahmad et al., 2017; Ahmed & Nandi, 2017; Aksu et al., 2018; Bhasin, Bedi, & Singhal, 2014; Cherrington et al., 2019; Gu et al., 2012a; Roffo & Melzi, 2016; Saqlain et al., 2019; Sharma et al., 2019; Song, Jiang, & Liu, 2017; Sun et al., 2019; Żbikowski, 2015). Yet, there are a few studies regarding implementation of feature selection based fisher score in order to eliminate the irrelevant Gabor features extraction (Li, Mao, Zhang, & Chai, 2010; Ma, Zhu, Wang, Liu, & Jing, 2019; Vamsidhar, PhaniKumar, & Gunna Kishore, 2016). The experimental results of the studies have shown better performance in classification result. In this way a significant reduction in computation and memory cost has been achieved. Hence, it has been motivated to propose a fisher score selection methods to be employed in this study for feature selection purposes.

Fisher score is one of the most widely and commonly used supervised feature selection technique and adopted to eliminate irrelevant features in order to choose the most useful features information. This approach provides a measure of features' ability to distinguish between different classes. The selected features were then fed as an input to the classification model. In this feature selection process, it computes a subset of features with a large distance between data points in different classes and small distance between data points in the same class, and the final feature selection occurs by the top ranked ones (Gu, Li, & Han, 2012b; Islam, Jeong, Bari, Lim, & Jeon, 2015; Ma et al., 2019; T. Zhang & Lu, 2010). This method are simple, reduce computational cost, fast and effective filtering method (Gu et al., 2012a). Given the input data matrix $Y \in R^{n \times j}$ reduces to $F \in R^{m \times j}$. Then, the index of a feature score f_s is computed as equation 3.32 follows:

$$f_s = \frac{\sum_{i=1}^c n_i (\mu_j^i - \mu_j)^2}{\sum_{i=1}^c n_i (\sigma_j^i)^2} \quad 3.1$$

Where μ_j is the mean of all data sample values on the j -th feature, n_i is the number of data samples in the i -th class, and μ_j^i and σ_j^i are the mean and variance in the i -th class corresponding to the j -th feature. By utilizing this formula, the experimental study will show that the size of high dimensional features and the computations involved in feature extraction process can be significantly reduced where features with top scores which is produce features with most discriminative power is selected by the fisher score.

. From the literature, the large size of the input data features will cause problems in the classification process.

2.3.1 ANOVA

The Df column displays the degrees of freedom for the independent variable (calculated by taking the number of levels within the variable and subtracting 1), and the degrees of freedom for the residuals (calculated by taking the total number of

observations minus 1, then subtracting the number of levels in each of the independent variables).

The Sum Sq column displays the sum of squares (a.k.a. the total variation) between the group means and the overall mean explained by that variable.

The Mean Sq column is the mean of the sum of squares, which is calculated by dividing the sum of squares by the degrees of freedom.

The F-value column is the test statistic from the F test: the mean square of each independent variable divided by the mean square of the residuals.

2.4 Classification

2.4.1 K-Fold Cross Validation in Multi-layer Artificial Neural Networks (MLANNs)

. ANN model is a faster, robust, more accurate technique and it is composed of numerous types. There is single layer ANNs as well as multiple layers of neurons. The Multilayer feed-forward network or called the Multi-layer Perceptron (MLP) is one of the architecture of ANN contains multiple layers of neurons that is formed by the interconnection of several layers. It is the best ANN model that can solve complex problems as it has many hidden layers to overcome the weakness of a single layer perceptron. Over the year, MLANN is one of the extensively used techniques for classification of class of objects in image processing fields. It is also applicable in various applications such are pattern recognition (Gaja & Liou, 2018), medical (Aruna Devi B., 2019; Mohammed et al., 2018), dental (Raith et al., 2017), electrical system (Bighnaraj Panda, 2018; Taheri-Garavand et al., 2015), mechanical system (B. Hizarci, 2019; Jain, Meenu, & Sardana, 2019) and so on.

There are several types of training functions used in ANN models and their selection is one of the behaviors for successful ANN modeling (Kamble, Pangavhane, & Singh, 2015; Karim, Niakan, & Safdari, 2018; Lassoued & Ketata, 2018). From some studies, comparative learning algorithm between ‘*trainlm*’ and ‘*trainbr*’ has been performed. As a result, ‘*trainbr*’ showed better performance classification in term of accuracy compared to ‘*trainlm*’ (Garg & Bansal, 2015; Kamble et al., 2015). Thus, in

this work, feed forward MLANNs with Lavenberg-Marquardt backpropagation (*'trainlm'*), Bayesian regularization backpropagation (*'trainbr'*) and Scaled conjugate gradient backpropagation (*'trainscg'*) training algorithms will be employed to fit the ANN model purpose. As well as evaluate the impact of all these three learning algorithms to the classification performance of the proposed MLANNs. A brief description of the differences training algorithms between *'trainlm'*, *'trainbr'* and *'trainscg'* types are shown in Table 3.3.

Table 3.1 Description of *'trainlm'* and *'trainbr'* training algorithms

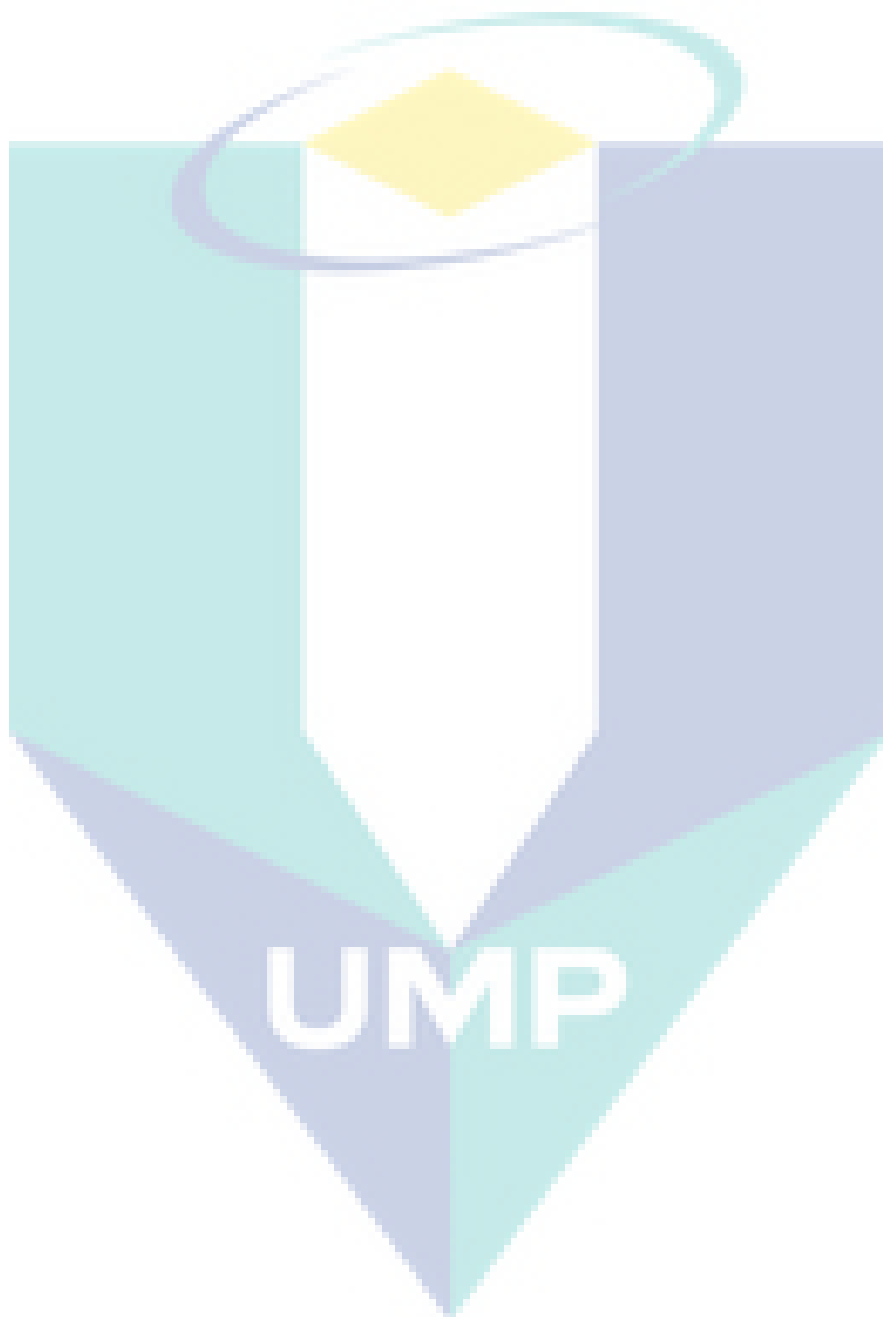
Training Function name	Algorithm	Description
Trainlm	Levenberg Marquardt	<p>(a) <i>'trainlm'</i> is a network training function that updates weight and bias values according to Levenberg-Marquardt optimization.</p> <p>(b) <i>'trainlm'</i> is an iterative technique which its performance function will always be reduced in each iteration of the algorithm. This feature makes <i>trainlm</i> the fastest training algorithm for networks of moderate size.</p> <p>(c) It has memory reduction feature for use when the training set is large</p> <p>(d) To minimize mean square error</p>
Trainbr	Bayesian regularization	<p>(a) The <i>'trainbr'</i> training algorithm is a modification of the Levenberg-Marquardt training algorithm approach. It is developed for reducing the memory employed by the <i>'trainlm'</i> optimization algorithm to gain the most excellent generalization of the network.</p> <p>(b) To minimize a weighted sum of squared errors and squared weights</p>
Trainscg	Scaled Conjugated	

Gradient Backpropag ation

Based on literature reports, there are many approaches used for data splitting. These methods include leave-one-out (LOO) CV, k -fold CV (Jiang & Wang, 2017; Jung & Hu, 2015; Kohavi, 2016) and bootstrapping (Hjorth, 2017). Among all the stated techniques, the K -Fold method is chosen because it is compatible with the application used in this work where all observations are used for training and validation and each observation is used for validation exactly once. Yet, this method is cheaper because of less computation time processing. The variance of the resulting estimate also is reduced as K increases.

A multi-layer feed-forward neural network has been used in training a data set on input patterns. A three-layer network was used: the input layer, a hidden layer and the output layer. For the input layer, the input feature vectors come from the Gabor filter feature extraction stage and consist of 100 neurons applied to the neural network. A single pattern p to be tested or fed to the neural network can be considered as a vertical vector of elements (features). Then t is called the target for this pattern and you have to know t in advance and to use it along with its conjugate pattern for the purpose of network training. For many features in an image set, the set P of vertical vectors represents the set of patterns (features) for which you know their desired target in advance in the form of T as a horizontal vector. Each element of the T vector corresponds to a column in P matrix. These vectors are processed in the hidden layer using the scaled conjugate gradient method as the training method and the mean square error with regularization as the performance function to adjust the network output to be in the range -1.0 to 1.0 . The output layer size depends on the obvious candidate features in each landmark. The following figure shows a typical multi-layer feed-forward neural network.

2.4.2 Linear Thresholding



CHAPTER 3

METHODOLOGY

3.1 Introduction

This chapter presents the thermal image processing that will be carried out to achieve the objectives in this study. The focus of this present study is to solve the problems that occur in the feature extraction method. The problem that occurred was from the experiment of the original GWT-based feature extraction method on images has been carried out in this study. There are limitations obtained from this experiments which is the result of the classification performance on the thermal motor bearing image group shows a poor performance. This is due to the thermal motor bearing images groups cannot be well distinguished. As a consequence, some modifications to the features of thermal motor bearing images based on the original GWT method will be executed to improve the visual quality of images in this study. This has contributed to the development of a proposed new feature extraction method in order to overcome the limitation found in the original GWT-based method.

Therefore, to achieve the objectives of this study, the entire image processing will be performed as illustrated in Figure 3.1. The image processing involved in this study is data acquisition, segmentation, feature extraction, feature selection and also the classification process. From the figure shown, it can be observed that there are three new feature extraction methods that will be developed based on the original GWT method. They are Enhanced Gabor Features (EGF), Enhanced GWSMH and also Enhanced GWCLAHE. These methods are the main focus of this study which is to improve the visual quality of the images. This feature extraction process will be explained further as in section 3.4. Next, the selection of the optimal features will be explained in detail in section 3.5. The classification performance is also the main focus

in this study. By modifying the pixel value (intensities) of the image, the classification performance will also be improved accurately. Furthermore, the features of thermal motor bearing images could also be distinguished well in this study. This classification process will be explained more clearly in section 3.7.

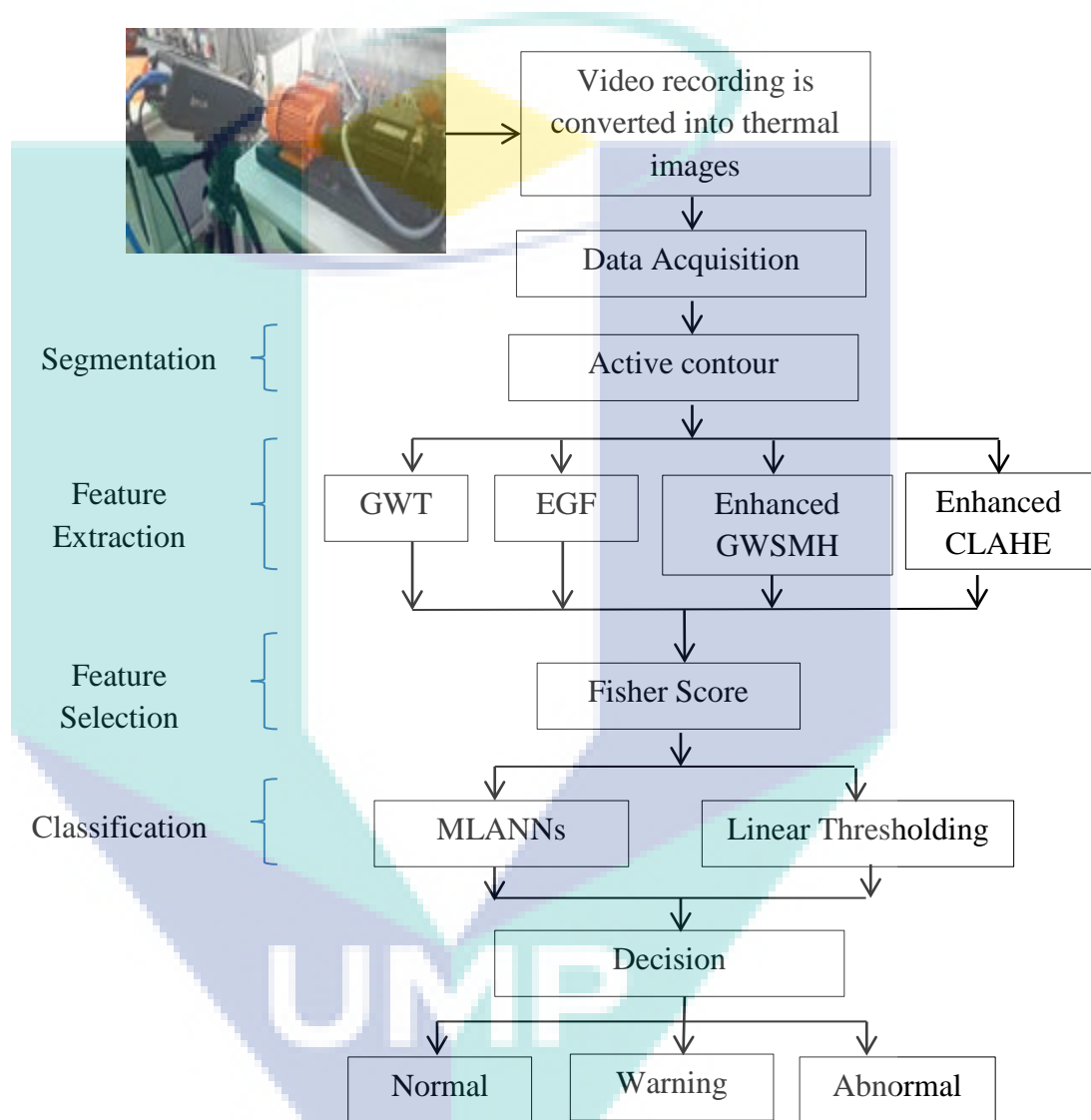


Figure 3.1 Block diagram of overall image processing in thermal motor bearing images

3.2 Data Acquisition

The experiment for test and observe the abnormality of the bearing machine conditions was performed on single phase 0.5hp, 0.37KW, 230/400V, 50Hz motor. The

monitoring system is implemented as illustrated in Figure 3.2 executed by using FLIR A615 thermal camera at a distance of 0.5m. The thermal camera's sensor used in this work is a long-wave IR camera. Motor current rated for this induction motor is 1.8Ampere. In the beginning, the speed motor value 1280rpm was executed for five minutes in this experiment in order to allow the machine to generate initial heat.

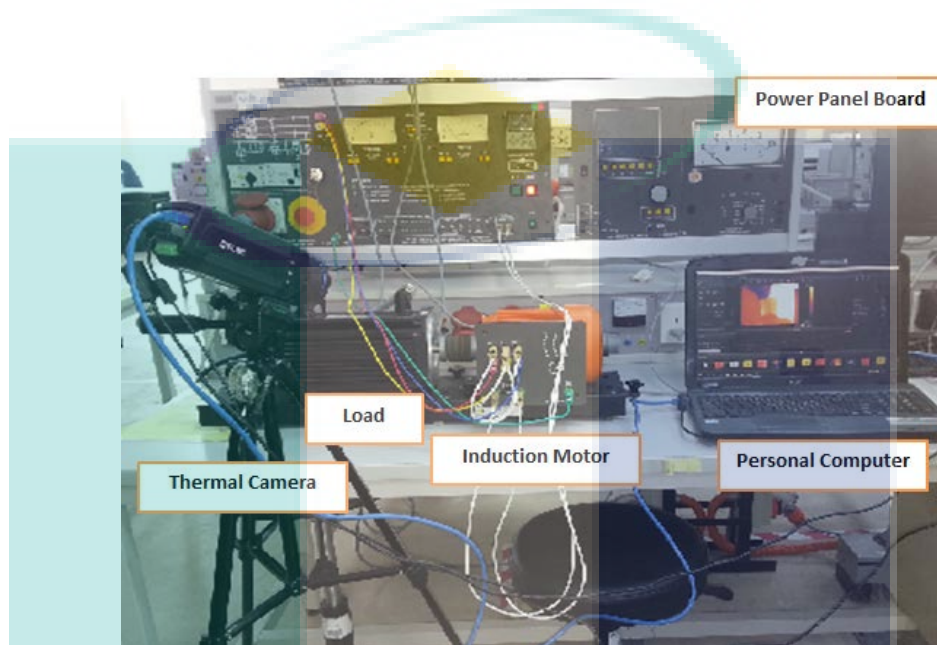


Figure 3.2 Experiment setup using thermal camera.

According to Figure 3.3, it denotes an experimental of single phase induction motor condition that shows bearing part that been analysed where it is placed on shaft induction machine part. At the beginning, the infrared thermal images of the normal bearing motor are acquired first. During the acquisition process, the load torque is increase slowly from 0.2 N-m until reach 0.8N-m in order to observe the thermal pattern of the normal condition of bearing machine. After that, to acquire the infrared thermal image of the abnormality of the bearing, excessive load condition is created manually by increase the value of torque until reach 2.0N-m. At this moment a large current is observed and drawn more than rated current at full load in the rotor windings as well as stator current also is increase; cause extremely high temperatures to be generated within the motor as well as in bearing machine part. This is made worse by the fact that the speed of the rotor decreases to a very low value and motor is not rotating completely, and hence no cooling process due to motor is unable to rotate. According to motor current rating in NEMA Std. MG 1, 12.47, during the motor operate at rated voltage, rated frequency, and rated horsepower output, the input in

amperes could not vary from the nameplate value by more than 10%. Thus, from this experiment, the higher current induced by the induction machine is 2.0Ampere and it has exceeded the current rated value of the motor rating and this condition known as an abnormal state. (TAMBAH LAGI)

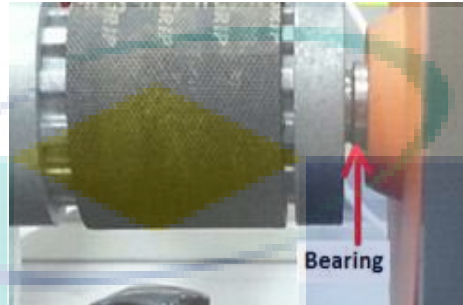


Figure 3.3 Surface bearing part of induction motor

3.3 Pre-Processing and Segmentation

After the image acquisition procedure, image segmentation process will be employed in order to obtain the region of interest (ROI) based on desired features. Through this process, it will simplify the representation of an image into something that is meaningful and easier to be analyzed.

To achieve this purpose, manual crop will be applied to the images according to the coordinates to be set in order to separate the foreground from the background. This process will be performed to retrieve the meaningful information from the bearing area. Nonetheless, to improve the segmentation of the bearing area well, the active contour or known as snake's model will be utilized in this operation. It acts as a curve propagation method that was first introduced by Kass et al (Kass, Witkin, & Terzopoulos, 1988). It will be implemented to detect the curve of an image object where to select the area (pixels) of interest required in an image (Kass et al., 1988). It's also to define smooth shape in the image and forms closed contour for the region.

From the previous studies, this active contour technique has successfully implemented in computer vision and image processing applications like object tracking, shape recognition, segmentation, edge detection and stereo matching (Blake & Isard, 2012; Qiao, Bao, Zeng, Zou, & Li, 2017). This approach will be applied due to simple, fast and accurate automatic segmenting (Eviatar & Somorjai, 1996; Fang, Wang, &

Wang, 2020; Medeiros et al., 2019; Nithila & Kumar, 2019; Williams & Shah, 1992). This method is also widely implemented in medical image processing for segmentation of regions from different medical images such as brain CT images, MRI images, cardiac images, liver vessel (Chung, Lee, Chung, & Shin, 2018; Eviatar & Somorjai, 1996; Fang et al., 2020; Han, Han, Gao, & Zhang, 2019; Hemalatha et al., 2018; Medeiros et al., 2019; Nithila & Kumar, 2019). The active contour will be applied to minimize the energy function from the different forces which are external and internal force in order to form a desired contour point at the shape of image boundaries. The energy forming this contour point can be written as equation 3.1 until equation 3.3:

$$E_c(s) = E_i(c(s)) + E_x(c(s)) \quad 3.1$$

$$E_i c(s) = \quad 3.2$$

$$E_x(c(s)) = \quad 3.3$$

According to (Vinay, Vinay, & Narendra, 2014), the active contour method had proven been successfully applied as medical image segmentation for partition a medical image of Anterior Cruciate Ligament (ACL) accurately. This has motivated this active contour method to be used in this study. Figure 3 illustrates a flow chart representation of pseudocode 2 regarding the active contour-based segmentation process to improve the segmentation of the bearing area in this study.

Pseudocode 1: Active Contour-based segmentation technique

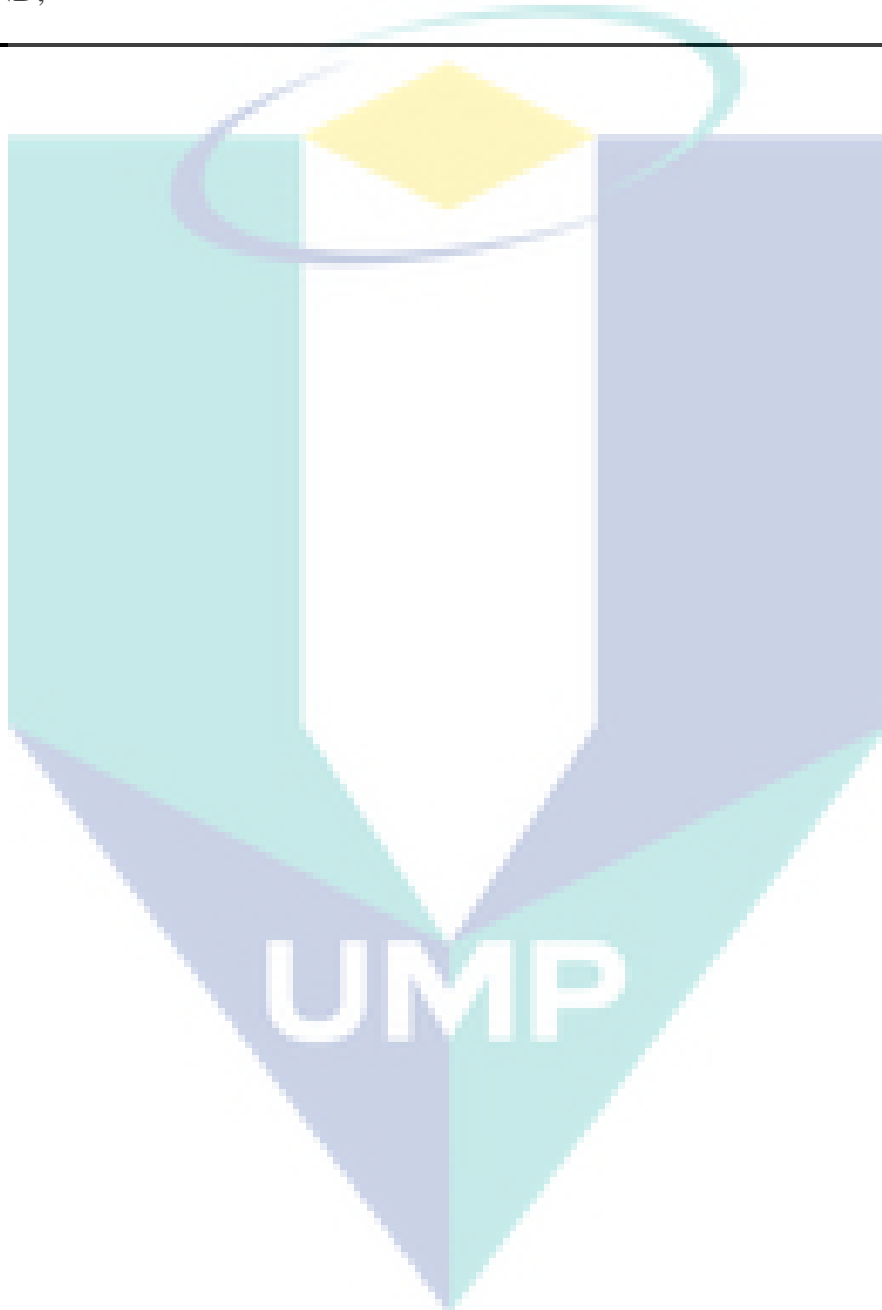
Input: RGB image for all thermal bearing conditions;

Output: Segmented image based on active contour technique;

Steps:

1. A;
2. Read the RGB image, I_{RGB} for all thermal bearing conditions beginning with normal, then warning and ending with abnormal image;
3. Convert RGB input image, I_{RGB} to grayscale image, $I_{grayscale}$;
4. Perform binary mask function on input grayscale image $I_{grayscale}$ to obtain the ROI and discard the background;
5. Manually initiate the boundary location of ROI by using coordinated masks (59: 163,349:372);
6. Interchange the binary image to uint8, I_{mask} ;
7. Multiply the original image, I_{RGB} with I_{mask} in order to obtain the boundaries or ROI of

-
- thermal bearing image, $I_{initial_ROI}$;
8. Perform active contour energy function, E along the boundaries image to form a particular contour;
 9. Crop the segmented image,
 $CroppedImage=imcrop(fullimage,[xLeft,yTop,width,height]);$
 10. Display the result of segmented RGB image, $I(x, y)$;
 11. END;
-



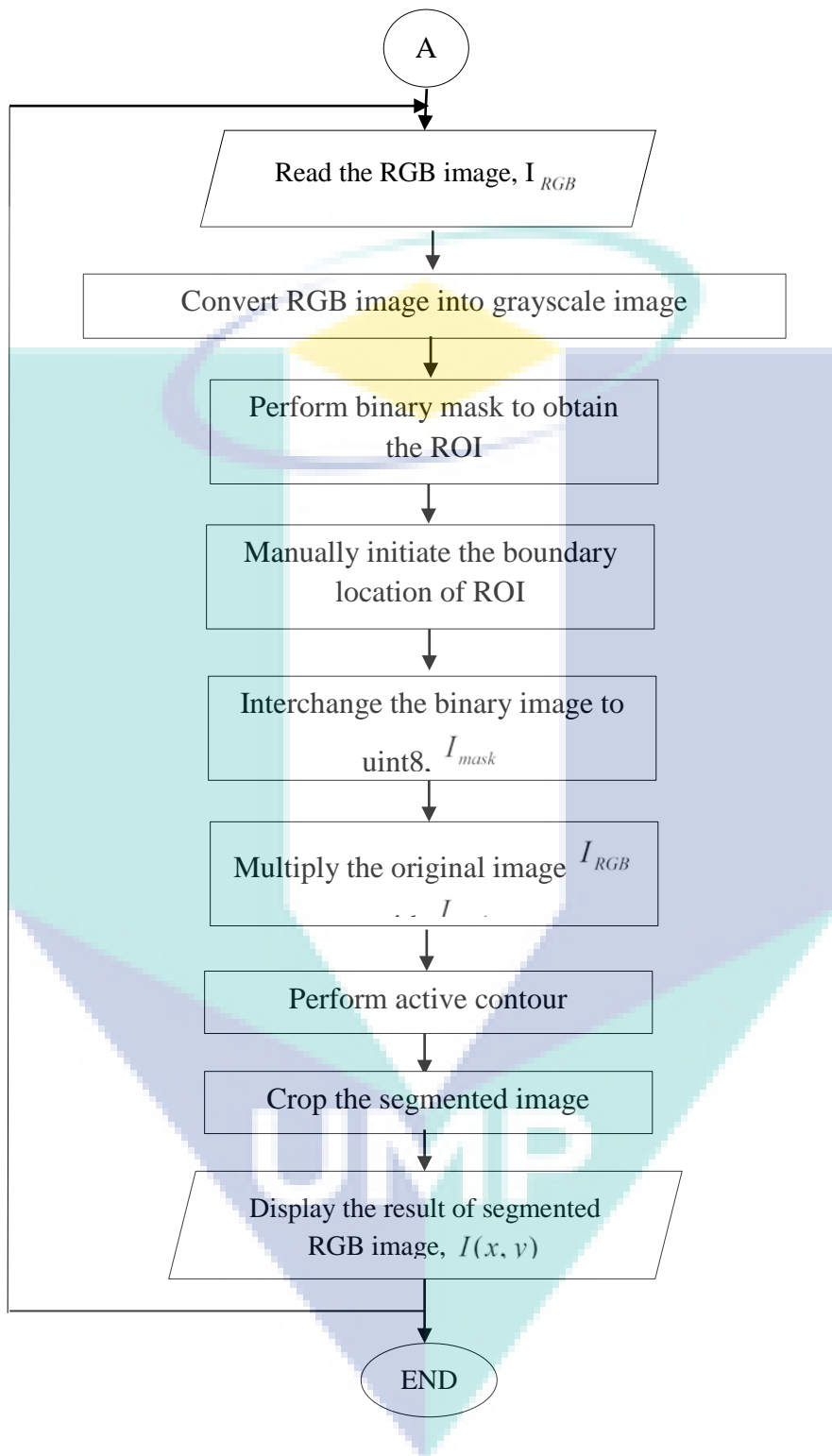


Figure 3.4 Flowchart of Active Contour-based segmentation technique

3.4 Feature Extraction

This section contains the main findings of this research. It is focused on the feature extraction approach in order to retrieve the significant features in distinguishing the features contained in the group of thermal motor bearing images. To achieve this stated purpose, an experiment of GWT-based feature extraction method on images has been carried out in this study.

Based on the previous image processing studies, GWT-based feature extraction method have been successfully performed in various fields in distinguishing the normal and abnormal groups images [cite]. The results of this good performance are measured in terms of classification results. The success of this performance has motivated this GWT-based method to be used in this study. One of the main advantages of this GWT-based method to be used, it is due to a good characteristic of space-frequency localization and effective to all images at different scale's level. With the benefits of this GWT method, a wide selection of features could be extracted in each orientation and each scale from the Gabor that will be deployed in this study. To construct this GWT-based filter, there are 5 different scales values and 8 orientations values that will be applied to extract the Gabor features. The values of the scale parameters that will be involved are $\{scale7x7, scale9x9, scale11x11, scale13x13, scale15x15\}$, while the orientation parameters is $\theta = \left\{0^\circ, \frac{\pi}{8}, \frac{\pi}{4}, 3\frac{\pi}{8}, \frac{\pi}{2}, 5\frac{\pi}{8}, 3\frac{\pi}{4}, 7\frac{\pi}{8}\right\}$. There are 2075 thermal motor bearing images representing the normal, warning and abnormal groups that will be tested in this study. Consequently, the total number of input data matrices that will be generated in the different orientations and scales conditions is $Y \in R^{(nx5) \times j} \in R^{10375 \times 8}$, where 'R' is the feature vector, 'n' is the number of samples and 'j' is the number of orientations. The processing for this method will be explained in detail in the section 3.5.1.

In spite of that, there are limitations obtained from the experiments that been conducted based on this GWT-based feature extraction. From this GWT-based experiment, the result of the classification performance on the thermal motor bearing image group shows a poor performance. Where the classification between groups cannot be well distinguished. As a consequence, some modifications to the features of

thermal motor bearing images based on the original GWT method will be executed to improve the visual quality of images in this study. This has contributed to the development of a proposed new feature extraction method in order to overcome the limitation found in the original GWT-based method.

There are 3 types of new feature extraction algorithms that will be develop in this study based on the original GWT for comparison purposes. Comparison of these methods will be tested in terms of features strength by using the ANOVA method, as well as classification performances in distinguishing the features contained in the group of thermal motor bearing images. Then, the best performance results will be an indicator to the selection of the best method in this study. The processing for all these methods will be explained in details in the section section 3.5.2, section 3.5.3 and section 3.5.4.

Before the GWT-based method as explained before was applied, the experiments on the color-based feature extraction were also tested in this study. The methods involved are HSV and $l * a * b$ based methods. The purpose is to perceive the difference in performance results between which method is better to distinguish the group features from thermal motor bearing images. From the experiments that been executed, the result of classification performance for this color-based method has shown lower performance. This has contributed to the use of another transformation-based method namely the GWT method for further processing. Nonetheless, the methods of operation of this color-based methods will also be explained briefly in sections 3.55 and 3.5.6.

3.4.1 Algorithm for the Original Gabor Wavelet Transform (GWT)-based Feature Extraction Method

This study discusses in detail the process that will be executed to apply the feature extraction process based on the original Gabor Wavelet Transform (GWT). The purpose of this method is implemented in this study to observe the effectiveness of this method to distinguish the optimal features in each group of thermal motor bearing image. Thus, the following procedures is the detailed process in order to differentiate the features for each group in the thermal motor bearing images based on the original GWT-based feature extraction method.

Step 1: Read the cropped segmented bearing image with the dimensional size of $m \times n$, where m and n are the number of rows and column respectively.

Step 2: Convert the input RGB bearing image into grayscale level image, $I(x, y)$;

Step 3: Create the Gabor wavelets to extract the Gabor features image by using the equation 3.4. Insert a number of parameters (5 scales and 8 orientations) as denoted in Table 3.2 into the Gabor function as in equation 3.5 and equation 3.6. The orientation parameters are: 0° , 22.5° , 45° , 67.5° , 90° , 112.5° , 135° and 157.5° .

Table 3.1 Gabor filter parameters (number of scales)

Filter Size (Scales)	σ	λ
7x7	2.8	3.5
9x9	3.6	4.6
11x11	4.5	5.6
13x13	5.4	6.8
15x15	6.3	7.9

Following are the equations that will be used to create the Gabor filter:

A complex Gabor filter as equation 3.4 is defined as the product of a Gaussian kernel times a complex sinusoidal.

$$G(x, y; \lambda, \theta, \psi, \sigma, \gamma) = \exp\left(-\frac{x^2 + \gamma^2 y^2}{2\sigma^2}\right) \exp\left(i\left(2\pi \frac{x'}{\lambda} + \psi\right)\right) \quad 3.4$$

Based on the complex Gabor filter equation as denoted in equation 3.10, the real part 2D-Gabor filter is described in equation 3.5 while the imaginary parts as denoted in equation 3.6.

$$G(x, y; \lambda, \theta, \psi, \sigma, \gamma) = \exp\left(-\frac{x^2 + \gamma^2 y^2}{2\sigma^2}\right) \cos\left(i\left(2\pi \frac{x'}{\lambda} + \psi\right)\right) \quad 3.5$$

$$G(x, y; \lambda, \theta, \psi, \sigma, \gamma) = \exp\left(-\frac{x^2 + \gamma^2 y^2}{2\sigma^2}\right) \sin\left(i\left(2\pi \frac{x'}{\lambda} + \psi\right)\right) \quad 3.6$$

$$\begin{aligned}x' &= x * \cos \theta + y * \sin \theta \\y' &= -x * \sin \theta + y * \cos \theta\end{aligned}\tag{3.7}$$

Step 4: Determine the Gabor features by convolved the input thermal motor bearing images, $I(x, y)$ with the GWT-based filters that have been created in the different scales and orientations values, $g(x, y)$. Then, a response of real and imaginary part will be produced and the equations are depicted in equation 3.8 and equation 3.9.

$$\text{Real}(G(x, y)) = I(x, y) * G(x, y, \lambda, \theta, \psi, \sigma, \gamma)\tag{3.8}$$

$$\text{Im}(G(x, y)) = I(x, y) * \text{Im}(G(x, y, \lambda, \theta, \psi, \sigma, \gamma))\tag{3.9}$$

Step 5: Define the magnitude response by convolved the original image with the Gabor filter. The complex convolution result will be generated. Then, decomposed it to the magnitude response as denoted in equation 3.10 and phase response image as denoted in equation 3.11 based on the real and imaginary part as in equation 3.8 and equation 3.9.

$$\text{Magnitude_response} = \text{abs}(\text{Real}(G(x, y)))\tag{3.10}$$

$$\text{Phase_response} = \text{abs}(\text{Im}(G(x, y)))\tag{3.11}$$

Step 6: Extract the feature vector based on the magnitude response obtained. There are two types of feature vector that will be generated, which are Local Energy and Mean Amplitude. Local energy will be obtained by calculating the sum of squared of the magnitude response which is summing up the squared value of each matrix value from a magnitude response matrix. Meanwhile mean amplitude will be obtained by calculating the sum of absolute values of each matrix value from a magnitude response matrix. The equations are described in equation 3.12 and 3.13.

$$\text{Local_energy} = \text{sumsqr}(\text{Magnitude_response})\tag{3.12}$$

$$\text{Mean_Amplitud} = \text{sumabs}(\text{Magnitude_response})\tag{3.13}$$

Figure 3 illustrates a flow chart representation of pseudocode 2 regarding the GWT-based feature extraction process to extract the features from thermal motor bearing image groups.

Pseudocode 2: Gabor Wavelet Transform (GWT) based feature extraction Algorithm

Input: RGB of segmented thermal motor bearing images,

Output: Multiscale and multi orientation features, $Y \in R^{n \times j} \in MA^{10375 \times 8} \in LA^{10375 \times 8}$

Steps:

1. Start;
2. For each scale, lambda ($\lambda_1 - \lambda_5$) and sigma ($\sigma_1 - \sigma_5$) in the scale list;
3. For each number of images;
4. A;
5. Convert the segmented RGB image into grayscale image;
6. For each orientation, $\theta = \left\{ 0^\circ, \frac{\pi}{8}, \frac{\pi}{4}, 3\frac{\pi}{8}, \frac{\pi}{2}, 5\frac{\pi}{8}, 3\frac{\pi}{4}, 7\frac{\pi}{8} \right\}$ in the orientation list;
7. Construct a Gabor filter, $g(\theta, \lambda, \sigma)$ using Gabor real and Gabor imaginary

$$\text{Gabor Real} = G(x, y; \lambda, \theta, \psi, \sigma, \gamma) = \exp\left(-\frac{x^2 + \gamma^2 y^2}{2\sigma^2}\right) \cos\left(i\left(2\pi \frac{x'}{\lambda} + \psi\right)\right);$$

$$\text{Gabor Img} = G(x, y; \lambda, \theta, \psi, \sigma, \gamma) = \exp\left(-\frac{x^2 + \gamma^2 y^2}{2\sigma^2}\right) \sin\left(i\left(2\pi \frac{x'}{\lambda} + \psi\right)\right);$$

8. Convolve the original of the segmented thermal bearing images with Gabor function $g(\theta, \lambda, \sigma)$ to generate the magnitude response image, R ;
9. Extracting the Gabor features: Extract the orientation and scale information for Gabor Feature vectors namely Local Energy and Mean Amplitude from the magnitude response, R by employing a Gabor filter bank with 8 orientations and 5 scales.

$$\text{Local energy (LE)} = \text{sumsqr}(\text{magnitude response});$$

$$\text{Mean Amplitude (MA)} = \text{sumabs}(\text{magnitude response});$$

10. End

11. End

12. Output Multi-features: $Y \in R^{n \times j} \in MA^{10375 \times 8} \in LE^{10375 \times 8}$

13. End

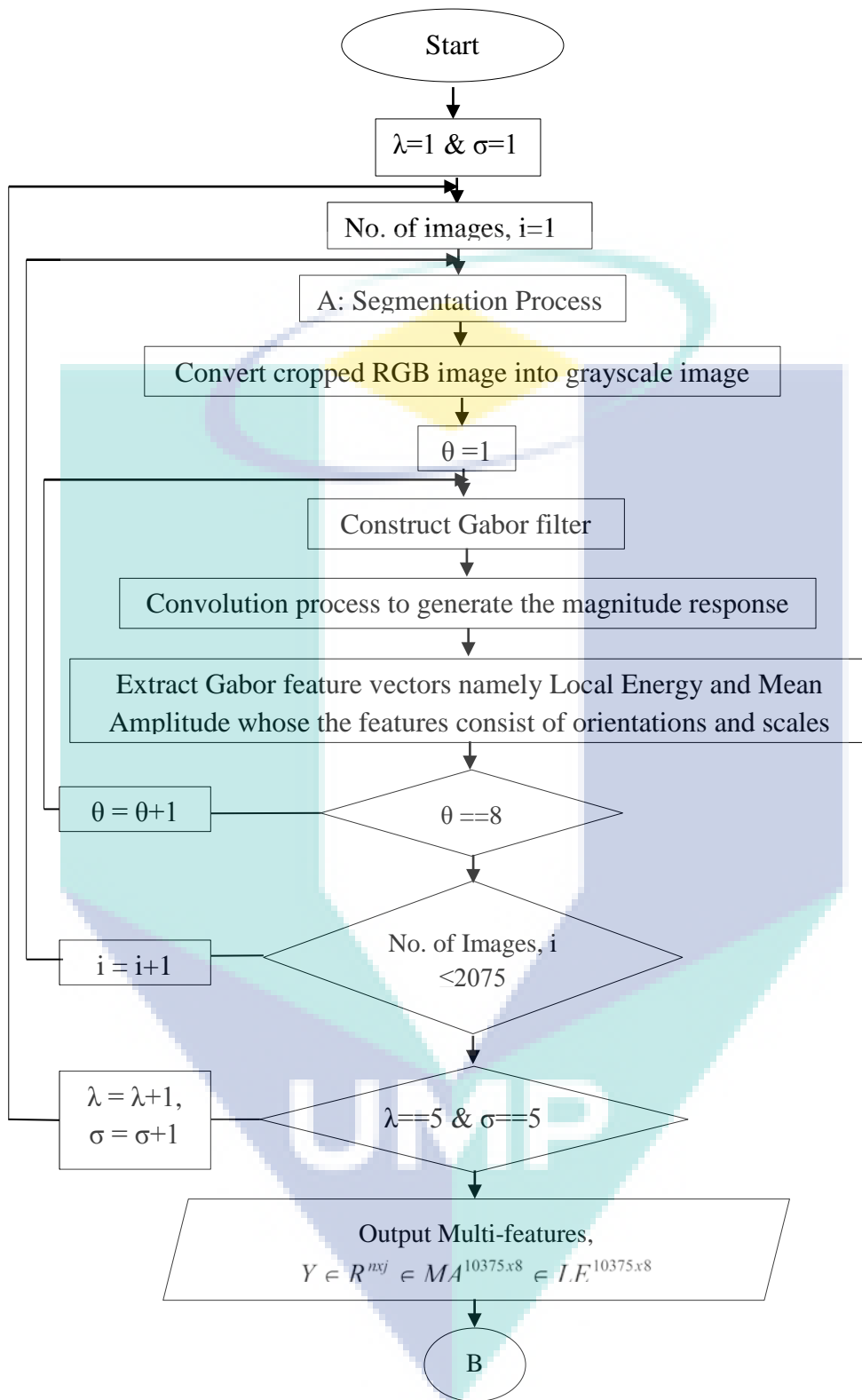


Figure 3.5 Flowchart of Gabor Wavelet Transform based feature extraction technique

3.4.2 Algorithm for the Proposed an Enhanced Gabor Features (EGF) -based Feature Extraction Method

This section contains the main findings in this study. It discusses in detail the process that will be executed to develop the new feature extraction process that has been proposed in this section based on the original GWT-based feature extraction process as in section 3.5.1.

In this present study, a combination of an independent image enhancement approach called Histogram Equalization method with the original GWT-based feature extraction technique will be developed. The combinations of these methods have been executed to modify the contrast and the distribution of the gray levels of pixels in the images. This proposed method is called Enhanced Gabor Features (EGF)-based feature extraction. The purpose of this EGF-based method utilized in this study is to overcome the limitations obtained from the experiment that been conducted on the original GWT-based method. As a consequence, **by modifying the pixel value (intensities) of the image**, the visual quality of images in this study will be able to be improved. Consequently, the features of thermal motor bearing images also will be distinguished well in this study. Thus, the following procedure is a detailed process for the proposed image quality improvement by using the Enhanced Gabor Feature (EGF)-based method:

Step 1: Read the cropped segmented bearing image with the dimensional size of $m \times n$, where m and n are the number of rows and column respectively.

Step 2: Convert the input RGB bearing image into grayscale level image, $I(x, y)$;

Step 3: Define the frequency of each pixel value in input image, $P_x(i) = n_i$;

Step 4: Calculate the probability of each frequency, $P_x(i) = n_i / N$, N = total number of pixels in the image;

Step 5: Calculate the cumulative distribution function of each pixel i , $cdf_x(i) = \sum_{j=0}^i P_x(j)$

Step 6: Calculate the cumulative distribution probability of each pixel,

$$cdf_x(i) = \sum_{j=0}^i \frac{P(j)}{no.ofpixel};$$

Step 7: Calculating final value of each pixel(histogram equalized) by multiplying $cdf_x(i)$ with number of bins;

Step 8: New input intensities, k of i by the function $T(k)$;

Step 9: Create the new Gabor wavelets to extract the new Gabor features image by using the equation 3.14. Insert a number of parameters (5 scales and 8 orientations) as denoted in Table 3.2 as presented in section 3.5.1 into the new Gabor function as in equation 3.15 and equation 3.16. The orientation parameters are: 0° , 22.5° , 45° , 67.5° , 90° , 112.5° , 135° and 157.5° .

Following are the equations will be used to create the Gabor filter:

A complex Gabor filter as equation 3.14 is defined as the product of a Gaussian kernel times a complex sinusoidal.

$$G(x, y; \lambda, \theta, \psi, \sigma, \gamma)_{new} = \left[\exp\left(-\frac{x^2 + \gamma^2 y^2}{2\sigma^2}\right) \exp\left(i\left(2\pi \frac{x'}{\lambda} + \psi\right)\right) \right]_{new} \quad 3.14$$

Based on the new complex Gabor filter equation as denoted in equation 3.14, the real part 2D-Gabor filter is described in equation 3.15 while the imaginary parts as denoted in equation 3.16.

$$G(x, y; \lambda, \theta, \psi, \sigma, \gamma)_{new} = \left[\exp\left(-\frac{x^2 + \gamma^2 y^2}{2\sigma^2}\right) \cos\left(i\left(2\pi \frac{x'}{\lambda} + \psi\right)\right) \right]_{new} \quad 3.15$$

$$G(x, y; \lambda, \theta, \psi, \sigma, \gamma)_{new} = \left[\exp\left(-\frac{x^2 + \gamma^2 y^2}{2\sigma^2}\right) \sin\left(i\left(2\pi \frac{x'}{\lambda} + \psi\right)\right) \right]_{new} \quad 3.16$$

$$\begin{aligned}x' &= x * \cos \theta + y * \sin \theta \\y' &= -x * \sin \theta + y * \cos \theta\end{aligned}\tag{3.17}$$

Step 10: Determine the new Gabor features by convolved the input thermal motor bearing images, $I(x, y)$ with the new EGF-based filters that have been created in the different scales and orientations values, $g_{new}(x, y)$. Then, a new response of real and imaginary part will be produced and the equations are depicted in equation 3.18 and equation 3.19.

$$\text{Real}(G(x, y))_{new} = I(x, y) * G(x, y, \lambda, \theta, \psi, \sigma, \gamma)_{new}\tag{3.18}$$

$$\text{Im}(G(x, y))_{new} = I(x, y) * \text{Im}(G(x, y, \lambda, \theta, \psi, \sigma, \gamma))_{new}\tag{3.19}$$

Step 11: Define the new magnitude response by convolved the original image with the new EGF-based filters. Then, decomposed it to the new magnitude response as denoted in equation 3.20 and new phase response image as denoted in equation 3.21 based on the real and imaginary part in equation 3.18 and equation 3.19.

$$\text{Magnitude_response}_{new} = \text{abs}(\text{Real}(G(x, y)_{new}))\tag{3.20}$$

$$\text{Phase_response}_{new} = \text{abs}(\text{Im}(G(x, y)_{new}))\tag{3.21}$$

Step 12: Extract the new feature vector the new pixel value of the output image based on the new magnitude response obtained. There are new Local Energy and new Mean Amplitude, $Y \in R^{n \times j} \in MA_{(new)}^{83000} \in LE_{(new)}^{83000}$. The new Local energy will be obtained by calculating the sum of squared of the new magnitude response which is summing up the squared value of each matrix value from a new magnitude response matrix. Meanwhile, the new mean amplitude will be obtained by calculating the sum of absolute values of each matrix value from a new magnitude response matrix. The equations are described in equation 3.22 and equation 3.23.

$$\text{Local_energy}_{new} = \text{sumsqr}(\text{Magnitude_response}_{new})\tag{3.22}$$

$$Mean_Amplitude_{new} = sumabs(Magnitude_response_{new})$$

3.23

Figure 3 illustrates a flow chart representation of pseudocode 3 regarding the EGF-based feature extraction process to extract the new features from thermal motor bearing image groups.

Pseudocode 3: Enhanced Gabor Features (EGF) based feature extraction Algorithm

Input: RGB of segmented thermal motor bearing images,

Output: Multiscale and multi orientation features,

$$Y \in R^{n \times j} \in MA_{(new)}^{10375 \times 8} \in LA_{(new)}^{10375 \times 8}$$

Steps:

1. Start;
2. For each scale, $(\lambda_1 - \lambda_5)$ and $(\sigma_1 - \sigma_5)$ in the scale list;
3. For each number of images;
4. A;
5. Convert the segmented RGB image into grayscale image, $I(x, y)$;
6. Define the frequency of each pixel value in input image, $P_x(i) = n_i$
7. Calculate the probability of each frequency, $P_x(i) = n_i / N$, N = total number of pixels in the image

8. Calculate the cumulative distribution function of each pixel i, $cdf_x(i) = \sum_{j=0}^i P_x(j)$

8. Calculate the cumulative distribution probability of each pixel,

$$cdf_x(i) = \frac{\sum_{j=0}^i P(j)}{no.ofpixel}$$

9. Calculating final value of each pixel(histogram equalized) by multiplying $cdf_x(i)$ with number of bins.

10. New input intensities, k of i by the function $T(k)$

11. For each orientation, $\theta = \left\{ 0^\circ, \frac{\pi}{8}, \frac{\pi}{4}, 3\frac{\pi}{8}, \frac{\pi}{2}, 5\frac{\pi}{8}, 3\frac{\pi}{4}, 7\frac{\pi}{8} \right\}$ in the orientation list;

12. Construct a new Gabor filter, $g(x, y)_{new}$ by using Gabor real and Gabor imaginary,

$$Gabor\ Real_{(new)} = G(x, y; \lambda, \theta, \psi, \sigma, \gamma) = \exp\left(-\frac{x^2 + \gamma^2 y^2}{2\sigma^2}\right) \cos\left(i\left(2\pi \frac{x'}{\lambda} + \psi\right)\right)$$

$$Gabor\ Img_{(new)} = G(x, y; \lambda, \theta, \psi, \sigma, \gamma) = \exp\left(-\frac{x^2 + \gamma^2 y^2}{2\sigma^2}\right) \sin\left(i\left(2\pi \frac{x'}{\lambda} + \psi\right)\right)$$

13. Convolve the original of the segmented thermal bearing images $I(x, y)$ with Gabor

function, $g(x, y)_{new}$ to generate the new magnitude response image, R ;

14. Extracting the new Gabor features: Extract the orientation and scale information for new Gabor Feature vectors namely Local Energy $(LE)_{(new)}$ and Mean Amplitude $(MA)_{(new)}$ from the new magnitude response, R by employing a EGF filter with 8 orientations and 5 scales.

$$Local\ energy\ (LE)_{(new)} = \text{sumsqr}(magnitude\ response_{new});$$

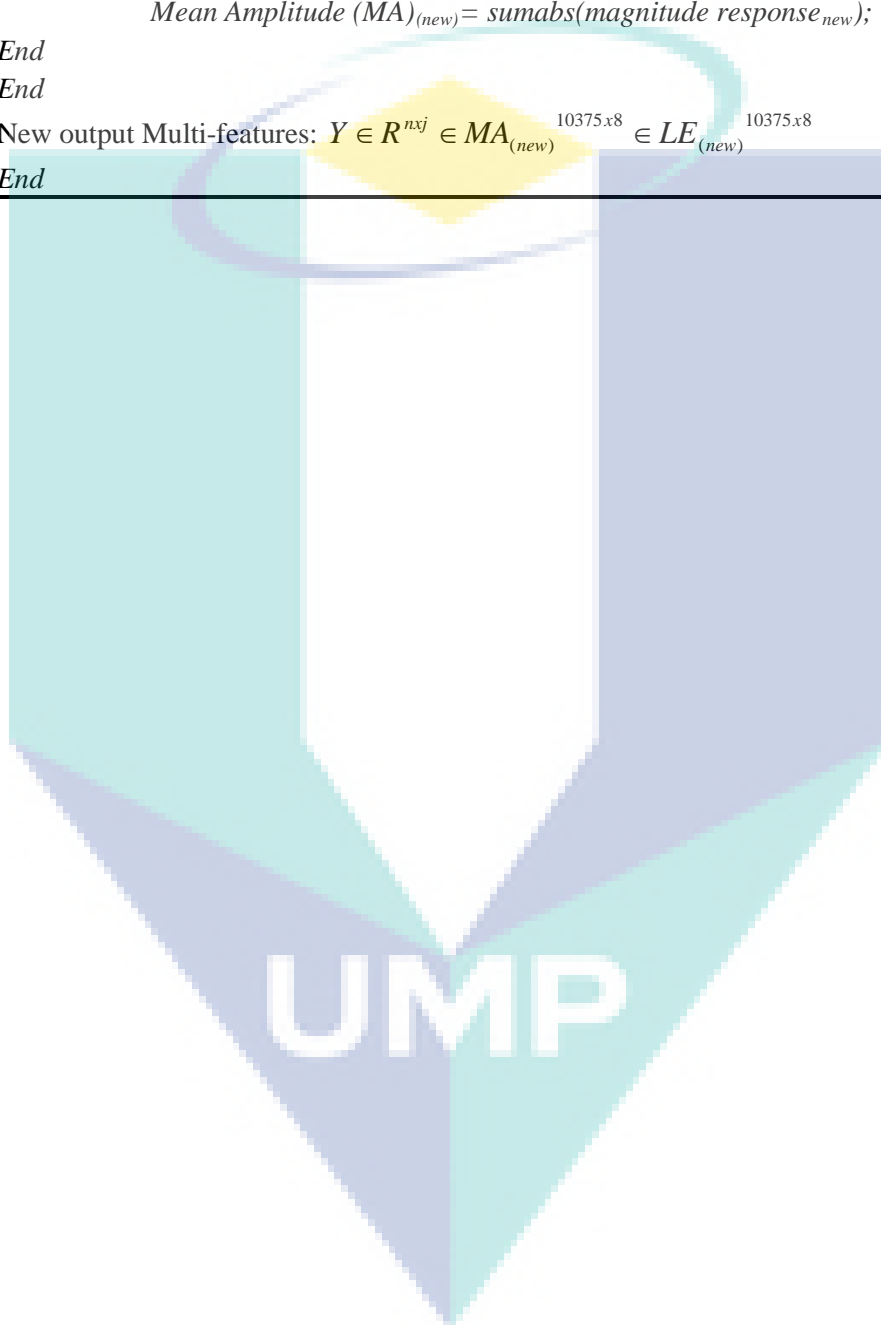
$$Mean\ Amplitude\ (MA)_{(new)} = \text{sumabs}(magnitude\ response_{new});$$

15. End

16. End

17. New output Multi-features: $Y \in R^{n \times j} \in MA_{(new)}^{10375 \times 8} \in LE_{(new)}^{10375 \times 8}$

18. End



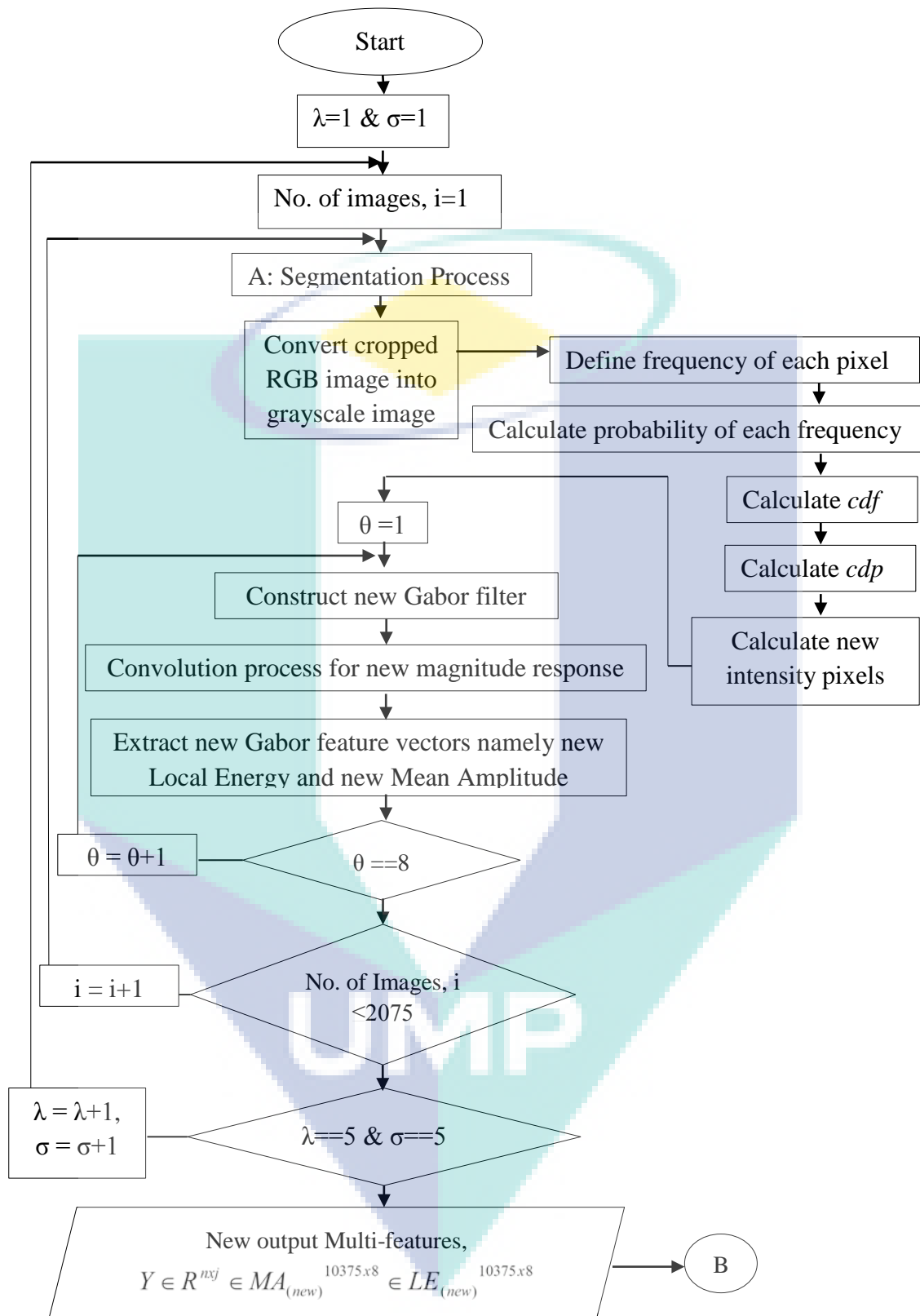


Figure 3.6 Flowchart of Enhanced Gabor Features (EGF) based feature extraction technique

3.4.3 Algorithm for the Proposed an Enhanced GWSMH -based Feature Extraction Method

This section discusses in detail the process that will be executed to develop the new feature extraction process that has been proposed in this section based on the original GWT-based feature extraction process as in section 3.5.1.

In this work, a combination of the pre-processing method with the new feature extraction method will be implemented. The pre-processing method consists of a combination of unsharp filters and median filters. The methods such as unsharp mask filter is intended for sharpen the image followed by a median filter will be employed for the removal of noise at the input thermal image. Meanwhile, the new feature extraction method consists of a combination of an independent image enhancement approach called Histogram Equalization method with the original GWT-based feature extraction technique. All the combinations of these methods will be developed to modify the contrast and the distribution of the gray levels of pixels in the images. This proposed method is called Enhanced GWSMH-based feature extraction. The purpose of this Enhanced GWSMH-based method utilized in this study is to overcome the limitations obtained from the experiment that been conducted on the original GWT-based method. As a consequence, by modifying the pixel value (intensities) of the image, the visual quality of images in this study will be able to be improved. Consequently, the features of thermal motor bearing images also will be distinguished well in this study. Thus, the following procedure is a detailed process for the proposed image quality improvement by using the Enhanced GWSMH-based method:

Step 1: Read the cropped segmented bearing image with the dimensional size of $m \times n$, where m and n are the number of rows and column respectively.

Step 2: Convert the input RGB bearing image into grayscale level image, $I(x, y)$;

Step 3: Define the frequency of each pixel value in input image, $P_x(i) = n_i$;

Step 4: Calculate the probability of each frequency, $P_x(i) = n_i / N$, $N =$ total number of pixels in the image;

Step 5: Calculate the cumulative distribution function of each pixel i , $cdf_x(i) = \sum_{j=0}^i P_x(j)$

Step 6: Calculate the cumulative distribution probability of each pixel,

$$cdf_x(i) = \sum_{j=0}^i \frac{P(j)}{no.ofpixel};$$

Step 7: Calculating final value of each pixel (histogram equalized) by multiplying $cdf_x(i)$ with number of bins;

Step 8: New input intensities, k of i by the function $T(k)$;

Step 9: Create the new Gabor wavelets, $G(x, y; \lambda, \theta, \psi, \sigma, \gamma)_{new}$ to extract the new Gabor features image by using the equation 3.14 as in section 3.5.2. Insert a number of parameters (5 scales and 8 orientations) as denoted in Table 3.2 as presented in section 3.5.1 into the new Gabor function as in equation 3.15 and equation 3.16 as in section 3.5.2. The orientation parameters are: 0° , 22.5° , 45° , 67.5° , 90° , 112.5° , 135° and 157.5° .

Step 10: Determine the new Gabor features by convolved the input thermal motor bearing images, $I(x, y)$ with the new GWSMH-based filters that have been created in the different scales and orientations values, $g_{new}(x, y)$. Then, a new response of real component, $Real(G(x, y))_{new}$ and imaginary component, $Im(G(x, y))_{new}$ will be produced and the equations are depicted in equation 3.18 and equation 3.19 as in section 3.5.2.

Step 11: Define the new magnitude response, $Magnitude_response_{new}$ by convolved the original image with the new GWSMH-based filters. Then, decomposed it to the new magnitude response as denoted in equation 3.20 and new phase response image as denoted in equation 3.21 based on the real and imaginary part in equation 3.18 and equation 3.19 as in section 3.5.2.

Step 12: Extract the new feature vector containing the new pixel value of the output image based on the new magnitude response obtained. There are new Local Energy and new Mean Amplitude, $Y \in R^{nxj} \in MA_{(new)}^{83000} \in LE_{(new)}^{83000}$. The new Local energy will

be obtained by calculating the sum of squared of the new magnitude response which is summing up the squared value of each matrix value from a new magnitude response matrix. Meanwhile, the new mean amplitude will be obtained by calculating the sum of absolute values of each matrix value from a new magnitude response matrix. The equations are described in equation 3.24 and equation 3.25.

$$Local_energy_{new} = \text{sumsqr}(Magnitude_response_{new}) \quad 3.24$$

$$Mean_Amplitude_{new} = \text{sumabs}(Magnitude_response_{new}) \quad 3.25$$

Figure 3 illustrates a flow chart representation of pseudocode 4 regarding the GWSMH-based feature extraction process to extract the new features from thermal motor bearing image groups.

Pseudocode 4: Enhanced GWSMH based feature extraction Algorithm

Input: RGB of segmented thermal motor bearing images,

Output: Multiscale and multi orientation features, $Y \in R^{nxj} \in MA_{(new)}^{10375 \times 8} \in LA_{(new)}^{10375 \times 8}$

Steps:

1. Start;
2. For each scale, $(\lambda_1 - \lambda_5)$ and $(\sigma_1 - \sigma_5)$ in the scale list;
3. For each number of images;
4. A;
5. Convert the segmented RGB image into grayscale image $I(x, y)$;
- 6.
- 7.
- 8.
- 9.
- 10.
- 11.
- 12.
6. Define the frequency of each pixel value in input image, $P_x(i) = n_i$
7. Calculate the probability of each frequency, $P_x(i) = n_i / N$, N = total number of pixels in the image
8. Calculate the cumulative distribution function of each pixel i, $cdf_x(i) = \sum_{j=0}^i P_x(j)$
8. Calculate the cumulative distribution probability of each pixel, $cdf_x(i) = \sum_{j=0}^i \frac{P(j)}{\text{no.ofpixel}}$
9. Calculating final value of each pixel(histogram equalized) by multiplying $cdf_x(i)$ with number of bins.

10. New input intensities, k of i by the function $T(k)$

11. For each orientation, $\theta = \left\{0^\circ, \frac{\pi}{8}, \frac{\pi}{4}, 3\frac{\pi}{8}, \frac{\pi}{2}, 5\frac{\pi}{8}, 3\frac{\pi}{4}, 7\frac{\pi}{8}\right\}$ in the orientation list;

12. Construct a new Gabor filter, $g(x, y)$ using Gabor real and Gabor imaginary

$$\text{Gabor Real}_{(new)} = G(x, y; \lambda, \theta, \psi, \sigma, \gamma) = \exp\left(-\frac{x^2 + \gamma^2 y'^2}{2\sigma^2}\right) \cos\left(i\left(2\pi \frac{x'}{\lambda} + \psi\right)\right);$$

$$\text{Gabor Img}_{(new)} = G(x, y; \lambda, \theta, \psi, \sigma, \gamma) = \exp\left(-\frac{x^2 + \gamma^2 y'^2}{2\sigma^2}\right) \sin\left(i\left(2\pi \frac{x'}{\lambda} + \psi\right)\right);$$

13. Convolve the original of the segmented thermal bearing images $I(x, y)$ with Gabor function $g(x, y)$ to generate the magnitude response image, R ;

14. Extracting the new Gabor features: Extract the orientation and scale information for new Gabor Feature vectors namely Local Energy $(LE)_{(new)}$ and Mean Amplitude $(MA)_{(new)}$ from the magnitude response, R by employing a Gabor filter bank with 8 orientations and 5 scales.

$$\text{Local energy } (LE)_{(new)} = \text{sumsqr}(\text{magnitude response});$$

$$\text{Mean Amplitude } (MA)_{(new)} = \text{sumabs}(\text{magnitude response});$$

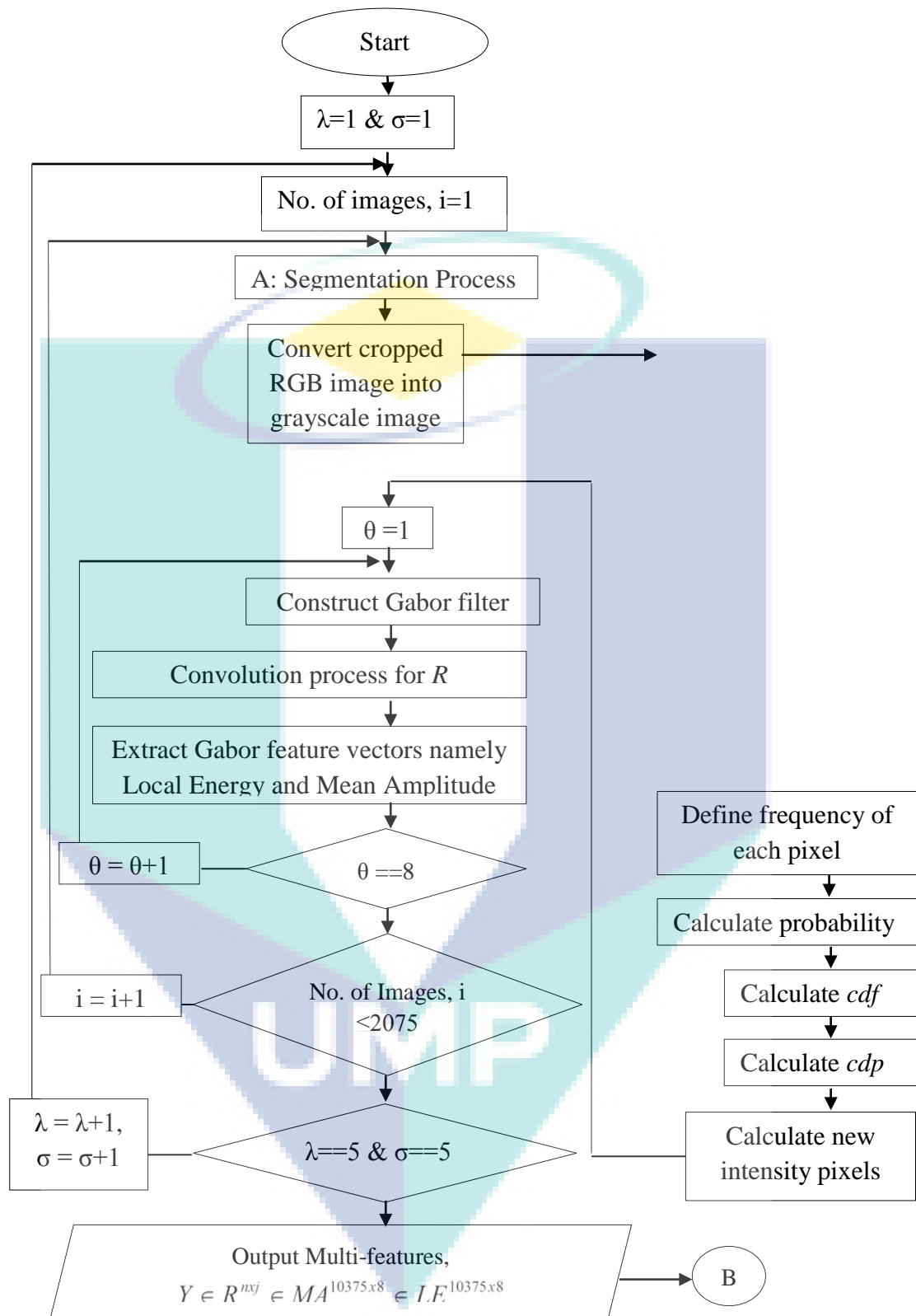
15. End

16. End

17. Output Multi-features: $Y \in R^{n \times j} \in MA_{(new)}^{10375 \times 8} \in LE_{(new)}^{10375 \times 8}$

18. End

UMP



3.4.4 Algorithm for the Proposed an Enhanced GWCLAHE -based Feature Extraction Method

This section discusses in detail the process that will be executed to develop the new feature extraction process that has been proposed in this section based on the original GWT-based feature extraction process as in section 3.5.1.

In this present study, a combination of an independent image enhancement approach called Contrast Limited Adaptive Histogram Equalization (CLAHE) method with the original GWT-based feature extraction technique will be developed. This proposed method is called Enhanced GWCLAHE-based feature extraction. The purpose of this Enhanced GWCLAHE-based method utilized in this study is to overcome the limitations obtained from the experiment that been conducted on the original GWT-based method. As a consequence, by modifying the pixel value (intensities) of the image, the visual quality of images in this study will be able to be improved. Consequently, the features of thermal motor bearing images also will be distinguished well in this study. Thus, the following procedure is a detailed process for the proposed image quality improvement by using the Enhanced GWCLAHE-based method:

Step 1: Read the cropped segmented bearing image with the dimensional size of $m \times n$, where m and n are the number of rows and column respectively.

Step 2: Convert the input RGB bearing image into grayscale level image, $I(x, y)$;

Step 3: Define the frequency of each pixel value in input image, $P_x(i) = n_i$;

Step 4: Calculate the probability of each frequency, $P_x(i) = n_i / N$, $N =$ total number of pixels in the image;

Step 5: Calculate the cumulative distribution function of each pixel i , $cdf_x(i) = \sum_{j=0}^i P_x(j)$

Step 6: Calculate the cumulative distribution probability of each pixel,

$$cdf_x(i) = \sum_{j=0}^i \frac{P(j)}{\text{no.ofpixel}};$$

Step 7: Calculating final value of each pixel(histogram equalized) by multiplying $cdf_x(i)$ with number of bins;

Step 8: New input intensities, k of i by the function $T(k)$;

Step 9: Create the new Gabor wavelets, $G(x, y; \lambda, \theta, \psi, \sigma, \gamma)_{new}$ to extract the new Gabor features image by using the equation 3.14 as in section 3.5.2. Insert a number of parameters (5 scales and 8 orientations) as denoted in Table 3.2 as presented in section 3.5.1 into the new Gabor function as in equation 3.15 and equation 3.16 as in section 3.5.2. The orientation parameters are: 0° , 22.5° , 45° , 67.5° , 90° , 112.5° , 135° and 157.5° .

Step 10: Determine the new Gabor features by convolved the input thermal motor bearing images, $I(x, y)$ with the new GWCLAHE-based filters that have been created in the different scales and orientations values, $g_{new}(x, y)$. Then, a new response of real component, $Real(G(x, y))_{new}$ and imaginary component, $Im(G(x, y))_{new}$ will be produced and the equations are depicted in equation 3.18 and equation 3.19 as in section 3.5.2.

Step 11: Define the new magnitude response, $Magnitude_response_{new}$ by convolved the original image with the new GWCLAHE-based filters. Then, decomposed it to the new magnitude response as denoted in equation 3.20 and new phase response image as denoted in equation 3.21 based on the real and imaginary part in equation 3.18 and equation 3.19 as in section 3.5.2.

Step 12: Extract the new feature vector containing the new pixel value of the output image based on the new magnitude response obtained. There are new Local Energy and new Mean Amplitude, $Y \in R^{nxj} \in MA_{(new)}^{83000} \in LE_{(new)}^{83000}$. The new Local energy will be obtained by calculating the sum of squared of the new magnitude response which is summing up the squared value of each matrix value from a new magnitude response matrix. Meanwhile, the new mean amplitude will be obtained by calculating the sum of absolute values of each matrix value from a new magnitude response matrix. The equations are described in equation 3.24 and equation 3.25.

$$Local_energy_{new} = \text{sumsqr}(Magnitude_response_{new}) \quad 3.26$$

$$Mean_Amplitude_{new} = \text{sumabs}(Magnitude_response_{new}) \quad 3.27$$

Figure 3 illustrates a flow chart representation of pseudocode 5 regarding the GWCLAHE -based feature extraction process to extract the new features from thermal motor bearing image groups.

Pseudocode 5: Enhanced GWCLAHE based feature extraction Algorithm

Input: RGB of segmented thermal motor bearing images,

Output: Multiscale and multi orientation features, $Y \in R^{nxj} \in MA^{10375 \times 8} \in LA^{10375 \times 8}$

Steps:

1. Start;
2. For each scale, $(\lambda_1 - \lambda_5)$ and $(\sigma_1 - \sigma_5)$ in the scale list;
3. For each number of images;
4. A;
5. Convert the segmented RGB image into grayscale image $I(x, y)$;
6. Define the frequency of each pixel value in input image, $P_x(i) = n_i$
7. Calculate the probability of each frequency, $P_x(i) = n_i / N$, $N = \text{total number of pixels in the image}$
8. Calculate the cumulative distribution function of each pixel i , $cdf_x(i) = \sum_{j=0}^i P_x(j)$
8. Calculate the cumulative distribution probability of each pixel, $cdf_x(i) = \sum_{j=0}^i \frac{P(j)}{\text{no.ofpixel}}$
9. Calculating final value of each pixel(histogram equalized) by multiplying $cdf_x(i)$ with number of bins.
10. New input intensities, k of i by the function $T(k)$
11. For each orientation, $\theta = \left\{ 0^\circ, \frac{\pi}{8}, \frac{\pi}{4}, 3\frac{\pi}{8}, \frac{\pi}{2}, 5\frac{\pi}{8}, 3\frac{\pi}{4}, 7\frac{\pi}{8} \right\}$ in the orientation list;
12. Construct a new Gabor filter, $g(x, y)$ using Gabor real and Gabor imaginary

$$Gabor\ Real_{(new)} = G(x, y; \lambda, \theta, \psi, \sigma, \gamma) = \exp\left(-\frac{x^2 + \gamma^2 y'^2}{2\sigma^2}\right) \cos\left(i\left(2\pi \frac{x'}{\lambda} + \psi\right)\right);$$

$$Gabor\ Img_{(new)} = G(x, y; \lambda, \theta, \psi, \sigma, \gamma) = \exp\left(-\frac{x^2 + \gamma^2 y'^2}{2\sigma^2}\right) \sin\left(i\left(2\pi \frac{x'}{\lambda} + \psi\right)\right);$$

13. Convolve the original of the segmented thermal bearing images $I(x, y)$ with Gabor function

$I(x, y)$ to generate the magnitude response image, R ;

14. Extracting the new Gabor features: Extract the orientation and scale information for new Gabor Feature vectors namely Local Energy $(LE)_{(new)}$ and Mean Amplitude $(MA)_{(new)}$ from the magnitude response, R by employing a Gabor filter bank with 8 orientations and 5 scales.

Local energy $(LE)_{(new)} = \text{sumsqr}(\text{magnitude response})$;

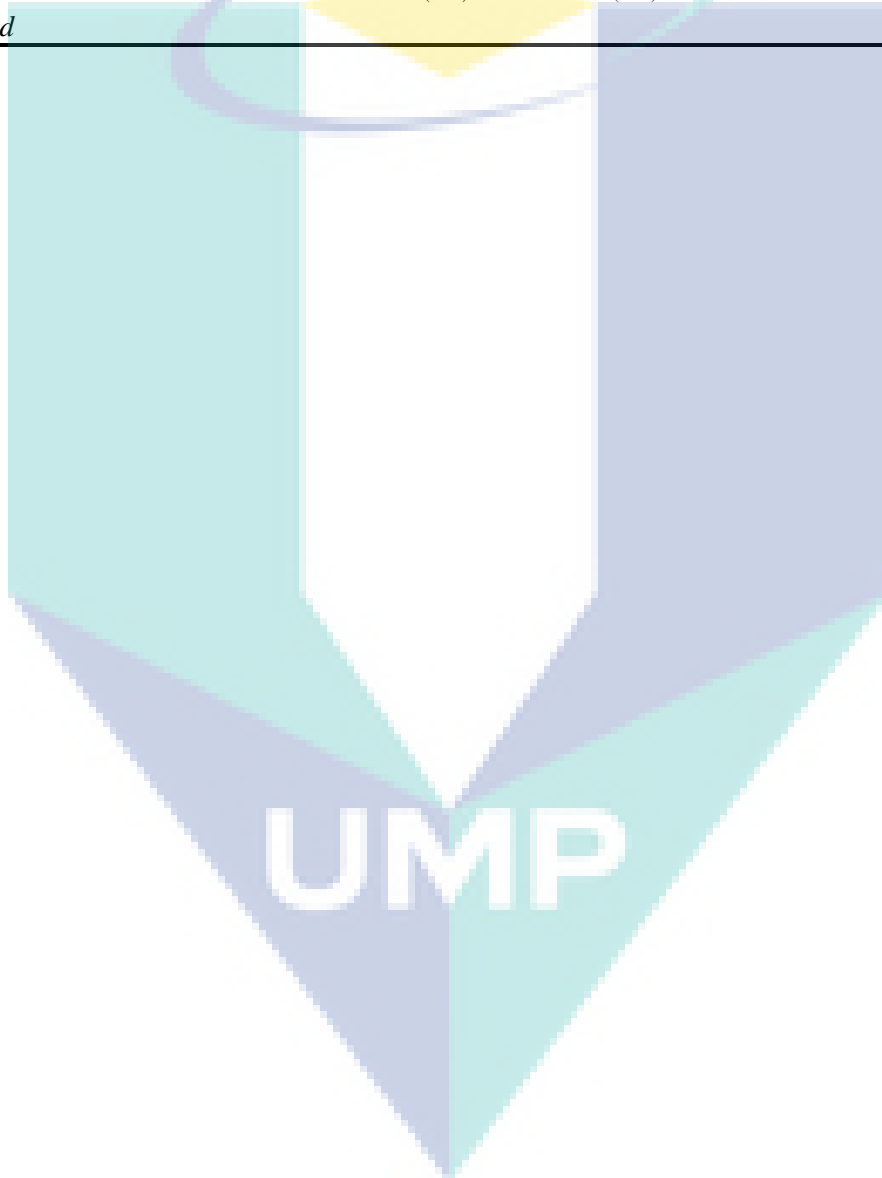
Mean Amplitude $(MA)_{(new)} = \text{sumabs}(\text{magnitude response})$;

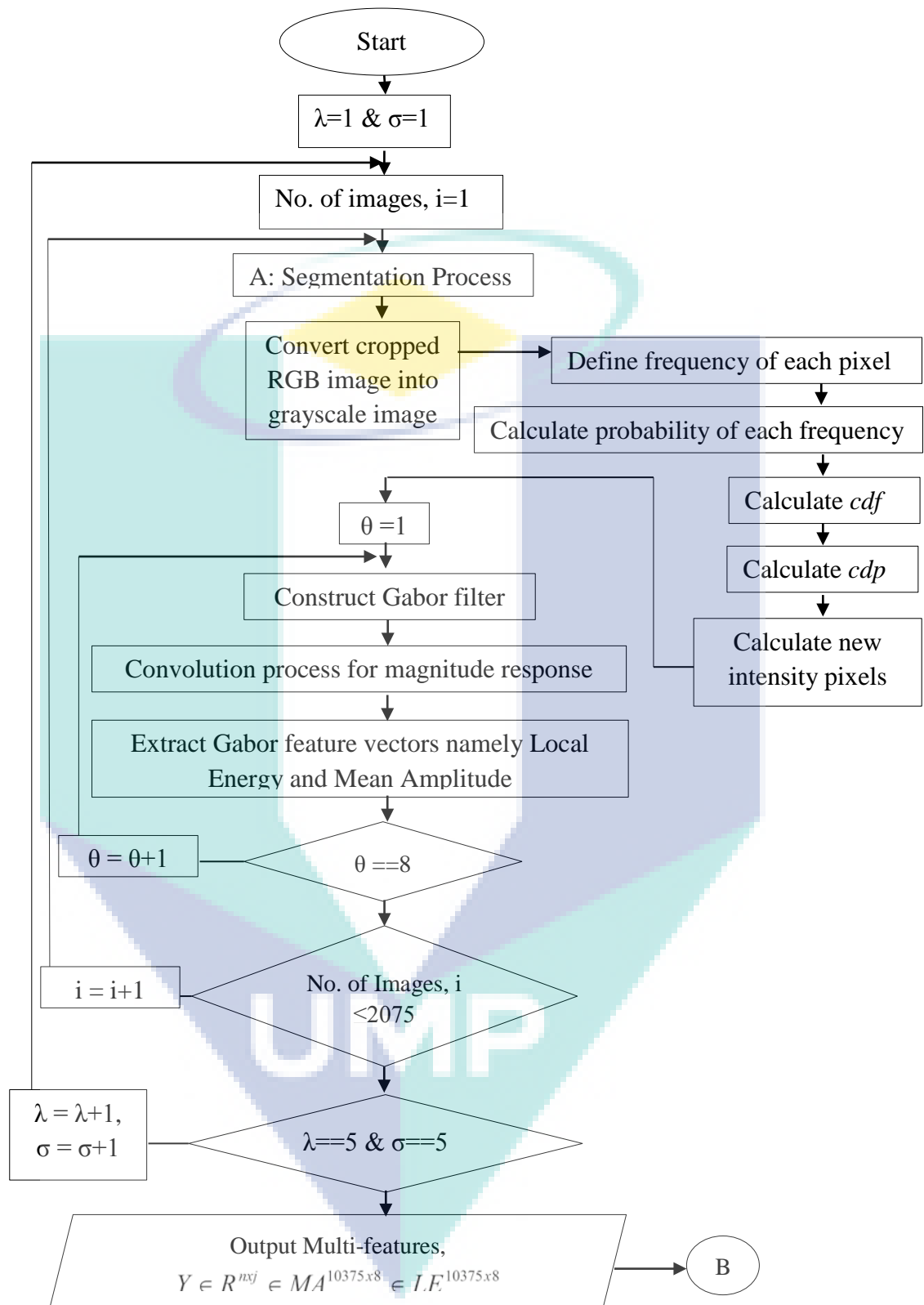
15. *End*

16. *End*

17. Output Multi-features: $Y \in R^{nxj} \in MA_{(new)}^{10375 \times 8} \in LE_{(new)}^{10375 \times 8}$

18. *End*





3.4.5 Algorithm for the HSV color-based Feature Extraction Method

This study discusses in detail the process that will be executed to apply the feature extraction process based on the HSV color method. The purpose of this method is to perceive the effectiveness of this method to distinguish the optimal features in each group of thermal motor bearing image. Thus, the following procedures is the detailed process:

Step 1: Read the cropped segmented bearing image with the dimensional size of $m \times n$, where m and n are the number of rows and column respectively.

Step 2: Convert the RGB of thermal motor bearing image input into HSV color space image, $I_{HSV}(x, y)$;

Step 3: Separate the three channels of H*S*V color space individually as in equation 3.28.

$$\begin{bmatrix} H = \\ S = \\ V = \end{bmatrix} \quad 3.28$$

Step 4: Extract the features based on the HSV obtained. There are two types of features that will be generated with statistical features which are mean and standard deviation. The mean is the average value which gives some information about general brightness of the image. Therefore, mean feature can be defined as equation 3.29 and equation 3.30:

$$g' = \sum_{g=0}^{L-1} g * P(g) = \sum_r \sum_c \frac{I(r, c)}{M} \quad 3.29$$

$$P(g) = N(g) / M \quad 3.30$$

Where $P(g)$ is histogram probability, M is the number of pixel in the image HSV ($M \times N$), $N(g)$ is the number of gray level g , L is a total number of gray level available range from 0-255.

Meanwhile, the standard deviation is known as square root of the variance tells something about the contrast. Thus, a high contrast image will have a high temperature or intensities image. The equation as in equation 3.31.

$$\sigma_g = \sqrt{\sum_{g=0}^{L-1} (g - g')^2 P(g)} \quad 3.31$$

Figure 3 illustrates a flow chart representation of pseudocode 6 regarding the HSV Color-based feature extraction process to extract the features from thermal motor bearing image groups.

Pseudocode 6: HSV Color-based feature extraction Algorithm

Input: RGB of segmented thermal motor bearing images,

Output: Output extracted features

Steps:

1. Start;
 2. Convert the segmented RGB image into individual HSV color space image;
 3. Extract the statistical features namely mean and standard deviation;
 4. Output features: $Y \in R^{n \times j} \in MEAN^{2075 \times 1} \in STD^{2075 \times 1}$
 5. End
-

UMP

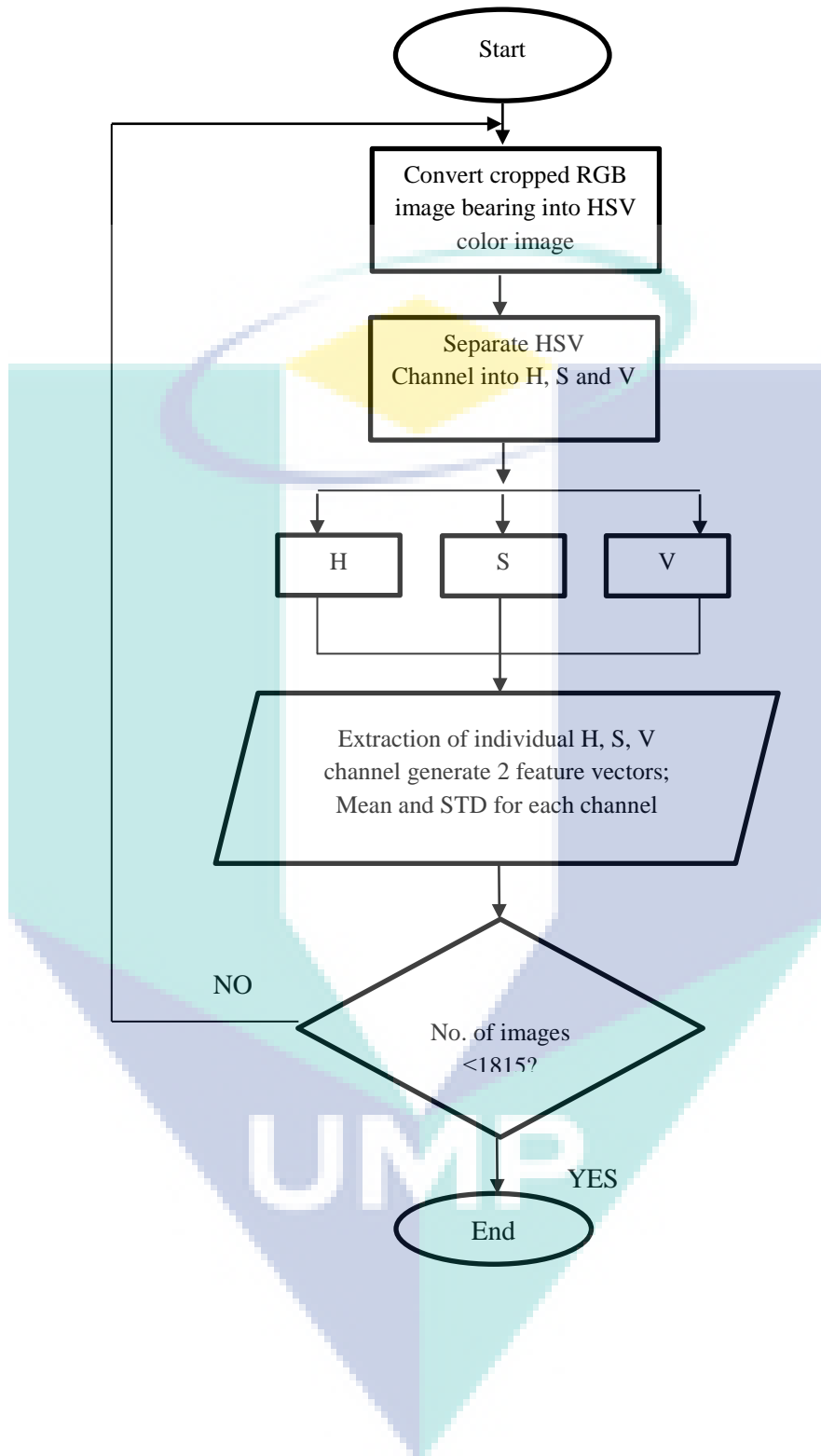


Figure 3.7 Flowchart of HSV Color-based feature extraction technique

3.4.6 Algorithm for the L*a*b color- based Feature Extraction Method

This study discusses in detail the process that will be executed to apply the feature extraction process based on the HSV color method. The purpose of this method is to perceive the effectiveness of this method to distinguish the optimal features in each group of thermal motor bearing image. Thus, the following procedures is the detailed process:

Step 1: Read the cropped segmented bearing image with the dimensional size of $m \times n$, where m and n are the number of rows and column respectively.

Step 2: Convert the RGB of thermal motor bearing image input into L^*a^*b color space image, $I_{l^*a^*b}(x, y)$;

Step 3: Separate the three channels of L^*a^*b color space individually as in equation 3.32. 'L' defines a lightness, a^* and b^* for the colour opponent dimensions which 'a*' indicating where color falls along the red-green axis and 'b*' indicating where the color falls along the blue-yellow axis (Chen, 2003).

$$\begin{bmatrix} L^* = 116f(Y/Y_n) - 16 \\ a^* = 500[f(X/X_n) - f(Y/Y_n)] \\ b^* = 200[f(Y/Y_n) - f(Z/Z_n)] \end{bmatrix} \quad 3.32$$

$X, Y, Z, X_n, Y_n,$ and Z_n are the coordinates of CIEXYZ colour space. The solution to convert digital images from the RGB space to the CIEXYZ colour space is in equation 3.33.

$$\begin{bmatrix} X_n \\ Y_n \\ Z_n \end{bmatrix} = \begin{bmatrix} 0.608 & 0.174 & 0.201 \\ 0.299 & 0.587 & 0.114 \\ 0.000 & 0.066 & 1.117 \end{bmatrix} \begin{bmatrix} R \\ G \\ B \end{bmatrix} \quad 3.33$$

$X_n, Y_n,$ and Z_n are respectively corresponding to the white value of the parameter.

Step 4: Extract the features based on the L^*a^*b obtained. There are two types of features that will be generated with statistical features which are mean and standard deviation. The

mean is the average value which gives some information about general brightness of the image. Therefore, mean can be defined as equation 3.34 and equation 3.35:

$$g' = \sum_{g=0}^{L-1} g * P(g) = \sum_r \sum_c \frac{I(r,c)}{M} \quad 3.34$$

$$P(g) = N(g) / M \quad 3.35$$

Where $P(g)$ is histogram probability, M is the number of pixel in the image $L*a*b$ ($M \times N$), $N(g)$ is the number of gray level g , L is a total number of gray level available range from 0-255.

Meanwhile, the Standard deviation is known as square root of the variance tells something about the contrast. Thus, a high contrast image will have a high temperature or intensities image. The equation is as equation 3.36.

$$\sigma_g = \sqrt{\sum_{g=0}^{L-1} (g - g')^2 P(g)} \quad 3.36$$

Figure 3 illustrates a flow chart representation of pseudocode 7 regarding the $l*a*b$ Color-based feature extraction process to extract the features from thermal motor bearing image groups.

Pseudocode 7: $l*a*b$ Color-based feature extraction Algorithm

Input: RGB of segmented thermal motor bearing images,

Output: Output extracted features

Steps:

1. Start;
 2. Convert the segmented RGB image into individual $l*a*b$ color space image;
 3. Extract the statistical features namely mean and standard deviation;
 4. Output features: $Y \in R^{n \times j} \in MEAN^{2075 \times 1} \in STD^{2075 \times 1}$
 5. End
-

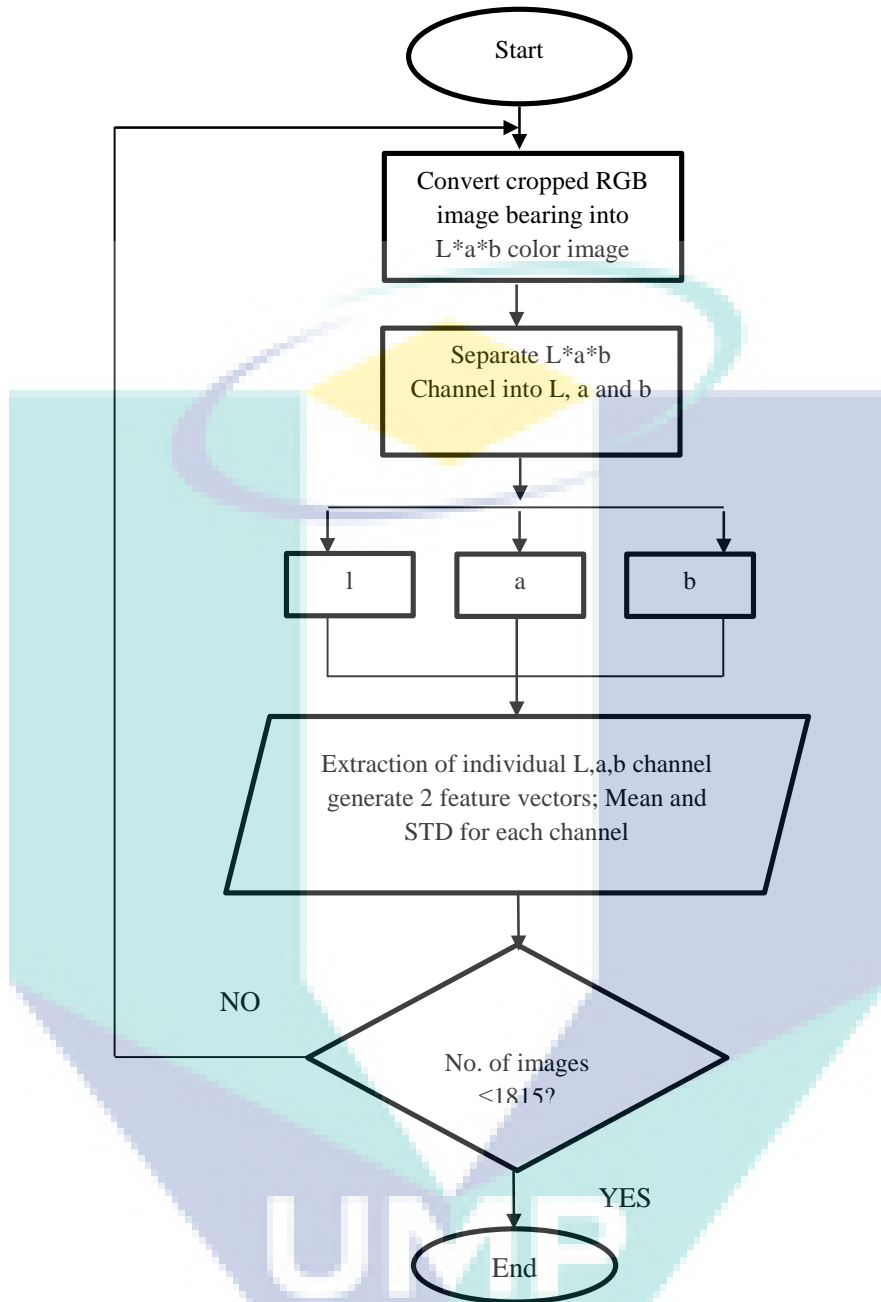


Figure 3.8 Flowchart of L*a*b Color based feature extraction technique

3.5 Feature selection based-Fisher score technique

From the previous studies, a multi-scale and multi-orientation features at each image points from the feature extraction based on GWT techniques will be generated [cited]. This high dimensional of the resultant Gabor feature vector that occurs will cause the computational and memory required for recognition are prohibitively large. To address this problem, feature reduction method will be employed to reduce the

dimensionality of the data in order to simplify the calculation analysis and improve the learning performances in term of higher learning accuracy for classification in this work. Feature selection is one of the most popular methods due to the preservation of the original meaning of features and it is an important part of machine learning. This feature selection is an approach to seek the most useful subset of the original variables or features for use in the implementation of the machine learning model in order to speed up the training time, enhance the learning interpretability, lowering computational **cost and complexity**. Furthermore, the current subset generated from these predictive features will improve the robustness of the classification models.

From the previous studies, there have demonstrated that the fisher score method have been implemented extensively in various application in image processing field for solving high dimensionality data resulting from feature extraction process (Ahmad et al., 2017; Ahmed & Nandi, 2017; Aksu et al., 2018; Bhasin et al., 2014; Cherrington et al., 2019; Gu et al., 2012a; Roffo & Melzi, 2016; Saqlain et al., 2019; Sharma et al., 2019; Song et al., 2017; Sun et al., 2019; Źbikowski, 2015). Yet, there are a few studies regarding implementation of feature selection based fisher score in order to eliminate the irrelevant Gabor features extraction (Li et al., 2010; Ma et al., 2019; Vamsidhar et al., 2016). The experimental results of the studies have shown better performance in classification result. In this way, a significant reduction in computation and memory cost has been achieved. This method is much simpler to build and faster in process, scalable with high dimensional datasets, reduce computational cost, computationally simple and effective filtering method (Gu et al., 2012a). In consequence, this has been motivated to use this proposed fisher score method in this study for feature selection purposes.

This approach provides a measure of features' ability to distinguish between different classes. The selected features were then fed as an input to the classification model. In this feature selection process, it computes a subset of features with a large distance between data points in different classes and small distance between data points in the same class, and the final feature selection occurs by the top ranked ones (Gu et al., 2012b; Islam et al., 2015; Ma et al., 2019; T. Zhang & Lu, 2010). Given the input data matrix $Y \in R^{m \times j}$, then it will be reduced to $F \in R^{m \times j}$. Then, the index of a feature score f_s will be computed as equation 3.32 follows:

$$f_s = \frac{\sum_{i=1}^c n_i (\mu_j^i - \mu_j)^2}{\sum_{i=1}^c n_i (\sigma_j^i)^2}$$

By utilizing this formula, the experimental study will show that the size of high dimensional features and the computations involved in feature extraction process will be significantly reduced. Next, the top score feature which is the most discriminative power will be selected as the top fisher score.

Hereby, this fisher score method will be applied to all the proposed of new feature extraction methods as well as to the original GWT-based method. The purpose is to seek the difference scores that will be obtained between the proposed methods. A higher score readings from all proposed new feature extraction methods along with the original score readings from GWT-based method became a priority in this section. The highest score ratio to be obtained will indicate the best discriminant features for the group of thermal motor bearing images in this study. The processing for these methods will be presented in detail in section 3.6.1 to section 3.6.5. Meanwhile, this fisher score-based feature selection will also be implemented on the color-based feature extraction techniques. The purpose is to perceive the difference in score results that will be obtained between the color-based methods compared to the original GWT-based methods. The methods of operation of this process will be explained briefly in sections 3.5.5 and 3.5.6.

3.5.1 Fisher Score Algorithm in the Original Gabor Wavelet Transform (GWT)-based Feature Extraction Method

In this section, the focus is on selecting the optimal scale and orientation for Gabor features used in the feature model. From the previous feature extraction process, a high dimensional of the resultant Gabor features vector namely Local Energy (LE) and Mean Amplitude (MA) will be generated. It consists the different scales parameters = $\{scale7 \times 7, scale9 \times 9, scale11 \times 11, scale13 \times 13, scale15 \times 15\}$ and orientations parameters,

$$\theta = \left\{ 0^\circ, \frac{\pi}{8}, \frac{\pi}{4}, 3\frac{\pi}{8}, \frac{\pi}{2}, 5\frac{\pi}{8}, 3\frac{\pi}{4}, 7\frac{\pi}{8} \right\}. 40 \text{ filters Gabor channel will be organized at each}$$

image point which means 40 multi-scales and multi-orientations feature images will be

constructed. Therefore, the computational time and memory required for recognition will be large and lengthy, as well as will increase the computational cost. The proposed fisher score-based feature selection method will address these issues. By applying this fisher score method, the subset of the most relevant features will be determined. Thus, the dimensionality of the data to simplify the calculation analysis will be reduced so that running time of the algorithm will also be reduced. In addition, the learning performances in terms of higher learning accuracy will also be improved for classification in this work.

Based on the studies in (Li et al., 2010; Ma et al., 2019), they have been stated that, Gabor filters that produce features with large discrimination power should be retained and those that produce features with less significant should be eliminated from the filters that have constructed. This selected optimal feature will eventually be utilized as input to the classification model. The purpose is to classify the differences in the group of thermal motor bearing images well. The following is a detailed procedure for generating the discrimination of orientations and scales that will be selected for both LE and MA features:

Step 1: Read all the high dimensional extracted data input Gabor features which are Local Energy (LE) and Mean Amplitude (MA), $Y \in R^{(nx5) \times j} \in LE^{10375 \times 8}, MA^{10375 \times 8}$.

Step 2: Calculate the sample mean and variance of each class along all the features in order to obtain the discriminability of the j -th scale in each feature group (orientation).

Step 3: Obtain the average fisher ratio for each feature group on each scale parameter. The features will be reduced to $F \in LE^{mxj} \in MA^{mxj}$.

Step 4: Rank the entire feature group based on their average fisher ratio in descending order on each scale parameter.

Step 5: Identify the best parameter features from Local Energy's and Mean Amplitude's scales and orientations by selecting the top fisher score from the entire fisher scores data, f_s

Figure 3 illustrates a flow chart representation of pseudocode 2 regarding the fisher score-based feature selection process. This process aims to select the optimal features of the high dimensions that will be generated from the GWT-based feature extraction process

Algorithm: Fisher Score-based feature selection Algorithm for features in Gabor Wavelet Transform (GWT)

Input: $Y \in R^{nj} \in LE^{10375 \times 8} \in MA^{10375 \times 8}$

Output: The top Fisher Score, $f_{s(LE\&MA)}$

Steps:

1. Begin

2. Read all the high dimensional extracted data input Gabor features at different orientations and scales, $Y \in R^{nj} \in LE^{10375 \times 8} \in MA^{10375 \times 8}$;

3. Calculate order values of all features using fisher ratio using equation:

$$f_s = \frac{\sum_{i=1}^c n_i (\mu_j^i - \mu_j)^2}{\sum_{i=1}^c n_i (\sigma_j^i)^2} ;$$

4. Obtain fisher ratio for each feature group, the features reduces to $F \in LE^{mj} \in MA^{mj}$

5. IF $\theta == \theta_g$ && Scale == Scale₅

 THEN Rank feature group in descending order;

 ELSE Read $Y \in R^{nj} \in LE^{10375 \times 8} \in MA^{10375 \times 8}$;

 END IF;

6. Top Fisher Score, $f_{s(LE\&MA)}$;

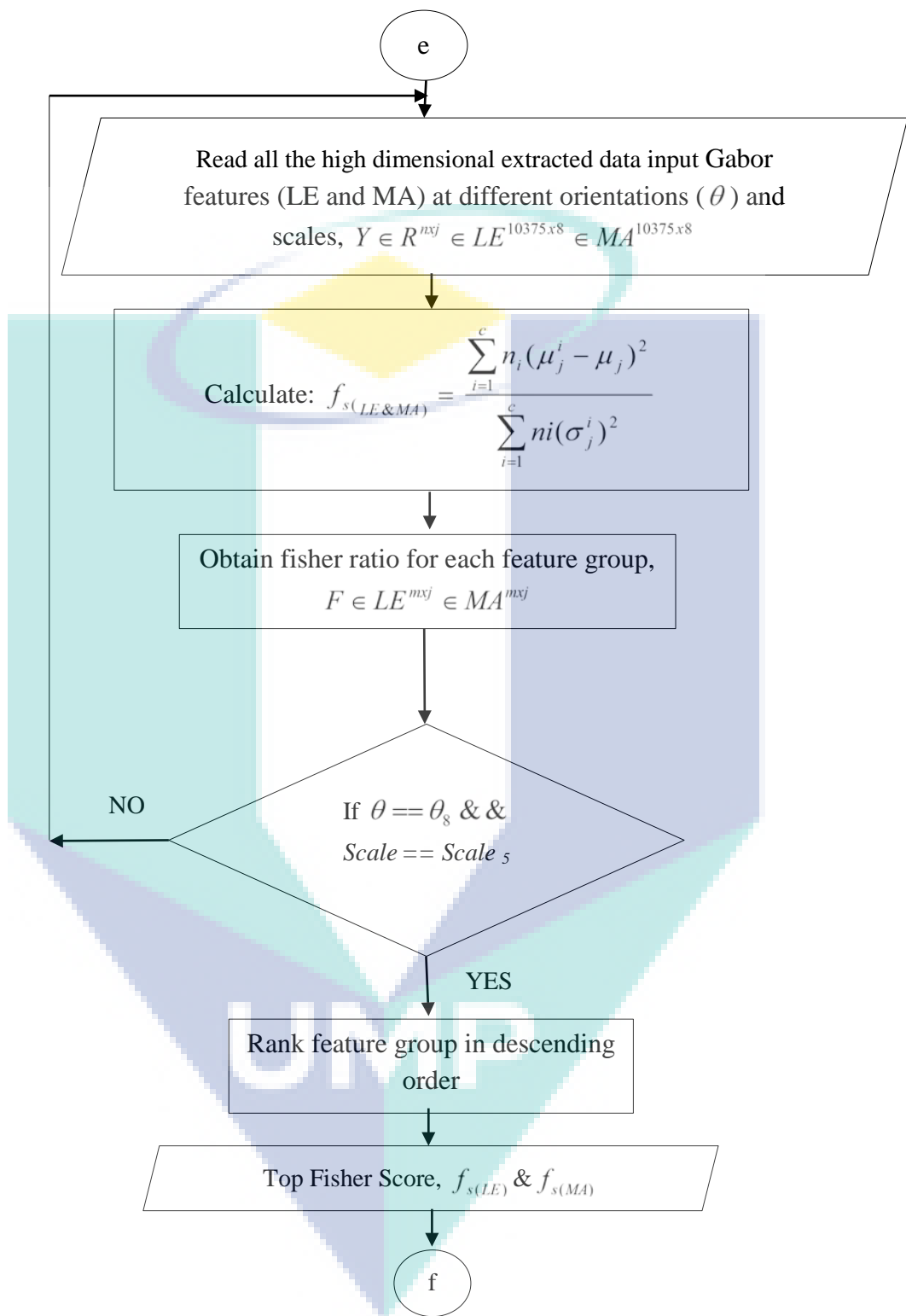


Figure 3.9 Gabor filter selection based on Fisher Score technique

3.5.2 Fisher Score Algorithm in the Proposed an Enhanced Gabor Features (EGF) -based Feature Extraction Method

In this section, the focus is on selecting the new optimal scales and orientations generated from the new Enhanced Gabor Features (EGF)-based feature extraction process. To achieve this goal, fisher score technique will be implemented in this study to produce a new score ratio value. A higher score readings from all proposed new feature extraction methods along with the original score readings from GWT-based method became a priority in this section. The highest score ratio to be obtained will indicate the best discriminant features of thermal motor bearing images group in this study.

From the previous new feature extraction process, a high dimensional of the resultant EGF features vector namely new Local Energy (LE) and new Mean Amplitude (MA) will be generated. It consists the different scales parameters= $\{scale7x7, scale9x9, scale11x11, scale13x13, scale15x15\}$ and orientations parameters, $\theta = \left\{0^\circ, \frac{\pi}{8}, \frac{\pi}{4}, 3\frac{\pi}{8}, \frac{\pi}{2}, 5\frac{\pi}{8}, 3\frac{\pi}{4}, 7\frac{\pi}{8}\right\}$. A new 40 EGF filter channel will be organized at each image point which means 40 multi-scales and multi-orientations feature images will be constructed. Therefore, the computational time and memory required for recognition will be large and lengthy, as well as will increases the computational cost. The proposed fisher score-based feature selection method will address these issues. By applying this fisher score method, the new subset of the most relevant features will be determined. Thus, the dimensionality of the data to simplify the calculation analysis will be reduced so that running time of the algorithm will also be reduced. In addition, the learning performances in term of higher learning accuracy will also be improved for classification in this work.

Based on the studies in (Li et al., 2010; Ma et al., 2019), they have been stated that, EGF filters that produce features with large discrimination power should be retained and those that produce features with less significant should be eliminated from the filters that have constructed. This selected optimal feature will eventually be utilized as input to the classification model. The purpose is to classify the differences in the group of thermal motor bearing images well. The following is a detailed procedure for

generating the discrimination of orientations and scales that will be selected for both new Local Energy ($LE_{(new)}$) and new Mean Amplitude ($MA_{(new)}$) features:

Step1: Read all the high dimensional extracted data input EGF features which are new Local Energy ($LE_{(new)}$) and new Mean Amplitude ($MA_{(new)}$),

$$Y \in R^{(nx5) \times j} \in LE_{new}^{10375 \times 8}, MA_{new}^{10375 \times 8}.$$

Step 2: Calculate the new sample mean and variance of each class along all the features in order to obtain the discriminability of the j -th scale in each feature group (orientation).

Step 3: Obtain the new average fisher ratio for each feature group on each scale parameter. The features will be reduced to $F \in LE_{new}^{mxj} \in MA_{new}^{mxj}$.

Step 4: Rank the new entire feature group based on their new average fisher ratio in descending order on each scale parameter.

Step 5: Identify the new best parameter features from new Local Energy's and new Mean Amplitude's scales and orientations by selecting the new top fisher score from the entire fisher scores data, $f_{s(LE(new))}$ & $f_{s(MA(new))}$

Figure 3 illustrates a flow chart representation of **pseudocode 2** regarding the fisher score-based feature selection process. This process aims to select the optimal features of the high dimensions that will be generated from the Enhanced Gabor Features (EGF)-based feature extraction process.

Algorithm: Fisher Score-based feature selection Algorithm for new features in Enhanced Gabor Features (EGF)

Input: $Y \in R^{nxj} \in LE_{new}^{10375 \times 8} \in MA_{new}^{10375 \times 8}$

Output: The top Fisher Score, $f_{s(LE(new))}$ & $f_{s(MA(new))}$

Steps:

1. Begin
2. Read all the high dimensional extracted data input EGF features at different orientations and scales, $Y \in R^{nxj} \in LE_{new}^{10375 \times 8} \in MA_{new}^{10375 \times 8}$;
3. Calculate order values of all features using fisher ratio using equation:

$$f_s = \frac{\sum_{i=1}^c n_i (\mu_j^i - \mu_j)^2}{\sum_{i=1}^c n_i (\sigma_j^i)^2};$$

4. Obtain fisher ratio for each feature group, the features reduces to

$$F \in LE_{new}^{m \times j} \in MA_{new}^{m \times j};$$

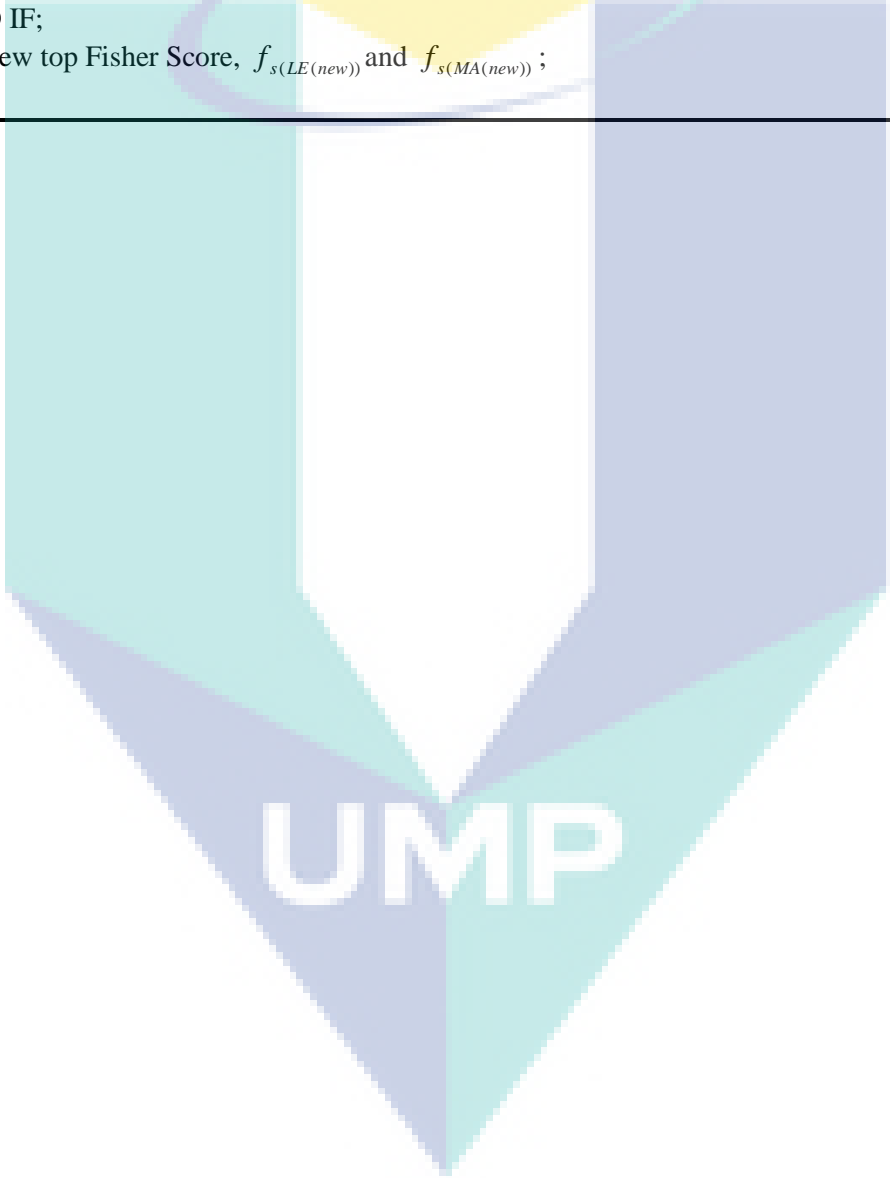
5. IF $\theta == \theta_8$ && Scale == Scale_s

THEN Rank feature group in descending order;

ELSE Read $Y \in R^{m \times j} \in LE_{new}^{10375 \times 8} \in MA_{new}^{10375 \times 8};$

END IF;

6. A New top Fisher Score, $f_{s(LE(new))}$ and $f_{s(MA(new))};$



UMP

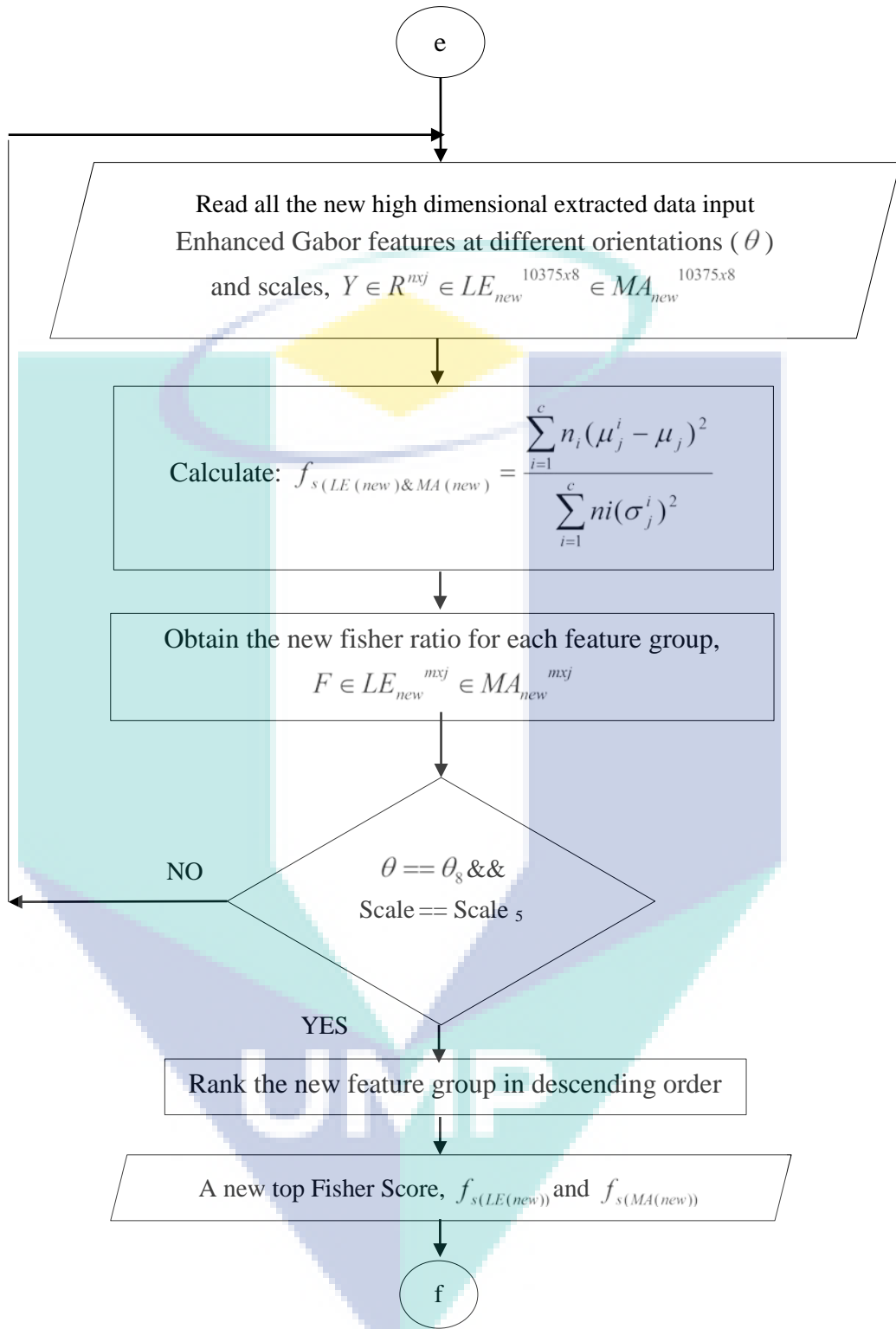


Figure 3.10 EGF filter selection based on Fisher Score technique

3.5.3 Fisher Score Algorithm in the Proposed an Enhanced GWSMH-based Feature Extraction Method

Same as in section 3.6.2, the focus in this section is on selecting the new optimal scales and orientations generated from the new Enhanced GWSMH-based feature extraction process. To achieve this goal, fisher score technique will be implemented in this study to produce a new score ratio value. A higher score readings from all proposed new feature extraction methods along with the original score readings from GWT-based method became a priority in this section. The highest score ratio to be obtained will indicate the best discriminant features of thermal motor bearing images group in this study.

From the previous new feature extraction process, a high dimensional of the resultant GWSMH features vector namely new Local Energy (LE) and new Mean Amplitude (MA) will be generated. It consists the different scales parameters= $\{scale7x7, scale9x9, scale11x11, scale13x13, scale15x15\}$ and orientations parameters, $\theta = \left\{0^\circ, \frac{\pi}{8}, \frac{\pi}{4}, 3\frac{\pi}{8}, \frac{\pi}{2}, 5\frac{\pi}{8}, 3\frac{\pi}{4}, 7\frac{\pi}{8}\right\}$. A new 40 GWSMH filter channel will be organized at each image point which means 40 multi-scales and multi-orientations feature images will be constructed. By applying the fisher score method, the new subset of the most relevant features will be determined. GWSMH filters that produce features with large discrimination power should be retained and those that produce features with less significant should be eliminated from the filters that have constructed. The following is a detailed procedure for generating the discrimination of orientations and scales that will be selected for both new Local Energy ($LE_{(new)}$) and new Mean Amplitude ($MA_{(new)}$) features:

Step1: Read all the high dimensional extracted data input GWSMH features which are new Local Energy ($LE_{(new)}$) and new Mean Amplitude ($MA_{(new)}$),

$$Y \in R^{(nx5)xj} \in LE_{new}^{10375x8}, MA_{new}^{10375x8}.$$

Step 2: Calculate the new sample mean and variance of each class along all the features in order to obtain the discriminability of the scale in each feature group (orientation).

Step 3: Obtain the new average fisher ratio for each feature group on each scale parameter, the features will be reduced to $F \in LE_{new}^{mxj} \in MA_{new}^{mxj}$.

Step 4: Rank the new entire feature group based on their new average fisher ratio in descending order on each scale parameter.

Step 5: Identify the new best parameter features from new Local Energy's and new Mean Amplitude's scales and orientations by selecting the new top fisher score from the entire fisher scores data, $f_{s(LE(new))} \& f_{s(MA(new))}$.

Figure 3 illustrates a flow chart representation of pseudocode 2 regarding the fisher score-based feature selection process. This process aims to select the optimal features of the high dimensions that will be generated from the Enhanced GWSMH-based feature extraction process.

Algorithm: Fisher Score-based feature selection Algorithm for new features in Enhanced GWSMH.

Input: $Y \in R^{nxj} \in LE_{new}^{10375 \times 8} \in MA_{new}^{10375 \times 8}$

Output: The top Fisher Score, $f_{s(LE(new))} \& f_{s(MA(new))}$

Steps:

1. Begin
2. Read all the high dimensional extracted data input EGF features at different orientations and scales, $Y \in R^{nxj} \in LE_{new}^{10375 \times 8} \in MA_{new}^{10375 \times 8}$;
3. Calculate order values of all features using fisher ratio using equation:

$$f_s = \frac{\sum_{i=1}^c n_i (\mu_j^i - \mu_j)^2}{\sum_{i=1}^c n_i (\sigma_j^i)^2};$$

4. Obtain fisher ratio for each feature group, the features reduces to

$$F \in LE_{new}^{mxj} \in MA_{new}^{mxj};$$

5. IF $\theta == \theta_g \&\& \text{Scale} == \text{Scale}_s$

THEN Rank feature group in descending order;

ELSE Read $Y \in R^{nxj} \in LE_{new}^{10375 \times 8} \in MA_{new}^{10375 \times 8}$;

END IF;

6. A New top Fisher Score, $f_{s(LE(new))}$ and $f_{s(MA(new))}$;
-

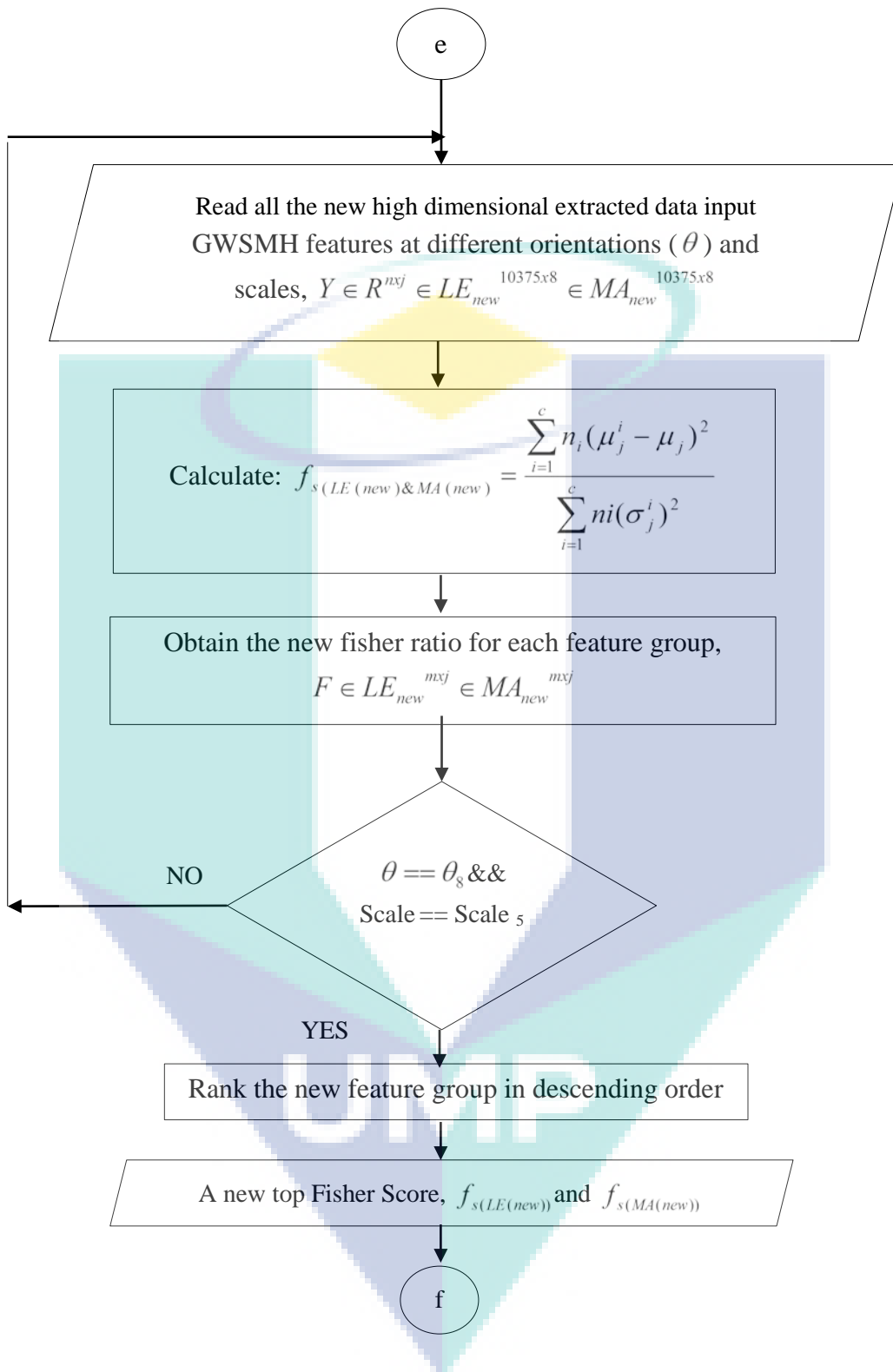


Figure 3.11 GWSMH filter selection based on Fisher Score technique

3.5.4 Fisher Score Algorithm in the Proposed an Enhanced GWCLAHE -based Feature Extraction Method

Same as in section 3.6.2 and section 3.6.3, the focus in this section is on selecting the new optimal scales and orientations generated from the new Enhanced GWCLAHE-based feature extraction process. To achieve this goal, fisher score technique will be implemented in this study to produce a new score ratio value. A higher score readings from all proposed new feature extraction methods along with the original score readings from GWT-based method became a priority in this section. The highest score ratio to be obtained will indicate the best discriminant features of thermal motor bearing images group in this study.

From the previous new feature extraction process, a high dimensional of the resultant GWCLAHE features vector namely new Local Energy (LE) and new Mean Amplitude (MA) will be generated. It consists the different scales parameters= $\{scale7x7, scale9x9, scale11x11, scale13x13, scale15x15\}$ and orientations parameters, $\theta = \left\{0^\circ, \frac{\pi}{8}, \frac{\pi}{4}, 3\frac{\pi}{8}, \frac{\pi}{2}, 5\frac{\pi}{8}, 3\frac{\pi}{4}, 7\frac{\pi}{8}\right\}$. A new 40 GWCLAHE filter channel will be organized at each image point which means 40 multi-scales and multi-orientations feature images will be constructed. By applying the fisher score method, the new subset of the most relevant features will be determined. GWCLAHE filters that produce features with large discrimination power should be retained and those that produce features with less significant should be eliminated from the filters that have constructed. The following is a detailed procedure for generating the discrimination of orientations and scales that will be selected for both new Local Energy ($LE_{(new)}$) and new Mean Amplitude ($MA_{(new)}$) features:

Step1: Read all the high dimensional extracted data input GWSMH features which are new Local Energy ($LE_{(new)}$) and new Mean Amplitude ($MA_{(new)}$),

$$Y \in R^{(nx5)xj} \in LE_{new}^{10375x8}, MA_{new}^{10375x8} .$$

Step 2: Calculate the new sample mean and variance of each class along all the features in order to obtain the discriminability of the scale in each feature group (orientation).

Step 3: Obtain the new average fisher ratio for each feature group on each scale parameter, the features will be reduced to $F \in LE_{new}^{mxj} \in MA_{new}^{mxj}$.

Step 4: Rank the new entire feature group based on their new average fisher ratio in descending order on each scale parameter.

Step 5: Identify the new best parameter features from new Local Energy's and new Mean Amplitude's scales and orientations by selecting the new top fisher score from the entire fisher scores data, $f_{s(LE(new))}$ & $f_{s(MA(new))}$.

Figure 3 illustrates a flow chart representation of pseudocode 2 regarding the fisher score-based feature selection process. This process aims to select the optimal features of the high dimensions that will be generated from the Enhanced GWCLAHE-based feature extraction process.

Algorithm: Fisher Score-based feature selection Algorithm for new features in Enhanced GWCLAHE.

Input: $Y \in R^{nxj} \in LE_{new}^{10375 \times 8} \in MA_{new}^{10375 \times 8}$

Output: The top Fisher Score, $f_{s(LE(new))}$ & $f_{s(MA(new))}$

Steps:

1. Begin
2. Read all the high dimensional extracted data input EGF features at different orientations and scales, $Y \in R^{nxj} \in LE_{new}^{10375 \times 8} \in MA_{new}^{10375 \times 8}$;
3. Calculate order values of all features using fisher ratio using equation:

$$f_s = \frac{\sum_{i=1}^c n_i (\mu_j^i - \mu_j)^2}{\sum_{i=1}^c n_i (\sigma_j^i)^2};$$

4. Obtain fisher ratio for each feature group, the features reduces to

$$F \in LE_{new}^{mxj} \in MA_{new}^{mxj};$$

5. IF $\theta == \theta_g$ && Scale==Scale_s

THEN Rank feature group in descending order;

ELSE Read $Y \in R^{nxj} \in LE_{new}^{10375 \times 8} \in MA_{new}^{10375 \times 8}$;

END IF;

6. A New top Fisher Score, $f_{s(LE(new))}$ and $f_{s(MA(new))}$;
-

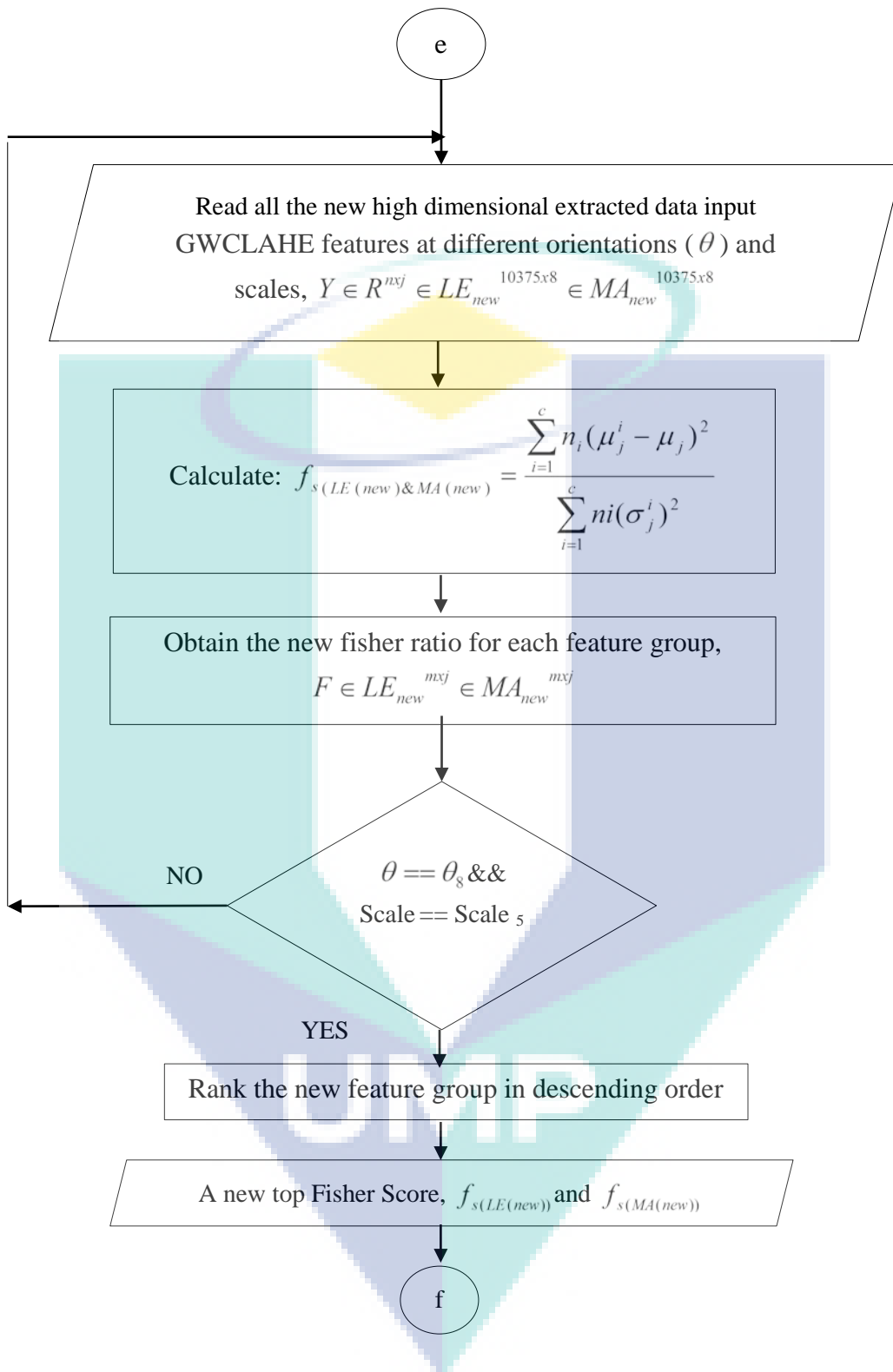


Figure 3.12 GWCLAHE filter selection based on Fisher Score technique

3.5.5 Fisher Score Algorithm for Color based Feature Extraction Method

In this section, the focus is on selecting the optimal features generated from the color-based feature extraction process. The color methods involved are HSV and $1 * a * b$ based methods. The purpose is to perceive the difference in score results that will be obtained between the color-based methods compared to the original GWT-based methods. To achieve this goal, fisher score technique will be implemented in this study to produce a score ratio value.

Based on the color feature extraction process, there are six types of features that will be generated namely mean and standard deviation for each HSV and $1 * a * b$ components. By applying the fisher score method, the new subset of the most relevant features will be determined. Thus, the detailed process of the proposed Fisher Score-based feature selection algorithm for the HSV and $1 * a * b$ color methods is described as follows:

(a) HSV color-based feature extraction

Step 1: Read all the input extracted data HSV color features, $Y \in R^{n \times j} \in HSV^{2075 \times 6}$

Step 2: Calculate sample mean and variance of each class along all the features in order to obtain the discriminability in each feature group.

Step 3: Obtain the average fisher ratio for each feature group, $F \in HSV^{m \times j}$

Step 4: Rank the entire feature group based on their average fisher ratio in descending order.

Step 5: Identify the best parameter features by selecting the top fisher score from the entire fisher scores data, $f_{s(HSV)}$.

Figure 3 illustrates a flow chart representation of pseudocode 2 regarding the fisher score-based feature selection process. This process aims to select the optimal features that will be generated from HSV Color-based feature extraction process.

Algorithm: Fisher Score-based feature selection for HSV color

Input: $Y \in R^{n \times j} \in mean^{2075 \times 6} \in std^{2075 \times 6}$

Output: The top Fisher Score, $f_{s(HSV)}$

Steps:

1. Begin
2. Read all the input extracted data HSV color features,
 $Y \in R^{n \times j} \in mean^{2075 \times 6} \in std^{2075 \times 6}$;
3. Calculate order values of all features using fisher ratio using equation:

$$f_s = \frac{\sum_{i=1}^c n_i (\mu_j^i - \mu_j)^2}{\sum_{i=1}^c n_i (\sigma_j^i)^2};$$

4. Obtain fisher ratio for each feature group, the features reduces to $F \in HSV^{m \times j}$;
 5. IF $f == f_0$
 THEN Rank feature group in descending order;
 ELSE Read $Y \in R^{n \times j} \in mean^{2075 \times 6} \in std^{2075 \times 6}$;
 END IF;
 6. Top Fisher Score, $f_{s(mean\&std)}$;
-

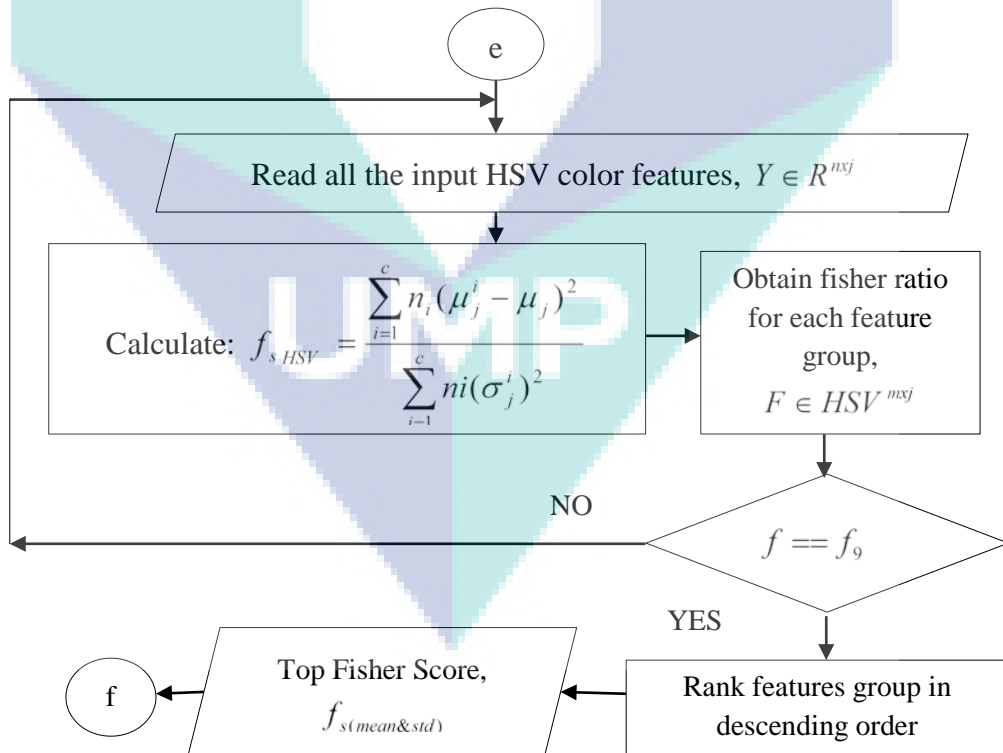


Figure 3.13 HSV color selection based on Fisher Score technique

(b) $l \times a \times b$ color-based feature extraction

Step 1: Read all the input extracted data $l \times a \times b$ color features, $Y \in R^{n \times j} \in l \times a \times b^{2075 \times 6}$

Step 2: Calculate sample mean and variance of each class along all the features in order to obtain the discriminability in each feature group.

Step 3: Obtain the average fisher ratio for each feature group, $F \in l \times a \times b^{m \times j}$.

Step 4: Rank the entire feature group based on their average fisher ratio in descending order.

Step 5: Identify the best parameter features by selecting the top fisher score from the entire fisher scores data, $f_{s(mean \& std)}$

Figure 3 illustrates a flow chart representation of **pseudocode 2** regarding the fisher score-based feature selection process. This process aims to select the optimal features that will be generated from $l \times a \times b$ Color-based feature extraction process.

Algorithm: Fisher Score-based feature selection for $l \times a \times b$ color

Input: $Y \in R^{n \times j} \in l \times a \times b^{2075 \times 6}$

Output: The top Fisher Score, $f_{s(mean \& std)}$

Steps:

1. Begin

2. Read all the input extracted data $l \times a \times b$ color features, $Y \in R^{n \times j} \in l \times a \times b^{2075 \times 6}$;

3. Calculate order values of all features using fisher ratio using equation:

$$f_s = \frac{\sum_{i=1}^c n_i (\mu_j^i - \mu_j)^2}{\sum_{i=1}^c n_i (\sigma_j^i)^2};$$

4. Obtain feature ratio for each feature group, the features reduces to $F \in l \times a \times b^{m \times j}$;

5. IF $f == f_9$

 THEN Rank feature group in descending order;

 ELSE Read $Y \in R^{n \times j} \in l \times a \times b^{2075 \times 6}$;

 END IF;

6. Top Fisher Score, $f_{s(mean \& std)}$;

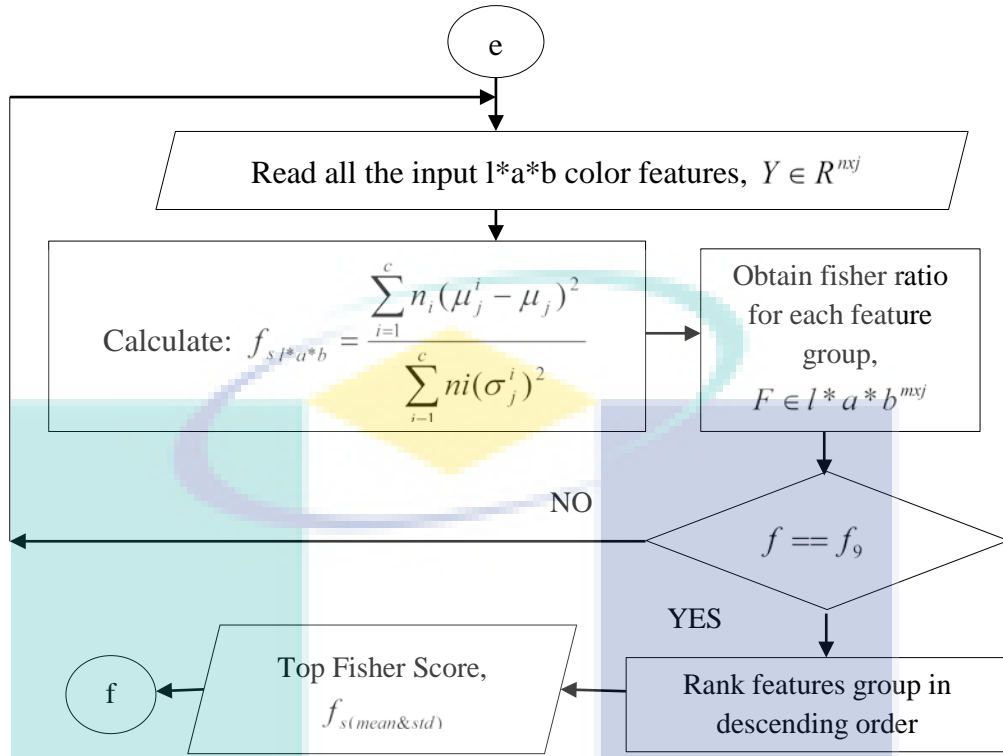


Figure 3.14 $l*a*b$ color selection based on Fisher Score technique

3.6 A one-way ANOVA test

A one-way ANOVA test method will be employed in this work since there are more than 2 groups that need to be evaluated in this work (El-Farrash, El Shimy, El-Sakka, Ahmed, & Abdel-Moez, 2019; Gertheiss, 2014; Marzook, Razek, Yousef, & Attia, 2020; Verma, 2013). This statistical method of ANOVA will be applied in this work to determine the extent of feature sensitivity to differentiate the three classes produced from each feature extraction based method in this work (Desai, Patel, & Prajapati, 2016). It also aims to analyze whether there are any significant differences between the mean of three independent groups features produced by the thermal motor bearing images in this work.

ANOVA test will give two important values which are F-value and P-value. The F-value is the ratio of the mean squares. It will be applied to statistically test the variability between group means is larger compared to the variability within group variation. According to (Kazerouni, 2009), the larger F-value value is, the more significant “between-group variation” would be. At this point, as between group variability increase, sample means will show further apart from each other. It is also

more probable to be belonging to totally different population. Yet, in (Desai et al., 2016), the larger the value of F-statistic, the better the feature will be. After the value of F-ratio is obtained, the level of significance for the samples will be determined by comparing it to the F-Critical value. If the F- ratio is larger than F-Critical, then the variation between the groups is statistically significant.

In addition to the F- ratio, P-value is the most important part in the ANOVA table . If P-value is less than the level of significance at $\alpha=0.05$, null hypothesis will be rejected. Otherwise, null hypothesis will be accepted. It means, the lower the value resulting from this P-value is, the more statistically significant the population parameter is (Kazerouni, 2009). Null hypothesis denotes that the mean value between two or more population groups are the same ie : $H_o = \mu_1 = \mu_2 = \mu_3$. This condition means there is no significant different between the population group. While alternative hypothesis are the opposite of null hypotheses. It shows that the mean values between two or more population groups are not the same, $H_1 = \mu_1 \neq \mu_2$. This condition means there is significant different between the population group. Level of significance, $\alpha = 0.05$ has also been set (Alkhudhairy, Al-Johany, Naseem, Bin-Shuwaish, & Vohra, 2020; Bahbishi, Mzain, Badeeb, & Nassar, 2020; Tian et al., 2020; Zimmermann, Valcanaia, Neiva, Mehl, & Fasbinder, 2019). This one-way ANOVA test will be performed by using IBM SPSS Statistics 20 software. The results of the measurements involved from this one-way ANOVA software will be shown as in the [table](#).

Table 3.2 A one-way ANOVA table

Sources of variation	Sums of squares (SS)	Degree of freedom (df)	Mean squares (MS)	F statistic
Between Groups	SSB	k-1	$MSB = \frac{SSB}{k-1}$	$\frac{MSB}{MSW}$
Within Groups	SSW	N-k	$MSW = \frac{SSW}{N-k}$	
Total	SST	N-1		

3.7 Classification

After the feature selection processing is explained, this section will discuss the classifier model to be used and how it works in this classification process. This classification process will be carried out to test the proposed classifier model to classify the condition of thermal motor bearing images whether they are normal, warning or abnormal images. There are two types of learning algorithm approaches that will be utilized in this classification process for comparative purposes, namely the Multilayer Artificial Neural Networks (MLANNs) and Linear thresholding (LT). The highest performance result in terms of accuracy between these two proposed classifier methods will be an indicator to the selection of the best classifier model in this study.

A general framework for classification process in this work is demonstrated in Figure 3.29. Before this classification process is carried out, the process of eliminating all the irrelevant features needs to be executed for the selection of the optimal feature. This is to reduce the time spent during running the learning algorithm. Next, the optimal features obtained will feed into the classifier model as a training data for processing in this study. By using the machine learning stated, the results of the classification performance in terms of precision (PRE), accuracy (ACC), specificity (SPEC), sensitivity (SENS) and CER will be generated.

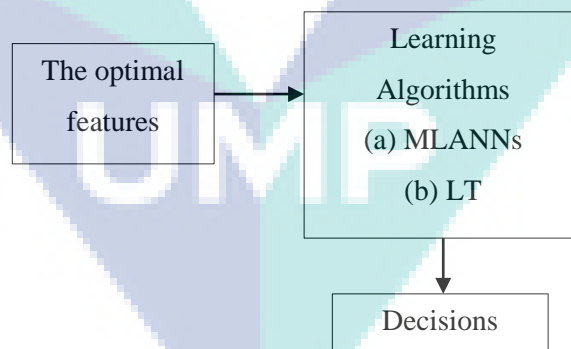


Figure 3.15 A general framework for classification process

All these processes will be explained in more detail in the next section in sections 3.8.1 and section 3.8.2.

3.7.1 Multi-Layer Artificial neural Networks (MLANNs) Algorithm for solving Classification Tasks

This study proposes a Multi-Layer Artificial Neural networks (MLANNs) with the supervised machine learning as the technique to classify the different conditions of thermal motor bearing images in this work. The input for this MLANNs model is based on the optimal features generated from the previous feature selection process.

This MLANNs method was selected in this study due to it is faster, robust and more accurate. Over the year, MLANN is one of the extensively used techniques for classification of class of objects in image processing fields. It is also applicable in various applications such are pattern recognition (Gaja & Liou, 2018), medical (Aruna Devi B., 2019; Mohammed et al., 2018), dental (Raith et al., 2017), electrical system (Bighnaraj Panda, 2018; Taheri-Garavand et al., 2015), mechanical system (B. Hizarci, 2019; Jain et al., 2019) and so on.

The architecture of MLANNs can be set up in a variety of ways. In this work, MLANNs model will be constructed consisting of three layers of nodes: two input layer, one hidden layer and three output layers feed forward network as denoted in **Figure 3.30**. Five different hidden neurons at $HN = 1, 2, 3, 4$ and 5 will be evaluated on each learning algorithm during the training process. This is to seek the impact on the MLANNs network model in terms of MSE performance and the accuracy value that will be obtained.

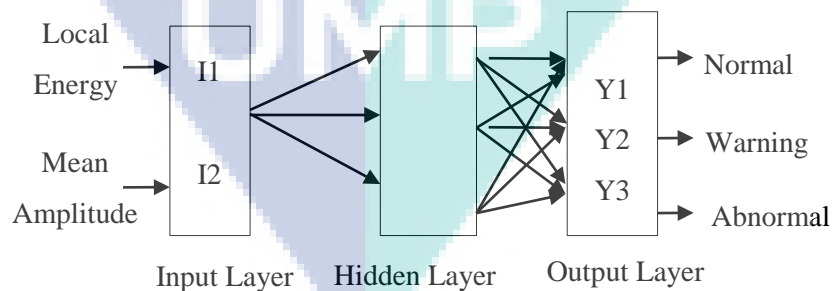


Figure 3.16 Single hidden layer architecture Artificial Neural Network

In the input layer, it represents the feature vectors namely Local Energy and Mean Amplitude. **These input features come from the set of selected features along with**

the desired output target. They will be applied to the ANNs in order to calculate the actual output. Since there is a 3-class classification problem, the target setting values that will be utilized are 000 010 and 001 representing the differences of group images. Next, the weighted inputs will be sent to a series of hidden layers by means of the input features signal multiplied by the weight of the first connection. This weighted input will cause ANN neurons to become active. Meanwhile, the activation signal passed by the transfer function consisting of weighted inputs from the hidden layer will be received at the output layer to produce a single neuron output. The tangent sigmoid function (*'tansig'*) will be the activation function, f in the hidden layer, while the linear transfer function (*'purelin'*) for the output layer. These transfer functions will be performed on the weighted input and output neurons.

Subsequently, feed forward MLANNs with Levenberg-Marquardt backpropagation (*'trainlm'*), Bayesian regularization backpropagation (*'trainbr'*) and Scaled conjugate gradient backpropagation (*'trainscg'*) training algorithms will be employed to fit the ANN model purpose. In addition, the impact of these three learning algorithms will be assessed based on the classification performance obtained in the MLANNs model. Furthermore, the training process will take place according to each parameter of the training algorithm with its default value determination. The value of weights and biases of the network will be randomized. At the output layer, the results of the classification performance of the thermal motor image groups (normal, warning, abnormal) will be generated according to the parameters set from the learning network. If the least errors are produced from the training process, the better the classification performance value will be obtained in this work. All the declared parameters will be utilized to process the information that will affect the behavior of the ANN model.

3.7.1.1 K-Folds Cross Validation

For learning process, data sets will be divided into three sets such as training, validation and testing dataset. Training set and validation set will be used iteratively for optimizing the parameters of the MLANNs classifier. Meanwhile testing set will be employed to validate the generalization performance of the final MLANNs classifier. Out of 2593 thermal motor bearing images dataset (normal, warning, abnormal), 2334 thermal motor bearing images will be taken to train the algorithms and the remaining

259 thermal images will be used to test a trained algorithms to check whether they provides the correct output as desired. Hence, the method to estimate the generalization capability of a learning model (MLANNs) is proposed.

In this work, the data training with the implementation of training algorithm namely 'trainlm', 'trainbr' and 'trainscg' will be validated by using *K*-Fold Cross Validation technique for structure the network. It is a process to limit the problems like overfitting in the ANN model by validates the training dataset via validating each subset of *K*-Fold validation sets. It's cross-validation error will be used as the performance indicator to select the best training model. This process will begin with the training and validation dataset is randomly sorted. Then, the data will be divided into subsets of *K*. *K*-1 folds subset will be selected as the training set that corresponds to the model to fit the model, and the remaining *K*th fold will be selected as the validation set to validate the model's effectiveness. This process will be repeated *K* times, where every data point gets to be in validation set once and gets to be in a training set (*k*-1) times. After train the classifier, the performance metric which is validation accuracy of *K* results of the algorithm will be measured. It will be calculated by average the validation record score over the *K*-rounds from the folds to produce single estimation as described in equation 3.38.

$$Final_Accuracy = Average(Round1, Round2, \dots, Round10) \quad 3.38$$

Furthermore, the performance for all training functions will be discern from the validation results of this cross-validation approach. The highest accuracy and the least error of the validation results will indicates the effectiveness of learning algorithm used in the classification process. Lastly, a testing process will be performed by using 259 thermal motor bearing images to test the performance of a trained model. In this study, 5-fold and 10-fold cross-validation will be used to evaluate the performance of the MLANNs model. Thus, Figure 3.31 demonstrates an example of the scenario of 10-fold cross validation technique.

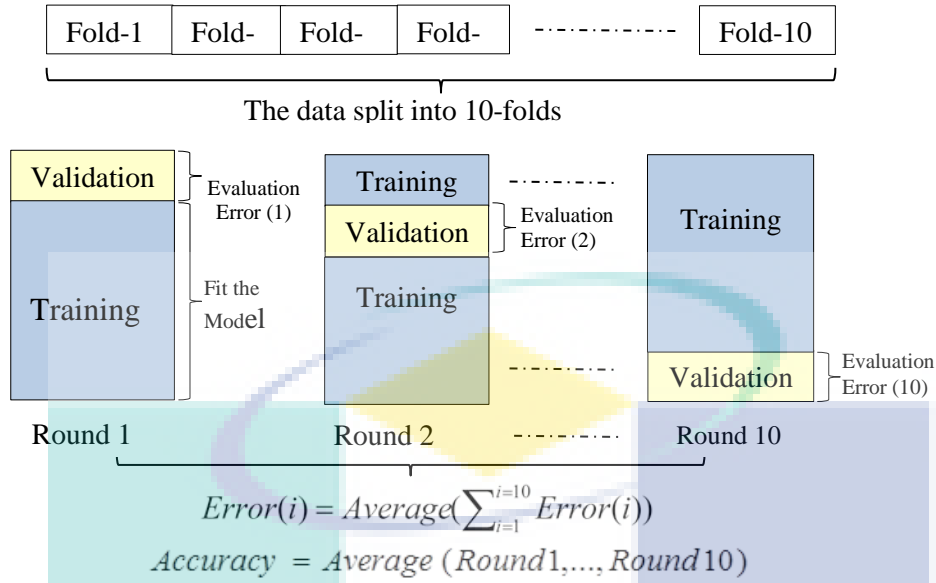


Figure 3.17 K-Fold Cross Validation procedure

Subsequently, five classification statistical performance metrics namely Precision (Pre), Sensitivity (Se), Specificity (Sp), Accuracy (Acc) and Classification Error Rate (CER) will be calculated on multi-class classification problem based on TP (True Positive), FP (False Positive), TN (True Negative) and FN (False Negative) of obtained confusion matrix (Tharwat, 2018). They are described in equations 3.39 to equation 3.44.

$$Precision(Pre) = \frac{TP}{TP + FP} \quad 3.39$$

$$Sensitivity(Se) = \frac{TP}{TP + FN} \quad 3.40$$

$$Specificity(Sp) = \frac{TN}{FP + TN} \quad 3.41$$

$$Accuracy(Acc) = \frac{TP + TN}{TP + TN + FP + FN} \quad 3.42$$

$$CER = \frac{FP + FN}{TP + TN + FP + FN} = 1 - Acc \quad 3.43$$

$$MSE = \frac{1}{N} \sum_{i=0}^N (Target_i - Output_i)^2 \quad 3.44$$

Where N is the total number of input vector, T_{arget_i} is the actual target vector and $Output_i$ is the desired output vector by MLANNs.

For further explanation, the implementation of the MLANN-based classification algorithm will be discussed in sections 3.8.1.2 to 3.8.1.5. Meanwhile, the process of the MLANN classification algorithm from two feature extracts based on HSV color technique and $1 * a * b$ color will also be included in this classification process study for comparison purposes in terms of classification performance.

3.7.1.2 MLANNs Algorithm for Original Gabor Wavelet Transform (GWT)

Method

This section will presents the whole procedures of the proposed MLANNs model with the implementation of training algorithm namely ‘trainlm’, ‘trainbr’ and ‘trainscg’ by using K -Fold Cross Validation for Gabor Wavelet Transform (GWT)-based feature extraction method. In this study, 5-fold and 10-fold cross-validation will be employed to evaluate the performance of the MLANNs model. **Figure 3** illustrates a flow chart representation of **pseudocode 7** regarding the MLANNs Algorithm for Gabor Wavelet Transform (GWT)-based feature extraction. This process will be executed to classify the condition of thermal motor bearing image in this study.

Algorithm: MLANNs Algorithm for Gabor Wavelet Transform (GWT)-based feature extraction

Input: Top Fisher Score dataset and validation dataset features;

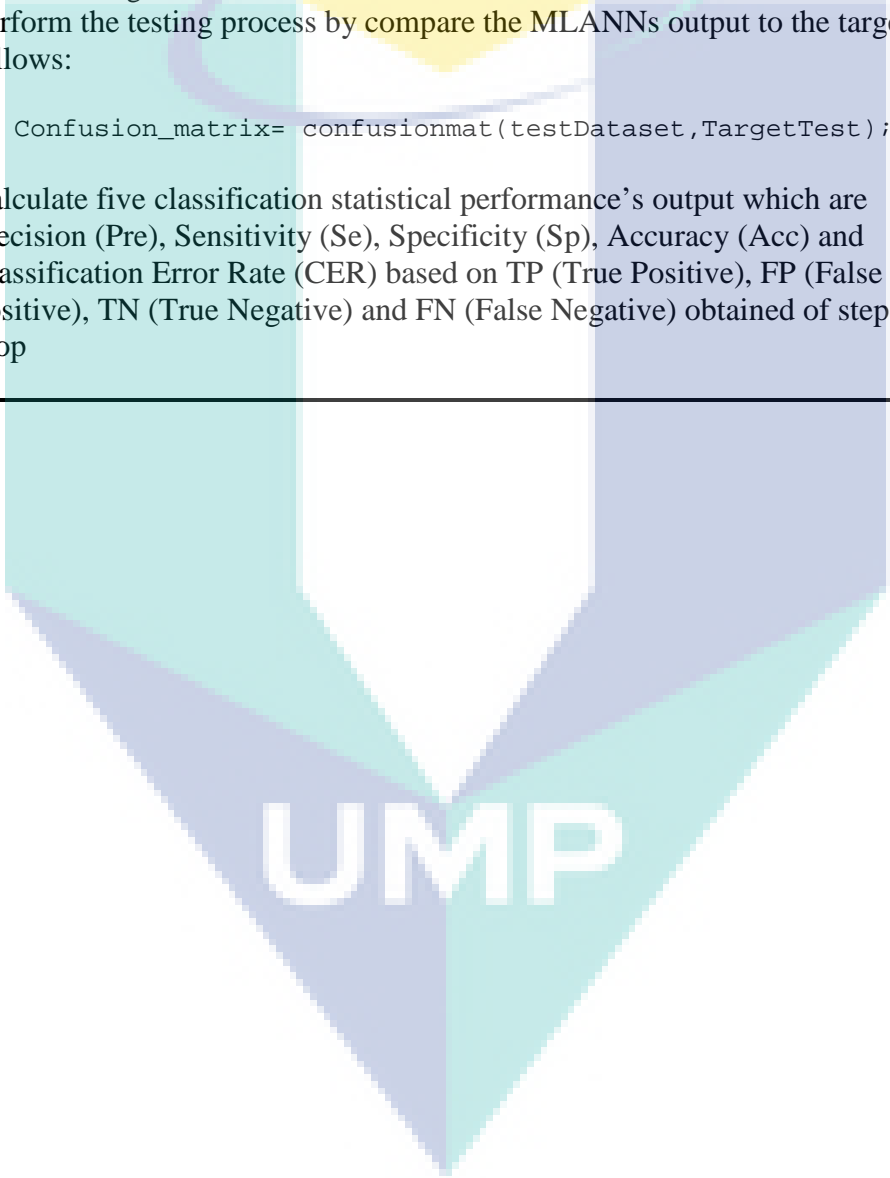
Output: Five classification statistical performance which are Precision (Pre), Sensitivity (Se), Specificity (Sp), Accuracy (Acc) and Classification Error Rate (CER) based on output from the testing set;

Steps:

1. Begin
2. Read the training top fisher score dataset and validation dataset features of Local Energy (LE) and Mean Amplitude (MA) for GWT-based feature extraction method ,
 $Y \in R^{n \times j} \in LE^{2334 \times 1} \in MA^{2334 \times 1}$;
3. Build the raw data patterns of input features for the ANN.
4. For $j=1:\text{length}(\text{Hidden Neuron})$ %Hidden Neuron=1,2,3,4,5
5. The dataset is randomly sorted and split dataset into ‘k’ groups equal-sized subsets;
6. For $i=1:k$ %k=5 & k=10
 - a) Take the group (k-1) folds for training dataset;
 - b) Take the remaining group fold as a validation dataset for evaluation learning;
 - c) Initialize the training parameters condition including number of nodes in hidden

-
- layer, training algorithms, transfer functions, epochs, goal, show and etc.;
- d) Fit a model by perform the training set and evaluate it on the validation set performance;
7. END For
 8. Compute the average validation classification performance based on confusion matrix layout for k-folds;
 9. END For
 10. Stop training when error validation is minimal. This is to ensure net can generalise to unseen data;
 11. Obtaining the best MLANNs architecture. Then, discard the unnecessary models;
 12. Save the net of MLANNs models;
 13. Call the testing datasets. Then, retrieve the save MLANNs model.
 14. Perform the testing process by compare the MLANNs output to the target as follows:

```
Confusion_matrix= confusionmat(testDataset,TargetTest);
```
 15. Calculate five classification statistical performance's output which are Precision (Pre), Sensitivity (Se), Specificity (Sp), Accuracy (Acc) and Classification Error Rate (CER) based on TP (True Positive), FP (False Positive), TN (True Negative) and FN (False Negative) obtained of step 14;
 16. Stop
-

The logo for UIMP (Universiti Malaysia Perlis) is a large, stylized shield shape. It is divided into four quadrants by a white 'V' shape pointing downwards. The top-left and bottom-right quadrants are light blue, while the top-right and bottom-left quadrants are light purple. The letters 'UIMP' are written in white, bold, sans-serif font across the center of the shield.

UIMP

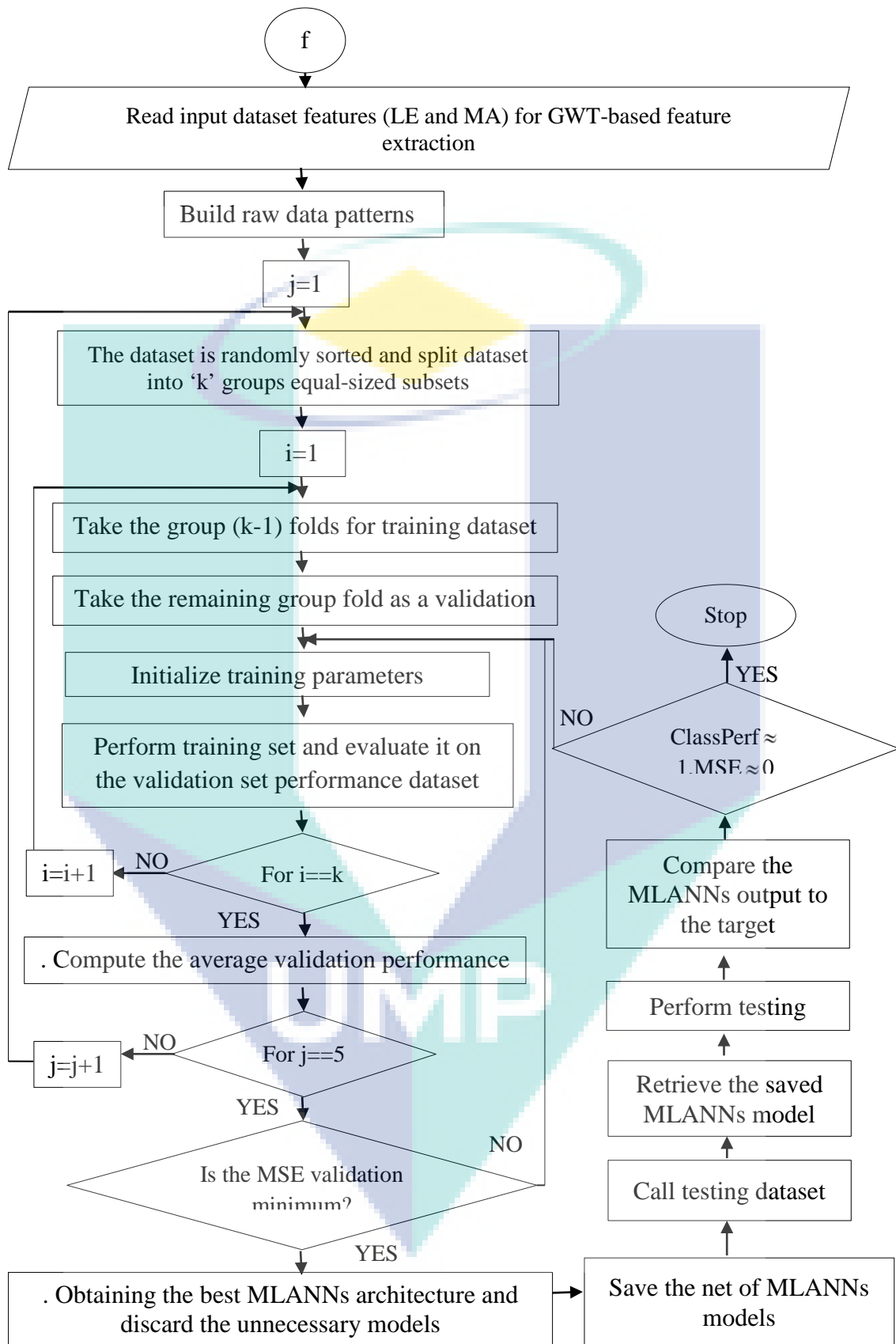


Figure 3.18 Flowchart for the proposed MLANNs for Gabor Wavelet Transform (GWT)

3.7.1.3 MLANNs Algorithm for Proposed Enhanced Gabor Features (EGF)

Method

This section will presents the whole procedures of the proposed MLANNs model with the implementation of training algorithm namely ‘trainlm’, ‘trainbr’ and ‘trainscg’ by using *K*-Fold Cross Validation for Enhanced Gabor Features (EGF)-based feature extraction method. In this study, 5-fold and 10-fold cross-validation will be employed to evaluate the performance of the MLANNs model. Figure 3 illustrates a flow chart representation of pseudocode 7 regarding the MLANNs Algorithm for Gabor Wavelet Transform (GWT)-based feature extraction. This process will be executed to classify the condition of thermal motor bearing image in this study.

Algorithm: MLANNs algorithm for Enhanced Gabor Features (EGF)-based feature extraction

Input: New top Fisher Score dataset and new validation dataset features;

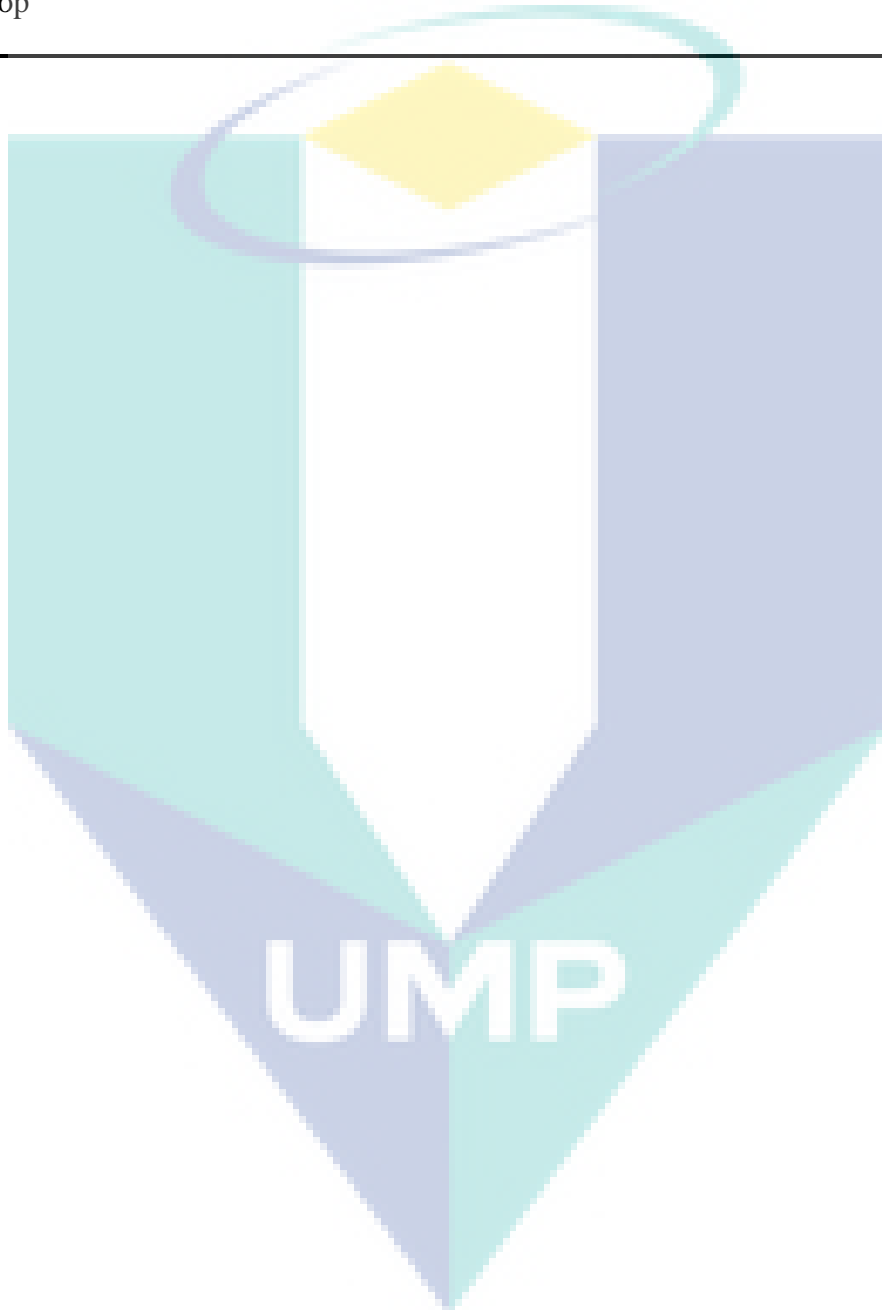
Output: New five classification statistical performance which are Precision (Pre), Sensitivity (Se), Specificity (Sp), Accuracy (Acc) and Classification Error Rate (CER) based on output from the testing set;

Steps:

1. Begin
2. Read the new training top fisher score dataset and validation dataset features which are new Local Energy (LE) and Mean Amplitude (MA) for EGF-based feature extraction method, $Y \in R^{n \times j} \in new_LE^{2334 \times 1} \in new_MA^{2334 \times 1}$;
3. Build the raw data patterns of input features for the ANN.
4. For $j=1:\text{length}(\text{Hidden Neuron})$ %Hidden Neuron=1,2,3,4,5
5. The dataset is randomly sorted and split dataset into ‘k’ groups equal-sized subsets;
6. For $i=1:k$ %Folds, $k=5$ & $k=10$
 - a) Take the group (k-1) folds for training dataset;
 - b) Take the remaining group fold as a validation dataset for evaluation learning;
 - c) Initialize the training parameters condition including number of nodes in hidden layer, training algorithms, transfer functions, epochs, goal, show and etc.;
 - d) Fit a model by perform the training set and evaluate it on the validation set performance;
7. END For
8. Compute the average validation classification performance based on confusion matrix layout for k-folds;
9. END For
10. Stop training when error validation is minimal. This is to ensure net can generalise to unseen data;
11. Obtaining the best MLANNs architecture. Then, discard the unnecessary models;
12. Save the net of MLANNs models;
13. Call the testing datasets. Then, retrieve the save MLANNs model.
14. Perform the testing process by compare the MLANNs output to the target as follows:

```
New_Confusion_matrix= confusionmat(testDataset,TargetTest);
```

15. Calculate new five classification statistical performance's output which are Precision (Pre), Sensitivity (Se), Specificity (Sp), Accuracy (Acc) and Classification Error Rate (CER) based on TP (True Positive), FP (False Positive), TN (True Negative) and FN (False Negative) obtained of step 14;
 16. Stop
-



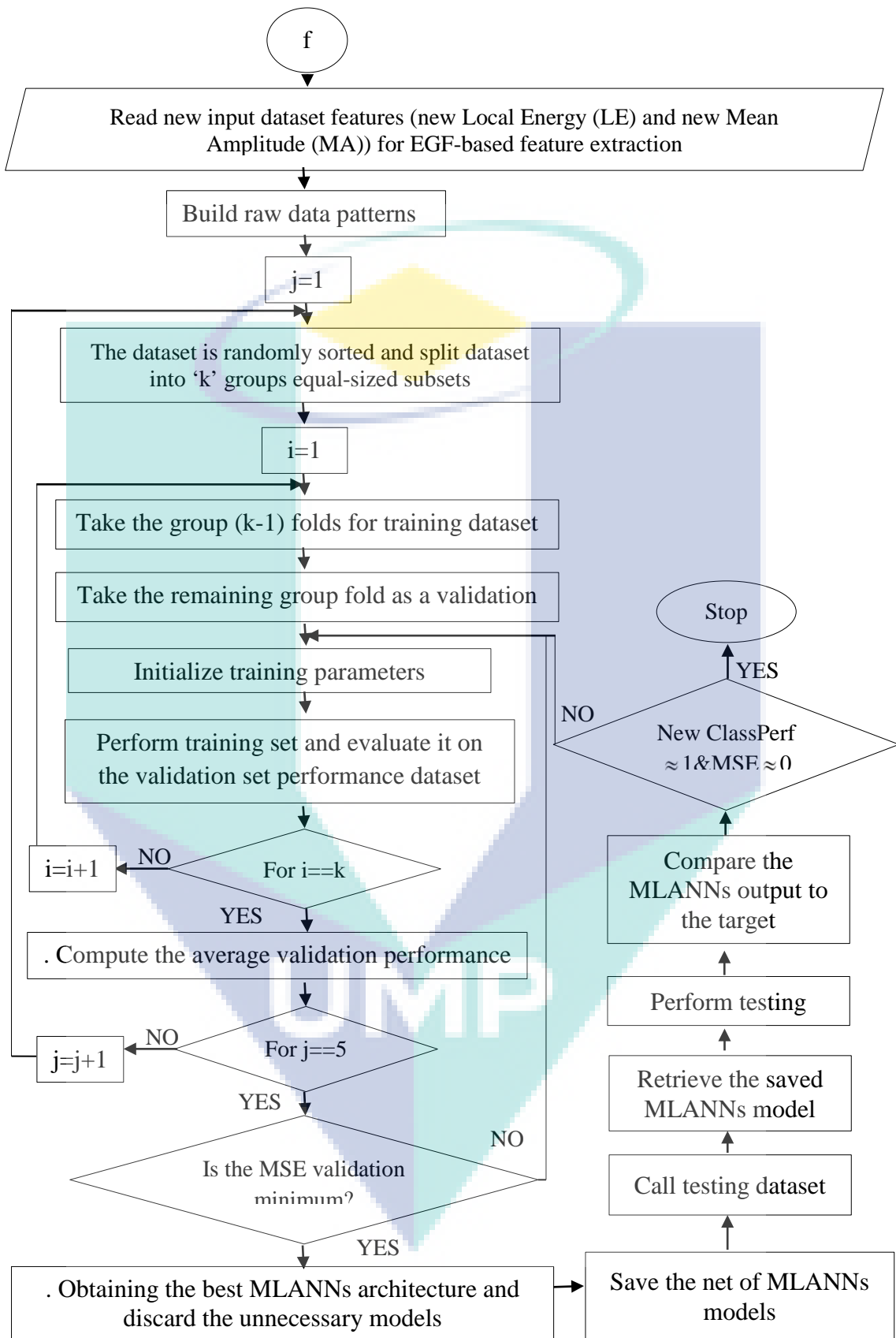


Figure 3.19 Flowchart for the proposed MLANNs for Enhanced Gabor Features (EGF)- based feature extraction

3.7.1.4 MLANNs Algorithm for Proposed Enhanced GWSMH Method

This section will presents the whole procedures of the proposed MLANNs model with the implementation of training algorithm namely ‘trainlm’, ‘trainbr’ and ‘trainscg’ by using *K*-Fold Cross Validation for Enhanced GWWSM-based feature extraction method. In this study, 5-fold and 10-fold cross-validation will be employed to evaluate the performance of the MLANNs model. Figure 3 illustrates a flow chart representation of pseudocode 7 regarding the MLANNs Algorithm for Gabor Wavelet Transform (GWT)-based feature extraction. This process will be executed to classify the condition of thermal motor bearing image in this study.

Algorithm: MLANNs-based classification for Enhanced Enhanced GWWSM -based feature extraction

Input: New top Fisher Score dataset and new validation dataset features;

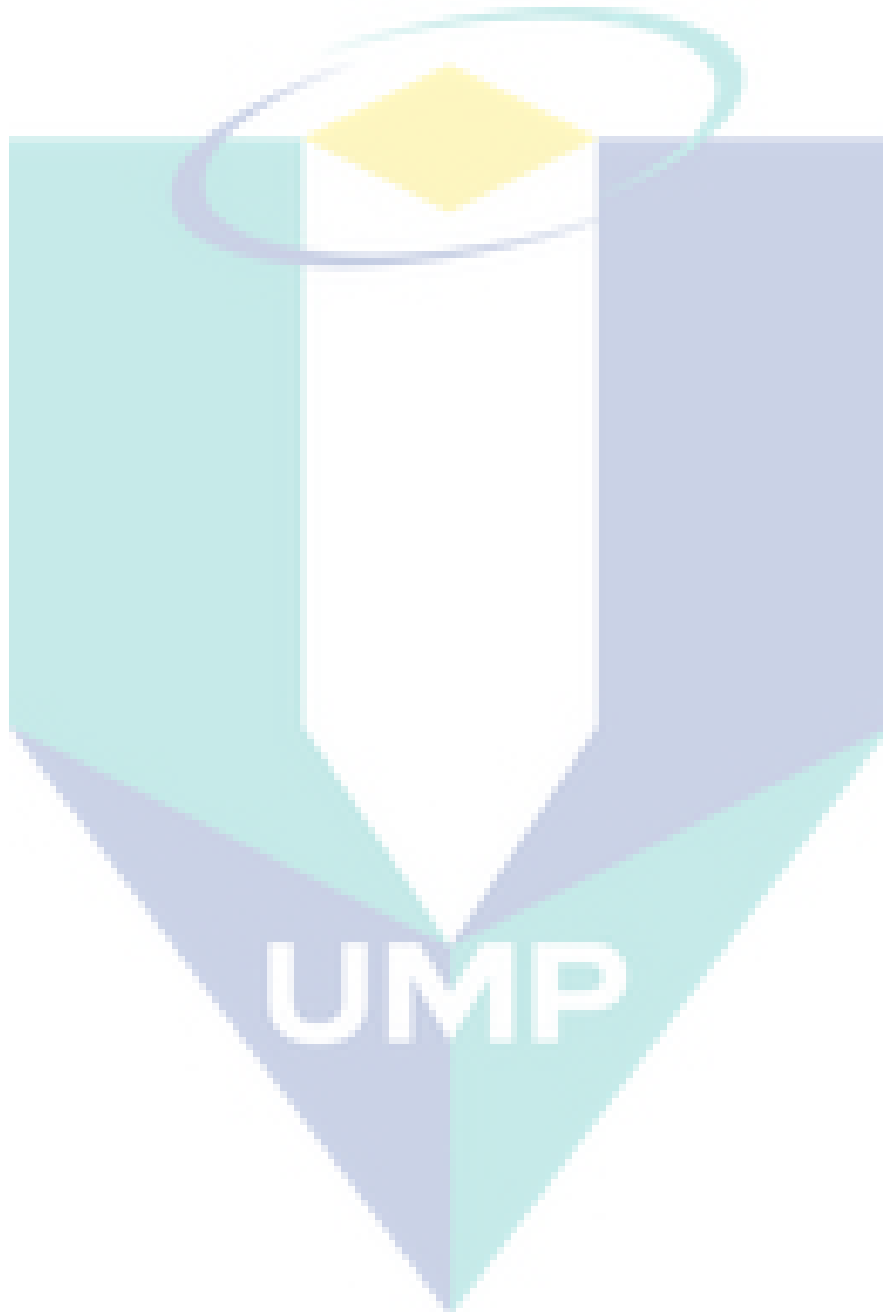
Output: New five classification statistical performance which are Precision (Pre), Sensitivity (Se), Specificity (Sp), Accuracy (Acc) and Classification Error Rate (CER) based on output from the test dataset;

Steps:

1. Begin
2. Read the new training top fisher score dataset and validation dataset features which are new Local Energy (LE) and new Mean Amplitude (MA) for Enhanced GWWSM-based feature extraction method, $Y \in R^{n \times j} \in new_LE^{2334 \times 1} \in new_MA^{2334 \times 1}$;
3. Build the raw data patterns of input features for the ANN.
4. For $j=1:\text{length}(\text{Hidden Neuron})$ %Hidden Neuron=1,2,3,4,5
5. The dataset is randomly sorted and split dataset into ‘k’ groups equal-sized subsets;
6. For $i=1:k$ %Folds, $k=5$ & $k=10$
 - a) Take the group (k-1) folds for training dataset;
 - b) Take the remaining group fold as a validation dataset for evaluation learning;
 - c) Initialize the training parameters condition including number of nodes in hidden layer, training algorithms, transfer functions, epochs, goal, show and etc.;
 - d) Fit a model by perform the training set and evaluate it on the validation set performance;
7. END For
8. Compute the average validation classification performance based on confusion matrix layout for k-folds;
9. END For
10. Stop training when error validation is minimal. This is to ensure net can generalise to unseen data;
11. Obtaining the best MLANNs architecture. Then, discard the unnecessary models;
12. Save the net of MLANNs models;
13. Call the testing datasets. Then, retrieve the save MLANNs model.
14. Perform the testing process by compare the MLANNs output to the target as follows:

```
New_Confusion_matrix= confusionmat(testDataset,TargetTest);
```

-
15. Calculate new five classification statistical performance's output which are Precision (Pre), Sensitivity (Se), Specificity (Sp), Accuracy (Acc) and Classification Error Rate (CER) based on TP (True Positive), FP (False Positive), TN (True Negative) and FN (False Negative) obtained of step 14;
 16. Stop
-



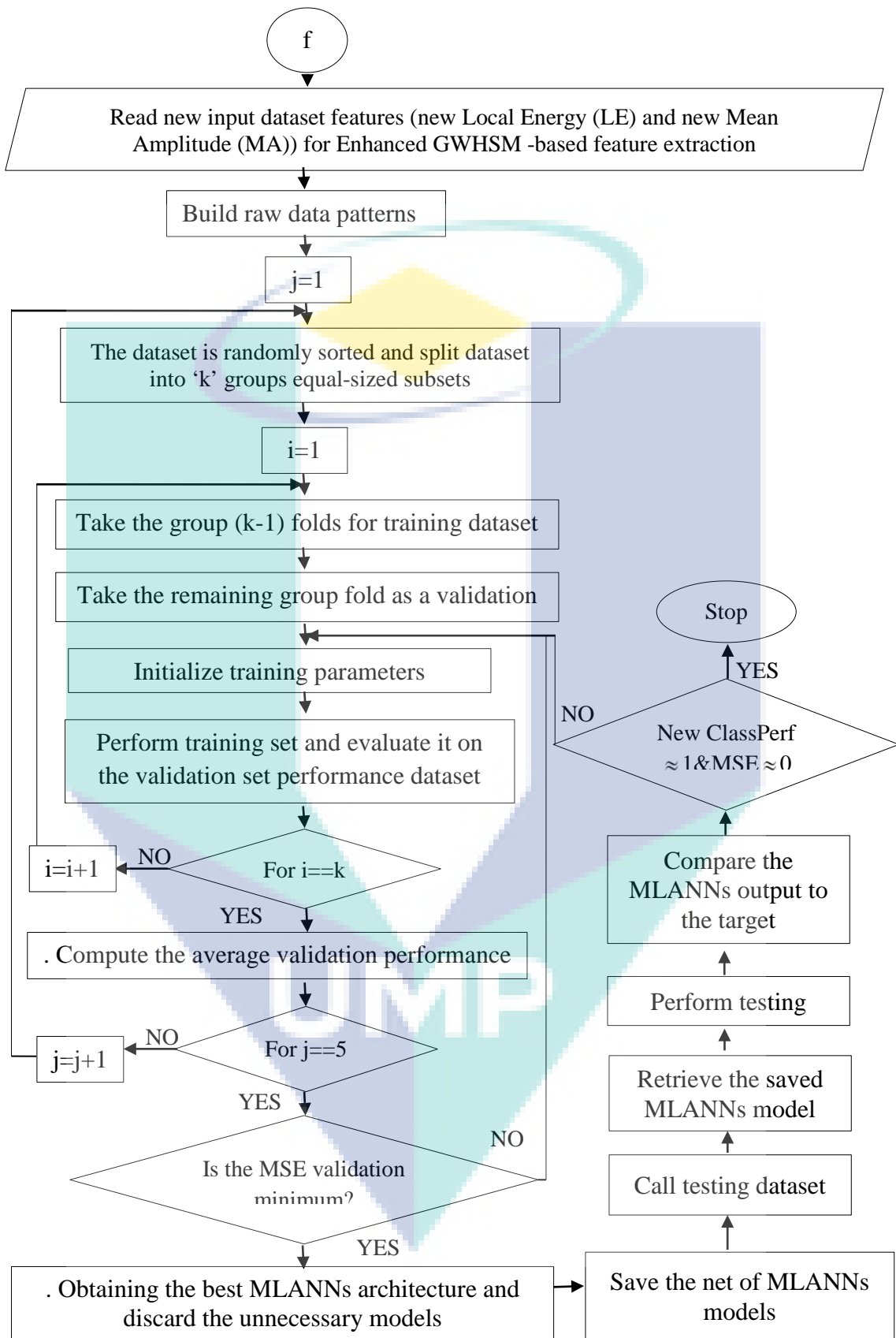


Figure 3.20 Flowchart for the proposed MLANNs for Enhanced GWHSM-based feature extraction

3.7.1.5 MLANNs Algorithm for Proposed Enhanced GWCLAHE Method

This section will presents the whole procedures of the proposed MLANNs model with the implementation of training algorithm namely ‘trainlm’, ‘trainbr’ and ‘trainscg’ by using *K*-Fold Cross Validation for Enhanced GWCLAHE-based feature extraction method. In this study, 5-fold and 10-fold cross-validation will be employed to evaluate the performance of the MLANNs model. Figure 3 illustrates a flow chart representation of pseudocode 7 regarding the MLANNs Algorithm for Gabor Wavelet Transform (GWT)-based feature extraction. This process will be executed to classify the condition of thermal motor bearing image in this study.

Algorithm: MLANNs Algorithm for Enhanced Enhanced GWCLAHE -based feature extraction

Input: New top Fisher Score dataset and new validation dataset features;

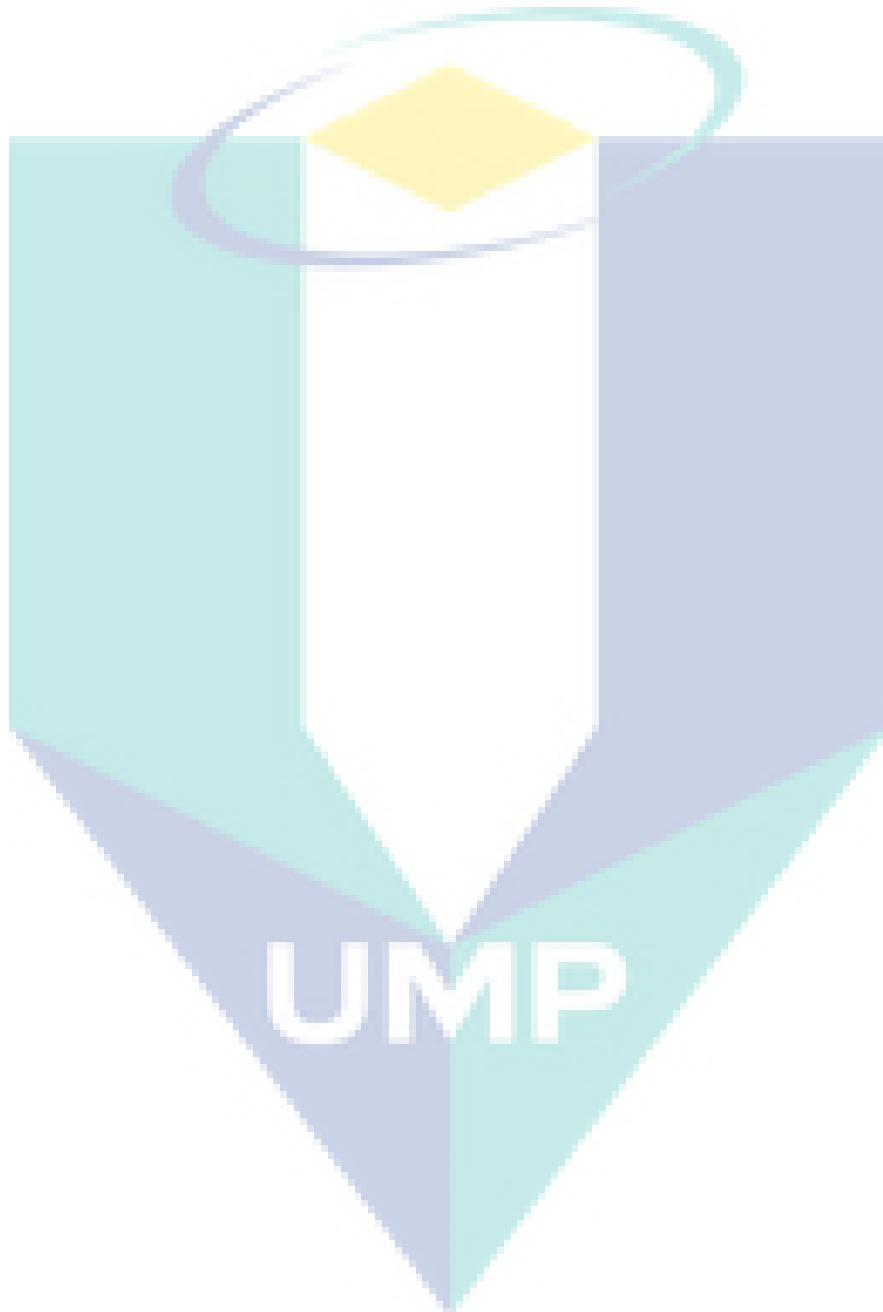
Output: New five classification statistical performance which are Precision (Pre), Sensitivity (Se), Specificity (Sp), Accuracy (Acc) and Classification Error Rate (CER) based on output from the test dataset;

Steps:

1. Begin
2. Read the new training top fisher score dataset and validation dataset features which are new Local Energy (LE) and new Mean Amplitude (MA) for Enhanced GWCLAHE-based feature extraction method, $Y \in R^{n \times j} \in new_LE^{2334 \times 1} \in new_MA^{2334 \times 1}$;
3. Build the raw data patterns of input features for the ANN.
4. For $j=1:\text{length}(\text{Hidden Neuron})$ %Hidden Neuron=1,2,3,4,5
5. The dataset is randomly sorted and split dataset into ‘k’ groups equal-sized subsets;
6. For $i=1:k$ %Folds, $k=5$ & $k=10$
 - a) Take the group (k-1) folds for training dataset;
 - b) Take the remaining group fold as a validation dataset for evaluation learning;
 - c) Initialize the training parameters condition including number of nodes in hidden layer, training algorithms, transfer functions, epochs, goal, show and etc.;
 - d) Fit a model by perform the training set and evaluate it on the validation set performance;
7. END For
8. Compute the average validation classification performance based on confusion matrix layout for k-folds;
9. END For
10. Stop training when error validation is minimal. This is to ensure net can generalise to unseen data;
11. Obtaining the best MLANNs architecture. Then, discard the unnecessary models;
12. Save the net of MLANNs models;
13. Call the testing datasets. Then, retrieve the save MLANNs model.
14. Perform the testing process by compare the MLANNs output to the target as follows:

```
New_Confusion_matrix= confusionmat(testDataset,TargetTest);
```

-
15. Calculate new five classification statistical performance's output which are Precision (Pre), Sensitivity (Se), Specificity (Sp), Accuracy (Acc) and Classification Error Rate (CER) based on TP (True Positive), FP (False Positive), TN (True Negative) and FN (False Negative) obtained of step 14;
 16. Stop
-



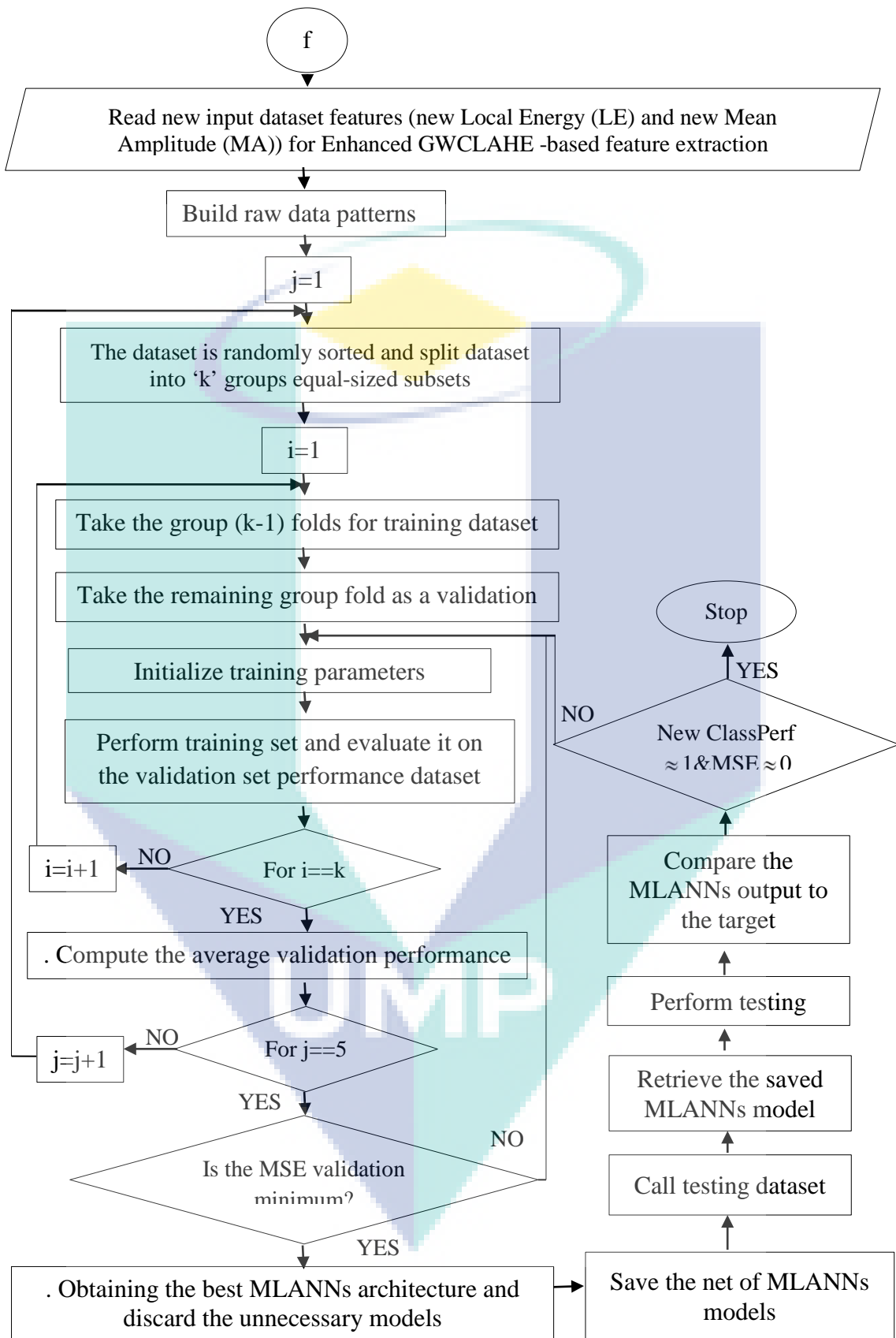


Figure 3.21 Flowchart for the proposed MLANNs for Enhanced GWCLAHE-based feature extraction.

3.7.1.6 MLANNs Algorithm for HSV color Method

In this section, the MLANN classification process from HSV color-based feature extraction techniques will be included for comparison purposes. This comparison will be executed to seek the differences in MLANNs classification performances output based on the color-based technique and the original GWT-based technique.

To fulfill the purpose of this study, the whole procedures of the proposed MLANNs model with the implementation of training algorithm namely 'trainlm', 'trainbr' and 'trainscg' by using K-Fold Cross Validation for HSV Color-based feature extraction method will be presented. In this study, 5-fold and 10-fold cross-validation will be employed to evaluate the performance of the MLANNs model. Figure 3 illustrates a flow chart representation of pseudocode 7 regarding the MLANNs Algorithm for HSV Color-based feature extraction. This process will be executed to classify the condition of thermal motor bearing image in this study.

Algorithm: MLANNs Algorithm for HSV Color-based feature extraction methods.

Input: Top Fisher Score dataset and validation dataset features;

Output: Five classification statistical performance which are Precision (Pre), Sensitivity (Se), Specificity (Sp), Accuracy (Acc) and Classification Error Rate (CER) based on output from the testing set;

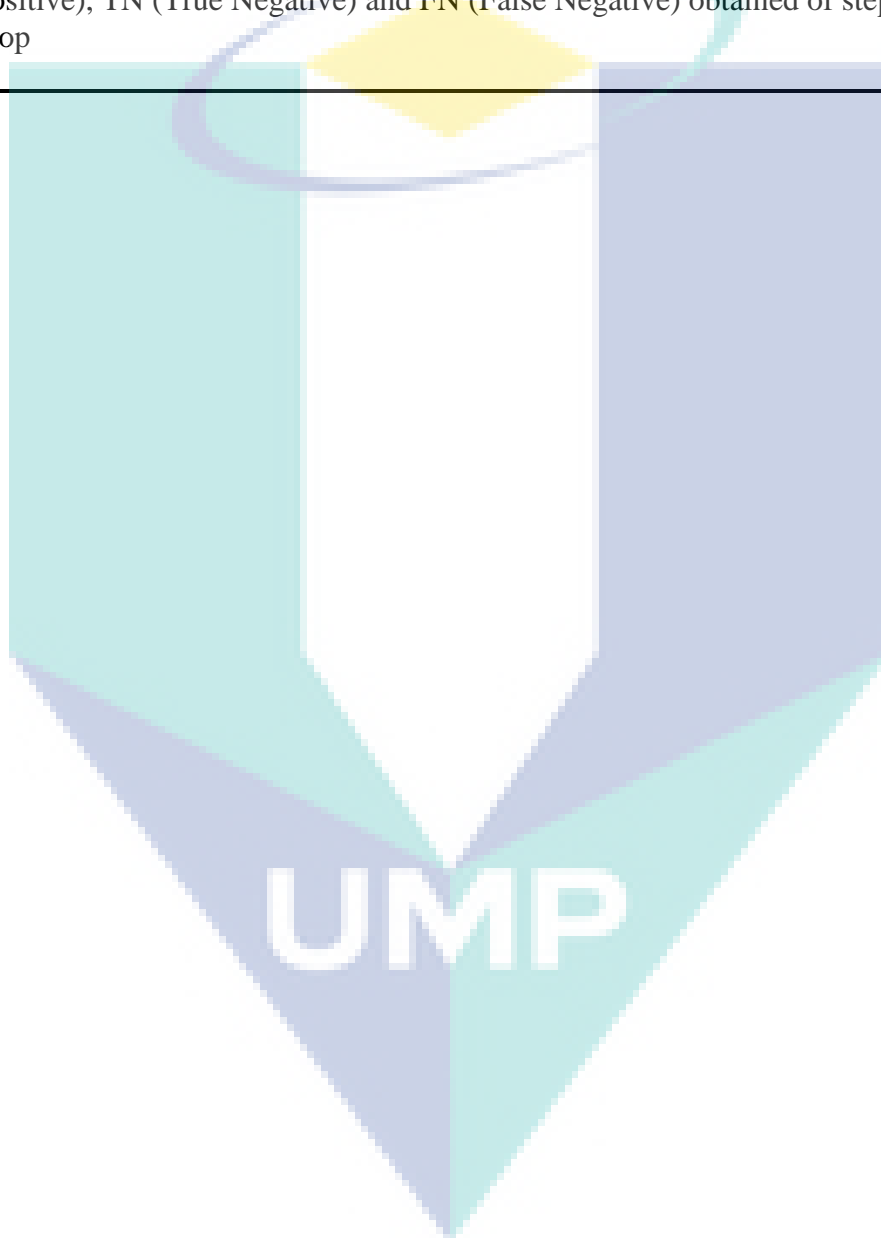
Steps:

1. Begin
2. Read the training top fisher score dataset and validation dataset features for HSV color-based feature extraction method , $Y \in R^{n \times j} \in R^{2334 \times 1}$;
3. Build the raw data patterns of input features for the ANN.
4. For j=1:length(Hidden Neuron) %Hidden Neuron=1,2,3,4,5
5. The dataset is randomly sorted and split dataset into 'k' groups equal-sized subsets;
6. For i=1:k %k=5 & k=10
 - a) Take the group (k-1) folds for training dataset;
 - b) Take the remaining group fold as a validation dataset for evaluation learning;
 - c) Initialize the training parameters condition including number of nodes in hidden layer, training algorithms, transfer functions, epochs, goal, show and etc.;
 - d) Fit a model by perform the training set and evaluate it on the validation set performance;
7. END For
8. Compute the average validation classification performance based on confusion matrix layout for k-folds;
9. END For
10. Stop training when error validation is minimal. This is to ensure net can generalise to unseen data;
11. Obtaining the best MLANNs architecture. Then, discard the unnecessary models;
12. Save the net of MLANNs models;

-
13. Call the testing datasets. Then, retrieve the save MLANNs model.
 14. Perform the testing process by compare the MLANNs output to the target as follows:

```
Confusion_matrix= confusionmat(testDataset,TargetTest);
```

15. Calculate five classification statistical performance's output which are Precision (Pre), Sensitivity (Se), Specificity (Sp), Accuracy (Acc) and Classification Error Rate (CER) based on TP (True Positive), FP (False Positive), TN (True Negative) and FN (False Negative) obtained of step 14;
 16. Stop
-



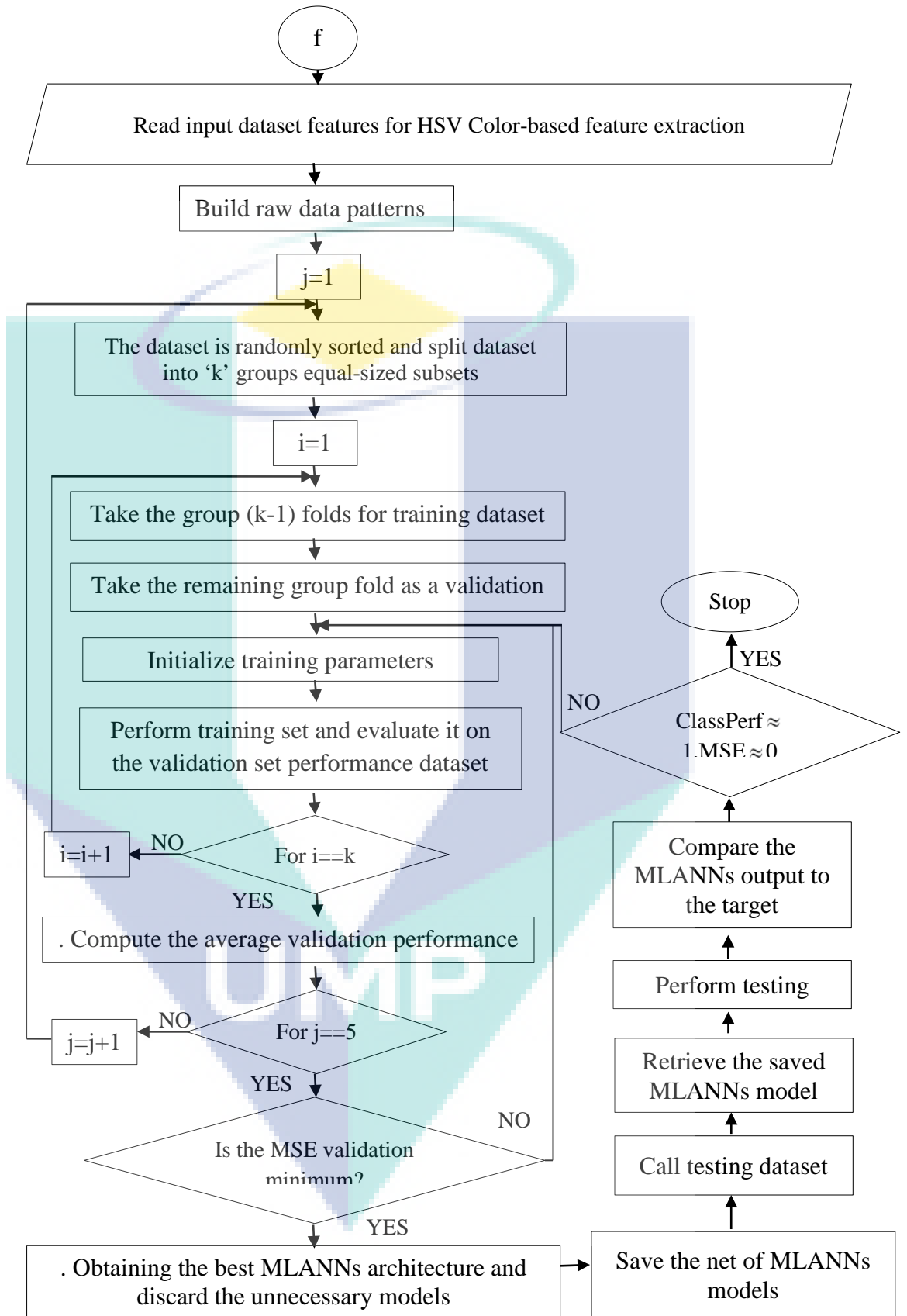


Figure 3.22 Flowchart MLANNs-based classification for HSV color-based feature extraction methods.

3.7.1.7 MLANNs Algorithm for I*a*b color Method

In this section, the MLANN classification process from $l*a*b$ color-based feature extraction techniques will be included for comparison purposes. This comparison will be executed to seek the differences in MLANNs classification performances output based on the color-based technique and the original GWT-based technique.

To fulfill the purpose of this study, the whole procedures of the proposed MLANNs model with the implementation of training algorithm namely ‘trainlm’, ‘trainbr’ and ‘trainscg’ by using *K-Fold Cross Validation* for $l*a*b$ Color-based feature extraction method will be presented. In this study, 5-fold and 10-fold cross-validation will be employed to evaluate the performance of the MLANNs model. Figure 3 illustrates a flow chart representation of pseudocode 7 regarding the MLANNs Algorithm for $l*a*b$ Color-based feature extraction. This process will be executed to classify the condition of thermal motor bearing image in this study.

Algorithm: MLANNs Algorithm for $l*a*b$ color-based feature extraction methods.

Input: Top Fisher Score dataset and validation dataset features;

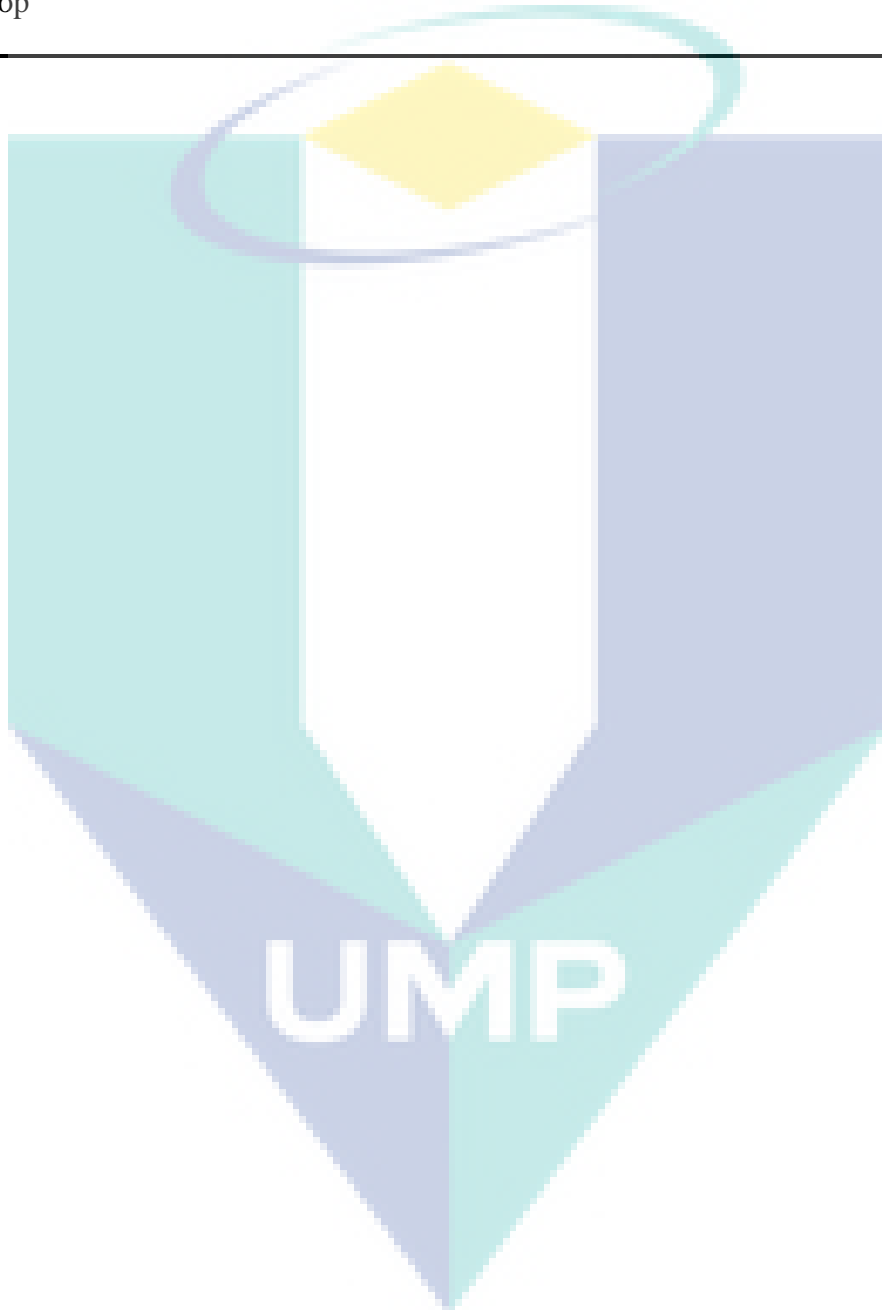
Output: Five classification statistical performance which are Precision (Pre), Sensitivity (Se), Specificity (Sp), Accuracy (Acc) and Classification Error Rate (CER) based on output from the testing set;

Steps:

1. Begin
2. Read the training top fisher score dataset and validation dataset features for $l*a*b$ color-based feature extraction method , $Y \in R^{n \times j} \in R^{2334 \times 1}$;
3. Build the raw data patterns of input features for the ANN.
4. For $j=1:\text{length}(\text{Hidden Neuron})$ %Hidden Neuron=1,2,3,4,5
5. The dataset is randomly sorted and split dataset into ‘k’ groups equal-sized subsets;
6. For $i=1:k$ %k=5 & k=10
 - a) Take the group (k-1) folds for training dataset;
 - b) Take the remaining group fold as a validation dataset for evaluation learning;
 - c) Initialize the training parameters condition including number of nodes in hidden layer, training algorithms, transfer functions, epochs, goal, show and etc.;
 - d) Fit a model by perform the training set and evaluate it on the validation set performance;
7. END For
8. Compute the average validation classification performance based on confusion matrix layout for k-folds;
9. END For
10. Stop training when error validation is minimal. This is to ensure net can generalise to unseen data;
11. Obtaining the best MLANNs architecture. Then, discard the unnecessary models;
12. Save the net of MLANNs models;
13. Call the testing datasets. Then, retrieve the save MLANNs model.
14. Perform the testing process by compare the MLANNs output to the target as follows:

```
Confusion_matrix= confusionmat(testDataset,TargetTest);
```

15. Calculate five classification statistical performance's output which are Precision (Pre), Sensitivity (Se), Specificity (Sp), Accuracy (Acc) and Classification Error Rate (CER) based on TP (True Positive), FP (False Positive), TN (True Negative) and FN (False Negative) obtained of step 14;
 16. Stop
-



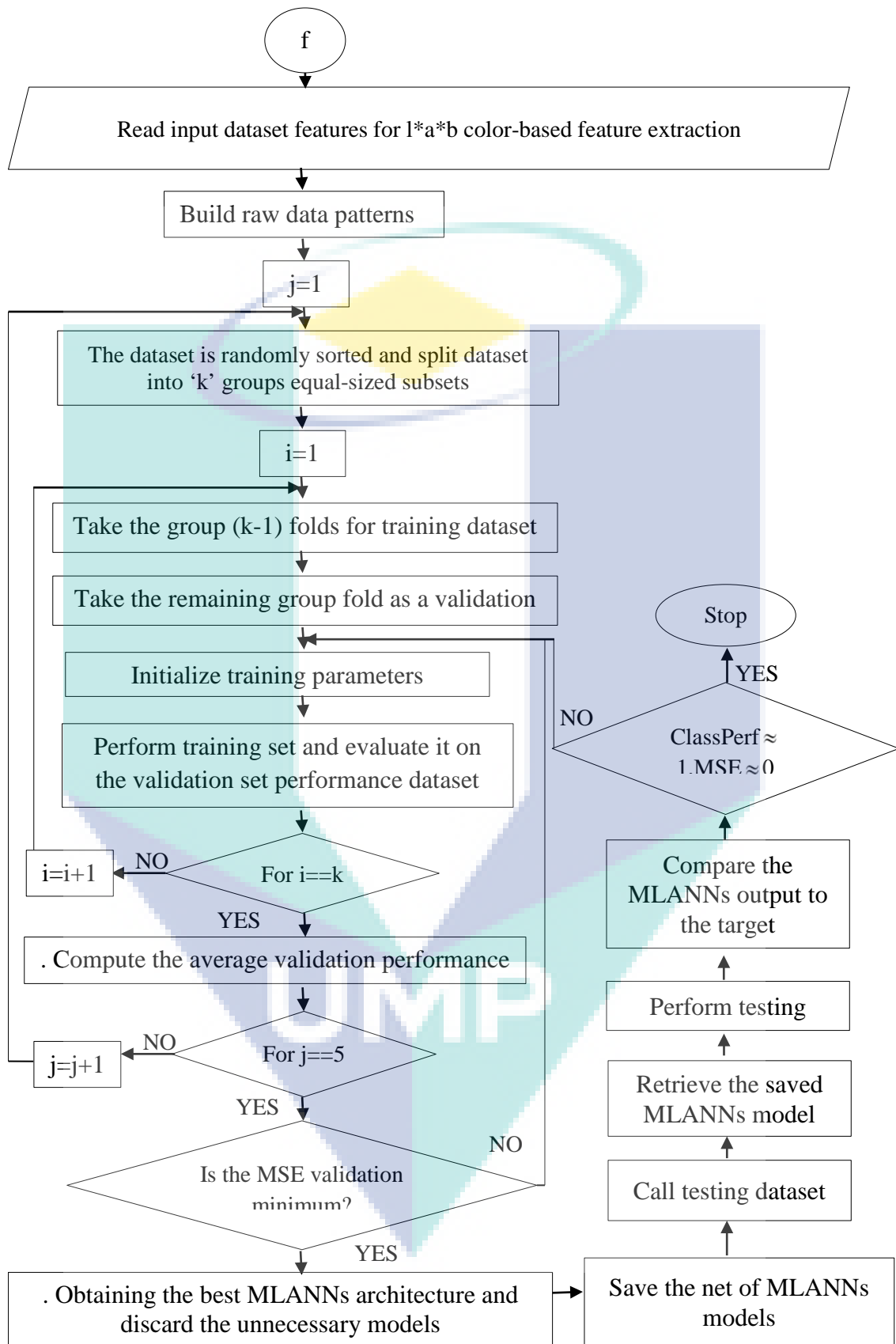
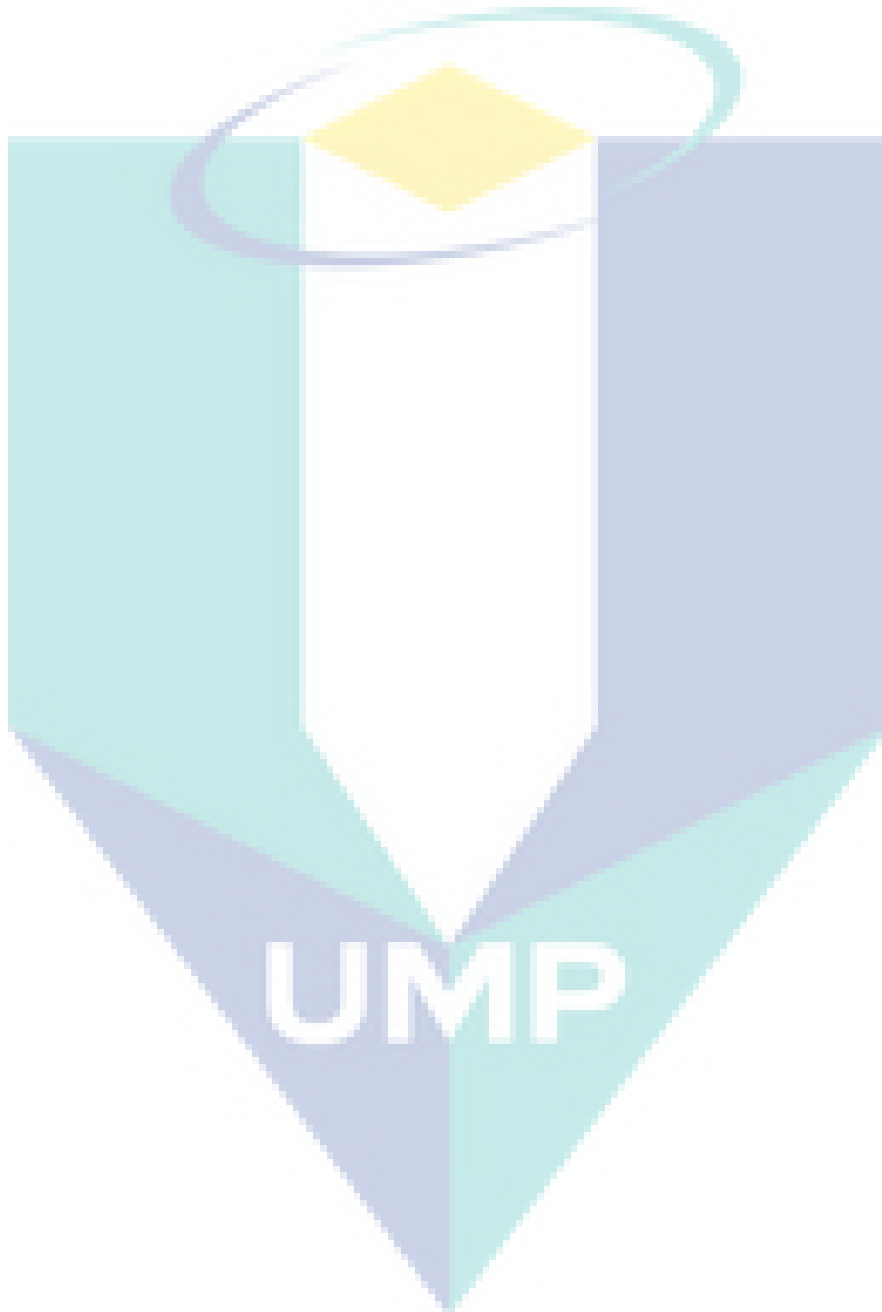


Figure 3.23 Flowchart MLANNs-based classification for l^*a^*b color-based feature extraction methods.

3.7.2 Linear Thresholding (LT)



CHAPTER 4

RESULT & DISCUSSION

4.1 Introduction

4.2 Image Acquisition and Image segmentation

4.2.1 Image Acquisition

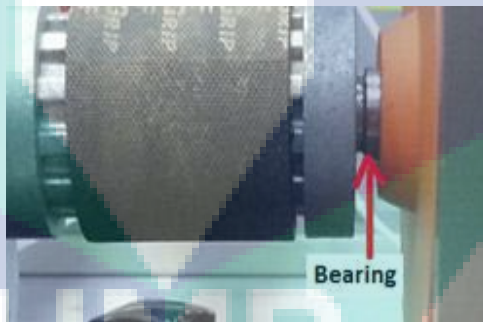


Figure 4.1 Motor bearing image

By implement thermal camera monitoring, the differences thermal images profile of bearing machine are clearly observed as illustrated in Figure 3.4. In this work, there are three conditions of bearing machine that been captured automatically; there are normal conditions, warning condition and abnormal condition that generates 2593 thermal images. All the acquired images are saved in computer and processed in Matlab software by using image processing approach. The video recording is then converted into thermal images and sorted in Joint Photographic Experts Group (JPEG) form.

Both pictures are represented as arrays of 512×512 pixels with 128 intensity levels.

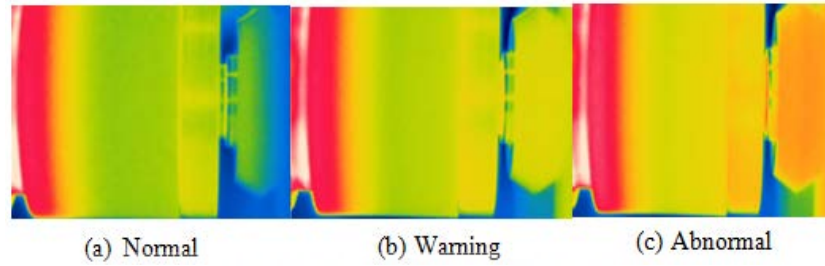


Figure 3.4 The differences thermal images profile of bearing machine

4.2.2 Data analysis

For implementing and testing the algorithms described in the this chapter, a thermal motor bearing images database are categorized into 3 different thermal image conditions which are normal, warning and abnormal. The total number of images for these 3 categories is 2593. This image database have been used for implementing the Enhanced Gabor Features (EGF) based feature extraction on each of the images and to train the system by implementing Artificial Neural Network and Linear Thresholding classification algorithms. When the training is done, 259 different full thermal motor bearing images from the original database were selected to test the system whether it can classify the condition of thermal motor bearing images properly. The distribution of data ratios for training, validation and testing is 80: 10: 10 as depicted in the Table 2.1.

Table 4.1 Distribution of training, validation and testing

Thermal motor bearing images	Training data	Validation data	Testing data
Normal	1621	180	180
Warning	259	40	40
Abnormal	195	39	39

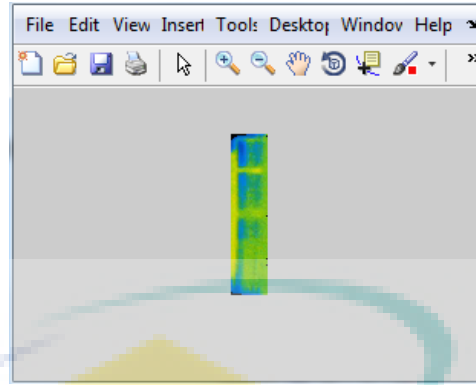


Figure 4.2 Cropped the segmented bearing image

4.3 Original Gabor Wavelet Transform (GWT)-based Feature Extraction Method

This study discusses in details the results obtained from the development of the original process of feature extraction based on Gabor Wavelet Transform (GWT). The purpose of this method was adopted in this study to see the effectiveness of this GWT based-extraction filter method in differentiating the significant features contained in the group of thermal motor bearing images. This GWT-based Filter contains the set of scale channels that can be configured to capture a specific band of frequency component from images. Also, the set of orientation channels used to extract the directional features from images.

Thermal image processing has begun with converting the segmented input RGB thermal images as in figure in section 4.2.2 into grayscale intensity image, $I(x, y)$. Next, the 2D-GWT feature extraction method is executed by transferring the input image, $I(x, y)$ into the Gabor function, $g(x, y)$. It means that, the Fourier Transform of the image is computed first with the number of different scale and orientation in order to extract out all those patterns. This 2D-Gabor based feature extraction will then provide information on the frequency and orientation representations of an image

Before this process is executed, the Gabor filter is constructed first by applying 5 different frequencies and 8 orientations as specified in the table in section 3.5.2. The purpose is to analyze whether there is any specific frequency content in a specific direction in the image in a localized region. All of the coefficient results from this conducted experiment are obtained according to the predetermined parameter values on

the images. Next, the result of this Gabor function representing the pixel value (intensities) of the output image has been depicted in the form of diagrams as in the **figure**. The figure denotes a perspective view of filter representing orthogonal directions that has a real (cosine) and a imaginary(sine) component in spatial domain.

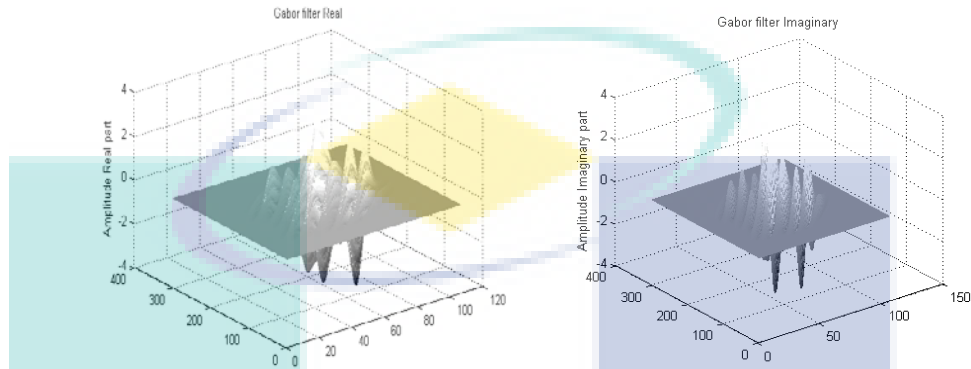


Figure 4.3 Sample of the 2D-Gabor function in the spatial domain (new Real (cosine) component and new Imaginary(sine) component) for normal thermal image condition

Meanwhile, figure illustrates the real (cosine) component of the entire Gabor filter in spatial domain with different 5 frequencies and 8 orientations. The row corresponds to different scales containing bandwidth ($\sigma_1 = 2.8$, $\sigma_2 = 3.6$, $\sigma_3 = 4.5$, $\sigma_4 = 5.4$, $\sigma_5 = 6.3$) and wavelength ($\lambda_1 = 3.5$, $\lambda_2 = 4.6$, $\lambda_3 = 5.6$, $\lambda_4 = 6.8$, $\lambda_5 = 7.9$), while the column corresponds to different orientation (0° , 22.5° , 45° , 67.5° , 90° , 112.5° , 135° and 157.5°). By varying these parameter values (θ, σ, λ) for Gabor function, the filter pattern will also change. Hereby, 40 filters Gabor channel at each image point i.e. 40 multi-scales and multi-orientations feature images have been generated. Thus, the overall total number of the Gabor features that have been produced in this present study is as much as 2075×40 equal to 83,000 including for normal, warning and abnormal groups.

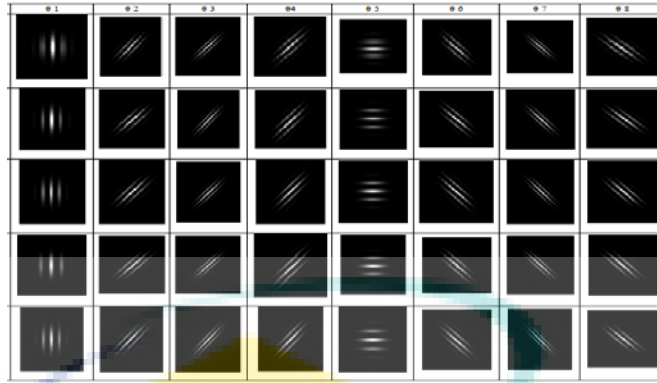


Figure 4.4 A new real componnets of EGF filters in spatial domain rotates at 5 scales and 8 orientations in normal conditon image

Afterwards, the process of convolving the two-dimensional Gabor filter, $g(x, y)$ with the input image, $I(x, y)$ has been acquired in order to detect the Gabor filter response from the input image itself. In this process, the complex convolution result were decomposed to the magnitude response image as denoted in figure and the phase response image based on the complex of Gabor real component and Gabor imaginary component images. Nonetheless, for the phase response image, it was not taken into account in this study. This is proven from the previous studies, they say the case of magnitude is the most effective while the original Gabor phase are considered unstable and are usually discarded (Hafez, Selim, & Zayed, 2015; Liu, Koga, & Fujisawa, 2005; Štruc & Pavešić, 2010a, 2010b).

From the figure, it can be seen, the different responses was shown according to the parameters that have been determined. The higher the scale of parameter are employed, the clearer the Gabor response stripes are observed. There are 40 different representation of an image (oriented magnitude response matrices, R) have been extracted and contain the component of the corresponding feature vector. At this point, when the input thermal bearing images passed through each orientation on the Gabor-based filter, the output of the resulting oriented extract features is according to the orientation of the filter at that time. Eventually, there are 2 feature vectors that have been extracted from this process, namely Local Energy, and Mean Amplitude, $Y \in R^{nxj} \in MA^{83000} \in LE^{83000}$. Where Local Energy feature has obtained by equal to summing up the squared value of each matrix value from a response matrix. Meanwhile, for Mean Amplitude feature has acquired by equal to sum of absolute values of each matrix value from a response matrix

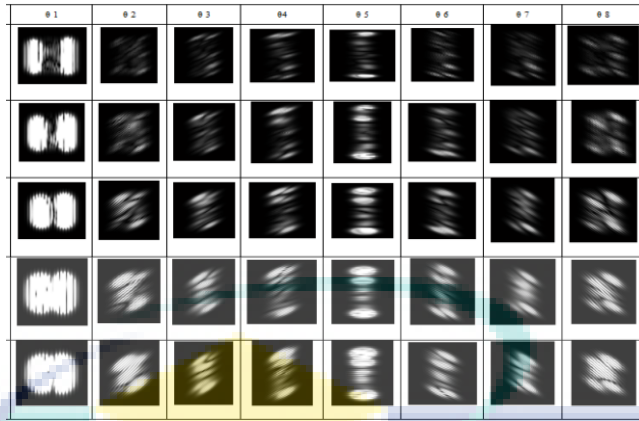


Figure 4.5 The oriented output sample of response matrices (features) for normal condition image when pass through individual Gabor filter with five scales and eight orientations

Figure illustrates the whole process performed with the feature extraction method that has been proposed in this section. A sample image of each database group with a parameter scale of 15×15 ($\sigma_s = 6.3, \lambda_s = 7.9$) at orientation 90° has been shown to differentiate the output of the magnitude response which will lead to the production of the feature vectors. Image convolution process is applied to achieve the goal of generating features based on the filter used.

Table 4.2 Three conditions of thermal motor bearing images before and after convolution of Gabor filter with scale 15×15 at orientation 90°

Thermal bearing image Conditions	Convolution (Input Image * Gabor filter)		Magnitude response
Normal	*		=
Warning	*		=

Abnormal  *  = 

Subsequently, the overall graph for the results of both feature vectors (Local Energy and Mean Amplitude) is shown as in the figure and figure. These graphs represent the pixel values (intensities) that have been generated based on the magnitude response obtained for each group from thermal motor bearing images.

There are 40 Gabor channel filters that have been deployed at each image point for each group of thermal images. The purpose is to extract the corresponding feature values according to the respective image groups. Then, the features extracted from these normal, warning and abnormal groups are arranged according to the same scale parameters. It is intended to see the differences group generated according to their respective orientation as shown in both figures. Herein, there are 40 multi-scales and multi-orientations of Gabor-based feature images that have been generated. It corresponds to the differences in the multi-scale and multi-orientation parameters deployed in this work in which the production of different features will be obtained.

From a visual point of view, it can be seen from the graph that the feature vector output from both Local Energy and Mean Amplitude have some insignificant variations features to differentiate the group of thermal motor bearing images. This can be clearly seen through the bar graph as in the figure. Inconsistent bar graph changes and overlaps between normal, warning and bearing groups can be clearly seen. However, the feature selection process will be executed to prove it and define the optimal features to distinguish the group from these thermal bearing images. It will be discussed in details in section 4.3.1. Only the most relevant features will be used for the next processing, while the irrelevant features will be discarded.

Table 4.3

Overall Local energy features for multi-scales and multi-orientations in GWT based feature extraction method

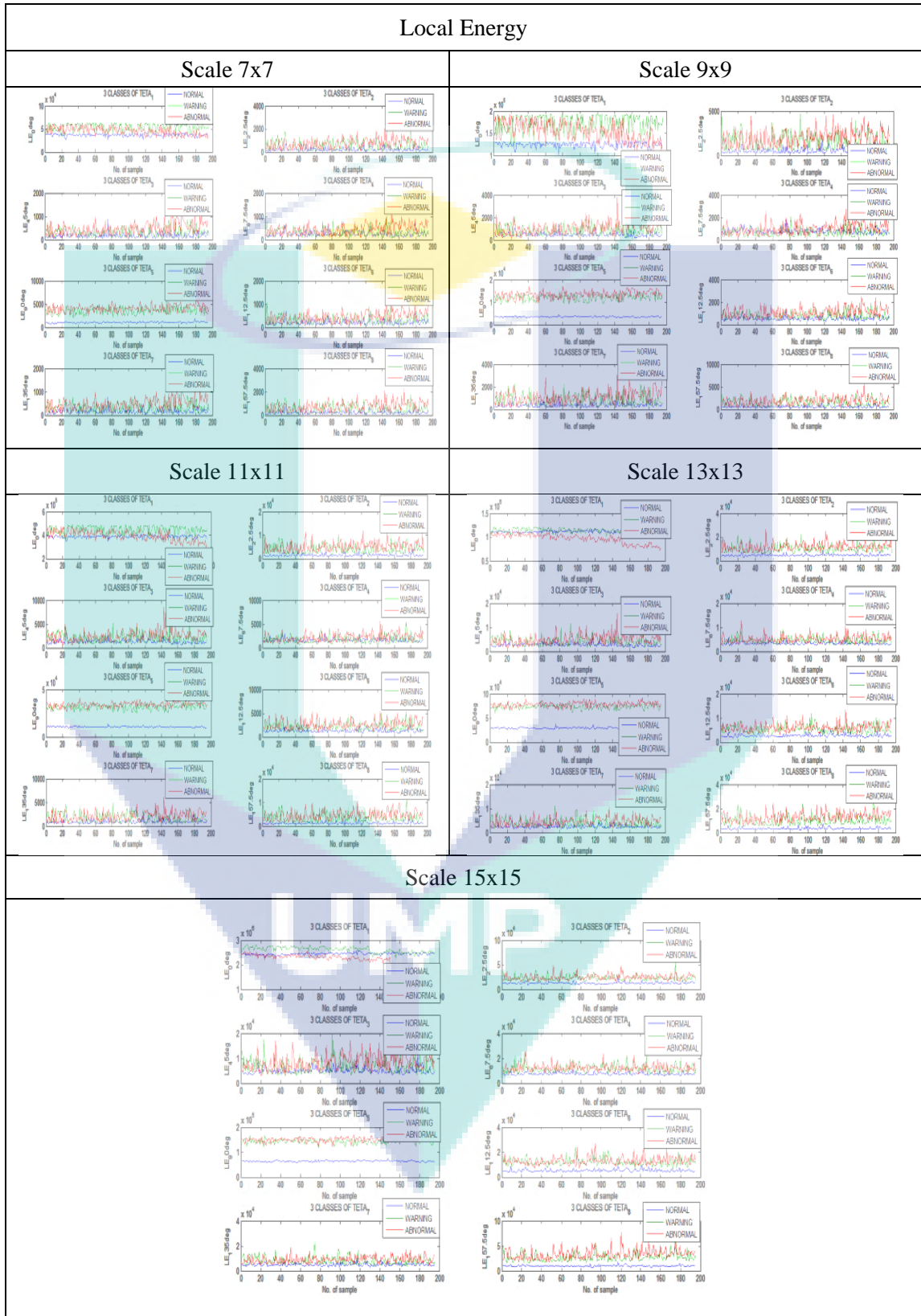
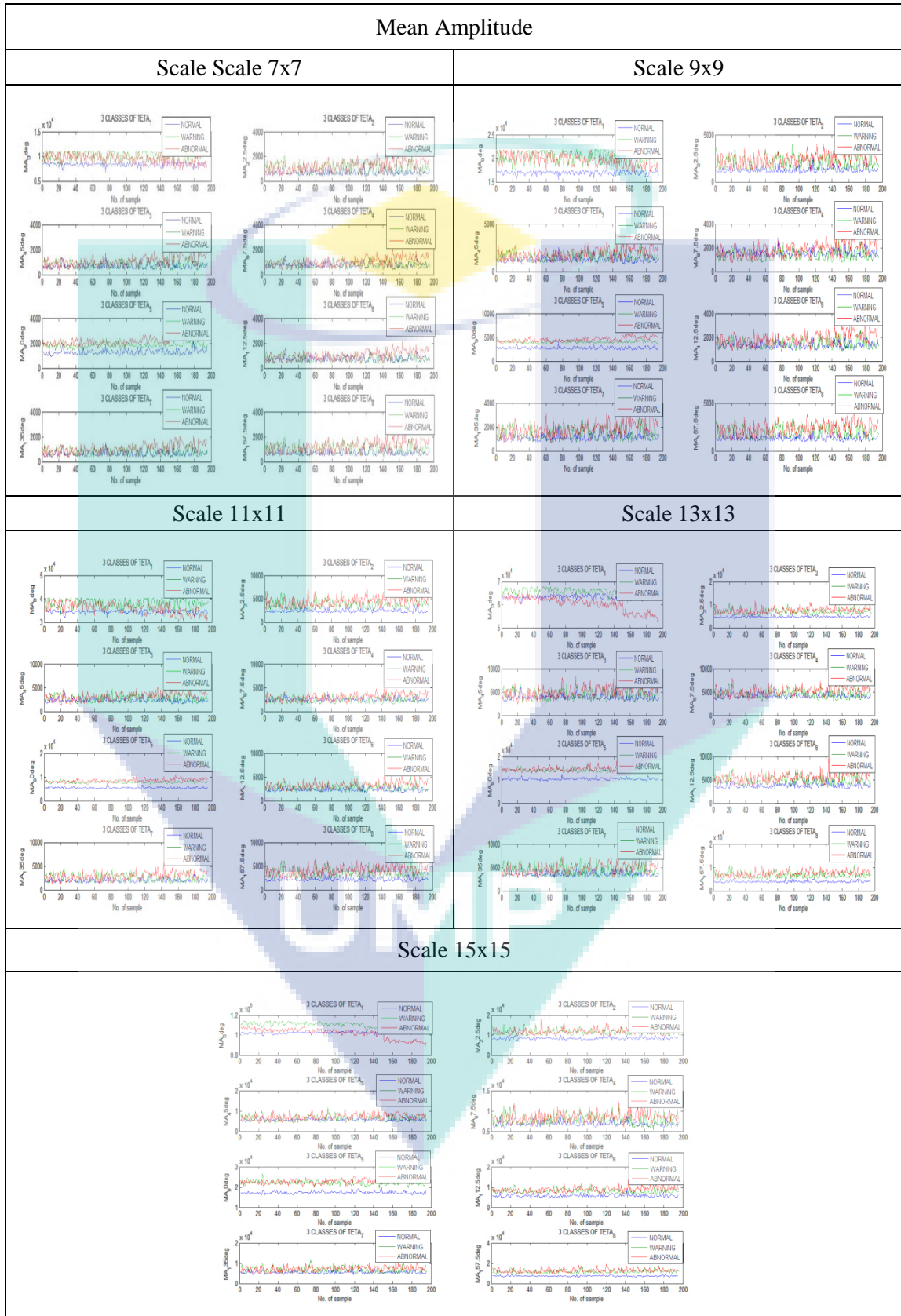


Table 4.4

Overall Mean Amplitude features for multi-scales and multi-orientations in GWT based feature extraction method



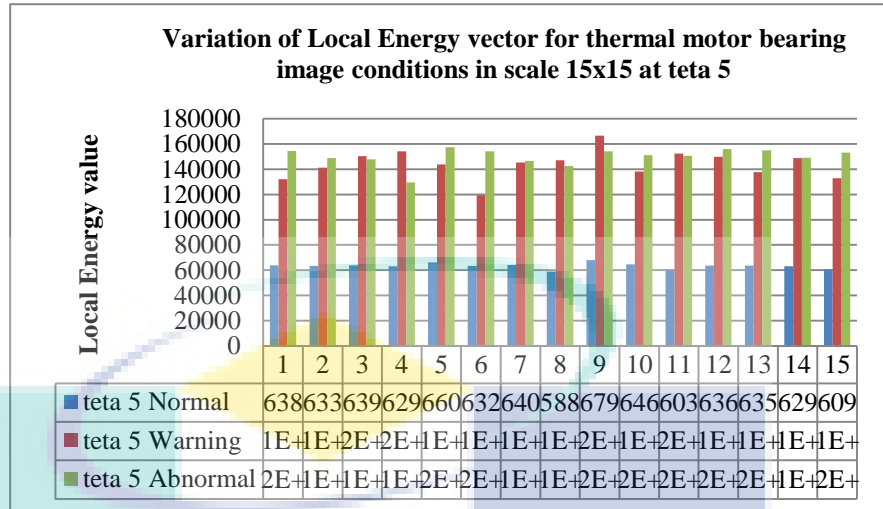


Figure 4.6 Variation of non consistent local energy vector for thermal motor bearing image groups in scale 15x15 at theta 5

4.3.1 Feature selection

The proposed fisher score based feature selection method has been implemented in this study to select the optimal features of high-dimensional vector output features from the GWT-based extraction process as in section 4.3. This proposed method also is employed to simplify the calculation analysis and improve learning performances in term of higher learning accuracy for classification in this work. It's also to reduce the computational time and memory required for feature recognition.

According to the feature extraction results as in section 4.3, 40 multi-scale and multi-orientation feature images were generated at each image point. Therefore, the total input data matrix generated in different orientations and scales for image data set training are $Y \in R^{(nx5) \times j} \in LE^{10375 \times 8}$, $MA^{10375 \times 8}$, where 'n' is the number of samples which have 2075 images and 'j' is the number of orientations. After calculate their scores by computes a subset of features with a large distance between data points in different classes and small distance between data points in the same class under the fisher criterion as in equation 3.32, the score for local energy and mean amplitude features were generated as in the table and table.

According to (Gu et al., 2012b; Islam et al., 2015; Ma et al., 2019; T. Zhang & Lu, 2010), the final feature selection is occurs by the top ranked ones as the optimal

fisher score value. This selected score will represent the discrimination power of a certain feature in order to evaluate the performance and importance of any feature. In addition to this, the optimal fisher values of the orientation and scale respectively are sorted in descending order. From the results obtained in the table, it can be seen that the fisher score is compiled from the highest values for the combination of scale and orientation to local energy features begin with F15 = 1517.18, followed by F13 = 1483.99, F11 = 1196.00, F9 = 867.78 and F7 = 484.61 . Therefore, the highest score value produced is at F15 = 1517.18, which is on a scale 15x15 ($\sigma = 6.3$, $\lambda = 7.9$) and orientation $\theta_5 = 90^\circ$.

Table 4.6 Fisher scoring for each Gabor filter's scale (Local Energy)

Filter Size (Scales)	θ_1	θ_2	θ_3	θ_4	θ_5	θ_6	θ_7	θ_8
7x7	185.45	63.04	48.44	42.48	484.61	43.89	46.75	66.01
9x9	317.48	109.00	42.04	30.74	867.78	69.66	58.28	85.81
11x11	181.52	199.34	44.46	36.86	1196.00	119.43	55.13	161.09
13x13	161.47	320.92	57.79	95.80	1483.99	257.25	60.26	390.39
15x15	132.01	350.13	67.79	214.27	1517.18	418.79	122.26	464.75

As well as for mean amplitude features in table, the order of decreasing fisher score values can be expressed starting with F15=507.38, followed by F13=492.24, F11=465.21, F9=448.22 and F7=194.49. From this result, the highest fisher's score can be read on a scale 15x15 and orientations $\theta_8 = 157.5^\circ$ and the value is F15=507.38.

Table 4.7 Fisher scoring for each Gabor filter's scale for Mean Amplitude

Filter Size (Scales)	θ_1	θ_2	θ_3	θ_4	θ_5	θ_6	θ_7	θ_8
7x7	179.03	46.69	33.30	26.95	194.49	30.17	32.84	51.18
9x9	448.22	104.73	29.79	28.41	357.12	41.12	42.62	75.63
11x11	193.92	221.89	30.81	27.96	465.21	68.92	40.80	181.94
13x13	131.46	358.86	40.18	53.70	492.24	150.72	44.42	417.68
15x15	126.76	430.83	50.45	103.74	437.00	268.83	105.26	507.38

Figure and figure demonstrates the distribution of fisher's scores obtained for the scale and orientation variations in the tables and tables according to their respective features. From the local energy diagram as in figure, it is clear that SCALE 15 (θ_5) gives the highest fisher score among the others. Meantime for the mean amplitude graph as in figure, it is observed that SCALE 15 (θ_8) gave the highest score among others.

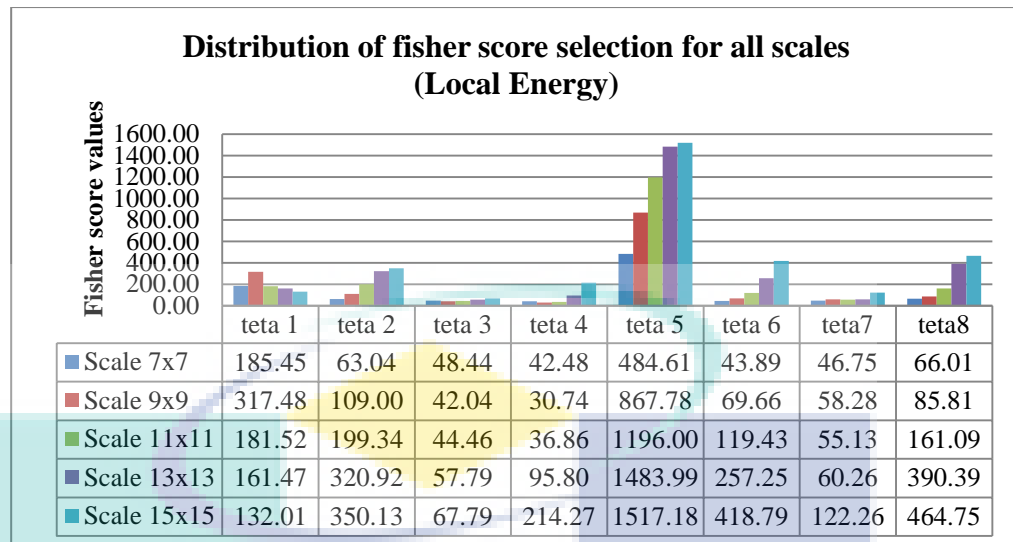


Figure 4.7 Variation of Fisher score value for local energy between normal, warning and abnormal thermal motor bearing images

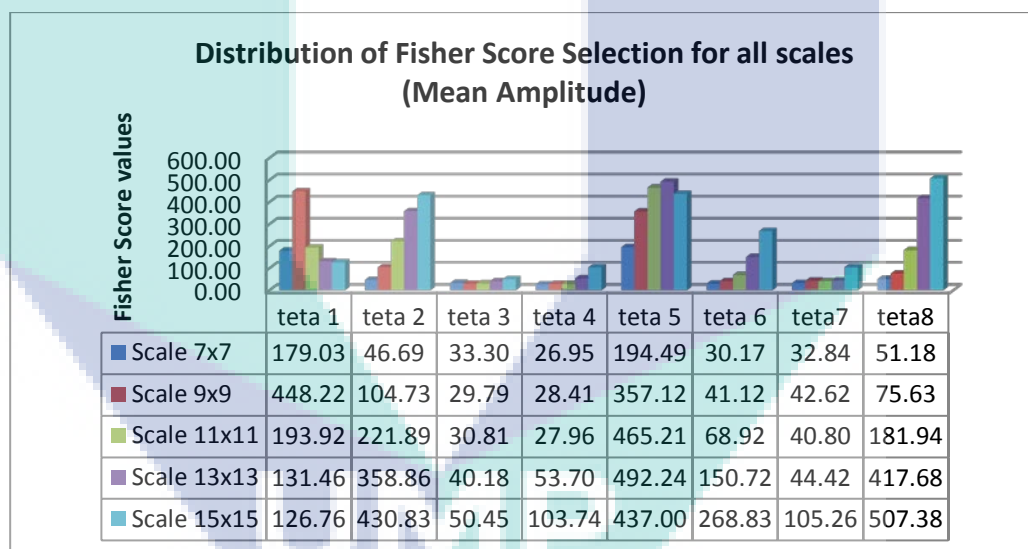


Figure 4.8 Variation of Fisher score value for Mean Amplitude between normal, warning and abnormal thermal motor bearing images

Figure and figure presents the overall group of thermal motor bearing image of local energy features and mean amplitude features for all eight orientations before any score is obtained. Those diagrams shown are only in the SCALE 15x15 as the highest score is contained in this scale. From those figures, the different variations of the graph can be seen in the different orientations. Hence, the fisher score or the discriminative power obtained will also vary according to the features produced by each orientation.

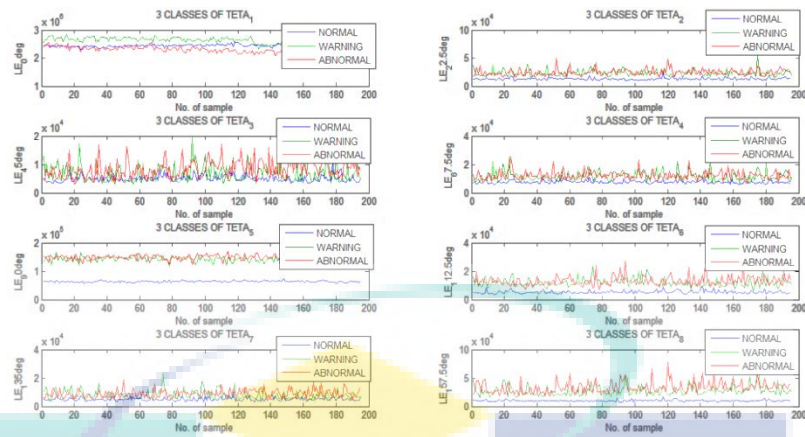


Figure 4.9 Variation Local Energy feature of condition thermal motor bearing images with 8 orientations for SCALE 15x15 in GWT

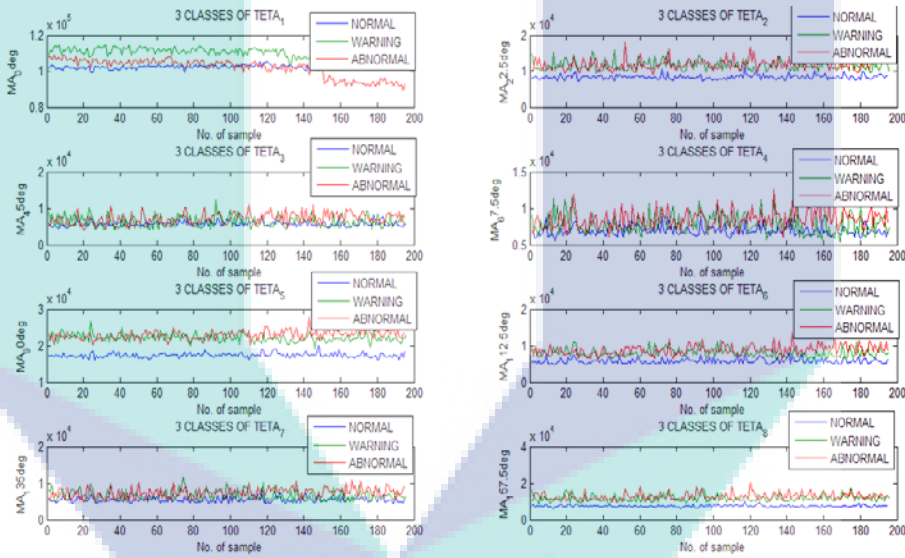


Figure 4.10 Variation Mean Amplitude feature of thermal motor bearing image conditions with 8 orientations for SCALE 15x15 in GWT

From the calculation of the fishery criteria, the highest reading was shown by the orientation $\theta_5 = 90^\circ$ representing for local energy features and the orientation $\theta_8 = 157.5^\circ$ representing for mean amplitude features. Their illustrations are shown individually as in the figure and figure. At this point, the dimensions for each of these matrix features have been reduced to $Y \in LE^{2075 \times 1}, MA^{2075 \times 1}$. From both graphs shown, it can be recognized that the three groups for thermal motor bearing image state are not in the desired result. Graph for normal group presents good results because it does not overlap with other categories. Whereas graph for warning group and abnormal group

indicate overlapping results. Therefore, from the visual view through graph results, it is proven that the features of thermal motor bearing image by using GWT-based feature extraction method cannot be well classified as the features of the group warning and abnormal group cannot be clearly distinguished. Nonetheless, the final selected features will be processed in the classification model in term of quantitative result in order to obtain the classification performance in this work. Furthermore, the performance evaluation for these features based was calculated and presented in section 4.3.1.1 by using analysis of variance (ANOVA) method.

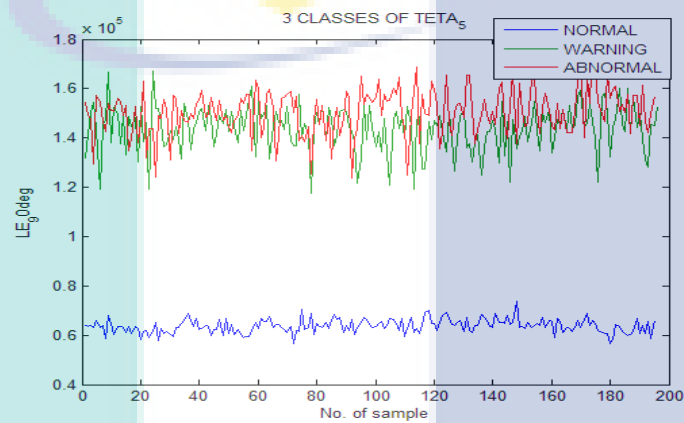


Figure 4.11 The optimal selection Local Energy feature for GWT is at SCALE 15x15 (orientation 90°)

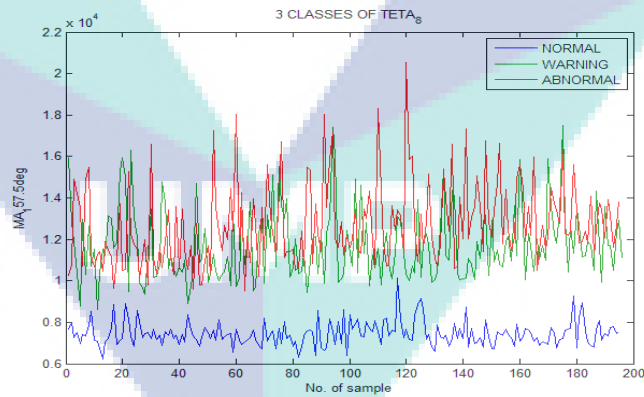


Figure 4.12 The optimal selection Mean Amplitude feature for GWT is at SCALE 15x15 (orientation 157.5°)

4.3.1.1 Evaluation Performance features by using ANOVA method

This section presents the results of the performance evaluation on the features of Local Energy and Mean Amplitude obtained by using ANOVA technique. Table and

table shows the descriptive statistics value generated by LE and MA features. The purpose of the ANOVA method was implemented in this work to evaluate the LE and MA features from thermal motor bearing images group whether there are significantly different or not. A 95% Confidence Interval for Mean has been implemented in this work which is basically a range of values for looking at parameters such as mean or proportion. Thus, $mean \pm 2SE$ is applied. From this formula, lower band and upper band values for the true mean for each normal population group, warning and abnormal were obtained. This value indicates that they have a 95% chance of being within the range of the mean as shown in the table and the table. From these tables, the 95% Confidence Interval for mean value of the normal group shows further apart from the other group. Whereas group warnings and abnormal groups indicate small values change between the two. Nonetheless, the descriptive statistic results for these LE and MA features still show different confidence interval for mean values for each population group.

Table 4.5 Descriptive statistics value for Local Energy feature

Thermal Image groups	N	Mean	Std Deviation	Std Error (SE)	95% Confidence Interval for Mean	
					Lower Bound	Upper Bound
Normal	1621	90110.71	24333.714	604.389	88925.25	91296.18
Warning	259	144255.01	8979.506	557.959	143156.27	145353.74
Abnormal	195	150579.63	9272.239	663.999	149270.05	151889.21
Total	2075	102551.59	32181.039	706.466	101166.13	103937.04

Figure 4.13 Descriptive statistics value for Mean Amplitude feature

Thermal Image groups	N	Mean	Std Deviation	Std Error (SE)	95% Confidence Interval for Mean	
					Lower Bound	Upper Bound
Normal	1621	8383.47	1798.550	44.672	8295.85	8471.09
Warning	259	11795.45	1794.116	111.481	11575.92	12014.98
Abnormal	195	12720.13	1968.814	140.990	12442.06	12998.20
Total	2075	9216.89	2411.799	52.946	9113.06	9320.72

Next, table and table presents the ANOVA readings generated using SPSS statistical software to obtain the value of F and the value of P. From these tables, the value of between group variability shows higher values than within group variability

values. This will generate a high F-ratio value where the F-ratio value for local energy feature is 1196.49 and the F-ratio value for mean amplitude feature indicates 795.843. These values are derived from the ratio of the mean squares (MS). Subsequently, these obtained F-ratio value then is used to define the level of significance for the samples by comparing them with the F-critical value. If the F-ratio is larger than the F-Critical, then the variation between the groups is statistically significant (Kazerouni, 2009). From the table of probability values for the F distribution with (2,2072) degree of freedom (df) in APPENDIX, a critical F value is found. The F-critical value for the local energy and mean amplitude features is $F_{2,2072,0.05} = 3.0$. Therefore, from the tables, it can be observed that the F-ratio is greater than the appropriate critical F distribution at $\alpha = 0.05$ (F-ratio > F-critical), thus the null hypothesis is rejected, and accept the alternative hypothesis. This means the variance between the means of population group are significantly different. Nonetheless, the most important parameter in ANOVA results is the P-value (Simsek & Uslu, 2020).

The value of P is the probability of obtaining results from all groups are differ significantly. Hence, from the statistical calculation using function 'fdist', P-value is obtained. From table, the P-value for the local energy feature is 0.000835. Meanwhile, from table, the P-value obtained from the mean amplitude feature is 0.001256. Based on the P-value obtained from the tables, it can be interpreted that the features of Local Energy and Mean Amplitude from all group of thermal motor bearing images are significantly different at $P < 0.05$.

Table 4.6 ANOVA for local energy feature

Source of variations	Sum of Squares	df	Mean Square (MS)	F-Ratio	F-Critical	P-Value
Between Groups	1151142340544.63	2	575571170272.31	1196.49	3.0	0.000835
Within Groups	996732001260.58	2072	481048263.157			
Total	2147874341805.221	2074				

Figure 4.14 ANOVA for Mean Amplitude features

Source of variations	Sum of Squares	df	Mean Square	F-Ratio	F-Critical	P-Value
Between Groups	5241194897.522	2	2620597448.761	795.843	3.0	0.001256
Within Groups	6822800071.426	2072	3292857.177			
Total	12063994968.947	2074				

4.3.2 Classification

There are two types of classifier used in this work, namely MLANNs and Linear Thresholding. Penggunaan classifier yang berbeza ini di apply untuk melihat classification performance algorithm manakah yang lagi bagus untuk membezakan group dari thermal motor bearing images ini. Section 4.4.2.1 and section 4.4.2.2 will discuss their performance results in more details.

4.3.2.1 MLANNs

In this section, the performance of the MLANNs model for selected features namely local energy and mean amplitude as in section 4.3.1 is evaluated based on three types of training algorithms. They are TRAINBR, TRAINLM and TRAINSCG. These three types of training algorithm are applied to achieve the best MLANNs model from the thermal images data obtained. Out of 2593 thermal motor bearing images dataset which contains normal group, warning group and abnormal group, 2334 thermal motor bearing images are taken to train the algorithms and the remaining 259 thermal images are used to test a trained algorithms to check whether they provides the correct output as desired. Besides, the results in this work are trained by using 5-fold and 10-fold cross-validation approach in order to evaluate the performance of the trained model for effective and stable model selection. The minimal error reflects better stability, and higher error reflects worst stability.

In the training phase, the results of the data involved such as data processing for each hidden neuron in the MLANNs network model, mean MSE training, mean MSE validation and mean accuracy performance. To fulfill this results, five different hidden neurons at $HN = 1, 2, 3, 4$ and 5 were evaluated on each learning algorithm. If the mean of MSE validation value does not display the minimum value, the data processing for the next hidden neuron will continue. If the mean of MSE validation has reached the minimum value, the training process is stopped before the MSE validation value is overfitting. If the least error is occurred from the validation process, the better the classification performance value obtained in this work due to net can generalize to testing data. All these results have been presented in the table. Next, five classification

statistical performance metrics namely Precision (Pre), Sensitivity (Se), Specificity (Sp), Accuracy (Acc) and Classification Error Rate (CER) for both training and testing were calculated based on multi-class classification problem through TP (True Positive), FP (False Positive), TN (True Negative) and FN (False Negative) according to the acquired confusion matrix (Tharwat, 2018).

Table 4.7 Training and validation performance results using TRAINLM, TRAINBR, TRAINSCG using 5-fold and 10-fold cross-validations in MLANNs model for LE and MA features

Training Function	K-Fold	HN	MSE		Accuracy (%)
			Training	Validation	
Trainbr	5	1	0.0437	0.0444	94.79
		2	0.0368	0.0373	
		3	0.0348	0.0357	
		4	0.0344	0.0370	
		5	0.0345	0.0365	
	10	1	0.0438	0.0441	94.67
		2	0.0351	0.0359	
		3	0.0349	0.0362	
		4	0.0347	0.0360	
		5	0.0347	0.0360	
Trainlm	5	1	0.0438	0.0442	94.55
		2	0.0386	0.0389	
		3	0.0367	0.0372	
		4	0.0346	0.0366	
		5	0.0344	0.0367	
	10	1	0.0438	0.0443	94.66
		2	0.0368	0.0374	
		3	0.0348	0.0363	
		4	0.0346	0.0367	
		5	0.0343	0.0366	
Trainscg	5	1	0.0437	0.0445	94.67
		2	0.0350	0.0359	
		3	0.0349	0.0363	
		4	0.0361	0.0361	
		5	0.0345	0.0363	
	10	1	0.0438	0.0442	
		2	0.0359	0.0370	

3	0.0358	0.0364	94.50
4	0.0348	0.0363	
5	0.0346	0.0370	

Observations of the learning curves graph for each training algorithm have been performed so that the performance of the training and validation process based on table 4.6 can be clearly distinguished. Next, the best K-fold selection for each training algorithm is performed. Figure shows graph validation performance for TRAINLM algorithm based on Kfold-5 and Kfold-10. From this result, it is observed that, the optimum mean MSE validation value can be read in Kfold-10 at hidden neuron 3 where the lowest value is 0.0363.

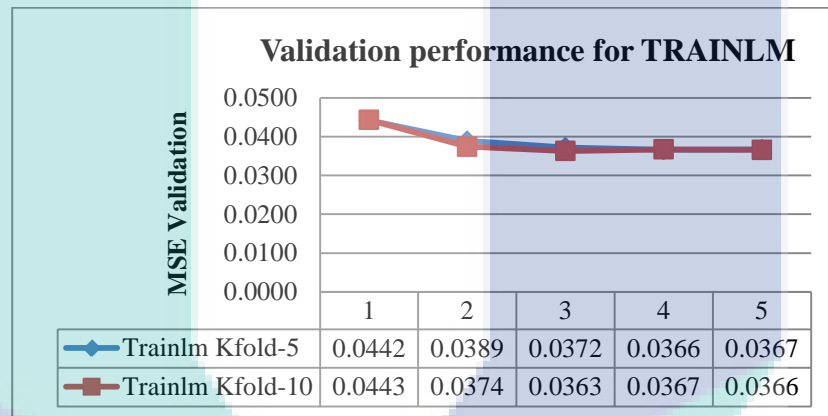


Figure 4.15 Validation performance for TRAINLM based on Kfold-5 and Kfold-10

Meanwhile, figure denotes a learning curves graph for the TRAINBR training algorithm. From the graph, it can be seen that readings in the hidden neuron 3 at kfold-5 gave the optimum mean MSE readings compared to all values of kfold-10. Its MSE lowest reading value is 0.0357.

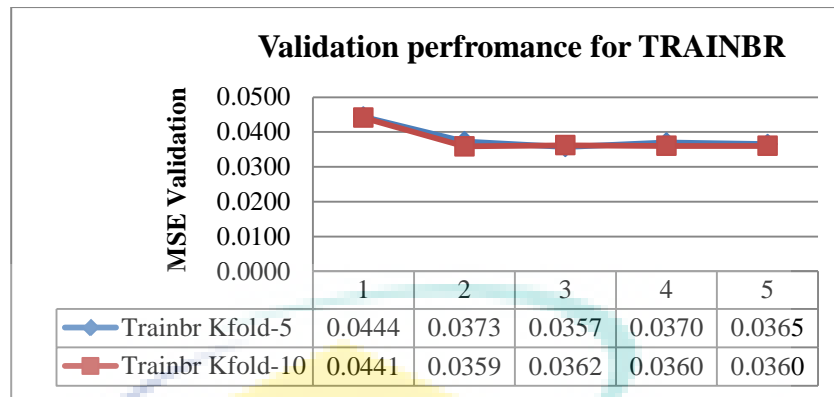


Figure 4.16 Validation performance for TRAINBR based on Kfold-5 and Kfold-10

Next, the third training algorithm is TRAINSCG. The optimum mean MSE reading of the training algorithm can be observed in the hidden neuron 2 on kfold-5. Its mean MSE value is 0.0359

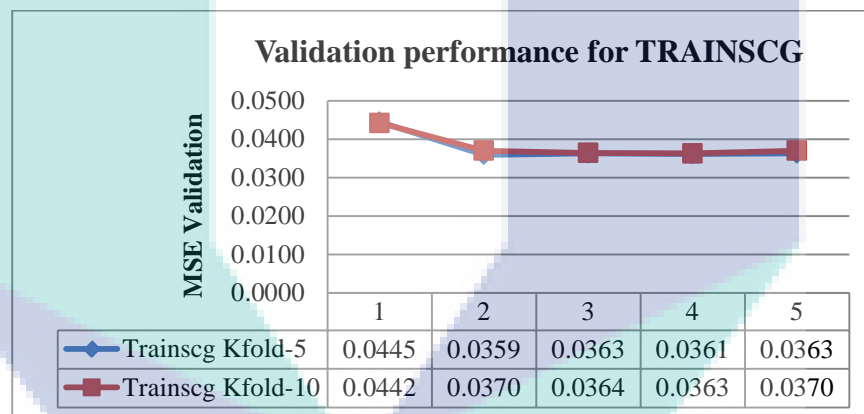


Figure 4.17 Validation performance for TRAINSCG based on Kfold-5 and Kfold-10

From all of the learning curve graphs shown above, the differences in mean MSE values between Kfold-5 and Kfold-10 did not differ significantly for each training algorithm. However, the differences error in the mean MSE value between both folds remains. Furthermore, the optimum mean MSE values for each training algorithm were extracted and combined in one graph as in the figure. This graph is intended to determine the best validation performance among all training algorithms. Hereby, as can be seen from the graph, TRAINBR gave the optimum mean MSE readings compared to TRAINLM and TRAINSCG for MLANNs models in this section. The minimum mean MSE value readings shown were 0.0357 at k-fold = 5, hidden neurons

= 3 and the average accuracy validation = 94.79% as observed in the table. Furthermore, once the mean error validation has been achieved to the minimum, the net will generalize to unknown samples through testing process.

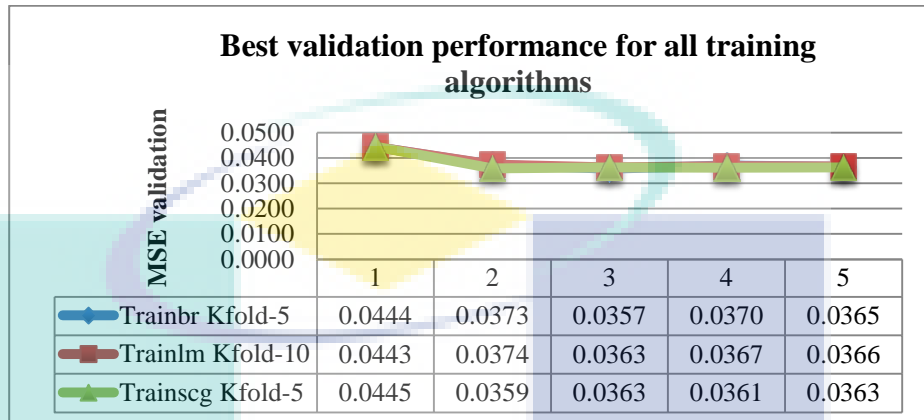


Figure 4.18 Best validation performances among all training algorithm types

Table shows the readings obtained from MATLAB software for best validation performance based on TRAINBR training algorithm in this section. Since K-fold = 5 is produced as the optimum mean cross validation error, so that the mean value for MSE validation and mean of accuracy validation value are measured 5 times according to the equation 3.33 as stated in section 3.7.1.1. From the table, it is seen that the best validation performance has been performed at various iterations at various times to determine how many times the learning algorithm works through the entire training data set.

Table 4.8 Best validation performance for TRAINBR in MLANNs model for Local Energy and Mean Amplitude features

K-fold	Best Epoch	Time (sec)	MSE Validation	ACC. Validation (%)
1	28	1s	0.0429	93.74
2	37	2s	0.0351	95.37
3	27	1s	0.0355	95.23
4	146	7s	0.0298	94.94
5	758	25s	0.0353	94.66
Total Mean:			0.0357	94.79

Subsequently, the overall results for training classification statistical performance metrics generated by TRAINBR algorithm for MA and LE features in this section are presented in table 4.7. Precision values = 78.4%, sensitivity = 79.49,

specificity = 96.01%, CER = 0.0521 and accuracy = 94.79%. All of these values are calculated based on the multi-class classification problem through TP, FP, TN and FN according to the confusion matrix acquired during training data processing.

Table 4.9 Validation performance results using TRAINBR in MLANNs model for Local Energy and Mean Amplitude features

Training Function	HN	Pre (%)	Sens (TPR) (%)	Spec (TNR) (%)	CER	ACC (%)
TRAINBR (K-fold=5)	3	78.40	79.49	96.01	0.0521	94.79

In this work, 10% of dataset was employed in MLANNs model testing for validation purposes. Thus, table indicates five classification statistical performance metrics obtained by using TRAINBR algorithm for classifying the conditions of thermal motor bearing images. The accuracy of neural networks for classifying all thermal bearing images conditions was 95.11% (240 correctly classified of 259), the sensitivity= 85.22%, the specificity =97.14%, precision=83.93% and Classification Error Rate=0.0504. Meanwhile, the testing values of the classification performances metrics for each state of thermal bearing images are denoted in the table. The results of these values have been calculated on multi-class classification problem based on TP (True Positive), FP (False Positive), TN (True Negative) and FN (False Negative) according to the acquired TRAINBR confusion matrix.

Table 4.10 Testing performance results using TRAINBR in MLANNs model for Local Energy and Mean Amplitude features

Training Function	HN	Class	TP	TN	FP	FN	Pre (%)	Sens (%)	Spec (%)	CER	ACC (%)
TRAINBR (K-fold=5)	3	N	180	77	0	2	1.0000	0.9890	1.0000	0.0077	.9923
		W	32	208	8	11	0.8000	0.7442	0.9630	0.0734	0.9266
		A	28	214	11	6	0.7179	0.8235	0.9511	0.0700	0.9344
		All					0.8393	0.8522	0.9714	0.0504	0.9507

Furthermore, the overall differences in the results performance of the MLANNs classification models for the testing phase and training phase in this section are graphically illustrated as in figure for easier observation.

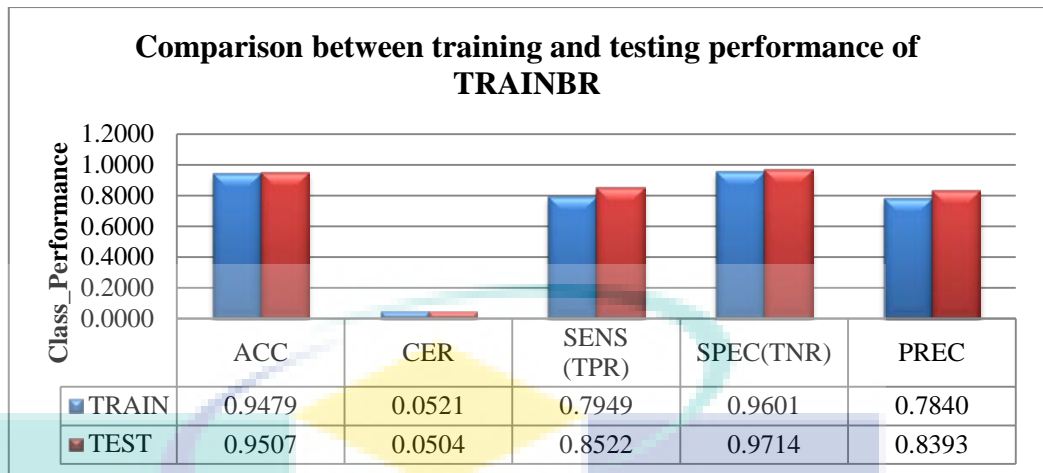


Figure 4.19 Comparison bar graph between training and testing performance using GWT based feature extraction algorithm

4.3.2.2 Linear Thresholding

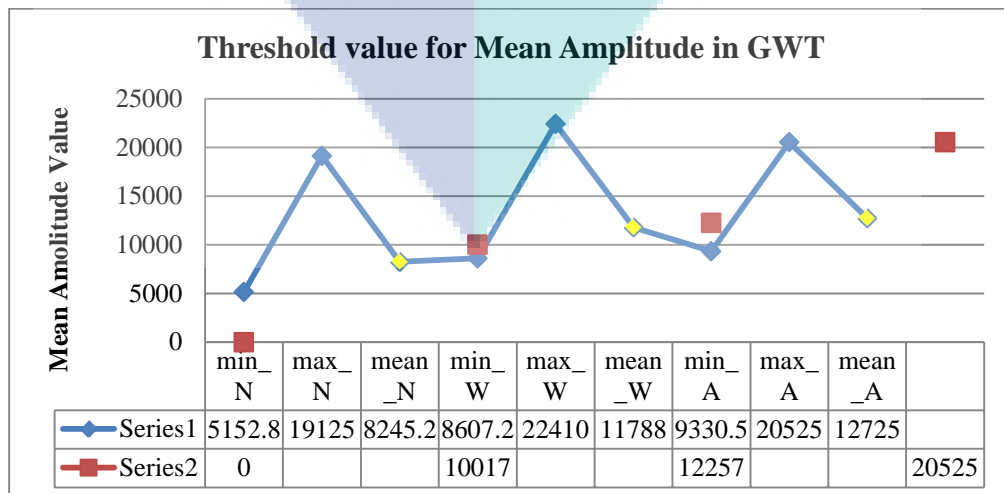
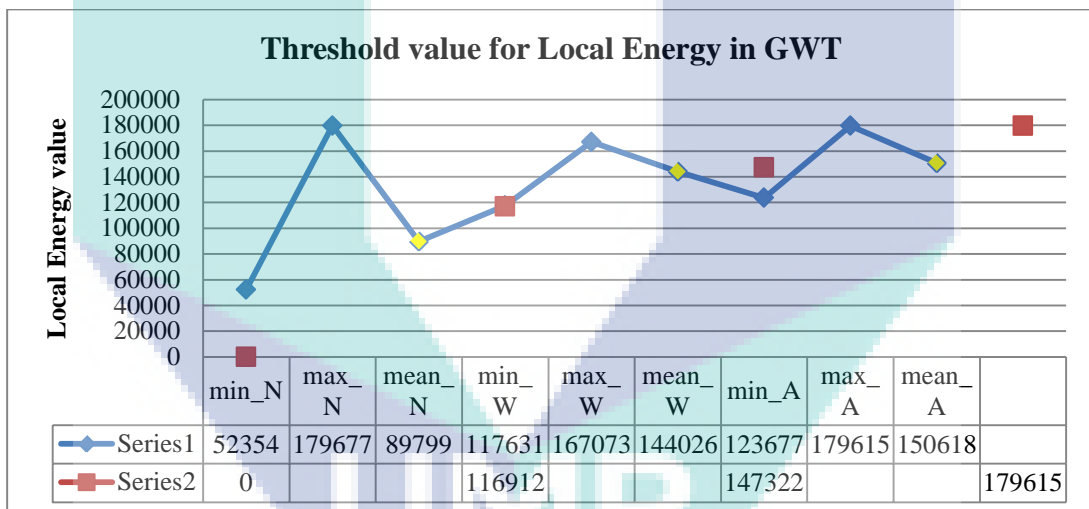


Table 4.11 Classification performances using Linear Thresholding model for GWT based feature extraction's features

Features	Condition of thermal bearing images	ACC TRAINING		ACC TESTING	
		Training (%)	No. of Classified image	Testing (%)	No. of Classified image
Local Energy	Normal	86.5630	1559	100.0000	180
	Warning	61.2040	183	67.5000	27
	Abnormal	65.3846	153	13.6752	32
	Average All	71.0505	Total: 1895	60.3917	Total: 239
Mean Amplitude	Normal	85.8967	1547	98.8889	178
	Warning	57.1906	171	57.5000	23
	Abnormal	51.2821	120	38.4615	15
	Average All	64.7898	1838	64.9501	Total: 216
		Average All:		62.6709	

4.4 Proposed an Enhanced Gabor Features (EGF) -based Feature Extraction Method

This chapter contains the main findings in this study. It discusses in detail the results obtained from the development of the new feature extraction process that has been proposed in this section to improve the quality features based on the original feature extraction process as in section 4.3. As explained in section 4.3, graph for warning group and abnormal group indicate the overlapping results. This cause the classification process did not work properly due to the graph **between the two cannot** be clearly distinguished. In addition, based on the performance features obtained from ANOVA method in section 4.3.1.1, it has also proven that the confidence interval for mean **reading between groups is also unbalanced. The results of this ANOVA correspond to the overlapping graph between the groups that have been shown in figure in section 4.3.1.** This has contributed to the proposed of development on the new feature extraction methods in this section where feature enhancements on thermal images based on the original GWT feature extraction method have been implemented.

In this present study, a combination of an independent image enhancement approach called Histogram Equalization method with the original GWT-based feature extraction technique has been developed. Combinations of these methods have been executed to modify the contrast and the distribution of the gray levels of pixels in the images. As a

consequence, by modifying the pixel value (intensities) of the image, the problems that have occurred in the section 4.3 could be overcome. When the quality of the thermal images is improved, the classification performance could also be improved accurately. Hence, the features of thermal motor bearing images could also be distinguished well in this study. This proposed method is called Enhanced EGF-based feature extraction.

Thermal image processing has begun with converting the segmented input RGB thermal images as in figure in section 4.2.2 into grayscale intensity image, $I(x, y)$. Next, the new feature extraction process has been performed by enhancing the features of thermal images by utilizing the method proposed which is Enhanced Gabor Features (EGF)-based feature extraction. From this proposed technique, the quality image features and classification performances in this work can be improved. This 2D-EGF extraction process begins by adjusting the contrast of the thermal input image first by using an independent image enhancement approach called Histogram equalization. Through this adjustment, the intensities can be better distributed on the histogram. This can be seen from the equalized image histogram as in the figure (b), where image contrast for all groups has been improved by changing the pixel value almost evenly to the entire range of possible values (0 to 255), $I_{Equalized Image}(x, y)$. Thus, all the situation for before equalized image and after equalized image have been presented as in figure.

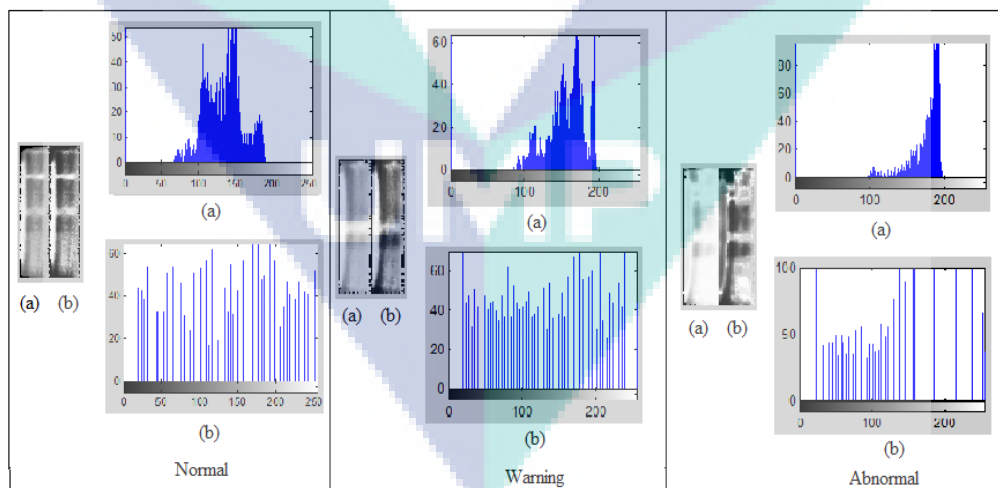


Figure 4.20 (a)Original Image and Original Image Histogram for group normal, warning and abnormal (b) Equalized Image and Equalized Image Histogram for group normal, warning and abnormal

Next, the process of extracting features continues with transferring the enhanced image, $I_{Equalized Image}(x, y)$ into the 2D-Gabor Wavelet Transform, $g(x, y)$. It means that, the Fourier Transform of the enhanced image is computed first by applying 5 different frequencies and 8 orientations as specified in the table in section 3.5.2 in order to extract out all those new patterns, $g_{new}(x, y)$. This 2D EGF-based feature extraction will then provide the coefficient results on the specific frequency content in a specific direction in the image in a localized region according to the predetermined parameter values on the images. As a consequence, a new feature modification of the pixel value (intensity) on the image has been produced in this section. Next, the new result of this EGF function representing the new pixel value (intensities) of the output image has been depicted in the form of diagrams as in the figure. The figure denotes a perspective view of filter representing orthogonal directions that has a new real (cosine) and a new imaginary(sine) component in spatial domain.

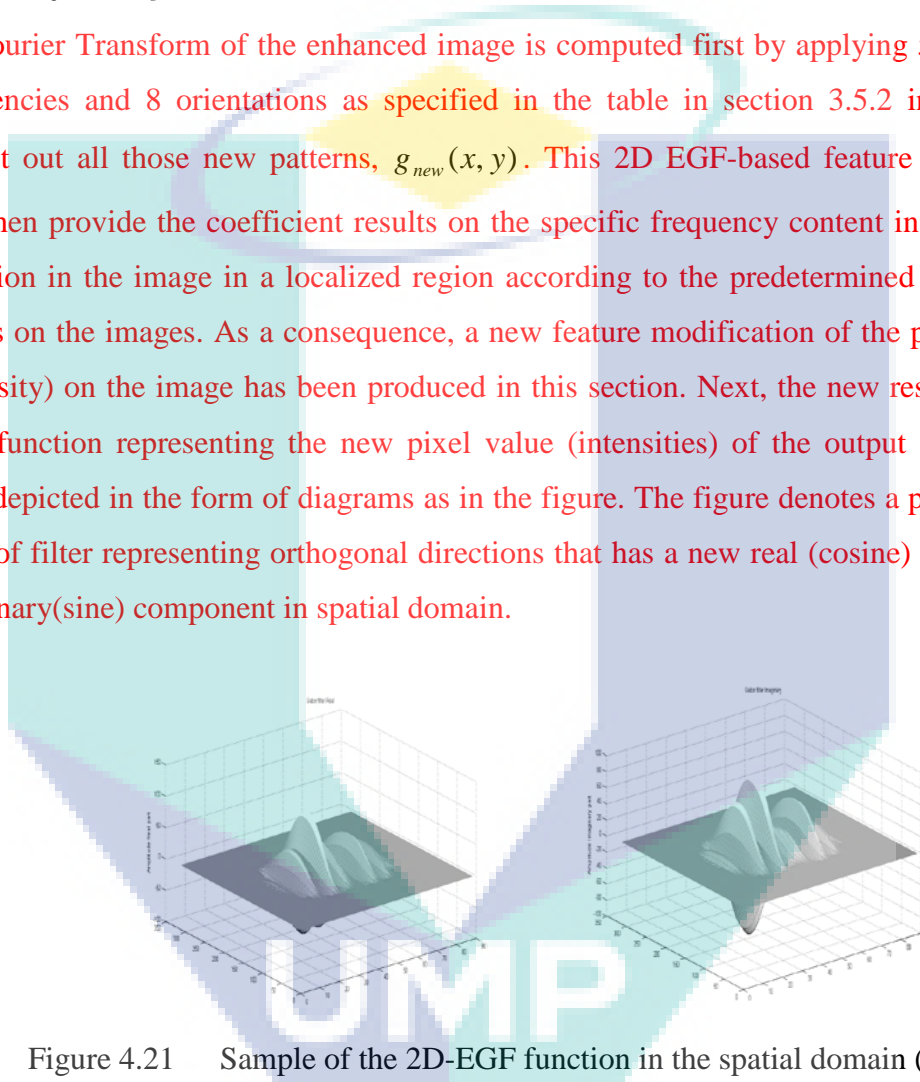


Figure 4.21 Sample of the 2D-EGF function in the spatial domain (new Real (cosine) component and new Imaginary(sine) component) for normal thermal image condition

Meanwhile, figure illustrates the new real (cosine) component of the entire EGF filter in spatial domain with different 5 frequencies and 8 orientations. The row corresponds to different scales containing bandwidth ($\sigma_1 = 2.8, \sigma_2 = 3.6, \sigma_3 = 4.5, \sigma_4 = 5.4, \sigma_5 = 6.3$) and wavelength ($\lambda_1 = 3.5, \lambda_2 = 4.6, \lambda_3 = 5.6, \lambda_4 = 6.8, \lambda_5 = 7.9$), while the column corresponds to different orientation ($0^\circ, 22.5^\circ, 45^\circ, 67.5^\circ, 90^\circ, 112.5^\circ, 135^\circ$ and 157.5°). By varying these parameter values (θ, σ, λ) for the new

EGF function, the filter pattern will also change. Hereby, 40 filters EGF channel at each image point i.e. 40 new multi-scales and new multi-orientations feature images have been generated. Thus, the overall total number of new EGF features that have been produced in this present study is as much as 2075×40 equal to 83,000 including for normal, warning and abnormal groups.

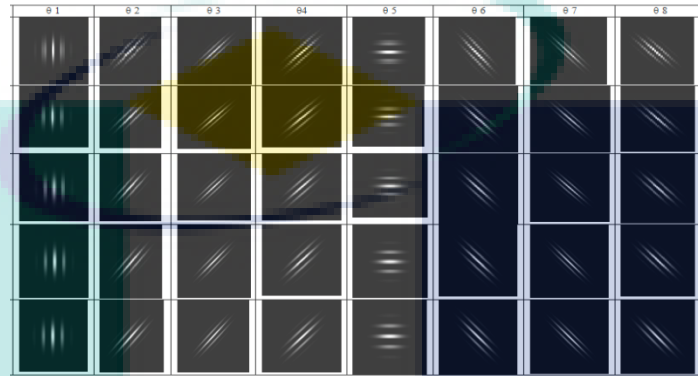


Figure 4.22 A new real componnets of EGF filters in spatial domain rotates at 5 scales and 8 orientations in normal conditon image

Subsequently, the process of convolving the two-dimensional EGF filter, $g_{new}(x, y)$ with the input image, $I(x, y)$ has been acquired in order to detect the new EGF filter response from the input image itself. In this process, the complex convolution result is decomposed to the new EGF filter real response as denoted in figure and also the EGF imaginary response image. From the figure, it can be seen the different responses was shown according to the parameters that have been determined. It can also be observed, the higher the scale of parameter are employed, the clearer the new EGF response stripes are shown.

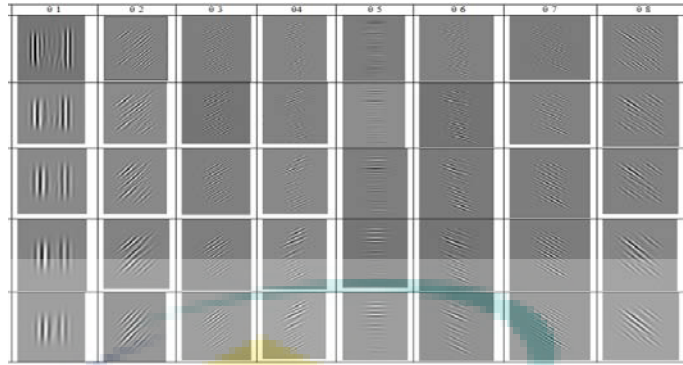


Figure 4.23 A new EGF magnitude response of the convolution of normal thermal motor bearing image with five scales and eight orientations

After implement the convolution operation, the convolution result were decomposed to the new magnitude response image as denoted in figure and the new phase response image based on the complex of EGF real component and EGF imaginary component images. Nonetheless, for the phase response image, it was not taken into account in this study. This is proven from the previous studies, they say the case of magnitude is the most effective while the original Gabor phase are considered unstable and are usually discarded (Hafez et al., 2015; Liu et al., 2005; Štruc & Pavešić, 2010a, 2010b). From the figure, it can be seen, a set of 40 different representation (oriented magnitude response matrices, R_{new}) of an image have been extracted and contain the component of the corresponding new feature vector. At this point, when the input thermal bearing images passed through each orientation on the EGF-based filter, the output of the resulting oriented extract features is according to the orientation of the filter at that time. Therefore, a new feature vector containing the new pixel value (intensities) of the output image based on the original Local Energy and the original Mean Amplitude in the section 4.3 has been generated in this work, $Y \in R^{nxj} \in MA_{(new)}^{83000} \in LE_{(new)}^{83000}$. Where new Local Energy feature has obtained by equal to summing up the squared value of each matrix value from a new response matrix. Meanwhile, for new Mean Amplitude feature has acquired by equal to sum of absolute values of each matrix value from a new response matrix

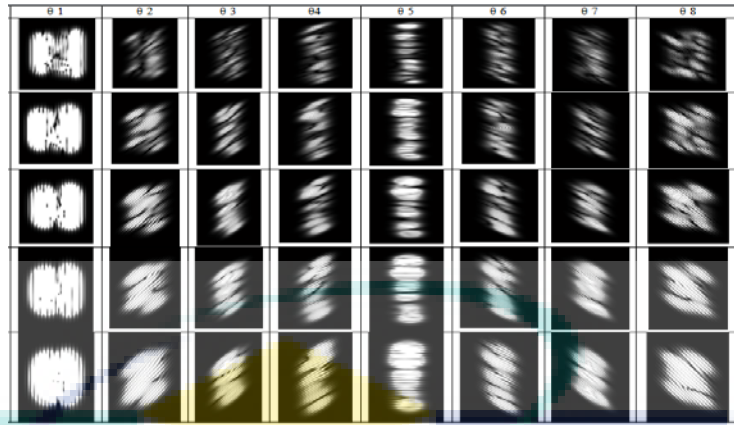
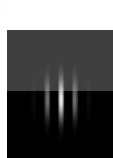
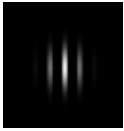


Figure 4.24 The oriented output sample of response matrices (features) for normal condition image when pass through individual EGF-based filter with five scales and eight orientations

Figure illustrates the whole process performed with the feature extraction method that has been proposed in this section. A sample image of each database group with a parameter scale of 15×15 ($\sigma_5 = 6.3, \lambda_5 = 7.9$) at orientation 0° has been shown to differentiate the output of the new magnitude response which will lead to the production of the new feature vector. Image convolution process is applied to achieve the goal of generating features based on the filter used.

Table 4.12 Feature Extraction based on proposed EGF filter for 1 sample from 3 groups of thermal motor bearing images with scale 15×15 at orientation 0°

Thermal bearing image Conditions	Convolution (Input Image * EGF)		Magnitude response
Normal		* 	= 
Warning		* 	= 

Abnormal  *  = 

Subsequently, the overall graph for the new results from both feature vectors (new Local Energy and new Mean Amplitude) is shown as in the figure and figure. These graphs represent the modifies in the value of new pixels (intensities) that have been generated based on the magnitude response obtained for each group from thermal motor bearing images.

There are 40 EGF channel filters that have been deployed at each image point for each group of thermal images. The purpose is to extract the corresponding of new feature values according to the respective image groups. Then, the features extracted from these normal, warning and abnormal groups are arranged according to the same scale parameters. it is intended to see the differences group generated according to their respective orientation as shown in both figures. Herein, there are 40 multi-scales and multi-orientations of EGF-based feature images that have been generated. It corresponds to the differences in the multi-scale and multi-orientation parameters deployed in this work in which the production of different features will be obtained.

From a visual point of view, it can be seen from the graph that the new feature vector output from both new Local Energy and new Mean Amplitude have some significant variations features to differentiate the group of thermal motor bearing images. Nevertheless, the feature selection process will be executed to define the optimal features to distinguish the group from these thermal bearing images. It will be discussed in details in section 4.4.1. Only the most relevant features will be used for the next processing, while the irrelevant features will be discarded.

Local Energy	
Scale 7x7	Scale 9x9

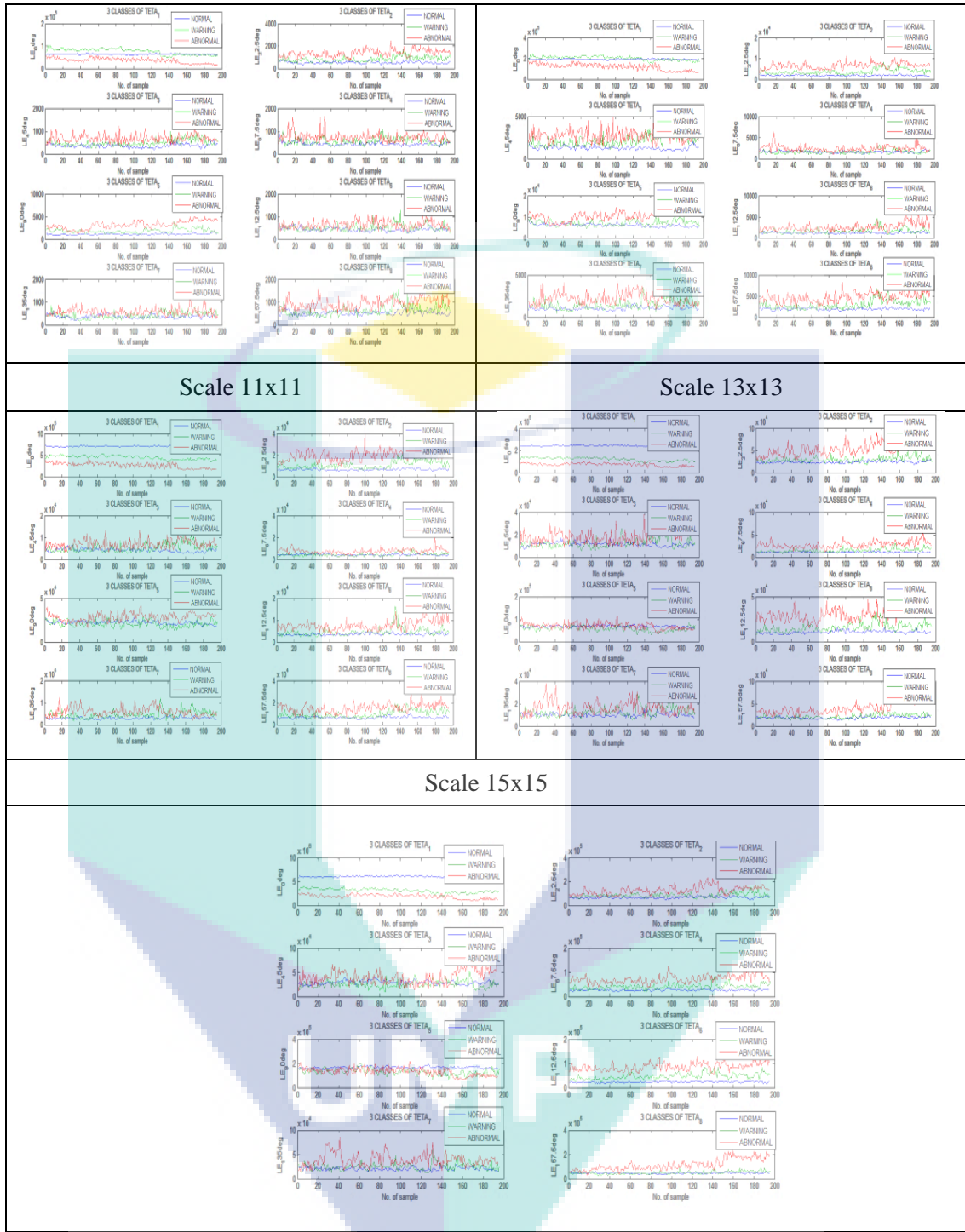


Figure 4.24 Overall new Local Energy features for multi-scales and multi-orientations in EGF based feature extraction method

Mean Amplitude	
Scale 7x7	Scale 9x9

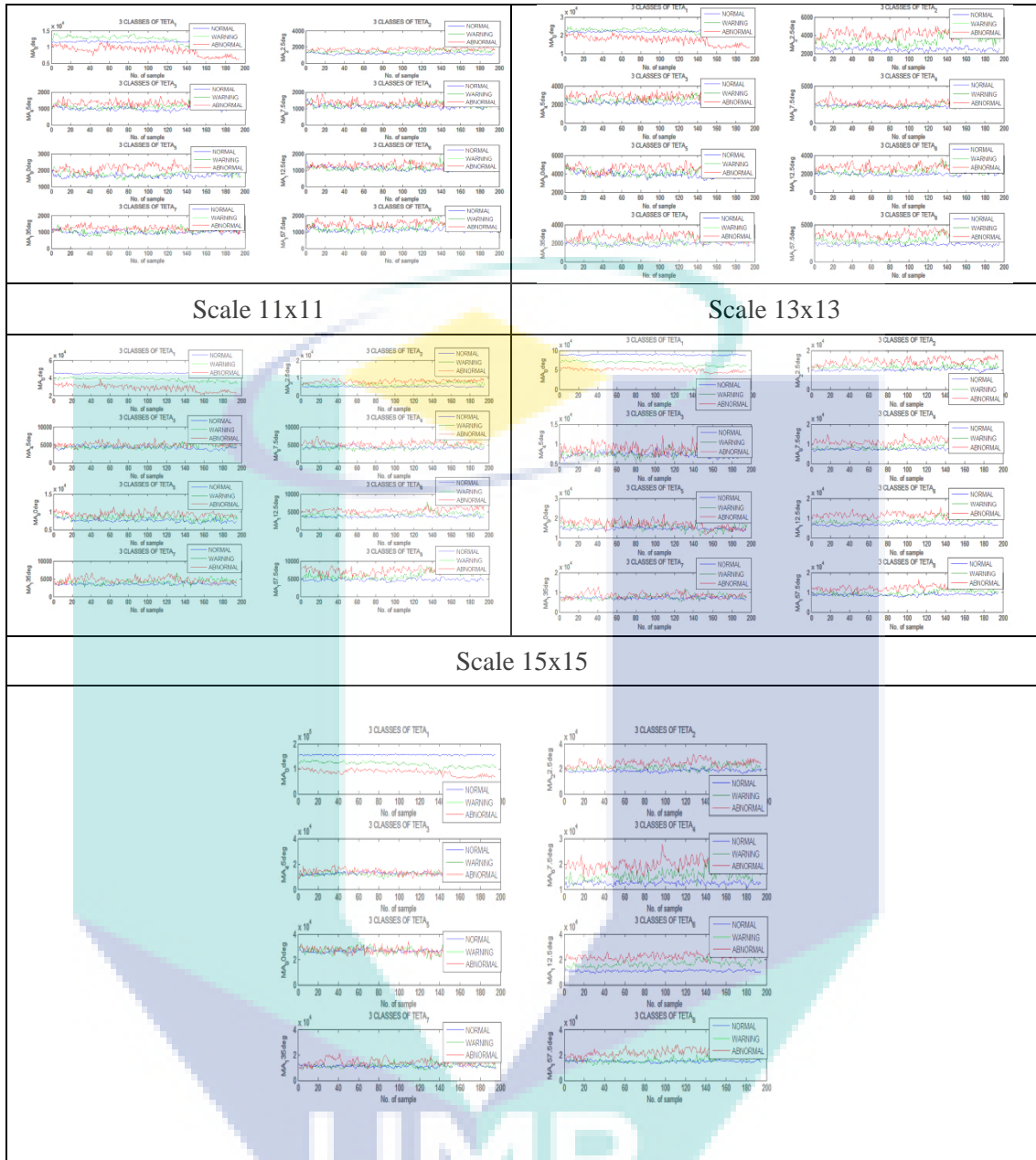


Figure 4.24 Overall new Mean Amplitude features for multi-scales and multi-orientations in EGF based feature extraction method

4.4.1 Feature Selection

In this section, a new optimum selection of scales and orientations for feature extraction methods based on Enhanced Gabor Features (EGF) using the proposed fisher score method is discussed. As in section 4.3.1, fisher score-based feature selection was employed in this work to select the optimal features of high-dimensional vector output features from the EGF-based feature extraction process as in section 4.4.

According to the feature extraction results as in section 4.4, a new 40 multi-scale and multi-orientation feature images have been generated at each image point. Thus, the new total input data matrix generated for image data set training in different orientations and scales is $Y \in R_{(new)}^{(nx5) \times j} \in LE_{(new)}^{10375 \times 8}, MA_{(new)}^{10375 \times 8}$, where ‘ n ’ is the number of samples which have 2075 images and ‘ j ’ is the number of orientations. After calculating their scores as in equation 3.32 according to the fishery criterion, the score for new local energy and new mean amplitude features were produced as in **table and table**. From the literatures, the final selection of features occurs as the optimum fisher score by the top ranked ones and it is sorted in descending order. (Gu et al., 2012b; Islam et al., 2015; Ma et al., 2019; T. Zhang & Lu, 2010).

Based on the results of the new local energy generated in the **table**, the scores of combination orientations and scales are arranged from the highest value starting with F15 = 3536.94, followed by F13=3216.28, F11=1552.86, F7=730.12 and F9= 725.71. Therefore, the highest score value produced is at F15 = 3536.94, which is on a scale 15x15 ($\sigma = 6.3, \lambda = 7.9$) and orientation $\theta_1=0^\circ$. From these observations, the new scores derived from this section have shown higher values compared to the scores for the original GWT-based extraction method in section 4.3.1. This has proven that scores from this section produce in higher discrimination power and better scores than GWT-based scores.

Table 4.13 Fisher scoring for each Enhanced Gabor filter’s scale for Local Energy

Filter Size (Scales)	θ_1	θ_2	θ_3	θ_4	θ_5	θ_6	θ_7	θ_8
7x7	345.53	677.31	399.59	278.06	730.12	260.25	252.15	451.39
9x9	417.67	725.71	412.55	141.21	553.98	397.84	355.24	629.88
11x11	1552.86	721.29	267.12	260.73	374.45	543.84	351.17	565.94
13x13	3216.28	785.88	230.26	617.78	32.95	1036.56	276.59	414.83
15x15	3536.94	641.53	159.71	850.19	30.89	1474.96	354.15	418.69

Meanwhile, in the table, the sequence of decreasing fisher score values for new mean amplitude features starts with F13=2779.01, followed by F15=2178.89, F11=1368.53, F9=981.31 and F7=864.01. From this result, the highest fisher's score can be read on a scale 13x13 and orientations $\theta_1=0^\circ$ and the value is F13=2779.01. In this section, the new mean amplitude scores have also been shown to have higher

discriminative power and better scores compared to GWT-based extraction scores as in section 4.3.1. This is due to the scores generated in this work are higher.

Table 4.14 Fisher scoring for each Enhanced Gabor filter's scale for Mean Amplitude

Filter Size (Scales)	θ_1	θ_2	θ_3	θ_4	θ_5	θ_6	θ_7	θ_8
7x7	291.53	864.01	502.65	293.99	731.06	279.89	363.42	611.02
9x9	347.58	949.99	509.82	194.90	512.01	596.06	457.32	981.31
11x11	1368.53	882.86	316.15	336.72	466.85	886.97	421.01	888.93
13x13	2779.01	1067.35	329.06	898.00	134.30	1473.78	309.20	777.93
15x15	2178.89	844.13	226.12	1246.16	3.82	1972.46	395.97	728.61

Figure and figure demonstrates the distribution of fisher's scores obtained for the scale and orientation variations in the tables and tables according to their respective features. As in figure, it is clear from the local energy graph that SCALE 15 (θ_1) gives the highest fisher score among the others. Meanwhile, for the mean amplitude graph as shown in figure, it is observed that among others, SCALE 13 (θ_1) has given the highest score.

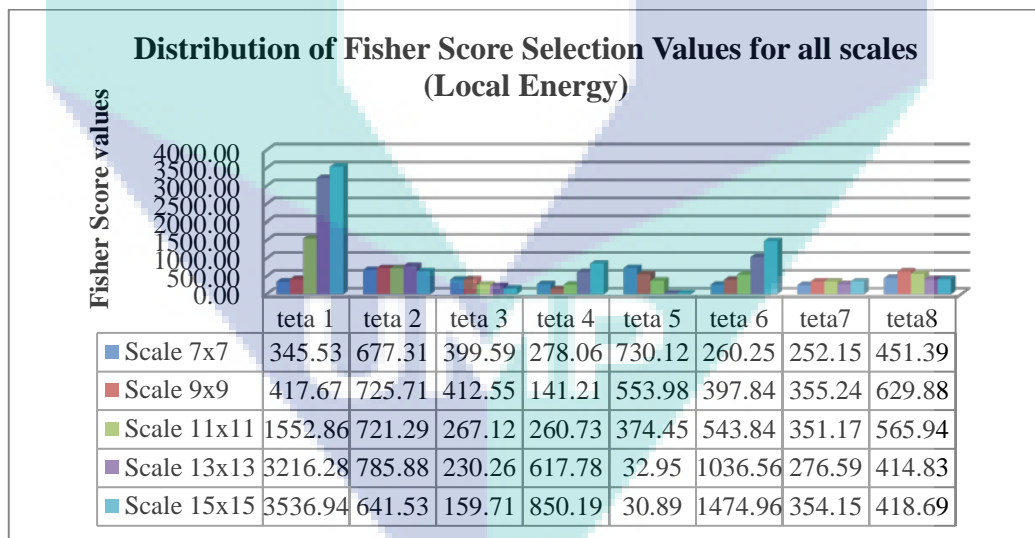


Figure 4.25 Variation of Fisher score value for local energy between normal, warning and abnormal thermal motor bearing images

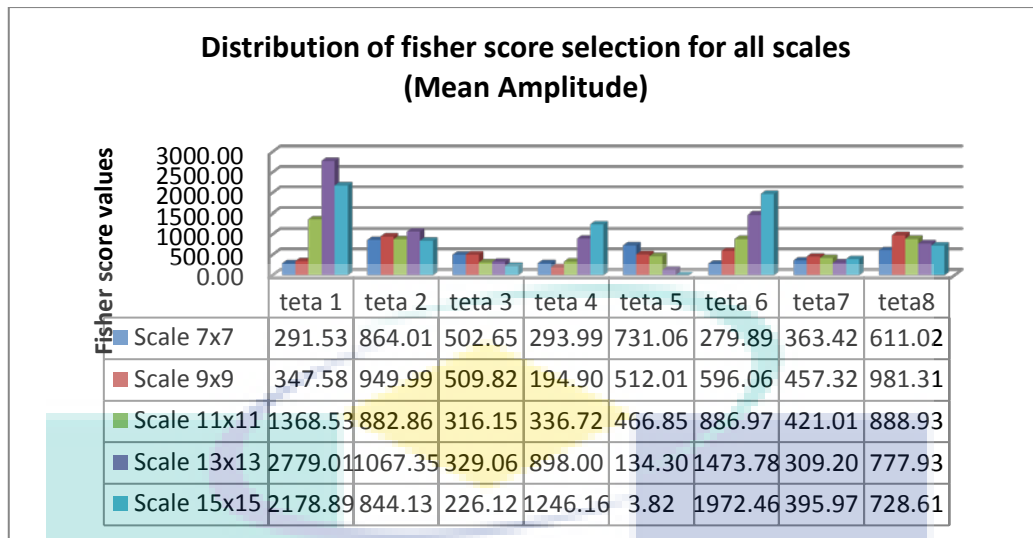


Figure 4.26 Variation of Fisher score value for Mean Amplitude between normal, warning and abnormal thermal motor bearing images

Figure and figure displays the overall group of thermal motor bearing image of local energy features and mean amplitude features for all eight orientations before any score is obtained. Those diagrams shown are in the SCALE 15x15 and SCALE 13x13 respectively as this scale includes the highest score. The various variations of the graph in the different orientations can be seen from those figures. Consequently, the fisher score or the discriminative power obtained will also vary according to the features produced by each orientation.

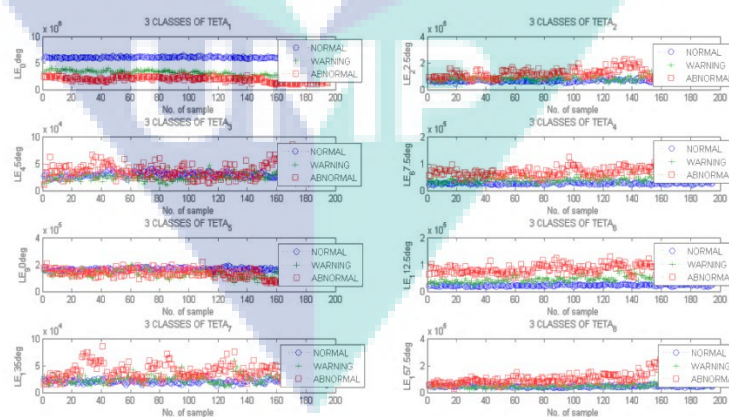


Figure 4.27 Variation Local Energy feature of condition thermal motor bearing images with 8 orientations for SCALE 15x15 in EGF

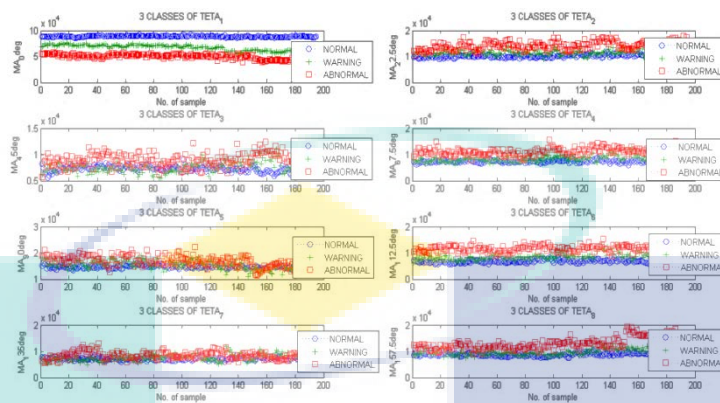


Figure 4.28 Variation Mean Amplitude feature of condition thermal motor bearing images with 8 orientations for SCALE 13x13

From the calculation of the fishery criteria, the highest reading was shown by the orientation $\theta_1 = 0^\circ$ representing for local energy features and the orientation $\theta_1=0^\circ$ representing for mean amplitude features. Their illustrations are shown individually as in the figure and figure. At this stage, the dimensions for each of these matrix features have been reduced to $Y \in LE_{(new)}^{2075 \times 1}, MA_{(new)}^{2075 \times 1}$. From both graphs shown, it can be observed that the three groups for the state of thermal motor bearing image are in the desired results. Graphs for all three groups which are normal, warning and abnormal demonstrate good results since they do not overlap with other categories. Therefore, from the visual view through graph results, it is proven that the enhancement features of thermal motor bearing image by using EGF-based feature extraction method can be classified well due to the features of the group with the other groups can be clearly distinguished. Furthermore, the final selected features in this section will be processed in the classification model in term of quantitative result in order to obtain the best classification performance results in this work.

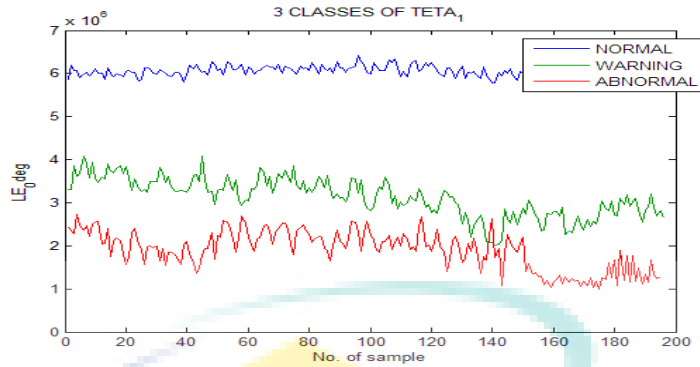


Figure 4.29 The optimal selection Local Energy feature for EGF is at SCALE 15x15 (teta 1)

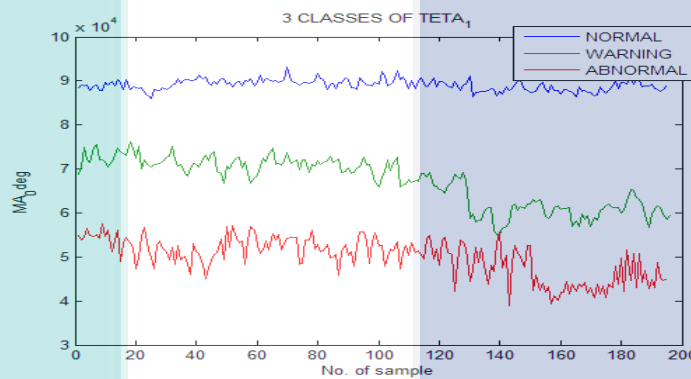


Figure 4.30 The optimal Mean Amplitude feature for EGF is at SCALE 13x13 (Orientation 0°)

4.4.1.1 Evaluation performance features by using ANOVA method

Same in section 4.3.1.1, this section presents the results of the performance evaluation on the features of new Local Energy and new Mean Amplitude obtained by using ANOVA technique. Table and table shows the descriptive statistics value generated by new Local Energy and new Mean Amplitude features. The purpose of the ANOVA method was implemented in this work to evaluate the new Local Energy and new Mean Amplitude features from thermal motor bearing images group whether there are significantly different or not. A 95% Confidence Interval for Mean has been implemented in this work which is basically a range of values for looking at parameters such as mean or proportion. Thus, $mean \pm 2SE$ is applied. From this formula, lower

band and upper band values for the true mean for each normal population group, warning and abnormal were obtained. These values indicates that they have a 95% chance of being within the range of the mean as shown in the **table and the table**. From these tables, the 95% Confidence Interval for the mean values for the normal, warning and abnormal groups shows the balanced change values between the population groups. This has shown that the results obtained from this proposed section are better compared to the original results in section 4.3.1.1.

Table 4.15 Descriptive statistics value for new Local Energy feature

Thermal Image groups	N	Mean	Std Deviation	Std Error	95% Confidence Interval for Mean	
					Lower Bound	Upper Bound
Normal	1621	5270263.09	596798.559	14823.005	5241188.81	5299337.36
Warning	259	2971402.51	497372.563	30905.227	2910543.90	3032261.13
Abnormal	195	1898839.64	442987.505	31722.994	1836273.40	1961405.87
Total	2075	4666488.41	1300485.426	28549.364	4610500.01	4722476.81

Table 4.16 Descriptive statistics value for new Mean Amplitude feature

Thermal Image groups	N	Mean	Std Deviation	Std Error	95% Confidence Interval for Mean	
					Lower Bound	Upper Bound
Normal	1621	83035.57	5101.139	126.700	82787.06	83284.08
Warning	259	64756.51	6390.292	397.073	63974.60	65538.43
Abnormal	195	49857.98	4444.405	318.270	49230.27	50485.70
Total	2075	77636.10	11970.961	262.797	77120.73	78151.47

Next, **table and table** presents the ANOVA readings generated using SPSS statistical software to obtain the value of F and the value of P. From these tables, the value of between group variability produces higher values than within group variability values. This will generate a high F-ratio value where the F-ratio value for new Local Energy feature is 4316.812 and the F-ratio value for new Mean Amplitude feature indicates 4411.581. These values are derived from the ratio of the mean squares (MS). Subsequently, these obtained F-ratio value then is used to define the level of significance for the samples by comparing them with the F-critical value. If the F-ratio is larger than the F-Critical, then the variation between the groups is statistically significant (Kazerouni, 2009). From the table of probability values for the F distribution

with (2,2072) degree of freedom (df) in APPENDIX, a critical F value is found. The F-critical value for the new local energy and new mean amplitude features is $F_{2,2072,0.05} = 3.0$. Therefore, from the tables, it can be observed that the F-ratio is greater than the appropriate critical F distribution at $\alpha = 0.05$ (F-ratio > F-critical), thus the null hypothesis is rejected, and accept the alternative hypothesis. This means the variance between the means of population group are significantly different. Nonetheless, the most important parameter in ANOVA results is the P-value (Simsek & Uslu, 2020).

The value of P is the probability of obtaining results from all groups are differ significantly. Hence, from the statistical calculation using function 'fdist', P-value is obtained. From table, the P-value for the new local energy feature is 0.000232. Meanwhile, from table, the P-value obtained from the new mean amplitude feature is 0.000227. According to (Kazerouni, 2009), the lower the value resulting from this P-value is, the more statistically significant the population parameter is. Thus, both of the P-value in this section has shown a better reading compared to the reading on the original P-value in section 4.3.1.1. This is due to the P-value in this section is more lower compared to the P-value in section 4.3.1.1.

Therefore, based on the P-value obtained from the tables, it can be interpreted that the features of new Local Energy and new Mean Amplitude from all group of thermal motor bearing images are significantly different at $P < 0.05$.

Table 4.7 ANOVA for new Local Energy features

Source of variations	Sum of Squares	df	Mean Square (MS)	F-Ratio	F-Critical	P-Value
Between Groups	2828791040329872.0	2	1414395520164936.00	4316.812	3.0	0.000232
Within Groups	678887062098701.6	2072	327648195993.58			
Total	3507678102428573.5	2074				

Table 4.7 ANOVA for new Mean Amplitude features

Source of variations	Sum of Squares	df	Mean Square (MS)	F-Ratio	F-Critical	P-Value
Between Groups	240689604115.125	2	120344802057.563	4411.581	3.0	0.000227
Within Groups	56522693512.819	2072	27279292.236			
Total	297212297627.944	2074				

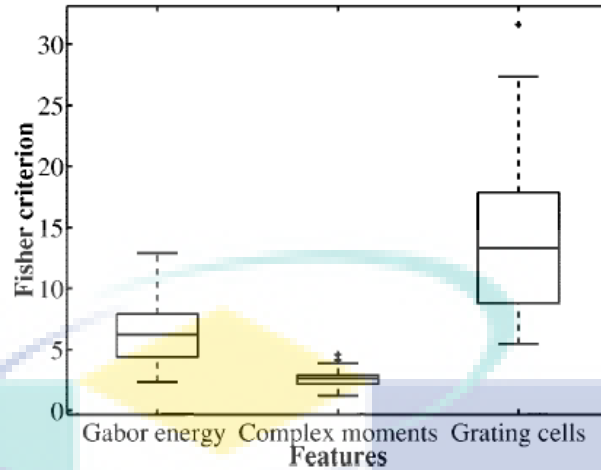


Fig. 2. Boxplot representation of the distribution of the Fisher criterion values obtained with different texture operators.

4.4.2 Classification

There are two types of classifier used in this work, namely MLANNs and Linear Thresholding. Section 4.4.2.1 and section 4.4.2.2 will discuss their performance results in more details.

4.4.2.1 MLANNs

In this section, the parameters and procedures of the MLANNs model applied to this work are same as those described in the previous sections in section 4.3.2.1. The purpose is to obtain the best MLANNs model in order to identify and distinguish the condition of thermal motor bearing images used in this study. The best measure for MLANNs model can be observed through classification statistical performance metrics obtained by looking at the highest accuracy value and the lowest MSE value. In order to achieve these outputs, the selected features namely local energy and mean amplitude as in section 4.5.1.1 were used. All these results have been presented in the table.

Table 4.17 Training and validation performance results using TRAINLM, TRAINBR, TRAINSCG using 5-fold and 10-fold cross-validations in MLANNs model for Local Energy and Mean Amplitude features

Training Function	K-Fold	HN	Avg MSE		Avg Acc (%)
			Training	Validation	Validation
Trainbr	5	1	0.0408	0.0412	
		2	0.0079	0.0096	

		3	0.0073	0.0098	98.97
		4	0.0071	0.0121	
		5	0.0071	0.0095	
	10	1	0.0409	0.0414	
		2	0.0080	0.0094	
		3	0.0076	0.0090	99.00
		4	0.0073	0.0094	
		5	0.0072	0.0109	
Trainlm	5	1	0.0408	0.0417	
		2	0.0080	0.0090	
		3	0.0073	0.0100	98.97
		4	0.0071	0.0102	
		5	0.0070	0.0122	
	10	1	0.0408	0.0415	
		2	0.0113	0.0125	
		3	0.0075	0.0216	98.45
		4	0.0073	0.0155	
		5	0.0071	0.0348	
Trainscg	5	1	0.0408	0.0415	
		2	0.0146	0.0154	
		3	0.0077	0.0116	99.02
		4	0.0079	0.0087	
		5	0.0780	0.0104	
	10	1	0.0408	0.0416	
		2	0.0114	0.0118	98.97
		3	0.0078	0.0089	
		4	0.0080	0.0093	
		5	0.0080	0.0092	

Observations of the learning curves graph for each training algorithm have been performed so that the performance of the training and validation process based on table 4.6 can be clearly distinguished. Next, the best K-fold selection for each training algorithm is performed. Figure shows graph validation performance for TRAINLM algorithm based on Kfold-5 and Kfold-10. From this result, it is observed that, the optimum mean MSE validation value can be read in Kfold-5 at hidden neuron 2 where the lowest value is 0.0090

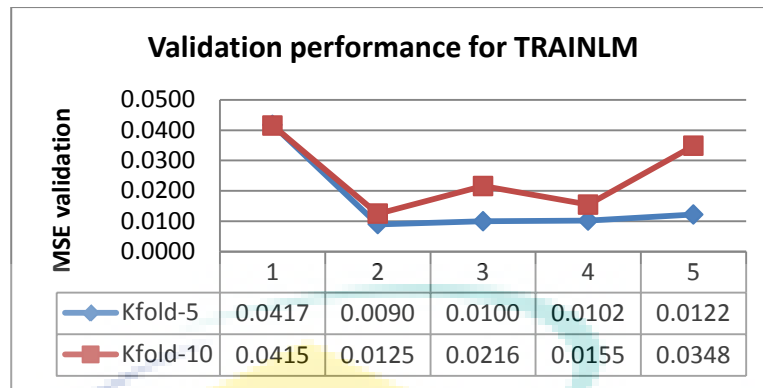


Figure 4.31 Validation performance for TRAINLM based on Kfold-5 and Kfold-10

Meanwhile, figure denotes a learning curves graph for the TRAINBR training algorithm. From the graph, it can be seen that readings in the hidden neuron 3 at kfold-10 gave the optimum mean MSE readings compared to all values of kfold-5. Its MSE lowest reading value is 0.0090.

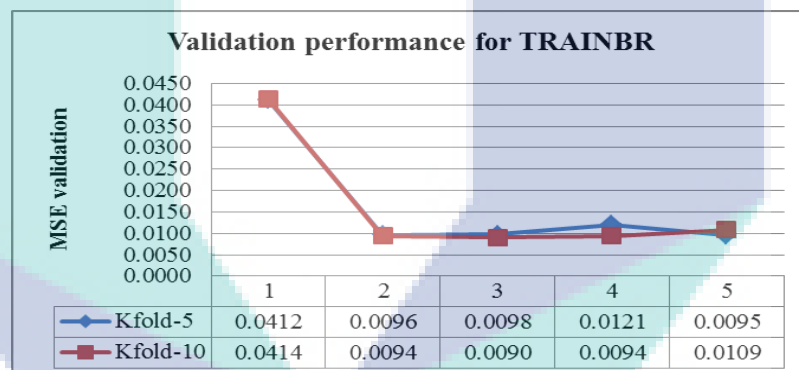


Figure 4.32 Validation performance for TRAINBR based on Kfold-5 and Kfold-10

Next, the third training algorithm is TRAINSCG. The optimum mean MSE reading of the training algorithm can be observed in the hidden neuron 4 on kfold-5. Its mean MSE value is 0.0087.

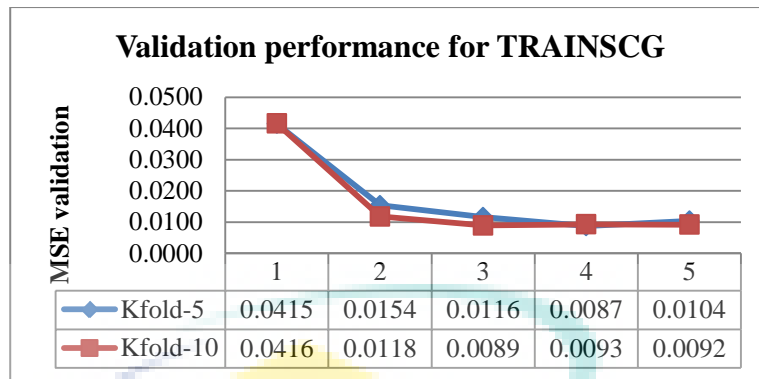


Figure 4.33 Validation performance for TRAINSCG based on Kfold-5 and Kfold-10

From all of the learning curve graphs shown above, the differences in mean MSE values between Kfold-5 and Kfold-10 did not differ significantly for each training algorithm. However, the differences error in the mean MSE value between both folds remains. Furthermore, the optimum mean MSE values for each training algorithm were extracted and combined in one graph as in the figure. This graph is intended to determine the best validation performance among all training algorithms. Hereby, as can be seen from the graph, TRAINSCG gave the optimum mean MSE readings compared to TRAINLM and TRAINBR for MLANNs models in this section. The minimum mean MSE value readings shown were 0.0087 at k-fold = 5, hidden neurons = 4 and the average accuracy validation = 99.02% as observed in the table. Furthermore, once the mean error validation has been achieved to the minimum, the net will generalize to unknown samples through testing process.

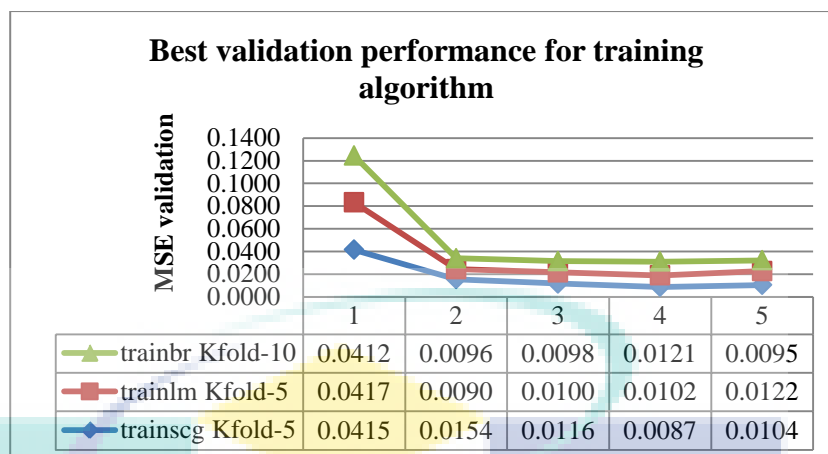


Figure 4.34 Best validation performances among all training algorithm types

Table shows the readings obtained from MATLAB software for best validation performance based on TRAINSCG training algorithm in this section. Since K-fold = 5 is produced as the optimum mean cross validation error, so that the mean value for MSE validation and mean of accuracy validation value are measured 5 times according to the equation 3.33 as stated in section 3.7.1.1. From the table, it is described that the best validation performance has occurred at 1000 iterations in 4 and 5 seconds per fold in order to define the number times that the learning algorithm works through the entire training dataset. Herein, it is observed that the performances produced by the MLANNs model in this section are fast. Herein, it is noted that the performance produced by the MLANN model in this section is not as fast as the MLANN model in section 4.4.2.1.

Table 4.18 Best validation performance for TRAINSCG in MLANNs model for Local Energy and Mean Amplitude features

K-fold	Best Epoch	Time (sec)	MSE Validation	Acc Validation (%)
1	1000	5s	0.0095	97.84
2	1000	4s	0.0081	99.43
3	1000	4s	0.0098	99.43
4	1000	4s	0.0079	99.43
5	1000	4s	0.0082	99.00
Total Mean:			0.0087	99.02

Subsequently, the overall results for training classification statistical performance metrics generated by TRAINSCG algorithm for MA and LE features in this section are presented in table 4.7. Precision values = 97.20%, sensitivity = 96.38, specificity = 98.88, CER = 0.0095 and accuracy = 99.02%. All of these values are

calculated based on the multi-class classification problem through TP, FP, TN and FN according to the confusion matrix acquired during training data processing.

Table 4.19 Training performance results using TRAINSCG in MLANNs model for Local Energy and Mean Amplitude features

Training Function	HN	Pre (PPV) (%)	Sens (TPR) (%)	Spec (TNR) (%)	CER	ACC (%)
TRAINSCG (K-fold=5)	4	97.20	96.38	98.88	0.0095	99.02

In this work, 10% of dataset was employed in MLANNs model testing for validation purposes. Thus, table indicates five classification statistical performance metrics obtained by using TRAINSCG algorithm for classifying the conditions of thermal motor bearing images. The accuracy of neural networks for classifying all thermal bearing images conditions was 99.47% (257 correctly classified of 259), the sensitivity= 99.63%, the specificity =99.7%, precision=98.29% and Classification Error Rate=0.0051. Meanwhile, the testing values of the classification performances metrics for each state of thermal bearing images are denoted in the table. The results of these values have been calculated on multi-class classification problem based on TP (True Positive), FP (False Positive), TN (True Negative) and FN (False Negative) according to the acquired TRAINSCG confusion matrix.

Table 4.20 Testing performance results using TRAINSCG in MLANNs model for Local Energy and Mean Amplitude features

Training Function	HN	Class	TP	TN	FP	FN	Pre (%)	Sens (%)	Spec (%)	CER	ACC (%)
TRAINSCG (K-fold=5)	4	Normal	180	77	0	2	100	98.90	100	0.0077	99.22
		Warning	40	219	0	0	100	100	100	0	100.00
		Abnormal	37	220	2	0	94.87	100	99.10	0.0077	99.18
		All					98.29	99.63	99.70	0.0051	99.47

Furthermore, the overall differences in the results performance of the MLANNs classification models for the testing phase and training phase in this section are graphically illustrated as in figure for easier observation.

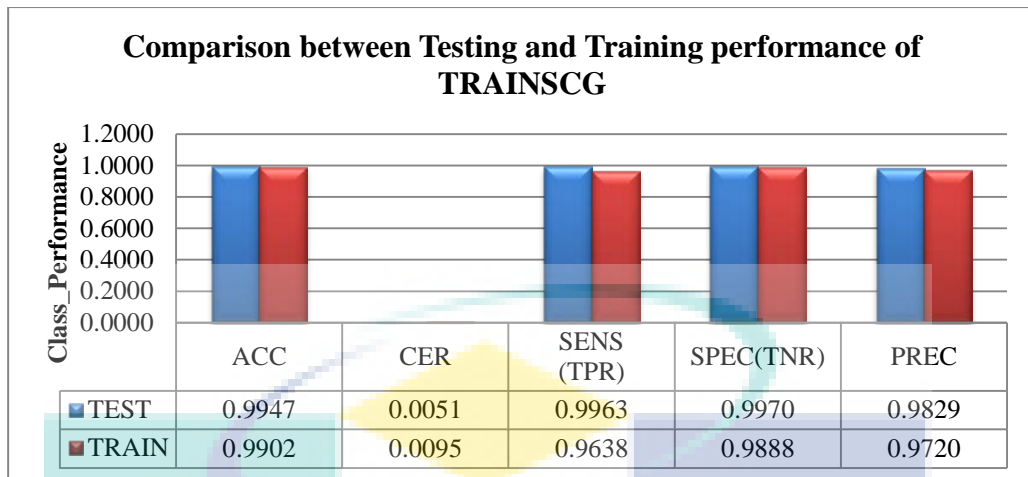


Figure 4.35 Comparison bar graph between training and testing performance using EGF based feature extraction algorithm

4.4.2.2 Linear Thresholding

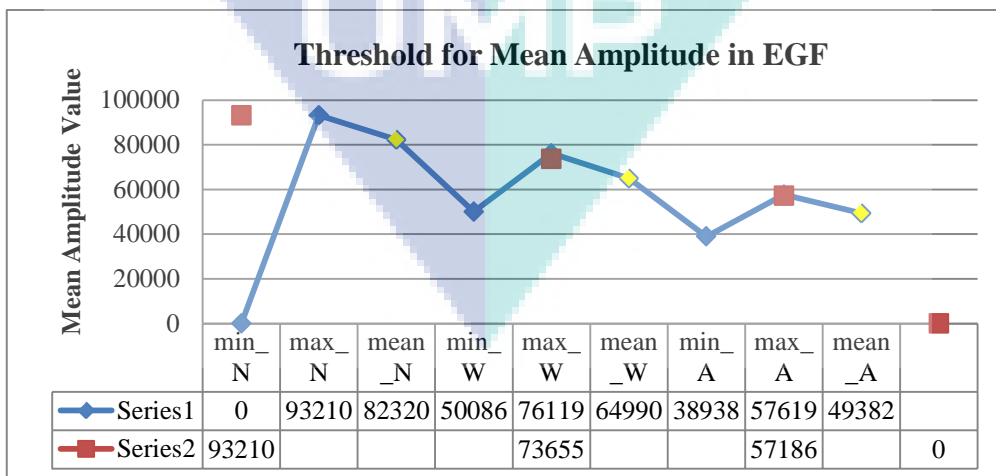
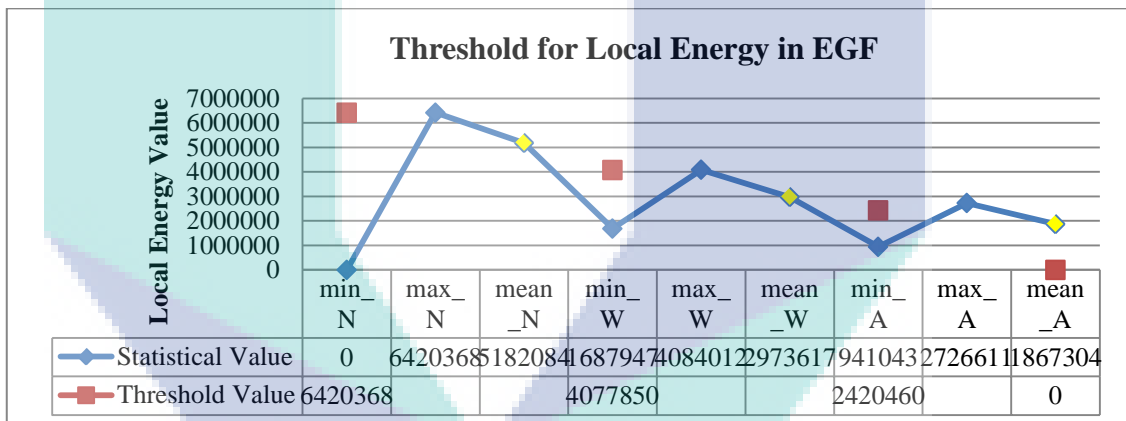


Table 4.21 Classification performances using Linear Thresholding model for EGF based feature extraction's features

Features	Condition of thermal bearing images	ACC TRAINING		ACC TESTING	
		Training (%)	No. of Classified image	Testing (%)	No. of Classified image
Local Energy	Normal	97.2238	1751	100.0000	180
	Warning	88.6288	265	95.0000	38
	Abnormal	91.4530	214	94.8718	37
	Average All	92.4352	Total: 2230	96.6239	Total: 255
Mean Amplitude	Normal	95.9467	1728	98.8889	178
	Warning	86.2876	258	100.0000	40
	Abnormal	99.5726	233	100.0000	39
	Average All	93.9357	Total: 2219	99.6296	Total: 257
		Average All:		98.1268	

4.5 Proposed Other Enhanced Methods based on GWT Feature Extraction

There are 3 new methods of enhanced feature extraction have been developed in this study. It aims to compare in terms of which method gives the best performance result after the image quality is improved. This method is constructed based on the original GWT feature extraction method which has been discussed in section 4.3. The EGF method is one of the new enhanced feature extraction methods that has given the best feature performance results compared to the other 2 methods. This EGF method is as the main findings in this study. However, 2 more methods based on GWMSH and GWCLAHE have also been developed and will be discussed further in section 4.5.1 and section 4.6.1. Briefly, these 2 methods provide less satisfactory on the evaluation performance features and classification results compared to the EGF-based feature extraction methods.

4.5.1 Propose an Enhanced GWSMH-based Feature Extraction Method

As in section 4.4, this section also discusses the results of the proposed new feature extraction method that has been developed to improve the quality features of the GWT-based feature extraction method as discussed in section 4.3. The problem that occurred in section 4.3 has contributed to the proposed development on the new feature enhancements method in this section.

In this work, a combination of the pre-processing method with the new feature extraction method has been implemented. The pre-processing method consists of a combination of unsharp filters and median filters. These methods has been developed where an unsharp mask filter intended to sharpen the image followed by a median filter for the removal of noise at the input thermal image. Meanwhile, the new feature extraction method consists of a combination of an independent image enhancement approach called Histogram Equalization method with the original GWT-based feature extraction technique. All the combinations of these methods have been developed to modify the contrast and the distribution of the gray levels of pixels in the images. As a consequence, by modifying the pixel value (intensities) of the image, the problems that have occurred in the section 4.3 could be overcome. When the quality of the thermal images is improved, the classification performance could also be improved accurately. Hence, the features of thermal motor bearing images could also be distinguished well in this study. This proposed method is called Enhanced GWSMH-based feature extraction.

Thermal image processing has begun with converting the segmented input RGB thermal images as in figure in section 4.2.2 into grayscale intensity image, $I(x, y)$. Next, the method proposed in this section namely GWSMH which is the combination of both pre-processing methods with the new feature extraction method has been executed. This process has started by performing the pre processing first by enhancing the features of input grayscale thermal images by utilizing the proposed method which is a combination of median filter with the unsharp filter technique, respectively, $I_{filtered}(x, y)$. The result of the image is illustrated in the figure.

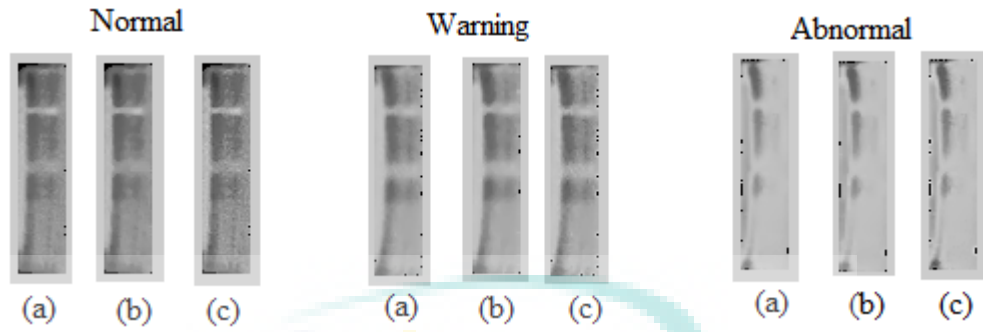


Figure 4.36 Noise removed in each input grayscale thermal images group by using Unsharp filter and Median filter (a) Input grayscale thermal image (b) Unsharp filter image (c) Median filter image

Furthermore, the process of extracting of the new features has been carried out by utilizing the combination method from Histogram Equalization with the original GWT-based extraction method. This process has begun by adjusting the contrast of the filtered image, $I_{filtered}(x, y)$ first by using an independent image enhancement approach called Histogram equalization. Through this adjustment, the intensities can be better distributed on the histogram, $I_{Filter_Equalized_Image}(x, y)$.

Afterwards, the process of extracting features continues with transferring the enhanced image, $I_{Filter_Equalized_Image}(x, y)$ into the 2D-Gabor Wavelet Transform, $g(x, y)$. It means that, the Fourier Transform of the enhanced image is computed first by applying 5 different frequencies and 8 orientations as specified in the table in section 3.5.2 in order to extract out all those new patterns, $g_{new}(x, y)$. This 2D GWSMH-based method will then provide the coefficient results on the specific frequency content in a specific direction in the image in a localized region according to the predetermined parameter values on the images. All of these generated coefficient results also represents an orthogonal direction that has a real component (cosine) and a new imaginary (sinus) in the spatial domain. As a consequence, a new feature modification of the pixel value (intensity) on the image has been produced in this section.

Figure(b) illustrates the new real (cosine) component of the entire GWSMH filter in spatial domain with different 5 frequencies and 8 orientations. The row corresponds to different scales containing bandwidth ($\sigma_1 = 2.8, \sigma_2 = 3.6, \sigma_3 = 4.5, \sigma_4 = 5.4, \sigma_5 = 6.3$)

and wavelength ($\lambda_1 = 3.5, \lambda_2 = 4.6, \lambda_3 = 5.6, \lambda_4 = 6.8, \lambda_5 = 7.9$), while the column corresponds to different orientation ($0^\circ, 22.5^\circ, 45^\circ, 67.5^\circ, 90^\circ, 112.5^\circ, 135^\circ$ and 157.5°). By varying these parameter values (θ, σ, λ) for the new GWSMH function, the filter pattern will also change. Hereby, 40 filters GWSMH channel at each image point i.e. 40 new multi-scales and new multi-orientations features images have been generated. Thus, the overall total number of new GWSMH features that have been produced in this present study is as much as 2075×40 equal to 83,000 including for normal, warning and abnormal groups.

Subsequently, the process of convolving the two-dimensional GWSMH filter, $g_{new}(x, y)$ with the input image, $I(x, y)$ has been acquired in order to detect the new GWSMH filter response from the input image itself. The convolution result were decomposed to the new magnitude response image as denoted in figure(a) based on the complex of GWSMH real component and GWSMH imaginary component images. As in the section 4.3 and section 4.4, for the phase response image, it was not taken into account in this study. This is due to the Gabor phase response are considered unstable and are usually discarded. From the figure, it can be seen, the oriented magnitude response matrices of image have been extracted and contain the component of the corresponding new feature vector. At this point, when the input thermal bearing images passed through each orientation on the GWSMH-based filter, the output of the resulting oriented extract features is according to the orientation of the filter at that time.

Thus, a new feature vector containing the new pixel value (intensities) of the output image based on the original Local Energy and Mean Amplitude in the section 4.3 has been generated in this work, $Y \in R^{n \times j} \in MA_{(new)}^{83000} \in LE_{(new)}^{83000}$. Where the new Local Energy feature has obtained by equal to summing up the squared value of each matrix value from a new response matrix. Meanwhile, for the new Mean Amplitude feature has acquired by equal to sum of absolute values of each matrix value from a new response matrix

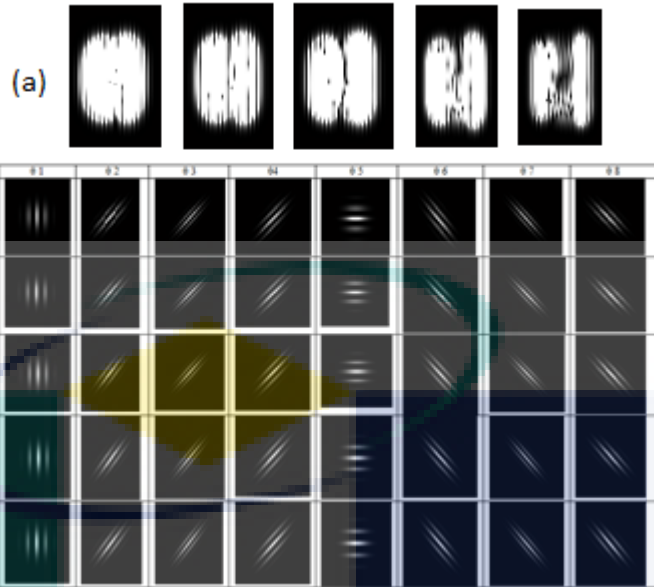
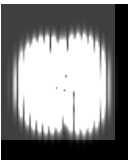
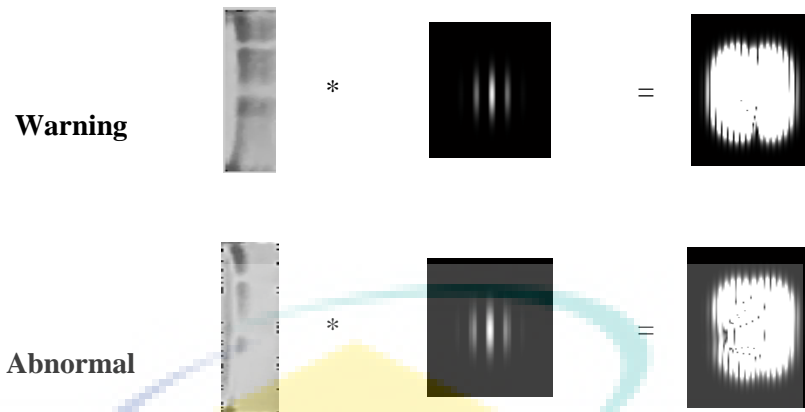


Figure 4.37 (a) A sample of Magnitude response for 5 scales at orientation 0°
 (b) A Sample of Real GWSMH-based filter with five scales and eight orientations

Figure illustrates the whole process performed with the feature extraction method that has been proposed in this section. A sample image of each database group with a parameter scale of 15×15 ($\lambda_5 = 7.9, \sigma_5 = 6.3$) at orientation 0° has been shown to differentiate the output of the new magnitude response which will lead to the production of the new feature vectors. Image convolution process is applied to achieve the goal of generating features based on the filter used.

Table 4.22 Three conditions of thermal motor bearing images before and after convolution of GWSMH-based filter with scale 15×15 at orientation 0°

Thermal bearing image Conditions	Convolution (Input Image * GWSMH)	Magnitude response
Normal	 *	



Next, the overall graph for the new results from both feature vectors (new Local Energy and new Mean Amplitude) is shown as in the [figure and figure](#). These graphs represent the modifies in the value of new pixels (intensities) that have been generated based on the magnitude response obtained for each group from thermal motor bearing images.

There are 40 GWSMH channel filters that have been deployed at each image point for each group of thermal images. The purpose is to extract the corresponding of new feature values according to the respective image groups. Then, the features extracted from these normal, warning and abnormal groups are arranged according to the same scale parameters. it is intended to see the differences group generated according to their respective orientation as shown in both figures. Herein, there are 40 multi-scales and multi-orientations of GWSMH-based feature images that have been generated. It corresponds to the differences in the multi-scale and multi-orientation parameters deployed in this work in which the production of different features will be obtained.

From a visual point of view, it can be seen from the graph that the feature vector output from both new Local Energy and new Mean Amplitude have some significant variations features to differentiate the group of thermal motor bearing images. Nevertheless, the feature selection process will be executed to define the optimal features to distinguish the group from these thermal bearing images. It will be discussed in details in section 4.4.1. Only the most relevant features will be used for the next processing, while the irrelevant features will be discarded.

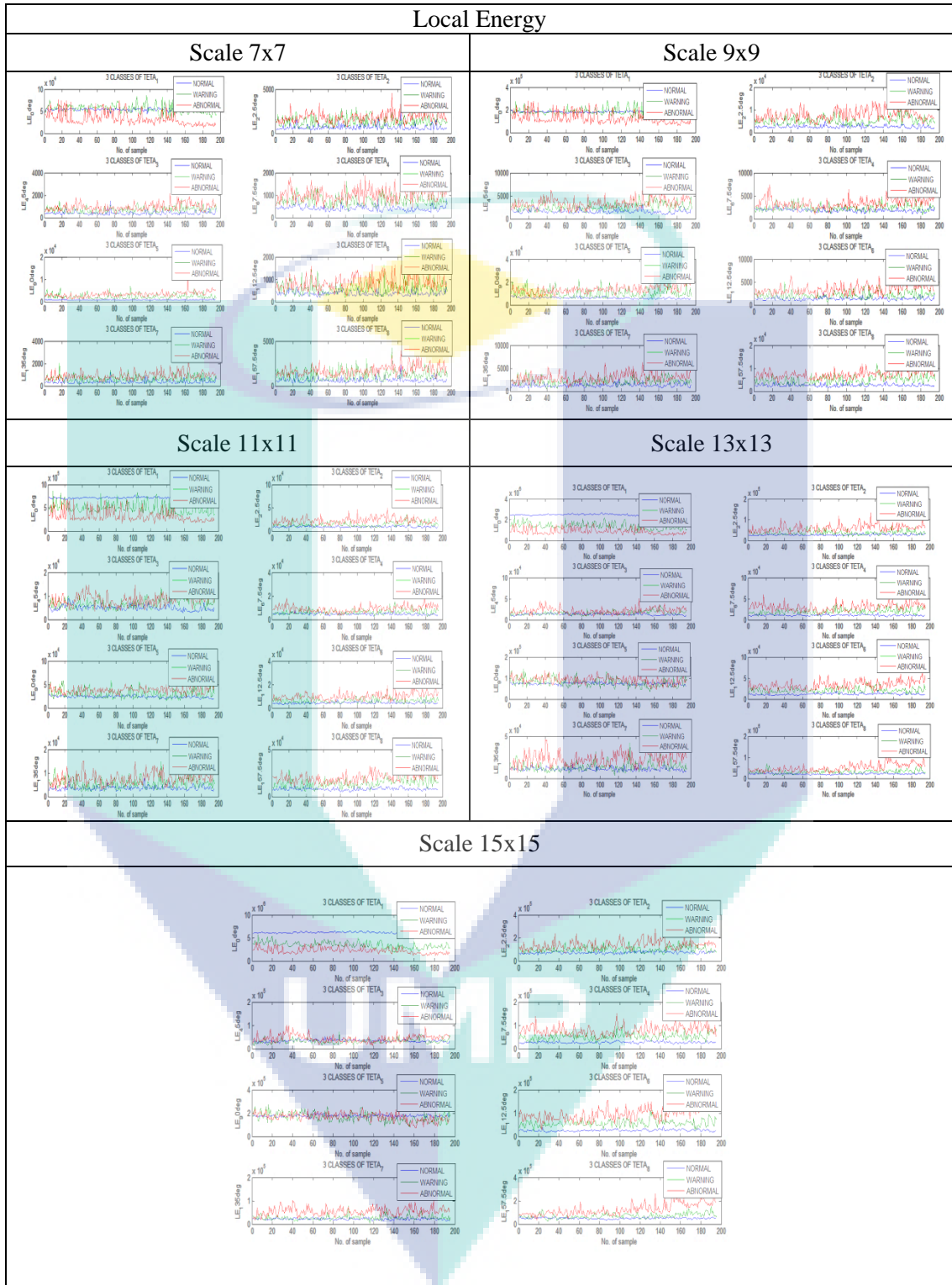


Figure 4.39 Overall new Local Energy features for multi-scales and multi-orientations in GWSMH based feature extraction method

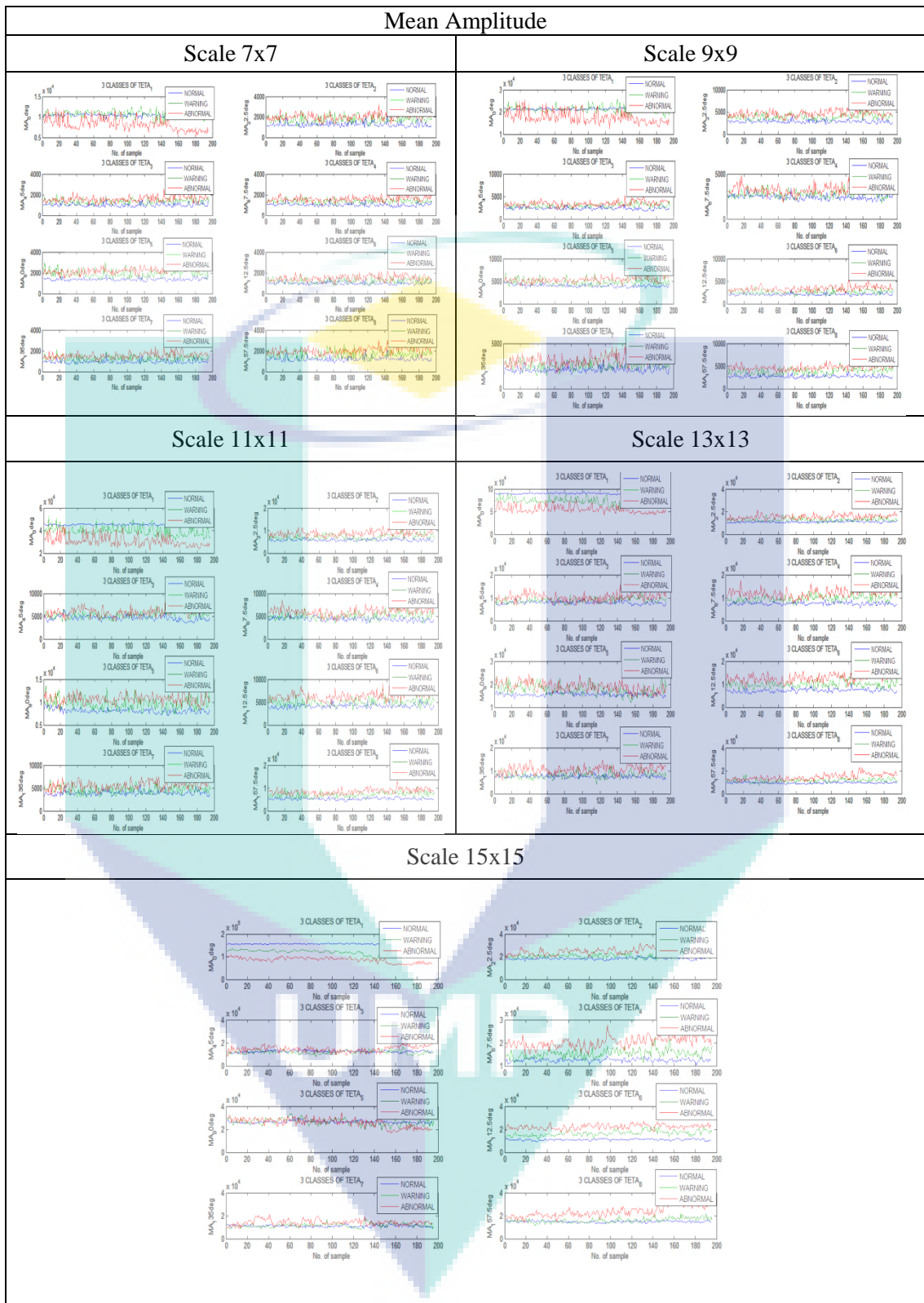


Figure 4.40 Overall new Mean Amplitude features for multiple scales and multiple orientations in GWSMH based feature extraction method

4.5.1.1 Feature Selection

In this section, a new optimum selection of scales and orientations for feature extraction methods based on GWSMH using the proposed fisher score method is explained. As in section 4.4.1, fisher score-based feature selection was employed in this work to select new optimal features of high-dimensional vector output features from the GWSMH-based feature extraction process as in section 4.5.1.

According to the feature extraction results as in section 4.5.1, a new 40 multi-scale and multi-orientation feature images have been generated at each image point. Thus, the new total input data matrix generated for image data set training in different orientations and scales is $Y \in R_{(new)}^{(n \times 5) \times j} \in LE_{(new)}^{10375 \times 8}, MA_{(new)}^{10375 \times 8}$, where ‘ n ’ is the number of samples which have 2075 images and ‘ j ’ is the number of orientations. After calculating each score for new local energy and new mean amplitude features according to the fishery criterion as in equation 3.32, their score was generated as in [table and table](#).

Based on the results of the new local energy generated in the [table](#), the scores of combination orientations and scales are arranged from the highest value starting with F15 = 1824.66, followed by F13=1137.42, F11=558.74, F9=513.64 and F7= 355.38. Therefore, the highest score value produced is at F15 = 1824.66, which is on a scale 15x15 ($\sigma = 6.3, \lambda = 7.9$) and orientation $\theta_1=0^\circ$. From this result, it can be seen that the new score obtained from this section shows lower reading compared to the new score from feature extraction based on EGF in section 4.4.1. Nonetheless, the new scores in this section have also shown higher value than the scores from the original GWT-based extraction method as in section 4.3.1. This has proven that new scores from this section have lower discriminatory power than EGF-based scores as well as higher discriminative power than GWT-based original scores

Table 4.23 Fisher scoring for each Enhanced Gabor filter’s scale for Local Energy

Filter Size (Scales)	θ_1	θ_2	θ_3	θ_4	θ_5	θ_6	θ_7	θ_8
7x7	188.38	216.21	244.04	271.88	299.71	327.54	355.38	227.32
9x9	86.50	363.45	280.24	236.51	482.09	406.65	284.88	513.64
11x11	309.24	407.99	238.92	300.60	466.73	558.74	303.81	486.20

13x13	1137.42	589.70	208.01	558.23	138.62	758.95	338.87	421.25
15x15	1824.66	564.05	124.14	722.03	1.04	862.91	511.05	425.64

Meanwhile, in the table, the sequence of decreasing fisher score values for new mean amplitude features starts with F15=1380.14, followed by F13=1110.96, F11=747.10, F9=649.78 and F7=495.20. From this result, the highest fisher's score can be read on a scale 15x15 and orientations $\theta_1=0^\circ$ and the value is F15=1380.14. It can be seen from this result that the mean amplitude score has a lower discriminatory power compared to the EGF-based extraction score as in section 4.4.1 as well as a higher discriminatory power compared to the original GWT-based score

Table 4.24 Fisher scoring for each Enhanced Gabor filter's scale for Mean Amplitude

Filter Size (Scales)	θ_1	θ_2	θ_3	θ_4	θ_5	θ_6	θ_7	θ_8
7x7	199.72	276.04	257.97	396.37	495.20	333.37	314.12	343.08
9x9	135.82	402.38	328.85	266.09	510.41	542.72	352.82	649.78
11x11	459.32	468.73	286.39	370.51	533.78	747.10	373.77	648.91
13x13	1063.77	782.38	295.87	766.60	255.28	1110.96	411.66	641.14
15x15	1380.14	762.58	190.26	1015.49	36.08	1266.71	641.56	671.09

Figure and figure demonstrates the distribution of fisher's scores obtained for the scale and orientation variations in the tables and tables according to their respective features. As in figure, it is clear from the local energy graph that SCALE 15 (θ_1) gives the highest fisher score among the others. Meanwhile, for the mean amplitude graph as shown in figure, it is observed that among others, SCALE 15 (θ_1) has given the highest score.

Distribution of fisher score selection values for all scales (Local Energy)

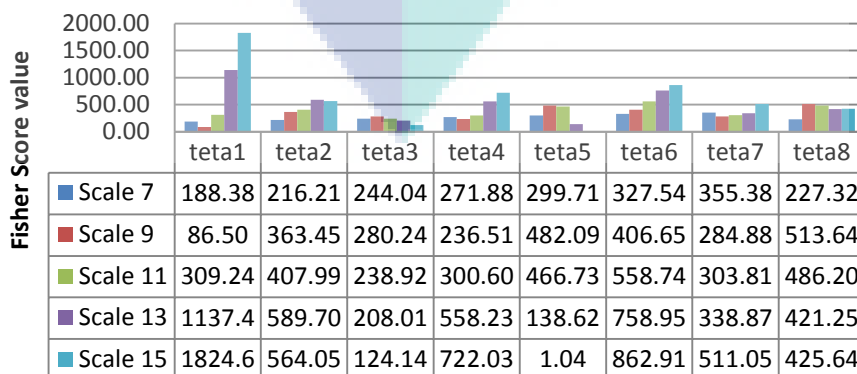


Figure 4.38 Variation of Fisher score value for local energy between normal, warning and abnormal thermal motor bearing images

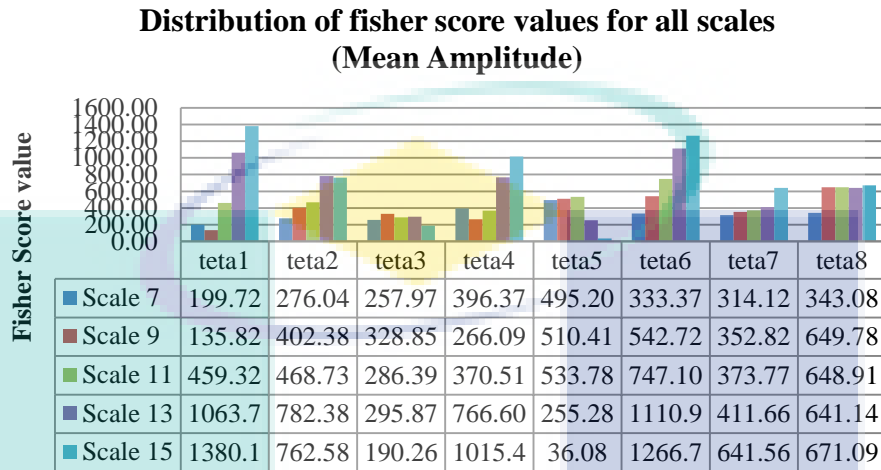


Figure 4.39 Variation of Fisher score value for Mean Amplitude between normal, warning and abnormal thermal motor bearing images

Figure and figure displays the overall group of thermal motor bearing image of local energy features and mean amplitude features for all eight orientations before any score is obtained. Those diagrams shown are in the SCALE 15x15 only as this scale includes the highest score. The various variations of the graph in the different orientations can be seen from those figures. Consequently, the fisher score or the discriminative power obtained will also vary according to the features produced by each orientation.

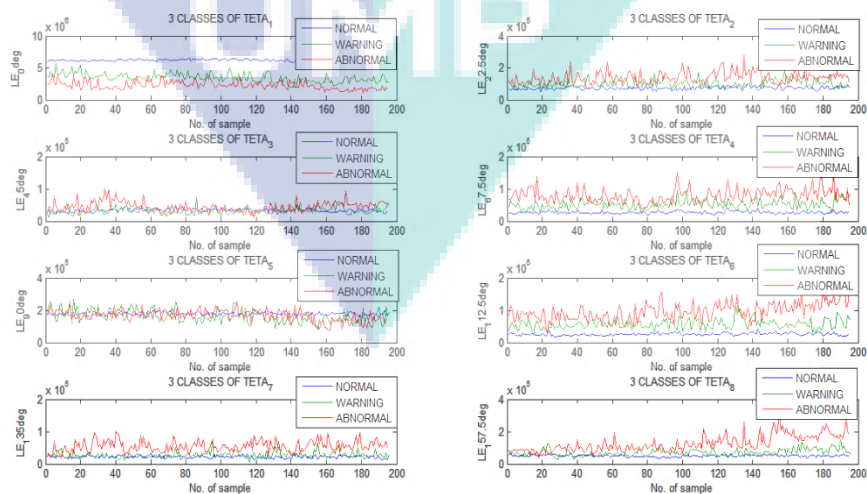


Figure 4.40 Variation Local Energy feature of condition thermal motor bearing images with 8 orientations for SCALE 15x15

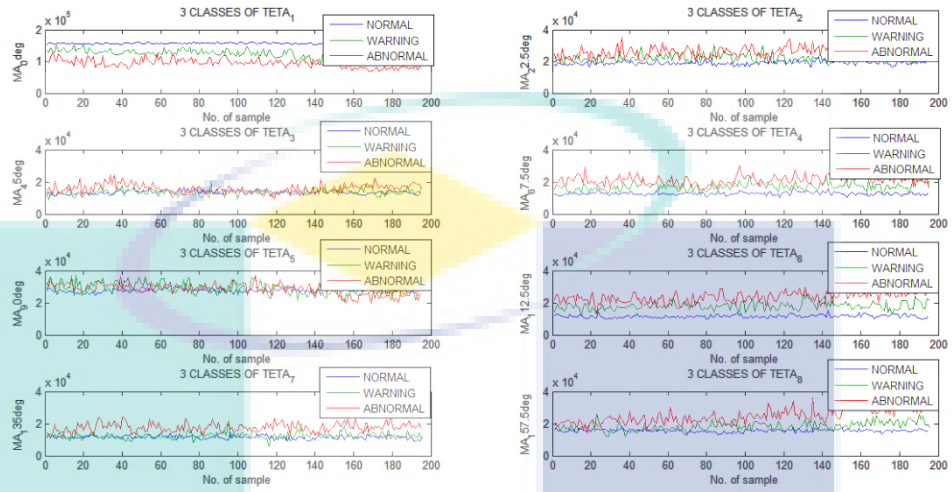


Figure 4.41 Variation Mean Amplitude feature of condition thermal motor bearing images with 8 orientations for SCALE 15x15

From the calculation of the fishery criteria, the highest reading was shown by the orientation $\theta_1 = 0^\circ$ representing for local energy features and the orientation $\theta_1=0^\circ$ representing for mean amplitude features. Their illustrations are shown individually as in the figure and figure. At this point, the dimensions for each of these matrix features have been reduced to $Y \in LE_{(new)}^{2075 \times 1}$, $MA_{(new)}^{2075 \times 1}$. From both graphs shown, it can be observed that the three groups for thermal motor bearing image state are not in the desired result. Graph for normal group presents good results because it does not overlap with other categories. Whereas graph for warning group and abnormal group indicate overlapping results. Therefore, from the visual view through graph results, it is evident that the enhancement features of thermal motor bearing image by using GWSMH-based feature extraction method cannot be well classified as the features of the group warning and abnormal group cannot be clearly distinguished. Nonetheless, the final selected features will be processed in the classification model in term of quantitative result in order to obtain the classification performance in this work.

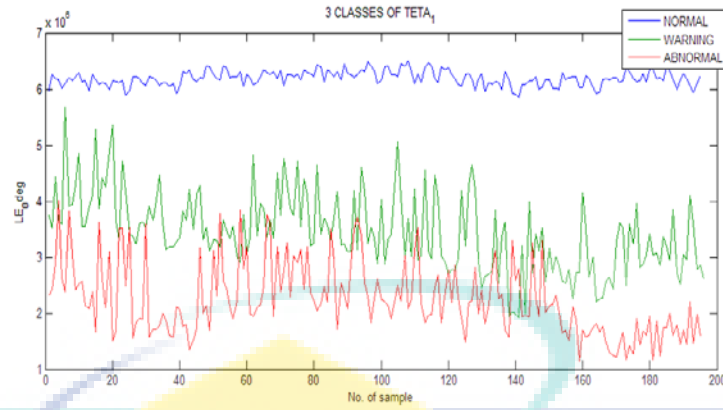


Figure 4.42 The optimal selection Local Energy feature for GWSMH is at SCALE 15x15 (orientation 0°)

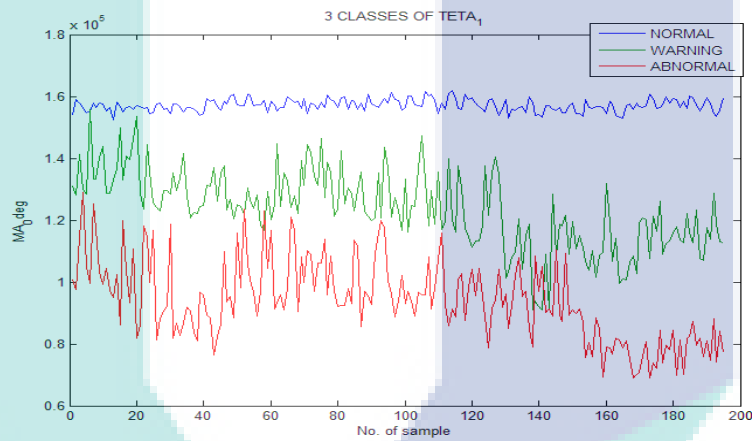


Figure 4.43 The optimal selection Mean Amplitude feature for GWSMH is at SCALE 15x15 (orientation 0°)

a. Evaluation Performance features by using ANOVA method

Same in section 4.3.1.1 and 4.4.1.1, this section presents the results of the performance evaluation on the features of new Local Energy and new Mean Amplitude obtained by using ANOVA technique. **Table and table** shows the descriptive statistics value generated by new Local Energy and new Mean Amplitude features. The purpose of the ANOVA method was implemented in this work to evaluate the new Local Energy and new Mean Amplitude features from thermal motor bearing images group whether there are significantly different or not. A 95% Confidence Interval for Mean has been implemented in this work which is basically a range of values for looking at parameters such as mean or proportion. Thus, $mean \pm 2SE$ is applied. From this formula, lower band and upper band values for the true mean for each normal

population group, warning and abnormal were obtained. These values indicates that they have a 95% chance of being within the range of the mean as shown in the **table and the table**. From these tables, the 95% Confidence Interval for the mean values for the normal, warning and abnormal groups shows the balanced change values between the population groups. This has shown that the results obtained from this proposed section are also as good as in section 4.4.1.1, even better than the original results in section 4.3.1.1. Nevertheless, the P-value in the next process is calculated to determine the results from all groups are actually significantly different.

Table 4.25 Descriptive statistics value for new Local Energy feature

Thermal Image groups	N	Mean	Std Deviation	Std Error	95% Confidence Interval for Mean	
					Lower Bound	Upper Bound
Normal	1621	5375046.17	601825.854	14947.871	5345726.97	5404365.36
Warning	259	3299974.95	727811.372	45223.998	3210919.79	3389030.11
Abnormal	195	2246129.09	646321.599	46284.051	2154844.56	2337413.62
Total	2075	4821994.47	1240993.536	27243.347	4768567.31	4875421.63

Table 4.26 Descriptive statistics value for new Mean Amplitude feature

Thermal Image groups	N	Mean	Std Deviation	Std Error	95% Confidence Interval for Mean	
					Lower Bound	Upper Bound
Normal	1621	147128.45	8592.418	213.414	146709.85	147547.05
Warning	259	119729.86	13734.992	853.451	118049.24	121410.47
Abnormal	195	93996.56	13070.762	936.017	92150.48	95842.63
Total	2075	138715.46	19633.404	431.009	137870.20	139560.72

Next, table and table presents the ANOVA readings generated using SPSS statistical software to obtain the value of F and the value of P. From these tables, the value of between group variability produces higher values than within group variability values. This will generate a high F-ratio value where the F-ratio value for new Local Energy feature is 3077.421 and the F-ratio value for new Mean Amplitude feature indicates 3076.046. These values are derived from the ratio of the mean squares (MS). Subsequently, these obtained F-ratio value then is used to define the level of significance for the samples by comparing them with the F-critical value. From the table of probability values for the F distribution with (2,2072) degree of freedom (df) in

APPENDIX, a critical F value is found. The F-critical value for the new local energy and new mean amplitude features is $F_{2,2072,0.05} = 3.0$. Therefore, from the tables, it can be observed that the F-ratio is greater than the appropriate critical F distribution at $\alpha = 0.05$ (F-ratio > F-critical), thus the null hypothesis is rejected, and accept the alternative hypothesis. This means the variance between the means of population group are significantly different.

The value of P is the probability of obtaining results from all groups are differ significantly. Hence, from the statistical calculation using function 'fdist', P-value is obtained. From table, the P-value for the new local energy feature is 0.000325. Meanwhile, from table, the P-value obtained from the new mean amplitude feature is 0.000325. This explains that both of P-Value from the tables has given a higher readings compared to the P-values in section 4.4.1.1. Its also shows a better reading compared to the original P-value in section 4.3.1.1. This indicates that the results of P-value in the previous section 4.4.1.1 has given a better reading compared to this section.

Nonetheless, based on the P-value obtained from the tables, it can be interpreted that the features of new Local Energy and new Mean Amplitude from all group of thermal motor bearing images are still shows significantly different at $P < 0.05$.

Table 4.27 ANOVA for Local Energy features

Source of variations	Sum of Squares	df	Mean Square	F	P-value
Between Groups	2389634901809379.500	2	1194817450904689.800	3077.421	0.000325
Within Groups	804459816159081.800	2072	388252807026.584		
Total	3194094717968461.000	2074			

Table 4.7 ANOVA for Mean Amplitude features

Source of variations	Sum of Squares	df	Mean Square	F	P-value
Between Groups	598046275102.431	2	299023137551.215	3076.046	0.000325
Within Groups	201419615815.038	2072	97210239.293		
Total	799465890917.469	2074			

4.5.1.2 Classification

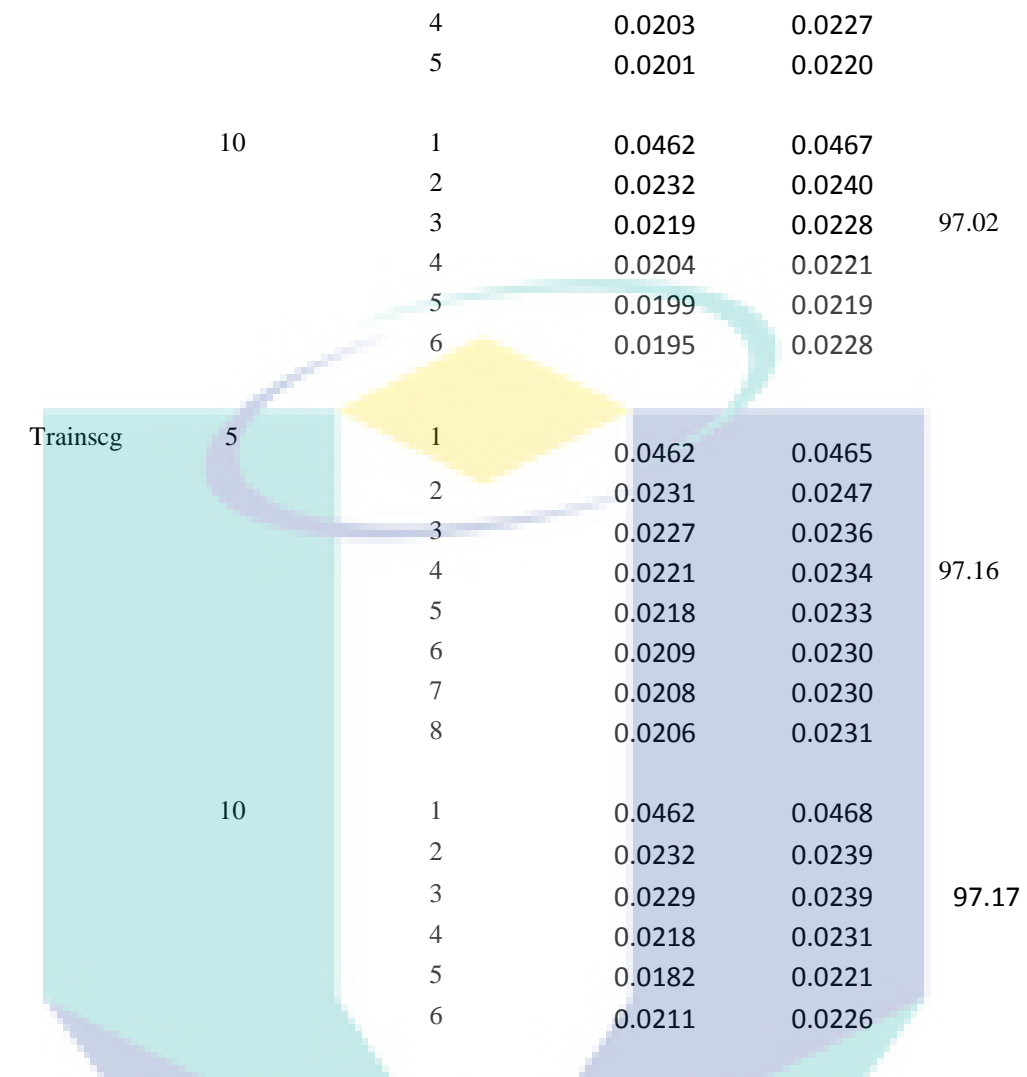
There are two types of classifier used in this work, namely MLANNs and Linear Thresholding. Section a and section b will discuss their performance results in more details.

a. MLANNs

In this section, the parameters and procedures of the MLANNs model applied to this work are same as those described in the previous sections in section 4.4.2.1 and section 4.3.2.1. The purpose is to obtain the best MLANNs model in order to identify and distinguish the condition of thermal motor bearing images used in this study. The best measure for MLANNs model can be observed through classification statistical performance metrics obtained by looking at the highest accuracy value and the lowest MSE value. In order to achieve these outputs, the selected features namely local energy and mean amplitude as in section 4.5.1.1 were used. All these results have been presented in the table.

Table 4.28 Training and validation performance results using TRAINLM, TRAINBR, TRAINSCG using 5- fold and 10-fold cross-validations in MLANNs model for Local Energy and Mean Amplitude feature

Training Function	K-Fold	HN	MSE		Accuracy (%)
			Training	Validation	
Trainbr	5	1	0.0462	0.0465	97.08
		2	0.0235	0.0239	
		3	0.0228	0.0224	
		4	0.0211	0.0233	
		5	0.0208	0.0226	
	10	1	0.0462	0.0470	97.23
		2	0.0232	0.0239	
		3	0.0216	0.0227	
		4	0.0209	0.0225	
		5	0.0204	0.0217	
Trainlm	5	1	0.0461	0.0471	97.17
		2	0.0231	0.0240	
		3	0.0215	0.0219	



In this section, due to the mean value of MSE validation from training has not reached the minimum value until hidden neuron = 5, processing of data on hidden neuron are then continued. Upon completion of data processing, the highest value of hidden neurons used in this work is 8. Next, the best fold selection for each training algorithm is performed. Figure shows graph validation performance for TRAINLM algorithm based on Kfold-5 and Kfold-10. From this result, it is observed that, the optimum mean MSE validation value can be read in Kfold-5 at hidden neuron 3 where the lowest value is 0.0219.

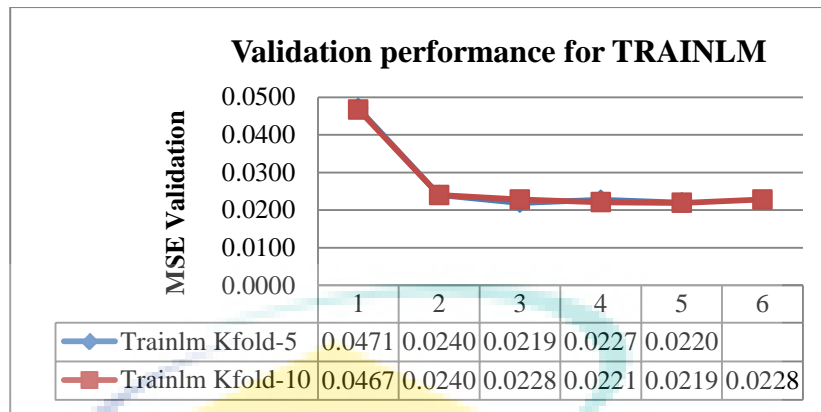


Figure 4.44 Validation performance for TRAINLM based on Kfold-5 and Kfold-10

Meanwhile, figure denotes a learning curves graph for the TRAINBR training algorithm. From the graph, it can be seen that readings in the hidden neuron 5 at kfold-10 gave the optimum mean MSE readings compared to all values of kfold-5. Its MSE lowest reading value is 0.0217.

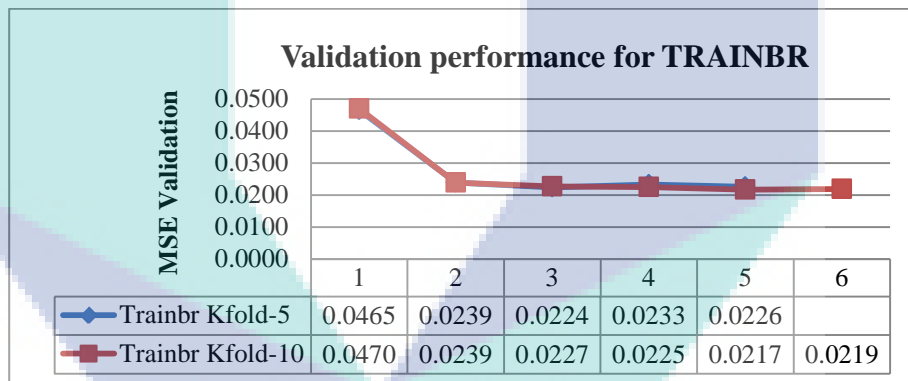


Figure 4.45 Validation performance for TRAINBR based on Kfold-5 and Kfold-10

Next, the third training algorithm is TRAINSCG. The optimum mean MSE reading of the training algorithm can be observed in the hidden neuron 5 on kfold-10. Its mean MSE value is 0.0221.

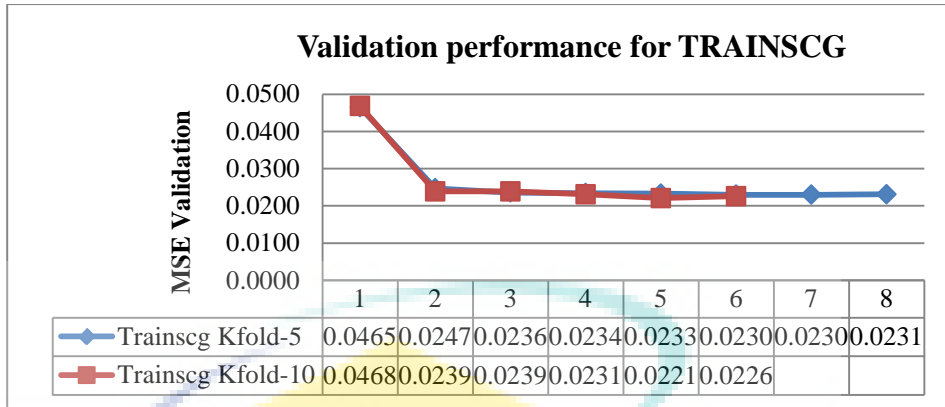


Figure 4.46 Validation performance for TRAINSCG based on Kfold-5 and Kfold-10

From all of the learning curve graphs shown above, the differences in mean MSE values between Kfold-5 and Kfold-10 did not differ significantly for each training algorithm. However, the differences error in the mean MSE value between both folds remains. Furthermore, the optimum mean MSE values for each training algorithm were extracted and combined in one graph as in the figure. This graph is intended to determine the best validation performance among all training algorithms. Hereby, as can be seen from the graph, TRAINBR gave the optimum mean MSE readings compared to TRAINLM and TRAINSCG for MLANNs models in this section. The minimum mean MSE value readings shown were 0.0217 at k-fold = 10, hidden neurons = 5 and the average accuracy validation = 97.23% as observed in the table. Furthermore, once the mean error validation has been achieved to the minimum, the net will generalize to unknown samples through testing process.

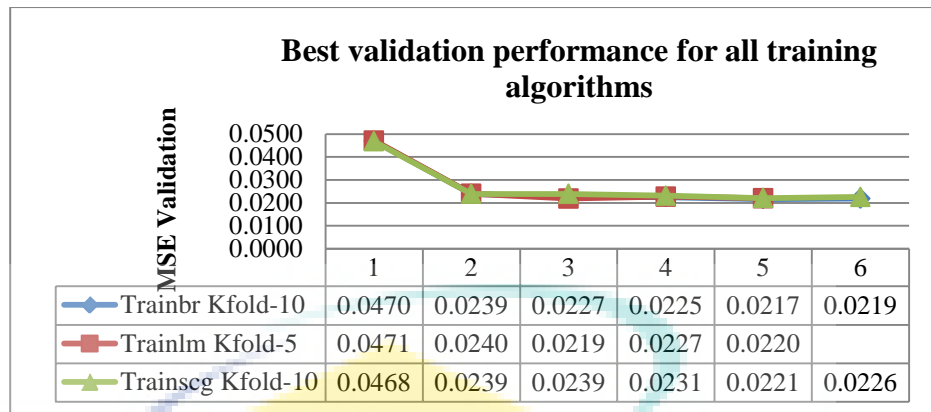


Figure 4.47 Best validation performances among all training algorithm types

Table shows the readings obtained from MATLAB software for best validation performance based on TRAINBR training algorithm in this section. Since K-fold = 10 is produced as the optimum mean cross validation error, so that the mean value for MSE validation and mean of accuracy validation value are measured 10 times according to the equation 3.33 as stated in section 3.7.1.1. From the table, it is seen that the best validation performance has been performed at various iterations at various times to determine how many times the learning algorithm works through the entire training data set. Herein, it is noted that the performance produced by the MLANN model in this section is not as fast as the MLANN model in section 4.4.2.1.

Table 4.29 Best validation performance for TRAINBR in MLANNs model for Local Energy and Mean Amplitude features

K-fold	Best Epoch	Time (sec)	MSE Validation	Acc Validation (%)
1	355	15	0.0147	98.28
2	207	9	0.0264	95.92
3	159	8	0.0155	98.00
4	83	2	0.0289	96.22
5	127	5	0.0298	96.24
6	237	10	0.0191	97.69
7	97	3	0.0134	98.56
8	1000	42	0.0272	96.82
9	118	4	0.0215	97.41
10	150	6	0.0206	97.12
		Mean:	0.0217	97.23

Subsequently, the overall results for training classification statistical performance metrics generated by TRAINBR algorithm for MA and LE features in this section are presented in table 4.7. Precision values = 90.24%, sensitivity = 90.26, specificity =

97.39, CER = 0.0278 and accuracy = 97.23%. All of these values are calculated based on the multi-class classification problem through TP, FP, TN and FN according to the confusion matrix acquired during training data processing.

Table 4.30 Validation performance results using TRAINBR in MLANNs model for Local Energy and Mean Amplitude features

Training Function	HN	Pre (%)	Sens (TPR) (%)	Spec (TNR) (%)	CER	ACC (%)
TRAINBR (K-fold=10)	5	90.24	90.26	97.39	0.0278	97.23

Just like the previous section, 10% of dataset was employed in MLANNs model testing for validation purposes. Thus, table indicates five classification statistical performance metrics obtained by using TRAINBR algorithm for classifying the conditions of thermal motor bearing images. The accuracy of neural networks for classifying all thermal bearing images conditions was 98.71% (254 correctly classified of 259), the specificity =99.26%, precision=95.83% and Classification Error Rate=0.0127. Meanwhile, the testing values of the classification performances metrics for each state of thermal bearing images are denoted in the table. The results of these values have been calculated on multi-class classification problem based on TP (True Positive), FP (False Positive), TN (True Negative) and FN (False Negative) according to the acquired TRAINBR confusion matrix.

Table 4.31 Testing performance results using TRAINBR in MLANNs model for Local Energy and Mean Amplitude features

Training Function	HN	Class	TP	TN	FP	FN	Pre (%)	Se (%)	Sp (%)	CER	ACC (%)
TRAINBR (K-fold=10)	5	N	180	77	0	2	1.0000	0.9890	1.0000	0.0077	0.9923
		W	35	219	5	0	0.8750	1.0000	0.9777	0.0193	0.9807
		A	39	217	0	3	1.0000	0.9286	1.0000	0.0112	0.9884
		All					0.9583	0.9725	0.9926	0.0127	0.9871

Furthermore, the overall differences in the results performance of the MLANNs classification models for the testing phase and training phase in this section are graphically illustrated as in figure for easier observation.

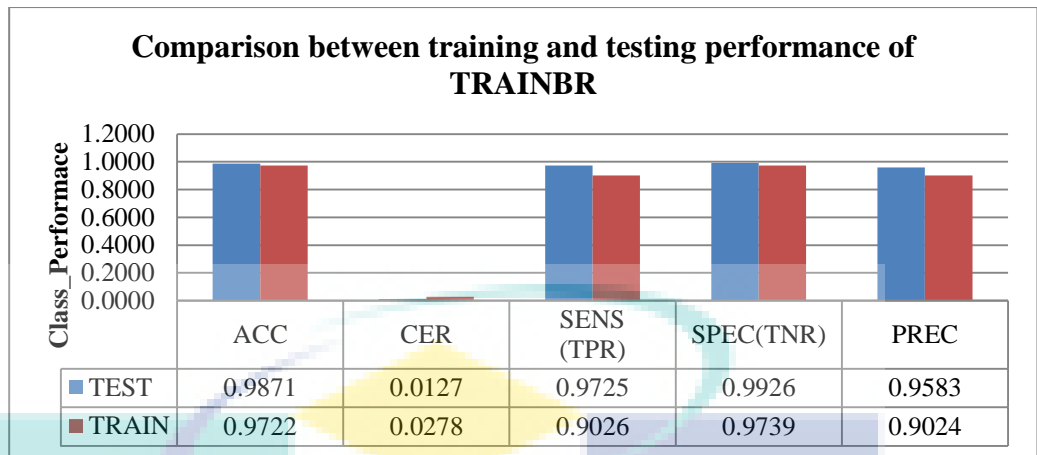


Figure 4.48 Comparison bar graph between training and testing performance using GWSMH based feature extraction algorithm

b. Linear Thresholding

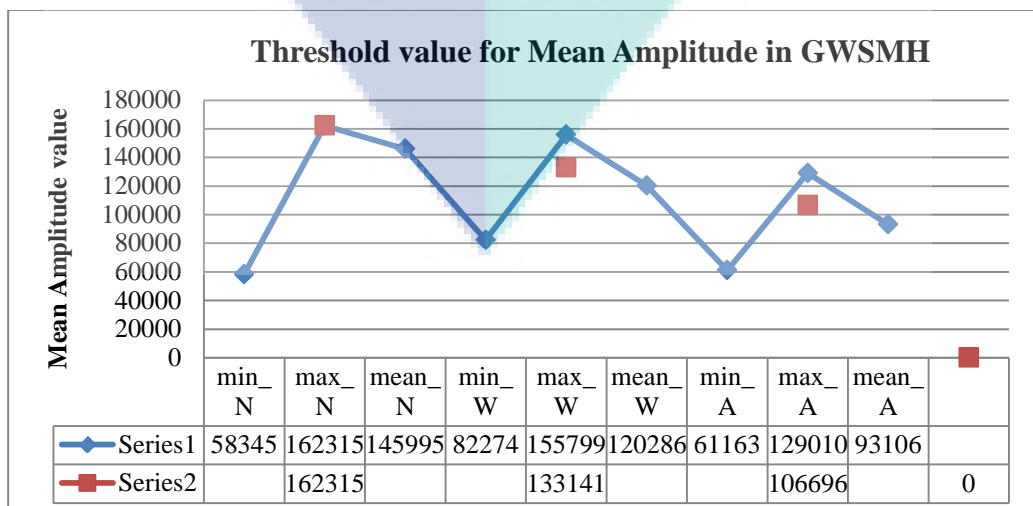
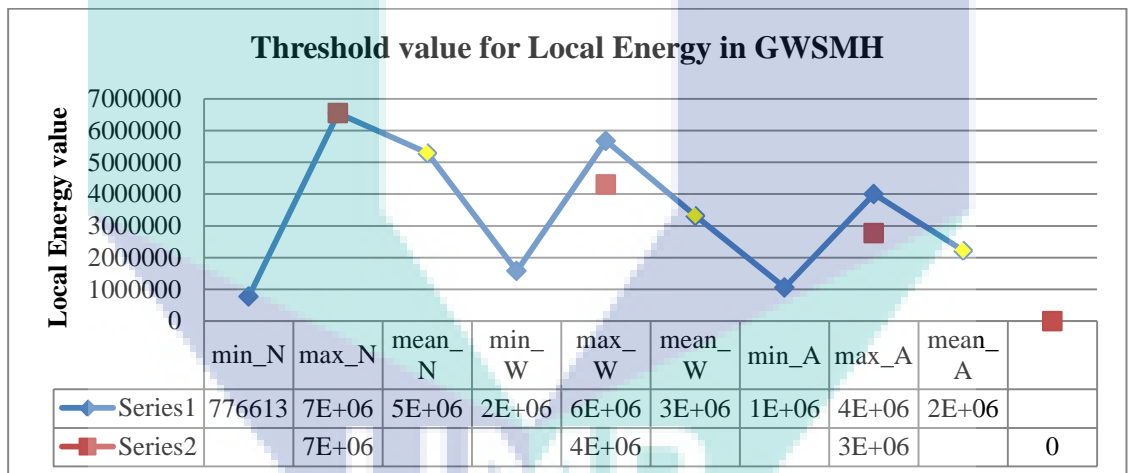


Table 4.32 Classification performances using Linear Thresholding model for GWSMH based feature extraction's features

Features	Condition of thermal bearing images	ACC TRAINING		ACC TESTING	
		Training (%)	No. of Classified image	Testing (%)	No. of Classified image
Local Energy	Normal	95.6135	1722	100.0000	180
	Warning	70.5686	211	72.5000	29
	Abnormal	80.3419	188	16.2393	38
	Average All	82.1747	2121	62.9131	247
Mean Amplitude	Normal	94.6696	1705	100.0000	180
	Warning	69.2308	207	80.0000	32
	Abnormal	84.6154	198	97.4359	38
	Average All	82.8386	2110	92.4786	250
			Average All:	77.6959	

4.5.2 Propose an Enhanced GWCLAHE-based Feature Extraction Method

As in section 4.4 and section 4.5.1, this section also discusses the results of the proposed new feature extraction method that has been developed to improve the quality features based on the GWT-based feature extraction method as discussed in section 4.3. The problem that occurred in section 4.3 has contributed to the proposed development on the new feature enhancements method in this section.

In this present study, a combination of an independent image enhancement approach called Contrast Limited Adaptive Histogram Equalization (CLAHE) method with the original GWT-based feature extraction technique has been developed. Combinations of these methods have been executed to modify the contrast and the distribution of the gray levels of pixels in the images. As a consequence, by modifying the pixel value (intensities) of the image, the problems that have occurred in the section 4.3 could be overcome. When the quality of the thermal images is improved, the classification performance could also be improved accurately. Hence, the features of thermal motor bearing images could also be distinguished well in this study. This proposed method is called Enhanced GWCLAHE-based feature extraction.

Thermal image processing has begun with converting the segmented input RGB thermal images as in figure in section 4.2.2 into grayscale intensity image, $I(x, y)$.

Next, the new feature extraction process is performed by enhancing the features of thermal images by utilizing the proposed method which is Enhanced GWCLAHE-based feature extraction. From this proposed technique, the quality image features and classification performances in this work can be improved. This 2D-Enhanced GWCLAHE extraction process has started by **adjusting the contrast** of the thermal input image first by using an independent image enhancement approach called CLAHE. **Through this adjustment, the intensities can be better distributed on the histogram, $I_{Equalized_Image}(x, y)$. The results can be illustrated in the figure.**

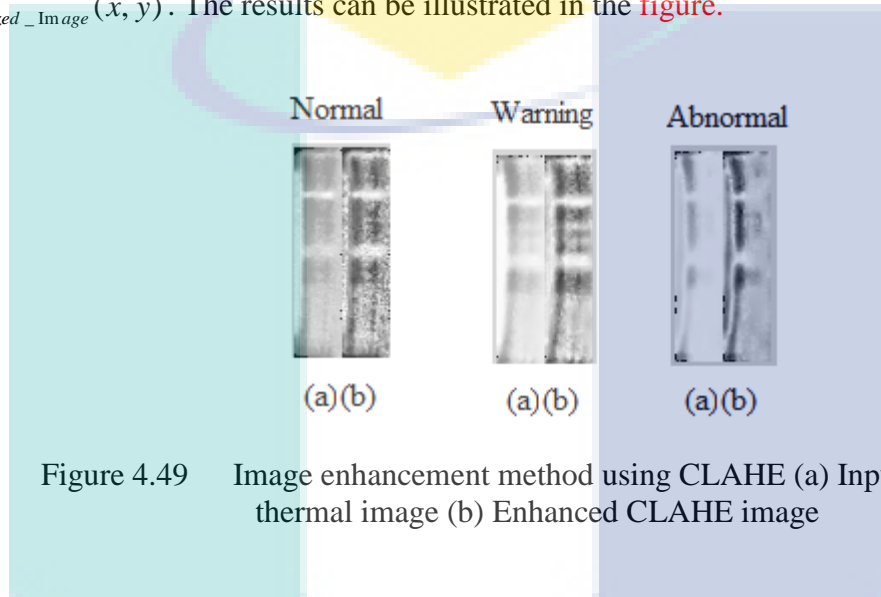


Figure 4.49 Image enhancement method using CLAHE (a) Input grayscale thermal image (b) Enhanced CLAHE image

Afterwards, the process of extracting features continues with transferring the enhanced image, $I_{Equalized_Image}(x, y)$ into the 2D-Gabor Wavelet Transform, $g(x, y)$. It means that, the Fourier Transform of the enhanced image is computed first by applying 5 different frequencies and 8 orientations as specified in the table in section 3.5.2 in order to extract out all those new patterns, $g_{new}(x, y)$. This 2D GWCLAHE-based feature extraction will then provide the coefficient results on the specific frequency content in a specific direction in the image in a localized region according to the predetermined parameter values on the images. All of these generated coefficient results also represents an orthogonal direction that has a real component (cosine) and a new imaginary (sinus) in the spatial domain. As a consequence, a new feature modification of the pixel value (intensity) on the image has been produced in this section.

Figure(b) illustrates the new real (cosine) component of the entire GWCLAHE filter in spatial domain with different 5 frequencies and 8 orientations. The row corresponds to different scales containing bandwidth ($\sigma_1 = 2.8$, $\sigma_2 = 3.6$, $\sigma_3 = 4.5$, $\sigma_4 = 5.4$,

$\sigma_5 = 6.3$) and wavelength ($\lambda_1 = 3.5, \lambda_2 = 4.6, \lambda_3 = 5.6, \lambda_4 = 6.8, \lambda_5 = 7.9$), while the column corresponds to different orientation ($0^\circ, 22.5^\circ, 45^\circ, 67.5^\circ, 90^\circ, 112.5^\circ, 135^\circ$ and 157.5°). By varying these parameter values (θ, σ, λ) for the new GWCLAHE function, the filter pattern will also change. Hereby, 40 filters GWCLAHE channel at each image point i.e. 40 new multi-scales and new multi-orientations features images have been generated. Thus, the overall total number of new GWCLAHE features that have been produced in this present study is as much as **2075x40 equal to 83,000** including for normal, warning and abnormal groups.

Subsequently, the process of convolving the two-dimensional GWCLAHE filter, $g_{new}(x, y)$ with the input image, $I(x, y)$ has been acquired in order to detect the new GWCLAHE filter response from the input image itself. The convolution result were decomposed to the new magnitude response image as denoted in **figure(a)** based on the complex of GWCLAHE real component and GWCLAHE imaginary component images. As in the section 4.3, section 4.4, and section 4.5, for the phase response image, it was not taken into account in this study. This is due to the Gabor phase response are considered unstable and are usually discarded. From the figure, it can be seen, the oriented magnitude response matrices of image have been extracted and contain the component of the corresponding new feature vector. At this point, when the input thermal bearing images passed through each orientation on the GWCLAHE -based filter, the output of the resulting oriented extract features is according to the orientation of the filter at that time.

Thus, a new feature vector containing the new pixel value (intensities) of the output image based on the original Local Energy and Mean Amplitude in the section 4.3 has been generated in this work, $Y \in R^{nxj} \in MA_{(new)}^{83000} \in LE_{(new)}^{83000}$. Where the new Local Energy feature has obtained by equal to summing up the squared value of each matrix value from a new response matrix. Meanwhile, for the new Mean Amplitude feature has acquired by equal to sum of absolute values of each matrix value from a new response matrix.

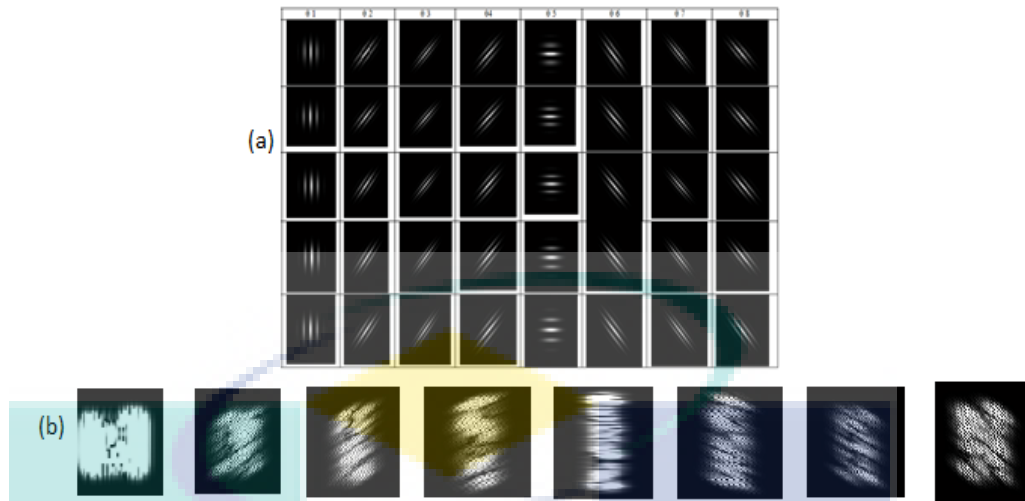
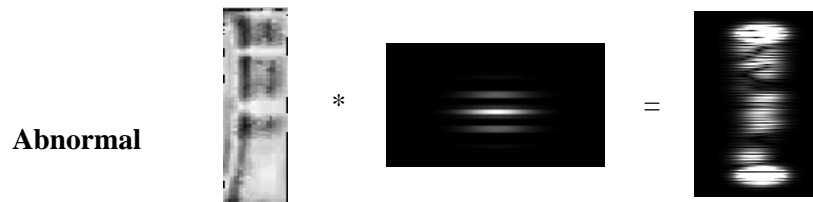


Figure 4.50 (a) A Sample of Real GWCLAHE-based filter with five scales and eight orientations (b) A sample of Magnitude response for 5 scales at orientation 0°

Table illustrates the whole process performed with the feature extraction method that has been proposed in this section. A sample image of each database group with a parameter scale of 9×9 ($\sigma_2 = 3.6$, $\lambda_2 = 4.6$) at orientation 90° has been shown to differentiate the output of the new magnitude response which will lead to the production of the new feature vectors. Image convolution process is applied to achieve the goal of generating features based on the filter used.

Table 4.33 Three conditions of thermal motor bearing images before and after convolution of Gabor filter with scale 9×9 at orientation 90°

Thermal bearing image Conditions	Convolution (Input Image * GWCLAHE)	Magnitude response
Normal		
Warning		



Next, the overall graph for the new results from both feature vectors (new Local Energy and new Mean Amplitude) is shown as in the figure and figure. These graphs represent the modifies in the value of new pixels (intensities) that have been generated based on the magnitude response obtained for each group from thermal motor bearing images.

There are 40 GWCLAHE channel filters that have been deployed at each image point for each group of thermal images. The purpose is to extract the corresponding of new feature values according to the respective image groups. Then, the features extracted from these normal, warning and abnormal groups are arranged according to the same scale parameters. it is intended to see the differences group generated according to their respective orientation as shown in both figures. Herein, there are 40 multi-scales and multi-orientations of GWCLAHE-based feature images that have been generated. It corresponds to the differences in the multi-scale and multi-orientation parameters deployed in this work in which the production of different features will be obtained.

From a visual point of view, it can be seen from the graph that the feature vector output from both Local Energy and Mean Amplitude have some insignificant variations features to differentiate the group of thermal motor bearing images. Nevertheless, the feature selection process will be executed to define the optimal features to distinguish the group from these thermal bearing images. It will be discussed in details in section 4.5.2.1. Only the most relevant features will be used for the next processing, while the irrelevant features will be discarded

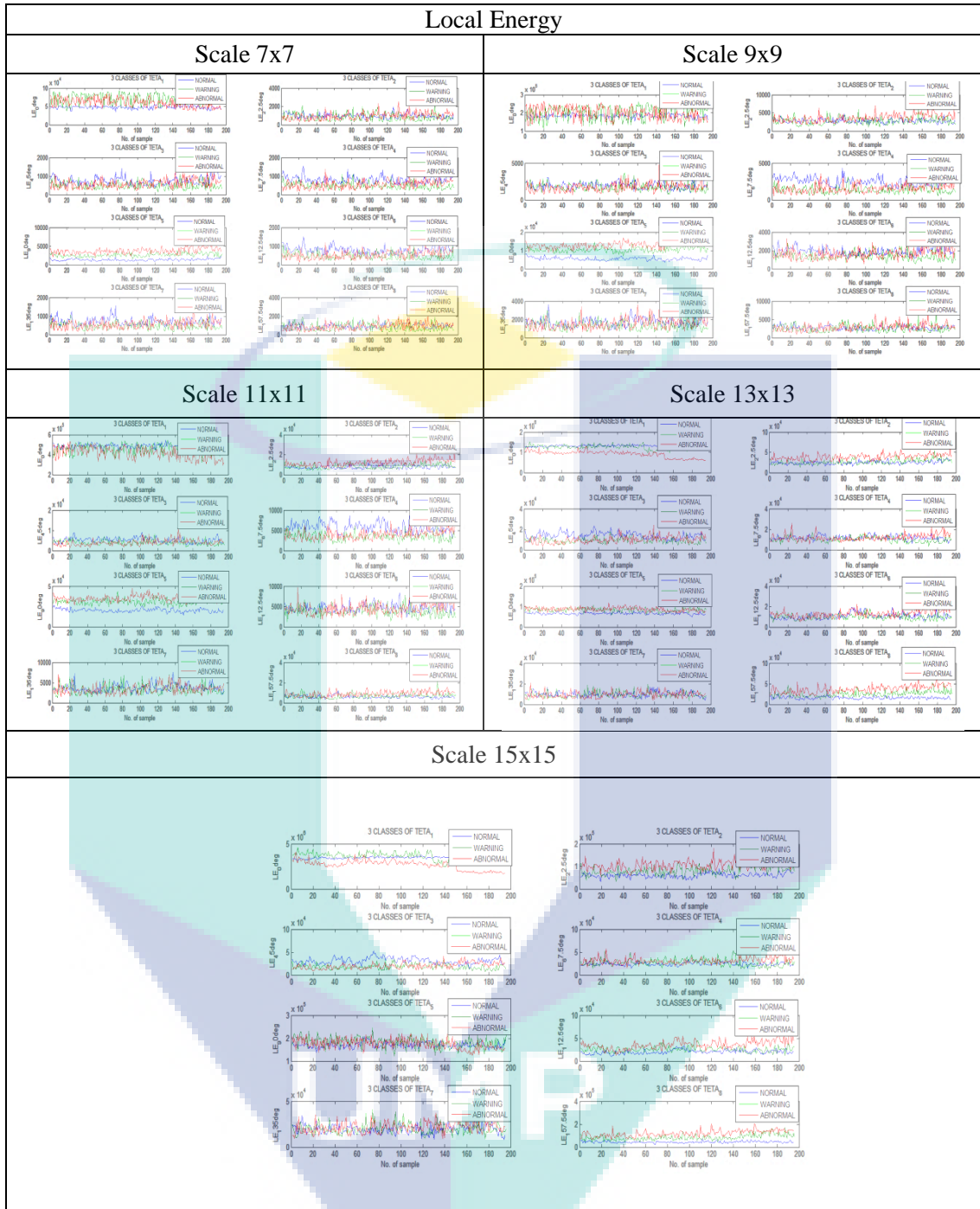


Figure 4.54 Overall new Local Energy features for multi-scales and multi orientations in GWCLAHE based feature extraction method

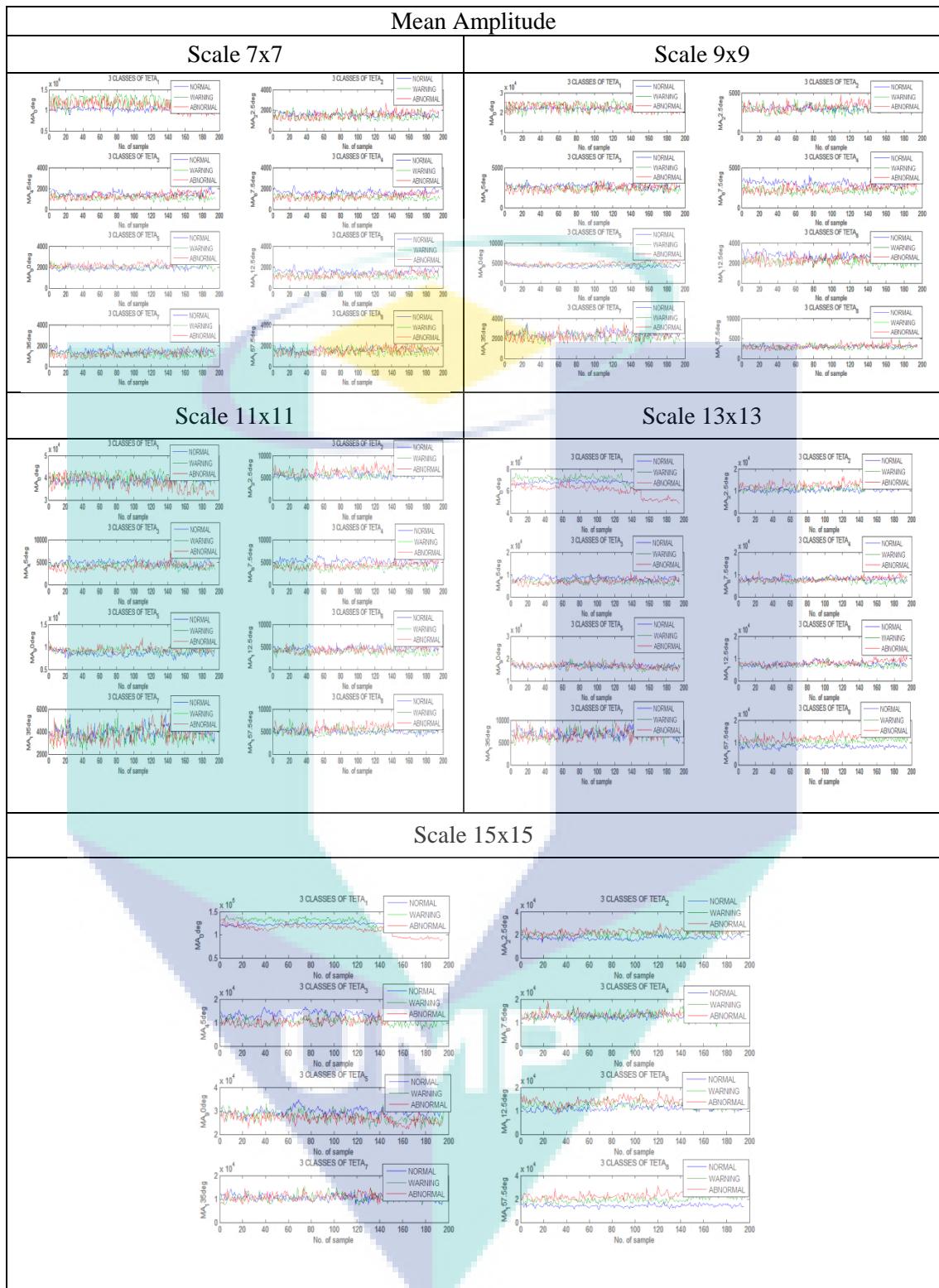


Figure 4.55 Overall new Mean Amplitude features for multiple scales and multiple orientations in GWCLAHE based feature extraction method

4.5.2.1 Feature Selection

In this section, a new optimum selection of scales and orientations for feature extraction methods based on GWCLAHE using the proposed fisher score method is explained. As in section 4.4.1 and section 4.5.1, fisher score-based feature selection was employed in this work to select new optimal features of high-dimensional vector output features from the GWCLAHE-based feature extraction process as in section 4.5.2.

According to the feature extraction results as in section 4.5.1, a new 40 multi-scale and multi-orientation feature images have been generated at each image point. Thus, the new total input data matrix generated for image data set training in different orientations and scales is $Y \in R_{(new)}^{(n \times 5) \times j} \in LE_{(new)}^{10375 \times 8}, MA_{(new)}^{10375 \times 8}$, where ‘n’ is the number of samples which have 2075 images and ‘j’ is the number of orientations. After calculating each score for new local energy and new mean amplitude features according to the fishery criterion as in equation 3.32, their score was generated as in [table and table](#).

Based on the results of the new local energy generated in the [table](#), the scores of combination orientations and scales are arranged from the highest value starting with F9 = 887.82, followed by F7=787.96, F15=755.10, F13=702.59, F11= 591.91. Therefore, the highest score value produced is at F9= 887.82, which is on a scale 9x9 ($\sigma = 3.6, \lambda = 4.6$) and orientation $\theta_5=90^\circ$. From this result, it can be seen that the new score obtained from this section shows lower reading compared to the new score from feature extraction based on EGF in section 4.4.1 and GWSMH in section 4.5.1. This has proven that new scores from this section have lower discriminatory power compared to EGF-based scores and GWSMH-based scores

Table 4.34 Fisher scoring for each Enhanced Gabor filter’s scale for Local Energy

Filter Size (Scales)	θ_1	θ_2	θ_3	θ_4	θ_5	θ_6	θ_7	θ_8
7x7	221.77	21.63	116.15	166.71	787.96	135.13	91.58	10.75
9x9	102.14	34.64	99.45	166.17	887.82	70.00	29.25	6.50
11x11	33.15	181.83	102.17	111.15	591.91	21.96	14.36	118.20
13x13	470.12	503.95	93.97	14.49	31.82	40.33	3.43	702.59
15x15	202.13	690.06	88.28	18.19	33.46	84.40	5.11	755.10

Meanwhile, in the table, the sequence of decreasing fisher score values for new mean amplitude features starts with F15=987.59, followed by F13=846.74, F7=195.82, F9=190.79 and F11=138.04. From this result, the highest fisher's score can be read on a scale 15x15 at orientations $\theta_8 = 157.5^\circ$ and the value is F15=987.59. It can be seen from this result that the mean amplitude score has a lower discriminatory power compared to EGF-based scores and GWSMH-based scores.

Table 4.35 Fisher scoring for each Enhanced Gabor filter's scale for Mean Amplitude

Filter Size (Scales)	θ_1	θ_2	θ_3	θ_4	θ_5	θ_6	θ_7	θ_8
7x7	139.64	47.06	144.78	221.84	65.04	195.82	120.85	32.71
9x9	57.63	21.05	130.85	190.79	59.83	127.03	45.14	14.95
11x11	53.67	127.28	138.04	134.51	12.76	52.28	20.81	94.01
13x13	241.84	420.12	104.95	23.19	47.51	47.62	5.03	846.74
15x15	154.02	757.90	92.27	16.62	171.72	89.10	8.64	987.59

Figure and figure demonstrates the distribution of fisher's scores obtained for the scale and orientation variations in the tables and tables according to their respective features. As in figure, it is clear from the local energy graph that SCALE 9 (θ_5) gives the highest fisher score among the others. Meanwhile, for the mean amplitude graph as shown in figure, it is observed that among others, SCALE 15 (θ_8) has given the highest score.

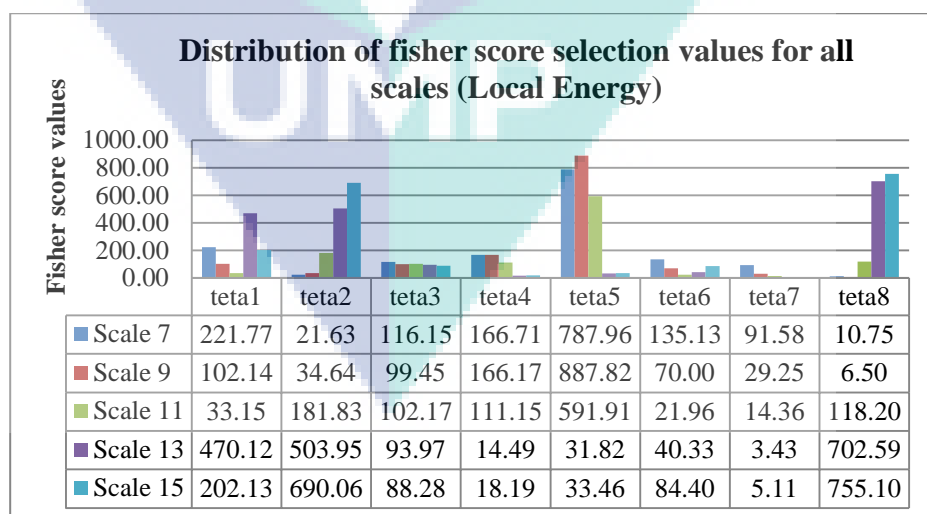


Figure 4.51 Variation of Fisher score value for local energy between normal, warning and abnormal thermal motor bearing images

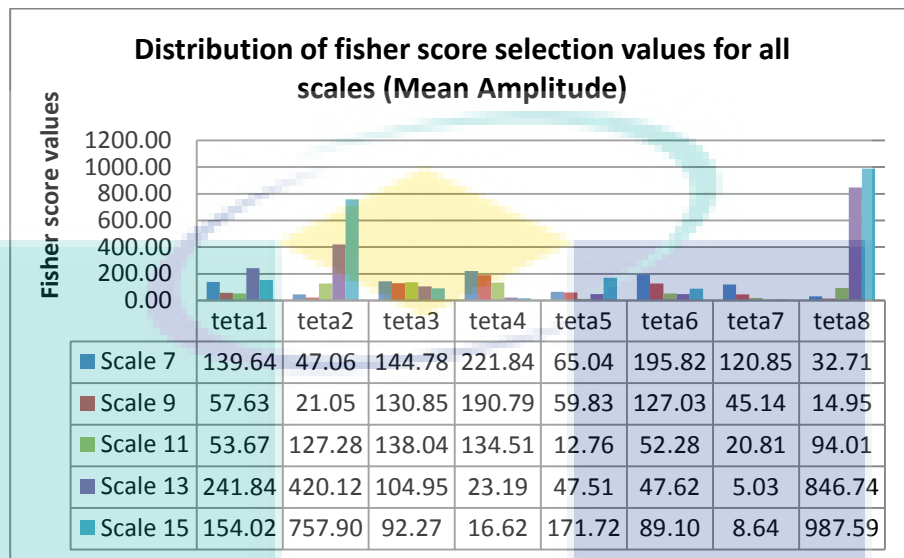


Figure 4.52 Variation of Fisher score value for Mean Amplitude between normal, warning and abnormal thermal motor bearing images

Figure and figure displays the overall group of thermal motor bearing image of local energy features and mean amplitude features for all eight orientations before any score is obtained. Those diagrams shown are in the SCALE 9x9 and SCALE 15x15 respectively as this scale includes the highest score. The various variations of the graph in the different orientations can be seen from those figures. Consequently, the fisher score or the discriminative power obtained will also vary according to the features produced by each orientation.

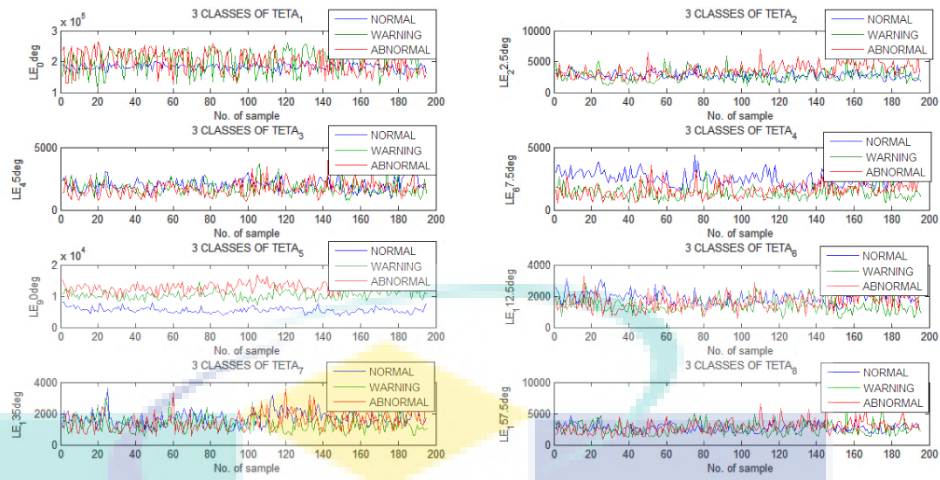


Figure 4.53 Variation Local Energy feature of condition thermal motor bearing images with 8 orientations for SCALE 9x9

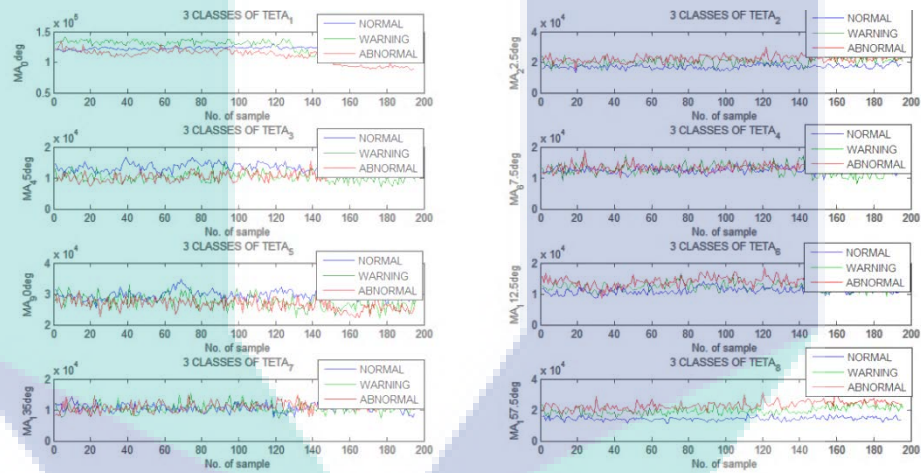


Figure 4.54 Variation Mean Amplitude feature of condition thermal motor bearing images with 8 orientations for SCALE 15x15

From the calculation of fishery criteria, the highest readings for local energy feature were shown at orientation $\theta_5 = 90^\circ$. While the highest values for the mean amplitude feature are shown in the orientation $\theta_8 = 157.5^\circ$. Their illustrations are shown individually as in the figure and figure. At this point, the dimensions for each of these matrix features have been reduced to $Y \in LE_{(new)}^{2075 \times 1}$, $MA_{(new)}^{2075 \times 1}$. From both graphs shown, it can be observed that the three groups for thermal motor bearing image state are not in the desired result. From figure, graph for normal group presents better performance due to it does not overlap with other categories. While graph for warning group and abnormal group indicate overlapping results. Meanwhile in figure, it can be

seen that graphs for all three groups which are normal, warning and abnormal demonstrates overlapping with each other's. Therefore, from the visual view through graph results, it is evident that the enhancement features of thermal motor bearing image by using GWCLAHE-based feature extraction method cannot be well classified as the features of all groups cannot be clearly distinguished. Nevertheless, the final selected features will be processed in the classification model in term of quantitative result in order to obtain the classification performance in this work.

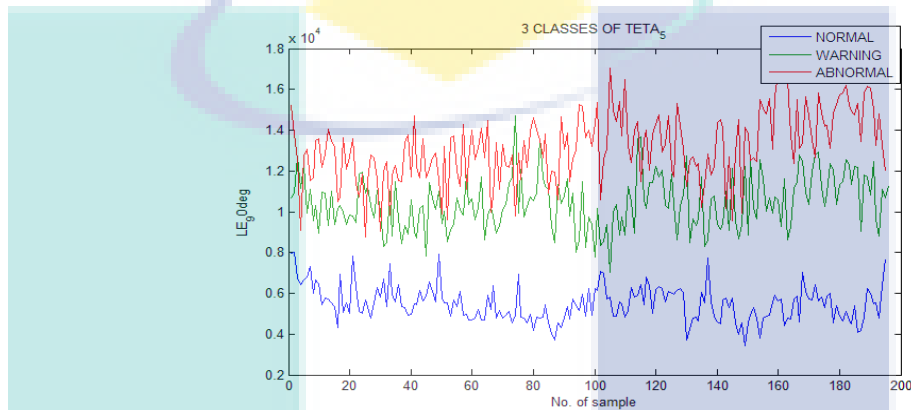


Figure 4.55 The optimal selection Local Energy feature for GWCLAHE is at SCALE 9x9 (orientation 90°)

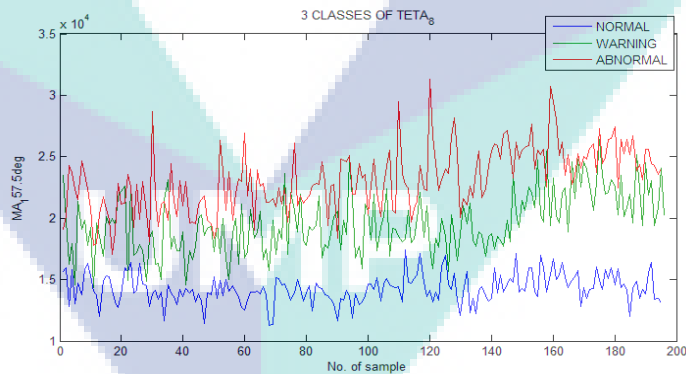


Figure 4.56 The optimal selection Mean Amplitude feature for GWCLAHE is at SCALE 15x15 (orientation 157.5°)

a. Evaluation Performance feature using ANOVA method

Same in section 4.3.1.1, 4.4.1.1, and 4.5.1.1.a, this section presents the results of the performance evaluation on the features of new Local Energy and new Mean Amplitude obtained by using ANOVA technique. **Table and table** shows the descriptive statistics value generated by new Local Energy and new Mean Amplitude features. The purpose

of the ANOVA method was implemented in this work to evaluate the new Local Energy and new Mean Amplitude features from thermal motor bearing images group whether there are significantly different or not. A 95% Confidence Interval for Mean has been implemented in this work which is basically a range of values for looking at parameters such as mean or proportion. Thus, $mean \pm 2SE$ is applied. From this formula, lower band and upper band values for the true mean for each normal population group, warning and abnormal were obtained. These values indicates that they have a 95% chance of being within the range of the mean as shown in the table and the table. From these tables, the 95% Confidence Interval for the mean values for the normal, warning and abnormal groups shows the balanced change values between the population groups. However, the distance of value change between all groups is close to each other. Next, the process of generating P values is calculated to determine the results from all groups are significantly different.

Table 4.36 Descriptive statistics value for new Local Energy feature

Thermal Image groups	N	Mean	Std Deviation	Std Error	95% Confidence Interval for Mean	
					Lower Bound	Upper Bound
Normal	1621	7397.85	1899.800	47.186	7305.29	7490.40
Warning	259	10695.03	1360.475	84.536	10528.56	10861.50
Abnormal	195	13164.82	1700.321	121.763	12924.67	13404.96
Total	2075	8351.35	2625.795	57.644	8238.31	8464.40

Table 4.37 Descriptive statistics value for new Mean Amplitude feature

Thermal Image groups	N	Mean	Std Deviation	Std Error	95% Confidence Interval for Mean	
					Lower Bound	Upper Bound
Normal	1621	14471.87	2110.085	52.409	14369.07	14574.67
Warning	259	20039.92	2663.340	165.492	19714.04	20365.81
Abnormal	195	23145.71	2578.521	184.652	22781.53	23509.89
Total	2075	15982.00	3694.039	81.095	15822.97	16141.04

Next, table and table presents the ANOVA readings generated using SPSS statistical software to obtain the value of F and the value of P. From these tables, the value of between group variability produces higher values than within group variability values. This will generate a high F-ratio value where the F-ratio value for new Local

Energy feature is 1115.608 and the F-ratio value for new Mean Amplitude feature indicates 1801.578. These values are derived from the ratio of the mean squares (MS). Subsequently, these obtained F-ratio value then is used to define the level of significance for the samples by comparing them with the F-critical value. From the table of probability values for the F distribution with (2,2072) degree of freedom (df) in APPENDIX, a critical F value is found. The F-critical value for the new local energy and new mean amplitude features is $F_{2,2072,0.05} = 3.0$. Therefore, from the tables, it can be observed that the F-ratio is greater than the appropriate critical F distribution at $\alpha = 0.05$ (F-ratio > F-critical), thus the null hypothesis is rejected, and accept the alternative hypothesis. This means the variance between the means of population group are significantly different.

The value of P is the probability of obtaining results from all groups are differ significantly. Hence, from the statistical calculation using function 'fdist', P-value is obtained. From table, the P-value for the new local energy feature is 0.000896. Meanwhile, from table, the P-value obtained from the new mean amplitude feature is 0.000555. This explains that both P-Values from the tables have given higher readings compared to the P-values in section 4.4.1.1 and section 4.5.1.1.a. It also presents a reading that is almost identical to the original P-value in section 4.3.1.1. This has proven that the enhancement based feature extraction method proposed in this section has given the worst reading among the other proposed methods in this study.

Nonetheless, based on the P-value obtained from the tables, it can be interpreted that the features of new Local Energy and new Mean Amplitude from all group of thermal motor bearing images are still shows significantly different at $P < 0.05$.

Table 4.38 ANOVA for new Local Energy feature

Source of variations	Sum of Squares	df	Mean Square	F-Ratio	F-Critical	P-value
Between Groups	7414450433.766	2	3707225216.883	1115.608	3.0	0.000896
Within Groups	6885368804.299	2072	3323054.442			
Total	14299819238.066	2074				

Table 4.7 ANOVA for new Mean Amplitude features

Source of variations	Sum of Squares	df	Mean Square	F-Ratio	F-Critical	P-value
Between Groups	17968709325.399	2	8984354662.700	1801.578	3.0	0.000555
Within Groups	10332932569.589	2072	4986936.568			
Total	28301641894.988	2074				

4.5.2.2 Classification

There are two types of classifier used in this work, namely MLANNs and Linear Thresholding. Section a and section b will discuss their performance results in more details.

a. MLANNs

In this section, the parameters and procedures of the MLANNs model applied to this work are same as those described in the previous sections in section 4.3.2.1, section 4.4.2.1 and section 4.5.2.1(a). The purpose is to obtain the best MLANNs model in order to identify and distinguish the condition of thermal motor bearing images used in this study. The best measure for MLANNs model can be observed through accuracy value and the lowest MSE value. In order to achieve these outputs, the selected features namely local energy and mean amplitude as in section 4.5.2.1 were used. All these results have been presented in the table.

Table 4.39 Training and validation performance results using TRAINLM, TRAINBR, TRAINSCG using 5- fold and 10-fold cross-validations in MLANNs model for Local Energy and Mean Amplitude feature

Training Function	K-Fold	HN	MSE		Accuracy (%)
			Training	Validation	
Trainbr	5	1	0.0550	0.0555	94.46
		2	0.0390	0.0402	
		3	0.0390	0.0401	
		4	0.0383	0.0395	
		5	0.0377	0.0396	
		6	0.0376	0.0400	
	10	1	0.0551	0.0556	
		2	0.0390	0.0398	

			3	0.0386	0.0400	94.37
			4	0.0383	0.0404	
			5	0.0379	0.0407	
Trainlm	5		1	0.0550	0.0555	
			2	0.0390	0.0401	
			3	0.0386	0.0402	
			4	0.0382	0.0397	94.27
			5	0.0377	0.0405	
			6	0.0373	0.0404	
Trainscg	10		1	0.0551	0.0557	
			2	0.0407	0.0413	
			3	0.0386	0.0400	
			4	0.0384	0.0399	94.18
			5	0.0379	0.0399	
			6	0.0366	0.1280	
Trainscg	5		1	0.0550	0.0556	
			2	0.0390	0.0397	
			3	0.0385	0.0400	94.25
			4	0.0383	0.0403	
			5	0.0381	0.0405	
			6	0.0373	0.0414	
Trainscg	10		1	0.0551	0.0555	
			2	0.0392	0.0401	
			3	0.0387	0.0397	94.28
			4	0.0385	0.0400	
			5	0.0381	0.0400	
			6	0.0376	0.0405	

Upon completion of data processing, the highest value of hidden neurons used in this work is 6. Next, the best fold selection for each training algorithm is performed. Figure shows graph validation performance for TRAINLM algorithm based on Kfold-5 and Kfold-10. From this result, it is observed that, the optimum mean MSE validation value can be read in Kfold-5 at hidden neuron 4 where the lowest value is 0.0397.

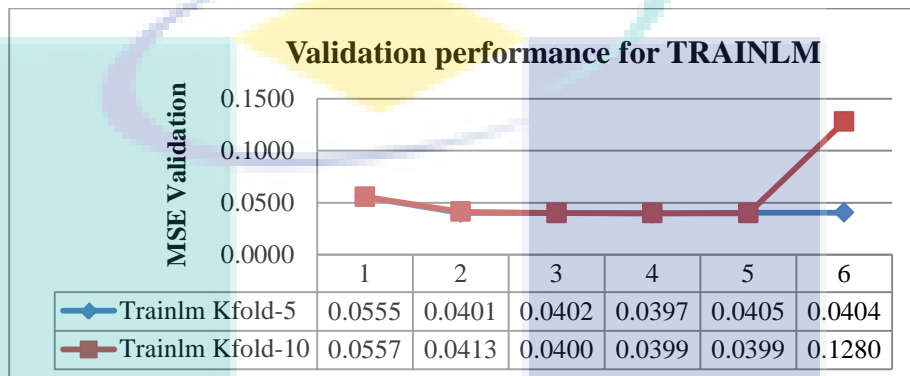


Figure 4.57 Validation performance for TRAINLM based on Kfold-5 and Kfold-10

Meanwhile, figure denotes a learning curves graph for the TRAINBR training algorithm. From the graph, it can be seen that readings in the hidden neuron 4 at kfold-5 gave the optimum mean MSE readings compared to all values of kfold-10. Its MSE lowest reading value is 0.0395.

UMP

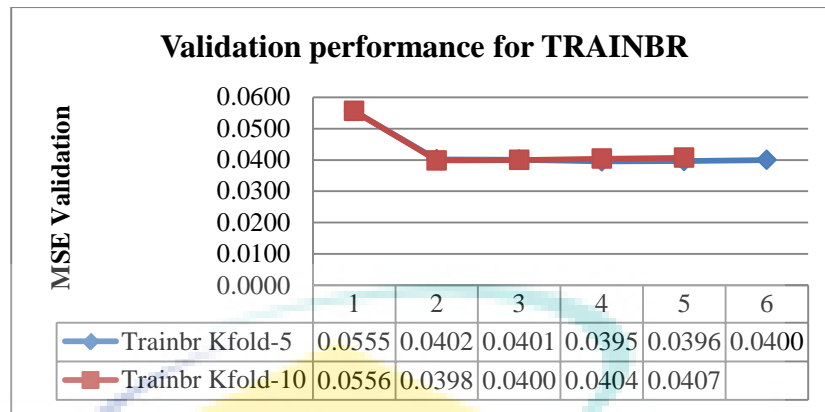


Figure 4.58 Validation performance for TRAINBR based on Kfold-5 and Kfold-10

Next, the third training algorithm is TRAINSCG. The optimum mean MSE reading of the training algorithm can be observed in the hidden neuron 2 on kfold-5. Its mean MSE value is 0.0397.

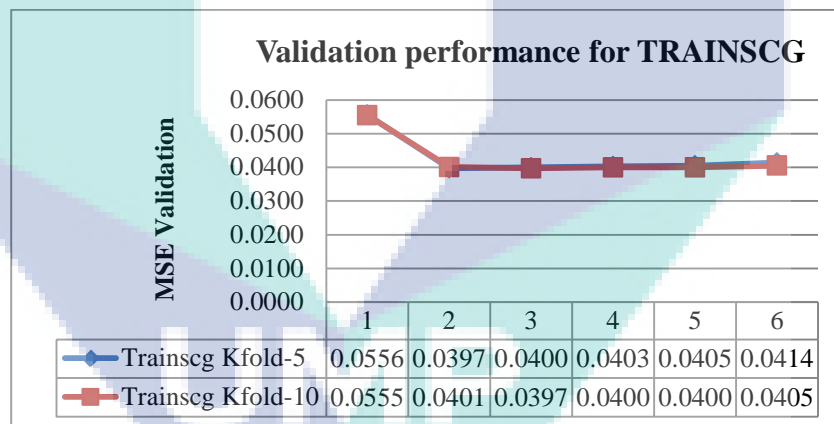


Figure 4.59 Validation performance for TRAINSCG based on Kfold-5 and Kfold-10

From all of the learning curve graphs shown above, the differences in mean MSE values between Kfold-5 and Kfold-10 did not differ significantly for each training algorithm. However, the differences error in the mean MSE value between both folds remains. Furthermore, the optimum mean MSE values for each training algorithm were extracted and combined in one graph as in the figure. This graph is intended to determine the best validation performance among all training algorithms. Hereby, as can be seen from the graph, TRAINBR gave the optimum mean MSE readings

compared to TRAINLM and TRAINSCG for MLANNs models in this section. The minimum mean MSE value readings shown were 0.0395 at k-fold = 5, hidden neurons = 4 and the average accuracy validation = 94.46% as observed in the table. Furthermore, once the mean error validation has been achieved to the minimum, the net will generalize to unknown samples through testing process.

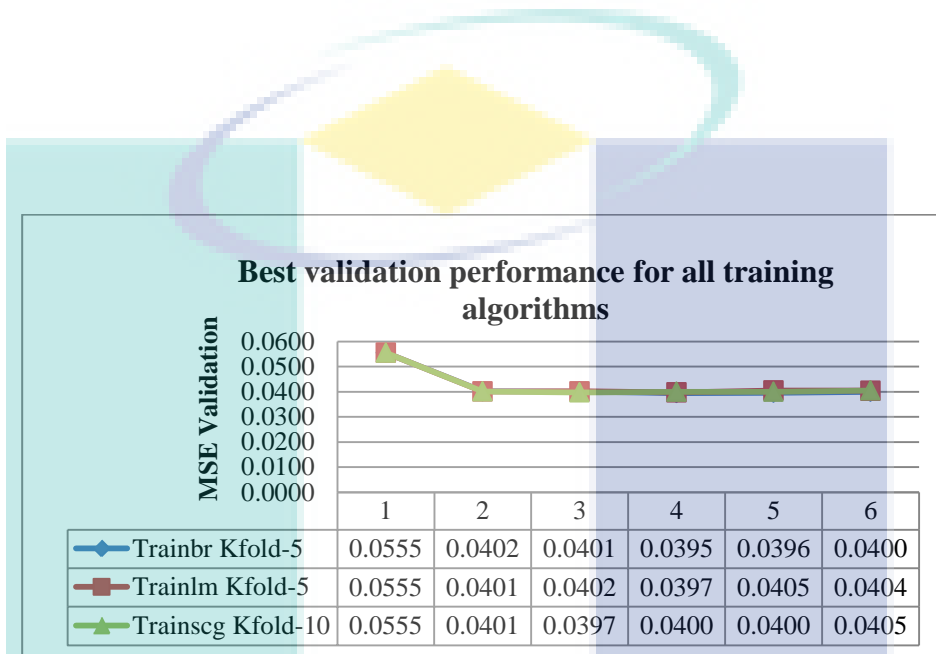


Figure 4.60 Best validation performances among all training algorithm types

Table shows the readings obtained from MATLAB software for best validation performance based on TRAINBR training algorithm in this section. Since K-fold = 5 is produced as the optimum mean cross validation error, so that the mean value for MSE validation and mean of accuracy validation value are measured 5 times according to the equation 3.33 as stated in section 3.7.1.1. From the table, it is seen that the best validation performance has been performed at various iterations at various times to determine how many times the learning algorithm works through the entire training data set. Herein, it is noted that the performance produced by the MLANN model in this section is not as fast as the MLANN model in section 4.4.2.1.

Table 4.40 Best validation performance for TRAINBR in MLANNs model for Local Energy and Mean Amplitude features

K-fold	Best Epoch	Time (sec)	MSE Validation	Acc Validation (%)
--------	------------	------------	----------------	--------------------

1	171	7	0.0385	94.46
2	118	4	0.0376	94.74
3	76	3	0.0408	94.31
4	61	2	0.0396	94.16
5	132	5	0.0411	94.61
Total Mean:			0.0395	94.46

Subsequently, the overall results for training classification statistical performance metrics generated by TRAINBR algorithm for MA and LE features in this section are presented in table 4.7. Precision values = 82.04%, sensitivity = 82.24, specificity = 93.88, CER = 0.0554 and accuracy = 94.46%. All of these values are calculated based on the multi-class classification problem through TP, FP, TN and FN according to the confusion matrix acquired during training data processing.

Table 4.41 Validation performance results using TRAINBR in MLANNs model for Local Energy and Mean Amplitude features

Training Function	HN	Pre (%)	Sens (TPR) (%)	Spec (TNR) (%)	CER	ACC (%)
TRAINBR (K-fold=5)	4	82.04	82.24	93.88	0.0554	94.46

Just like the previous section, 10% of dataset was employed in MLANNs model testing for validation purposes. Thus, table indicates five classification statistical performance metrics obtained by using TRAINBR algorithm for classifying the conditions of thermal motor bearing images. The accuracy of neural networks for classifying all thermal bearing images conditions was 94.08% (236 correctly classified of 259), the specificity =95.89%, precision=81.98% and Classification Error Rate=0.0595. Meanwhile, the testing values of the classification performances metrics for each state of thermal bearing images are denoted in the table. The results of these values have been calculated on multi-class classification problem based on TP (True Positive), FP (False Positive), TN (True Negative) and FN (False Negative) according to the acquired TRAINBR confusion matrix.

Table 4.42 Testing performance results using TRAINBR in MLANNs model for Local Energy and Mean Amplitude features

Training Function	HN	Class	TP	TN	FP	FN	Pre (%)	Sens (%)	Spec (%)	CER	ACC (%)
-------------------	----	-------	----	----	----	----	---------	----------	----------	-----	---------

TRAINBR	4	N	178	64	2	15	0.9889	0.9223	0.9697	0.0656	0.9344
(K-fold=5)		W	26	212	14	7	0.6500	0.7879	0.9381	0.0811	0.9189
		A	32	219	7	1	0.8205	0.9697	0.9690	0.0319	0.9691
		All					0.8198	0.8933	0.9589	0.0595	0.9408

Furthermore, the overall differences in the results performance of the MLANNs classification models for the testing phase and training phase in this section are graphically illustrated as in figure for easier observation.

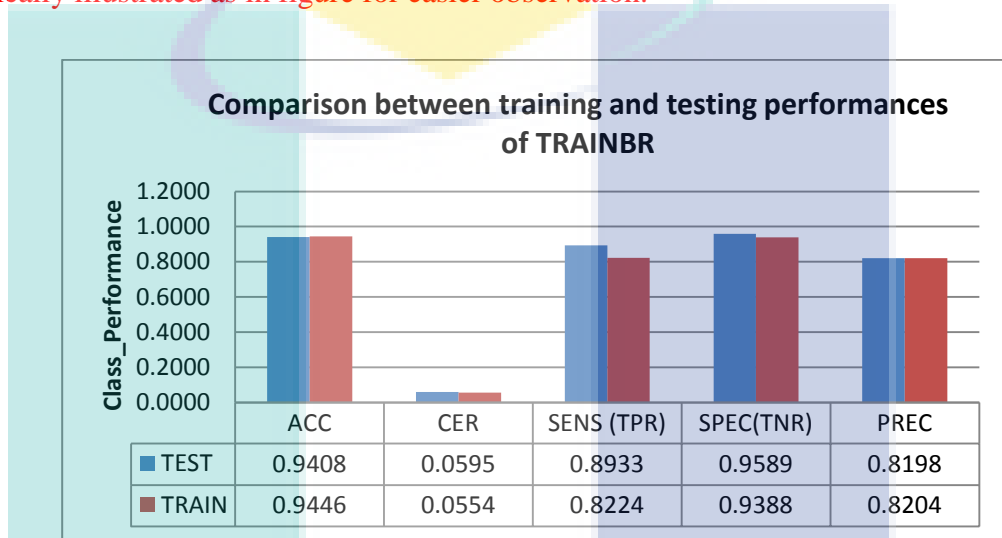
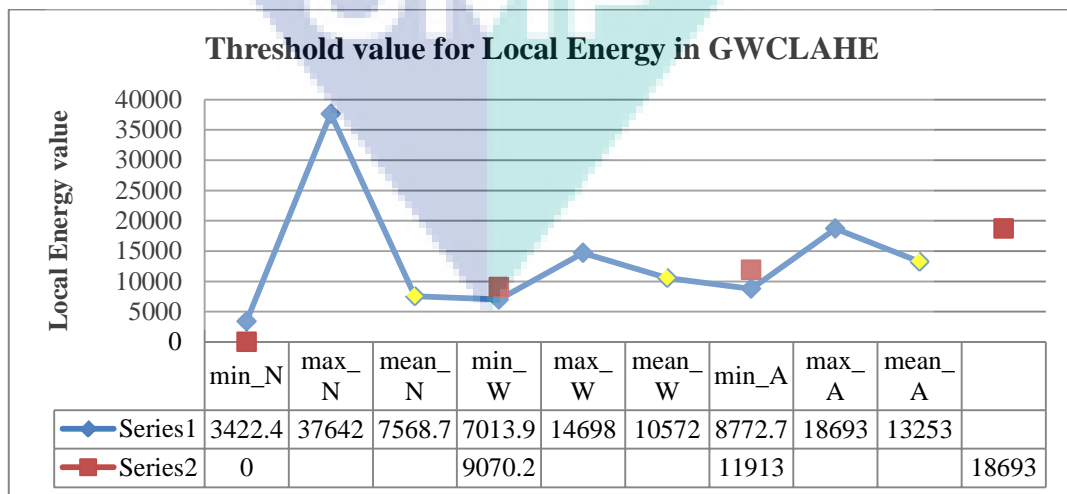


Figure 4.61 Comparison bar graph between training and testing performance using GWCLAHE based feature extraction algorithm

b. Linear Thresholding



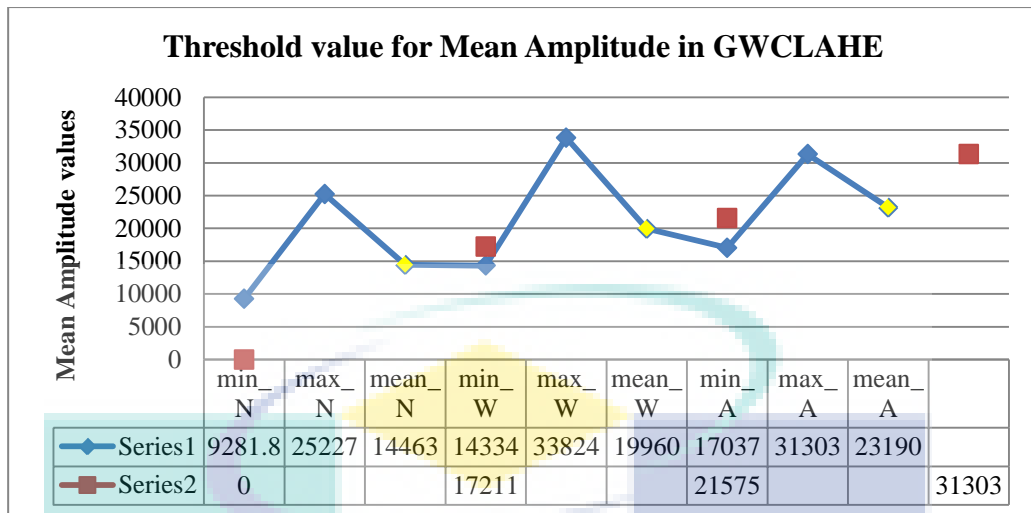


Table 4.43 Classification performances using Linear Thresholding model for GWCLAHE based feature extraction's features

Features	Condition of thermal bearing images	ACC TRAINING		ACC TESTING	
		Training (%)	No. of Classified image	Testing (%)	No. of Classified image
Local Energy	Normal	78.4564	1413	61.1111	110
	Warning	68.8963	206	55.0000	22
	Abnormal	79.0598	185	15.3846	36
	Average All	75.4709	1804	43.8319	168
Mean Amplitude	Normal	91.8379	1654	98.8889	178
	Warning	63.5452	190	80.0000	32
	Abnormal	70.9402	166	53.8462	21
	Average All	75.4411	2010	77.5783	231
			Average All:	60.7051	

4.6 Color based feature extraction for comparison purpose

In this work, a study to differentiate the features of the thermal motor bearing images group has been executed. Two types of color-based feature extraction methods, namely HSV-based and $l * a * b$ -based have been employed to accomplish this objective.

4.6.1 HSV color-based feature extraction algorithm

4.6.1.1 Feature selection

Table 4.2 represents the selection for HSV features which are mean, standard deviation and entropy.

Table 4.44 Data selection for HSV color fetaures

Color Extraction	Hue (H)		Saturation (S)		Value(V)	
	Mean	Std	Mean	Std	Mean	Std
HSV	1758.0161	33.1593	780.8380	478.5082	3570.7435	652.7770

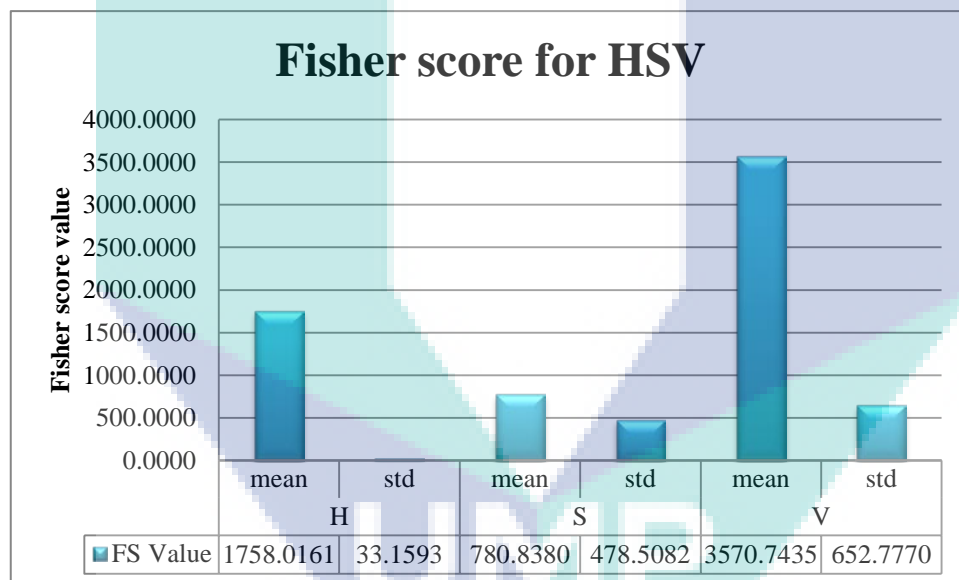


Figure 4.62 Variation of Fisher score value for HSV color method between normal, warning and abnormal thermal motor bearing images

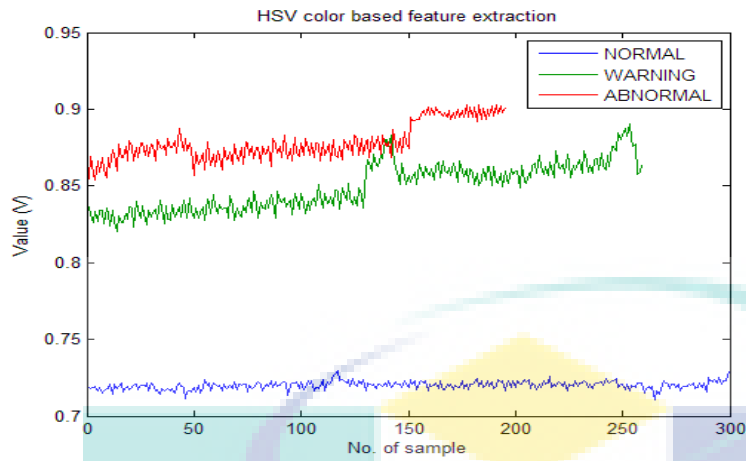
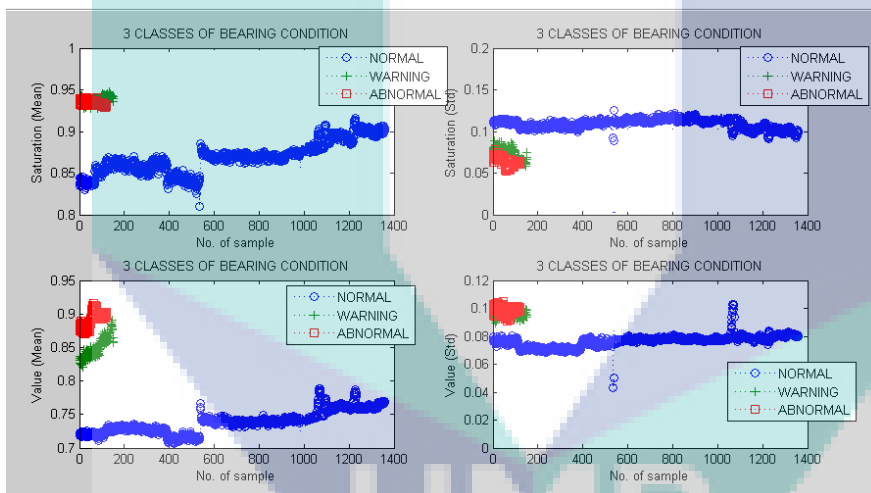


Figure 4.63 The optimal selection for HSV

4.6.1.2 Classification

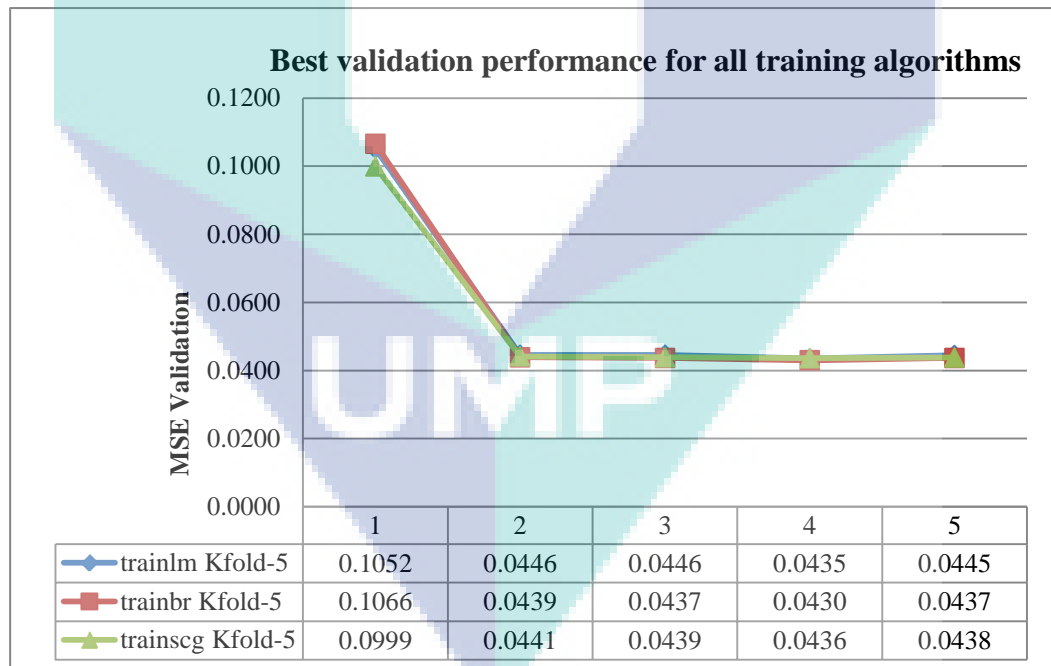


a. ANN

Table 4.45 Training and validation performance results using TRAINLM, TRAINBR, TRAINSCG using 5- fold and 10-fold cross-validations in MLANNs model for Local Energy and Mean Amplitude feature

Training Function	K-Fold	HN	MSE		Accuracy (%)
			Training	Validation	
Trainbr	5	1	0.1057	0.1066	
		2	0.0434	0.0439	
		3	0.0427	0.0437	92.87
		4	0.0427	0.0430	
		5	0.0428	0.0437	
	10	1	0.1142	0.1152	
		2	0.0434	0.0438	
		3	0.0430	0.0430	92.87
		4	0.0427	0.0432	
		5	0.0426	0.0436	
Trainlm	5	1	0.1060	0.1052	
		2	0.0433	0.0446	
		3	0.0430	0.0446	92.90
		4	0.0426	0.0435	
		5	0.0423	0.0445	
	10	1	0.1142	0.1149	
		2	0.0434	0.0439	
		3	0.0433	0.0440	92.67

		4	0.0426	0.0435	
		5	0.0425	0.0440	
Trainscg	5	1	0.0969	0.0999	
		2	0.0434	0.0441	
		3	0.0434	0.0439	92.49
		4	0.0433	0.0436	
		5	0.0431	0.0438	
	10	1	0.0933	0.0937	
		2	0.0451	0.0464	
		3	0.0462	0.0468	92.41
		4	0.0431	0.0436	
		5	0.0435	0.0436	



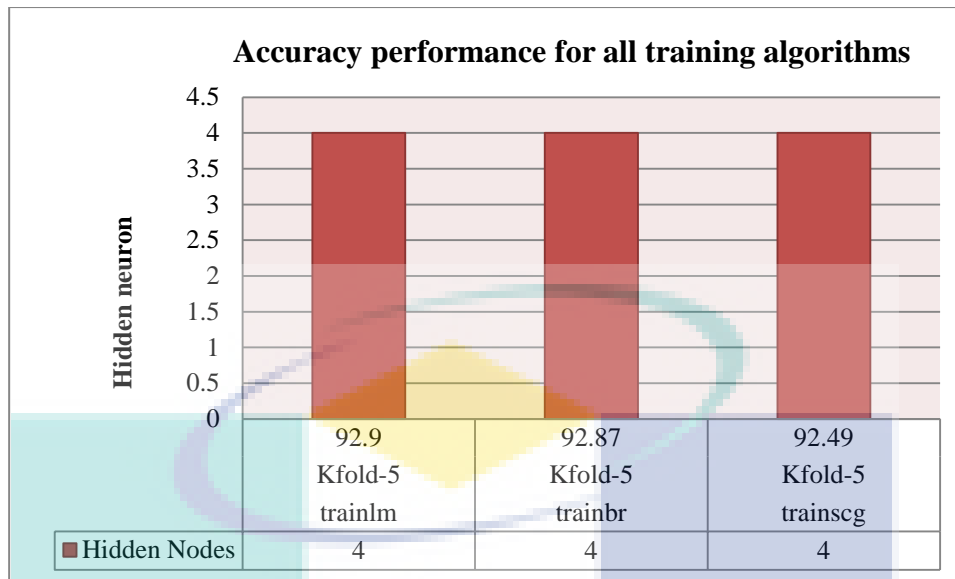


Table 4.46 Validation performance results using TRAINLM in MLANNs model for Local Energy and Mean Amplitude features

Training Function	HN	Pre (%)	Sens (TPR) (%)	Spec (TNR) (%)	CER	ACC (%)
TRAINLM (K-fold=5)	4	69	70.91	95.19	0.1906	92.90

Table 4.47 Best validation performance for TRAINLM in MLANNs model for Local Energy and Mean Amplitude features

K-fold	Best Epoch	Time (sec)	MSE Validation	Acc Validation (%)
1	745	29	0.0496	91.14
2	487	15	0.0401	94.49
3	1000	38	0.0395	93.22
4	297	11	0.0470	92.01
5	460	18	0.0411	93.63
Mean:			0.0435	92,90

Table 4.48 Testing performance results using TRAINLM in MLANNs model for Local Energy and Mean Amplitude features

Training Function	HN	Class	TP	TN	FP	FN	Pre (%)	Se (%)	Sp (%)	CER	ACC (%)
TRAINLM (K-fold=5)	4	N	180	36	0	4	100.00	97.83	100.00	0.0182	98.18
		W	29	187	11	30	72.50	49.15	94.44	0.1595	84.05
		A	7	209	32	9	17.95	43.75	86.72	0.1595	84.05
		All					63.48	63.58	93.72	0.1124	88.76

b. Linear Thresholding

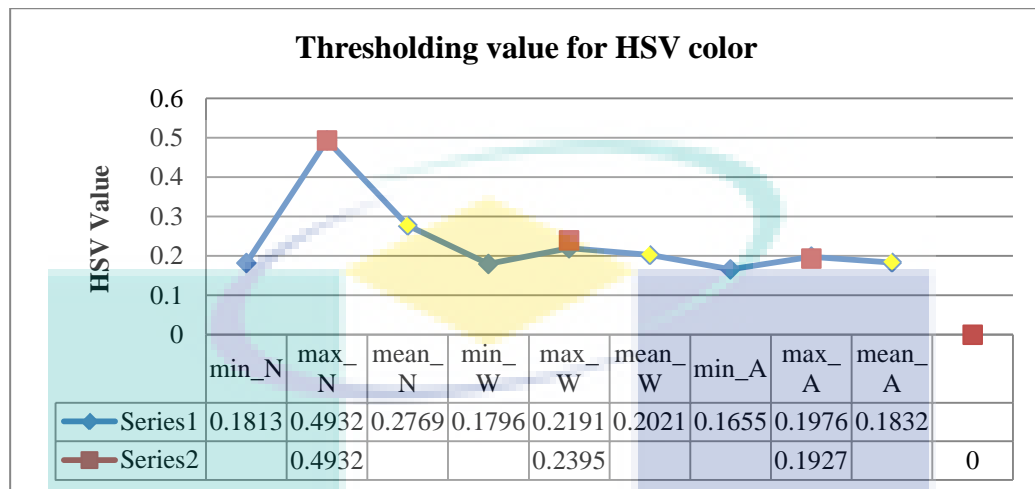


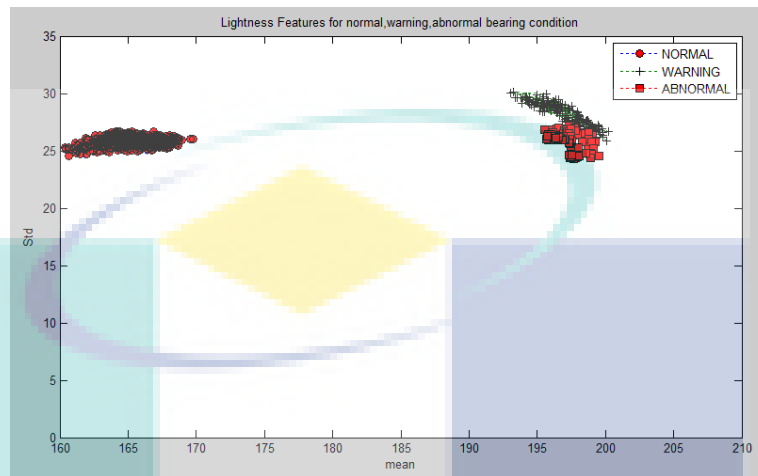
Table 4.49 Classification performances using Linear Thresholding model for HSV color features

Features	Condition of thermal bearing images	ACC TRAINING		ACC TESTING	
		Training (%)	No. of Classified image	Testing (%)	No. of Classified image
Mean	Normal	81.2882	1464	3.3333	6
	Warning	81.2709	243	65.0000	26
	Abnormal	92.7350	217	100.0000	39
	Average All	85.0980	1924	56.1111	71

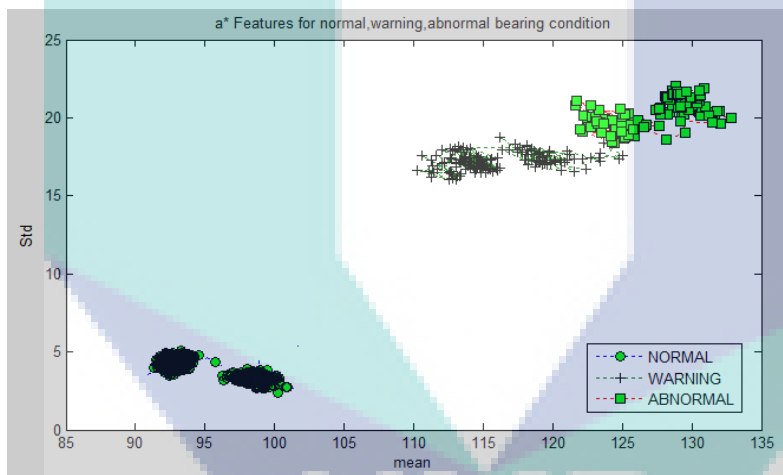
UMP

4.6.2 Lab color

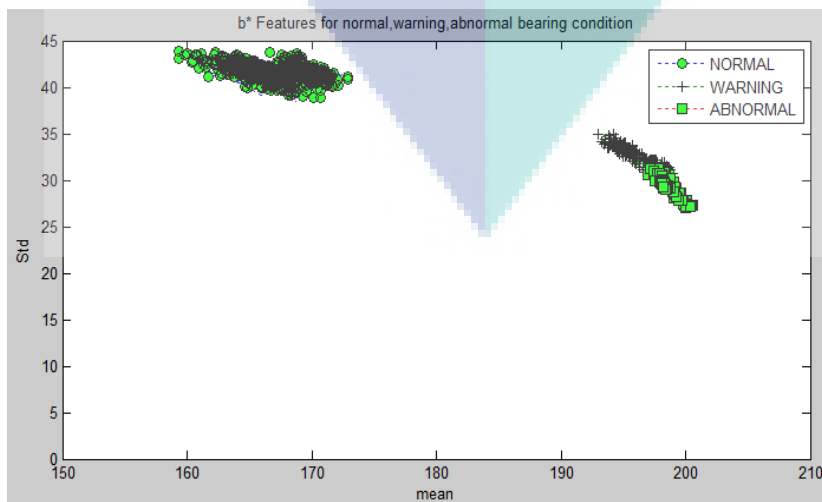
Features to be extracted image is color and texture,



Lightness (L)



a*



b*

4.6.2.1 Feature selection

Table 4.50 Sample table

Color Extraction	Lightness*		a*		b*	
	Mean	Std	Mean	Std	Mean	Std
L*a*b*	3926.5122	17.1731	1714.5057	439.2835	1168.8136	145.6867

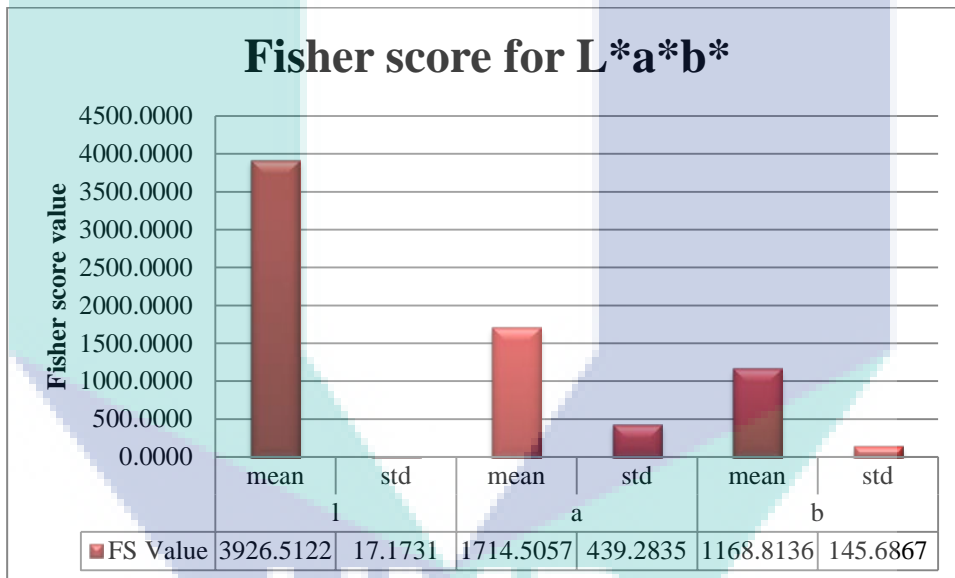


Figure 4.64 Variation of Fisher score value for l*a*b color method between normal, warning and abnormal thermal motor bearing images

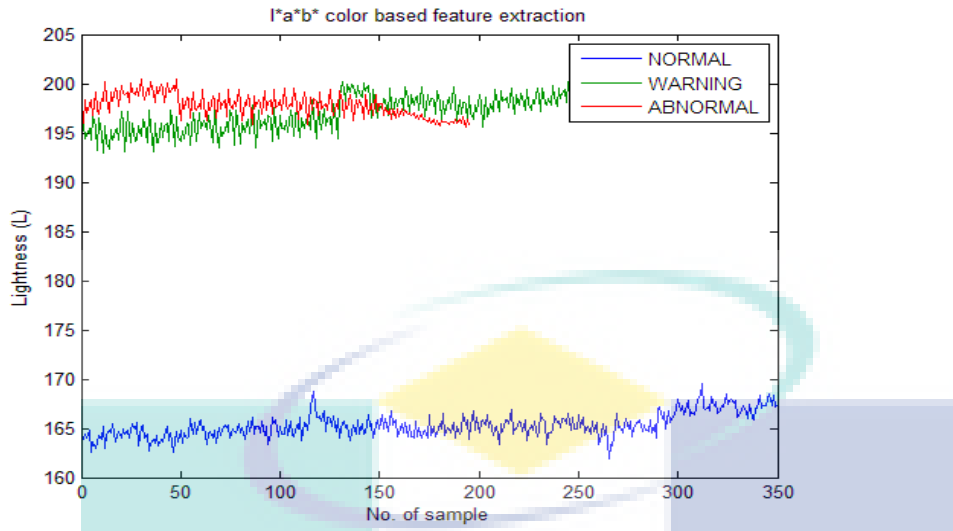
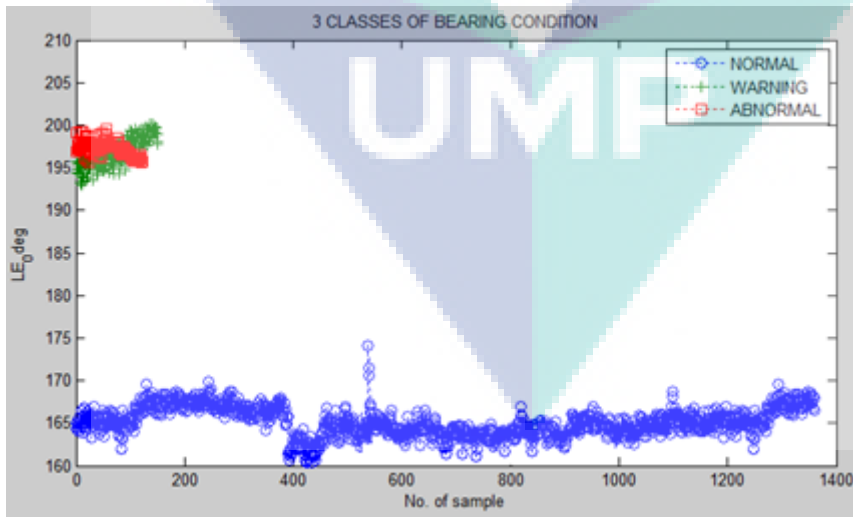


Figure 4.65 The optimal selection for l*a*b*

4.6.2.2 Classification



a. ANN

Table 4.51 Training and validation performance results using TRAINLM, TRAINBR, TRAINSCG using 5- fold and 10-fold cross-validations in MLANNs model for L*a*b based feature extraction algorithm

Training Function	K-Fold	HN	MSE		Accuracy (%)
			Training	Validation	
Trainscg	5	1	0.1152	0.1156	88.860
		2	0.0972	0.0959	
		3	0.0706	0.0715	
		4	0.0651	0.0658	
		5	0.0650	0.0659	
		6	0.0612	0.0624	
		7	0.0611	0.0620	
		8	0.0609	0.0629	
	10	1	0.0651	0.0655	
		2	0.0620	0.0630	

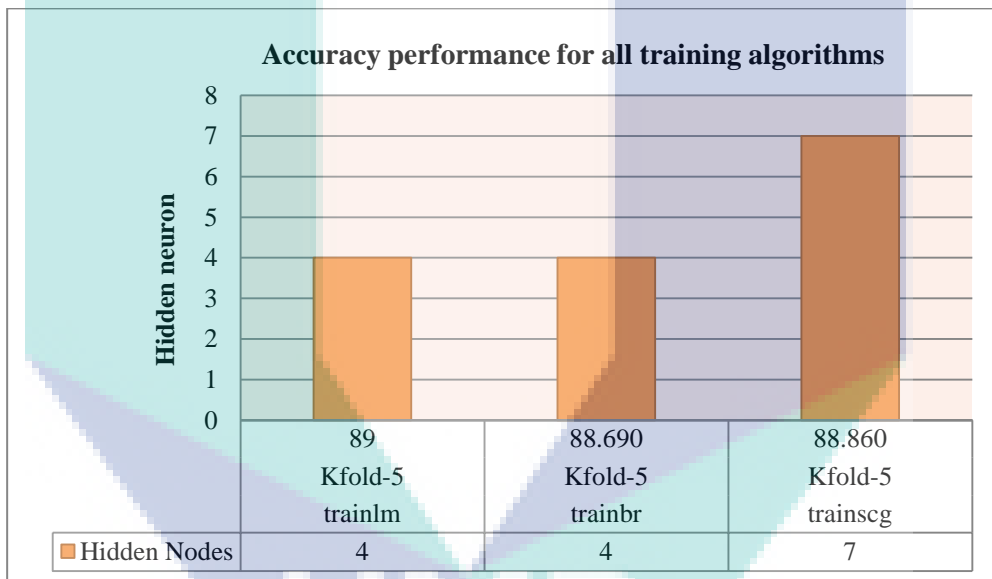
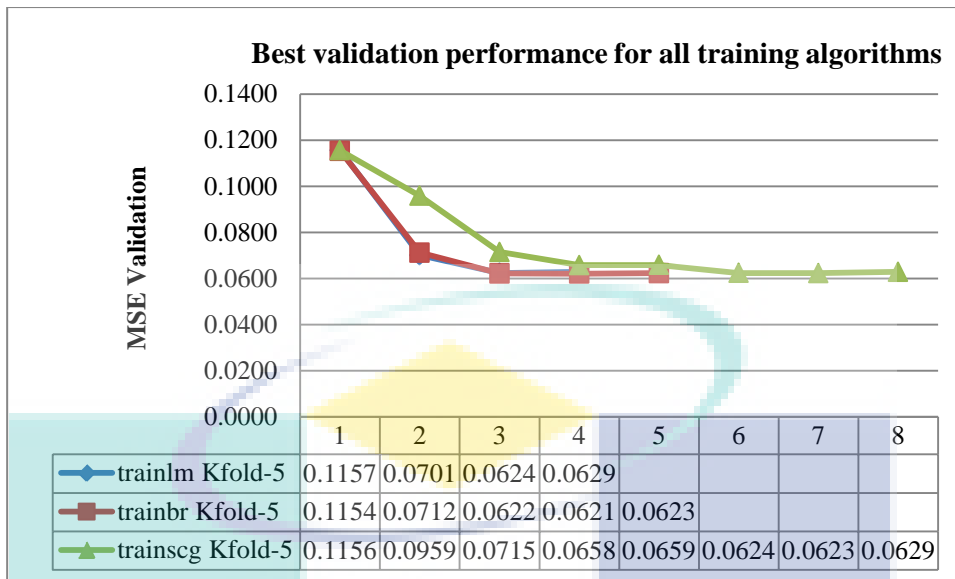


Table 4.52 Validation performance results using TRAINLM in MLANNs model for Local Energy and Mean Amplitude features

Training Function	HN	Pre (%)	Sens (TPR) (%)	Spec (TNR) (%)	CER	ACC (%)
TRAINLM (K-fold=5)	4	61.96	61.47	88.86	0.1100	89.0

Table 4.53 Best validation performance for TRAINLM in MLANNs model for Local Energy and Mean Amplitude features

K-fold	Best Epoch	Time (sec)	MSE Validation	Acc Validation (%)
1	349	14	0.0586	0.8920

2	48	2	0.0623	89.65
3	902	37	0.0626	88.14
4	460	19	0.0611	89.27
5	1000	41	0.0654	88.73
Mean:			0.8900	89.00

Table 4.54 Testing performance results using TRAINLM in MLANNs model for Local Energy and Mean Amplitude features

Training Function	HN	Class	TP	TN	FP	FN	Pre (%)	Se (%)	Sp (%)	CER	ACC (%)
TRAINLM (K-fold=5)	4	N	145	37	35	13	80.56	91.77	51.39	0.2087	79.13
		W	2	180	38	16	5.00	11.11	82.57	0.2288	77.12
		A	35	147	4	48	89.74	42.17	97.35	0.2222	77.78
		All					58.43	48.35	77.10	0.2199	78.01

b. Linear Thresholding

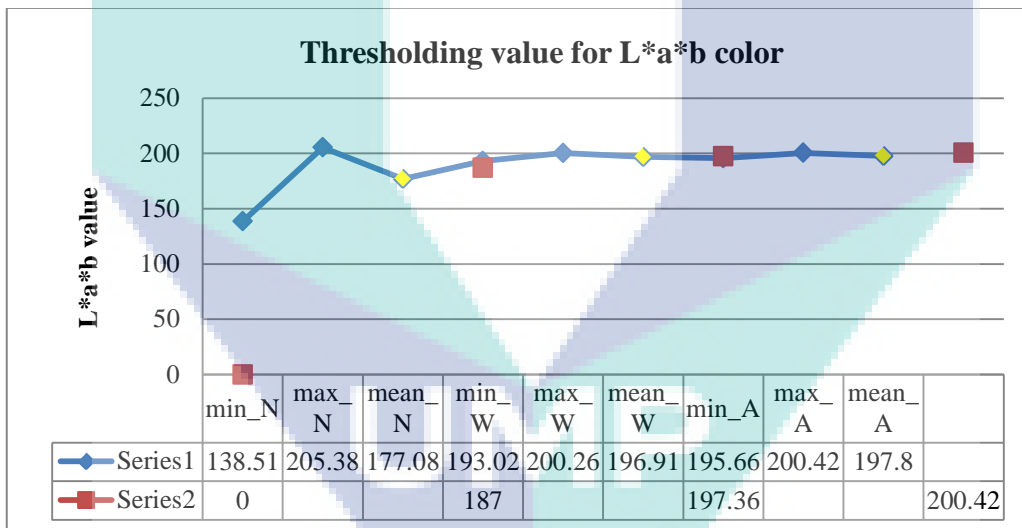
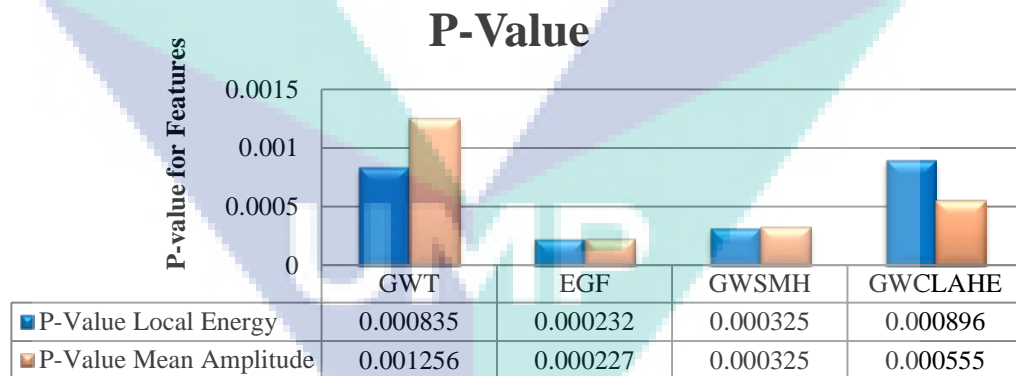


Table 4.55 Classification performances using Linear Thresholding model for l*a*b color features

Features	Condition of thermal bearing images	ACC TRAINING		ACC TESTING	
		Training (%)	No. of Classified image	Testing (%)	No. of Classified image
Mean	Normal	78.6230	1416	3.3333	6
	Warning	59.5318	178	42.5000	17
	Abnormal	64.9573	152	74.3590	29
	Average All	67.7040	1746	40.0633	52

4.7 Summary

Nilai P-value untuk semua teknik enhancement based feature extraction method. P-value paling rendah adalah yang terbaik (cited). Ini dibuktikan dari figure 1 dimana nilai dari kaedah EGF telah memberikan nilai P-value paling rendah. ini dapat disimpulkan fetures dari group thermal motor bearing image telah menunjukkan significantly diferent antara semua group.



EGF- Therefore, the performance evaluations for the features in this section is higher compared to the features generated based on GWT method. (LE)

(MA)

GWSMH-Therefore, this has proven that the evaluation feature performances in this section have shown lower discriminant power value compared to the feature performance based on the EGF extraction method. As well, the evaluation feature performances in this section have denoted higher discriminant power value compared to the feature performance based on GWT extraction method. (LE)

(MA)

GWCLAHE- Therefore, this has proven that the evaluation feature performances in this section have shown lower discriminant power value compared to the feature performance based on the EGF extraction method. As well, the evaluation feature performances in this section have denoted lower discriminant power value compared to the feature performance based on GWT extraction method. (LE)

(MA)

4.7.1 Testing and Validation

The experiment result confirms the robust of this algorithm.

Table 4.56 Comparison performance results in MLANNs model for all enhancement based feature extraction methods

Method	Name of Method	TEST	ACC (%)	Sens (TPR) (%)	Spec (TNR) (%)	CER	PREC (%)
Original Feature Extraction	GWT	TEST	95.07	85.22	97.14	0.0504	83.93
		TEST	99.47	99.63	99.70	0.0051	98.29
Enhanced Feature Extraction	GWSMH	TEST	98.71	97.25	99.26	0.0127	95.83
		TEST	94.08	89.33	95.89	0.0595	81.98
		TEST					

Comparison Enhancement Methods with the Original GWT

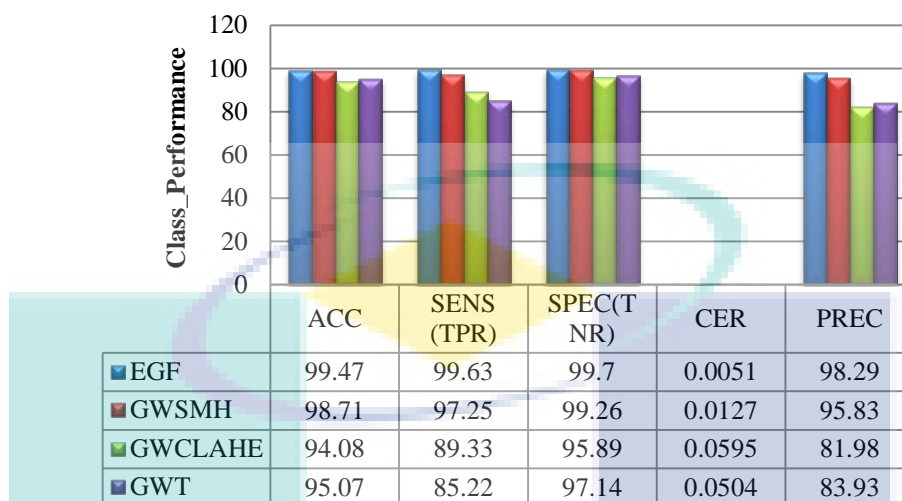


Figure 4.66 Distribution of comparison classification performance enhancement method with the original GWT based feature extraction method using MLANNs

This study have shown, the newly developed method which is feature extraction based on Enhanced Gabor Features (EGF) provided the efficient solution for solving feature extraction problem performance. It's classification performances reading is much better compared to the original GWT.

The CER of the new method shows the lowest reading. This indicates that the misclassification rate or number of misclassified samples is low.

Table 4.57 Comparison performance results in MLANNs model for all methods

Type of Methods	Methods	TEST	ACC (%)	Sens (TPR) (%)	Spec (TNR) (%)	CER	PREC (%)
Transformation Methods	EGF	TEST	99.49	99.63	99.70	0.0051	98.29
	GWSMH	TEST	98.71	97.25	99.26	0.0129	95.83
	GWCLAHE	TEST	93.94	89.33	95.70	0.0606	81.98
	GWT	TEST	94.79	79.49	96.01	0.0521	78.40
Color Methods	HSV	TEST	88.75	63.57	93.72	0.1124	63.48
	L*a*b	TEST	78.00	48.35	77.10	0.2199	58.43

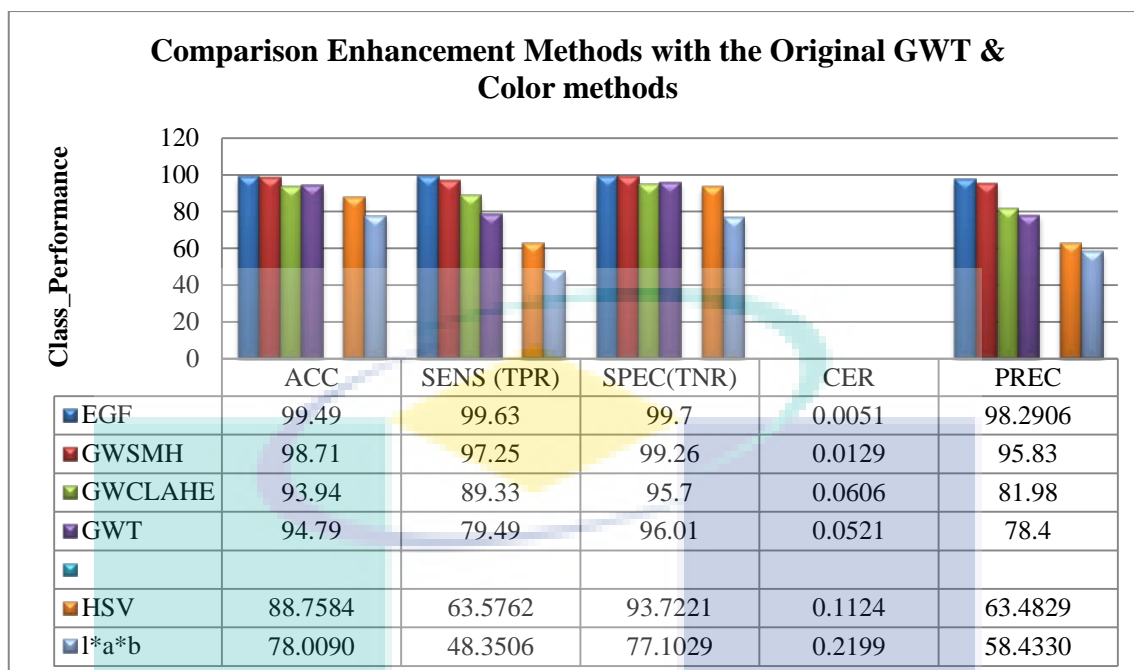


Figure 4.67 Distribution of comparison classification performance using MLANNs for all methods

Table 4.58 Comparison classification performance results in Linear Thresholding model for all enhancement based feature extraction methods

Methods	TEST	ACC (%)
EGF	TEST	98.1268
GWSMH	TEST	77.6959
GWCLAHE	TEST	60.7051
GWT	TEST	62.6709

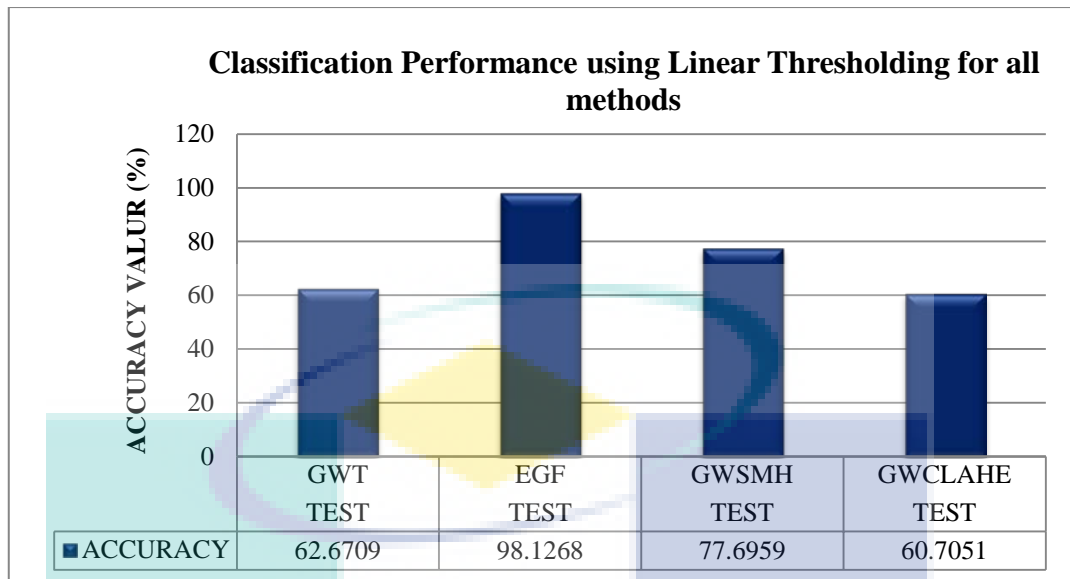


Figure 4.68 Distribution of comparison classification performance using Linear Thresholding for all methods

Table 4.59 Comparison classification performance results in Linear Thresholding model for all enhancement based feature extraction methods

Methods	TEST	ACC (%)
EGF	TEST	98.1268
GWSMH	TEST	77.6959
GWCLAHE	TEST	60.7051
GWT	TEST	62.6709
HSV	TEST	56.1111
L*a*b	TEST	40.0633

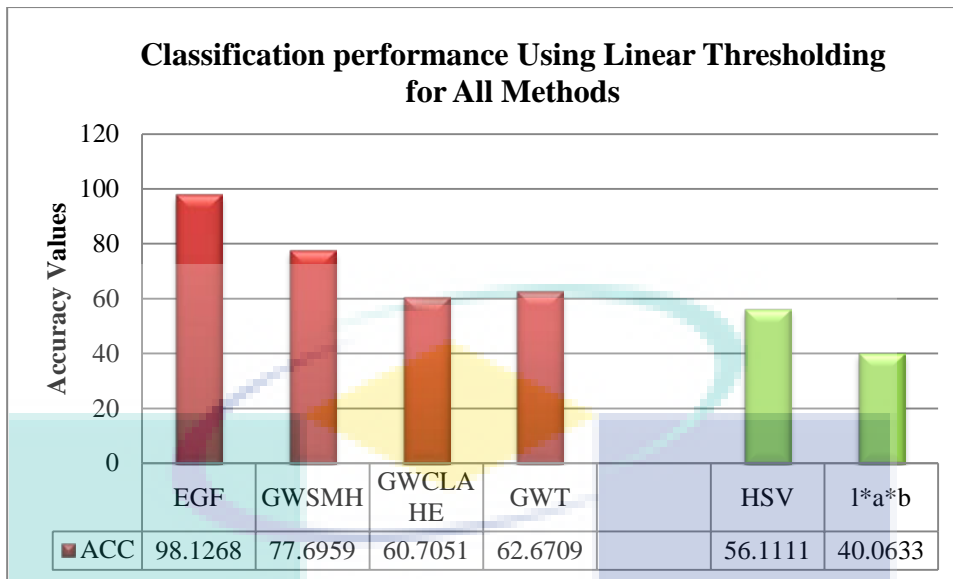
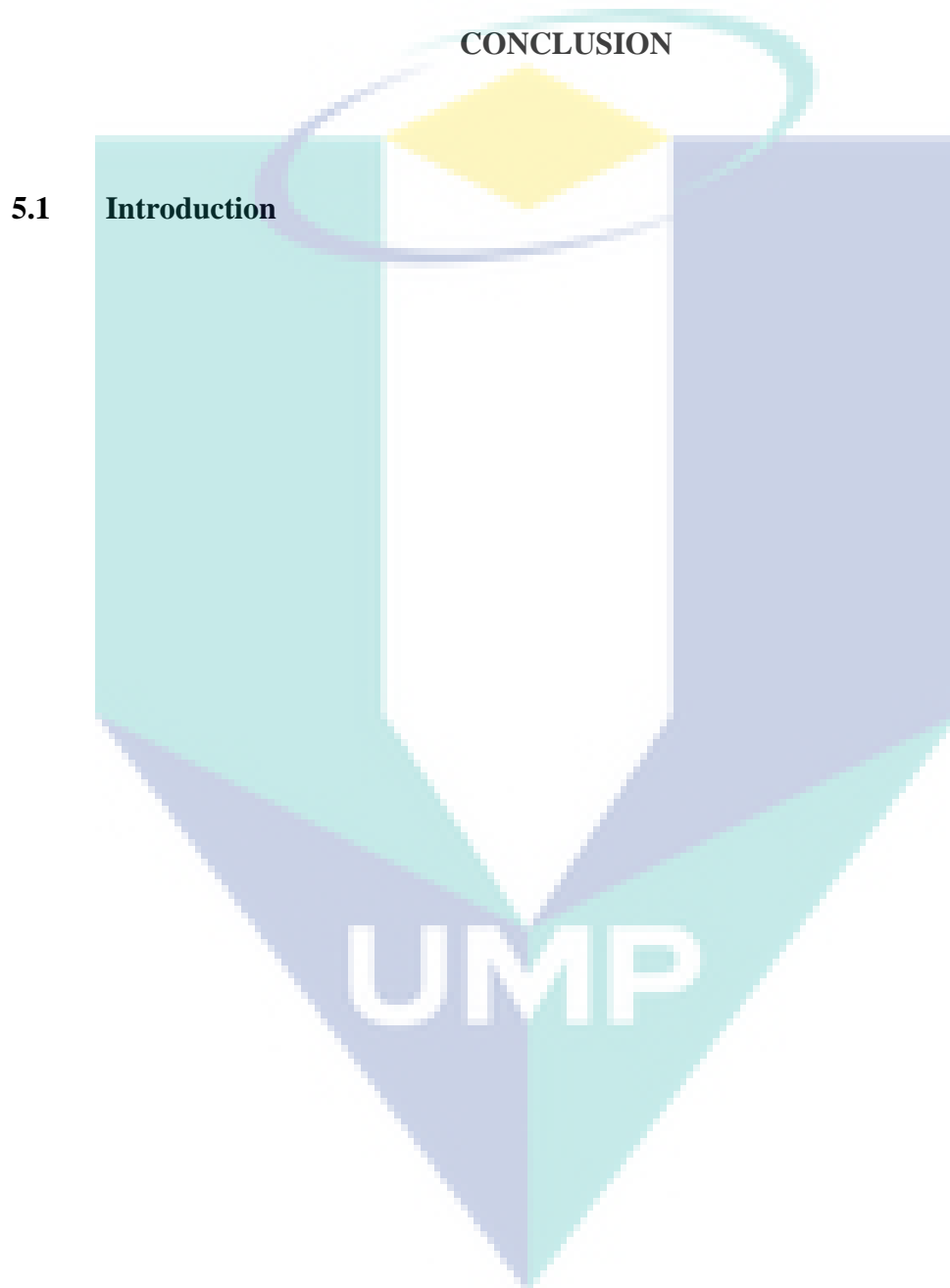


Figure 4.69 Distribution of comparison classification performance using Linear Thresholding for all methods

The results indicate that the proposed method can recognize/identify/differentiate the....

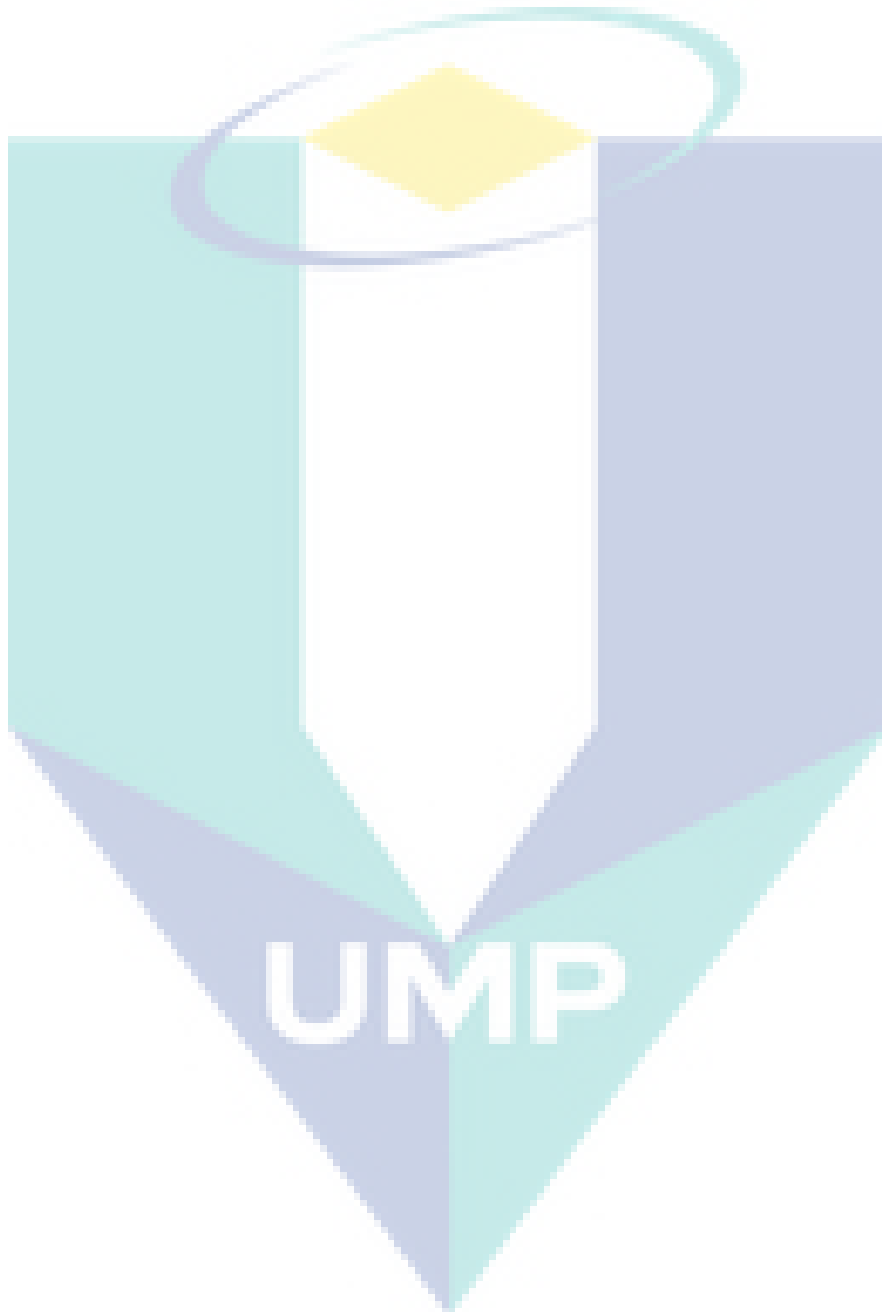
UMP

CHAPTER 5



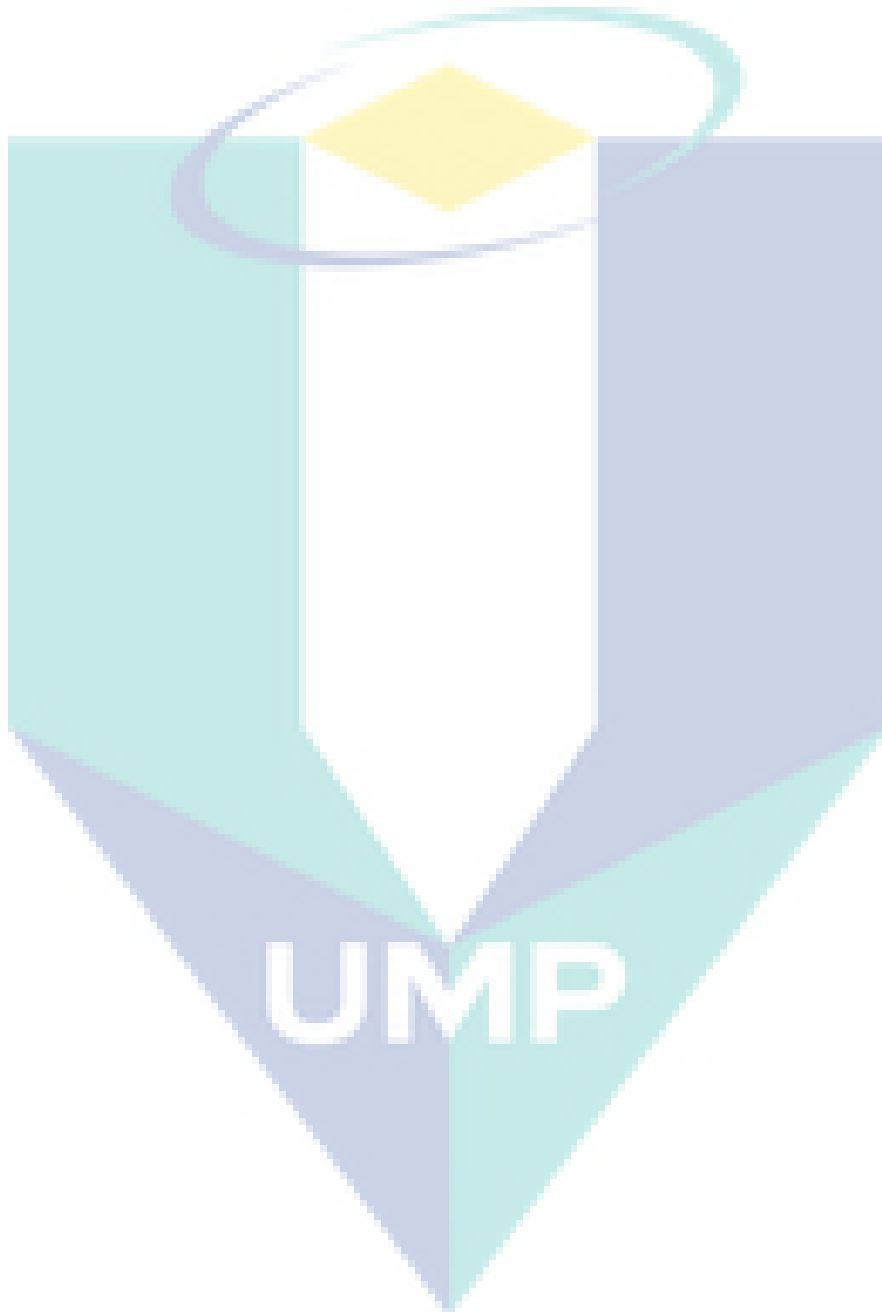
REFERENCES

Use reference manager such as Mendeley or Endnote to generate references list here.



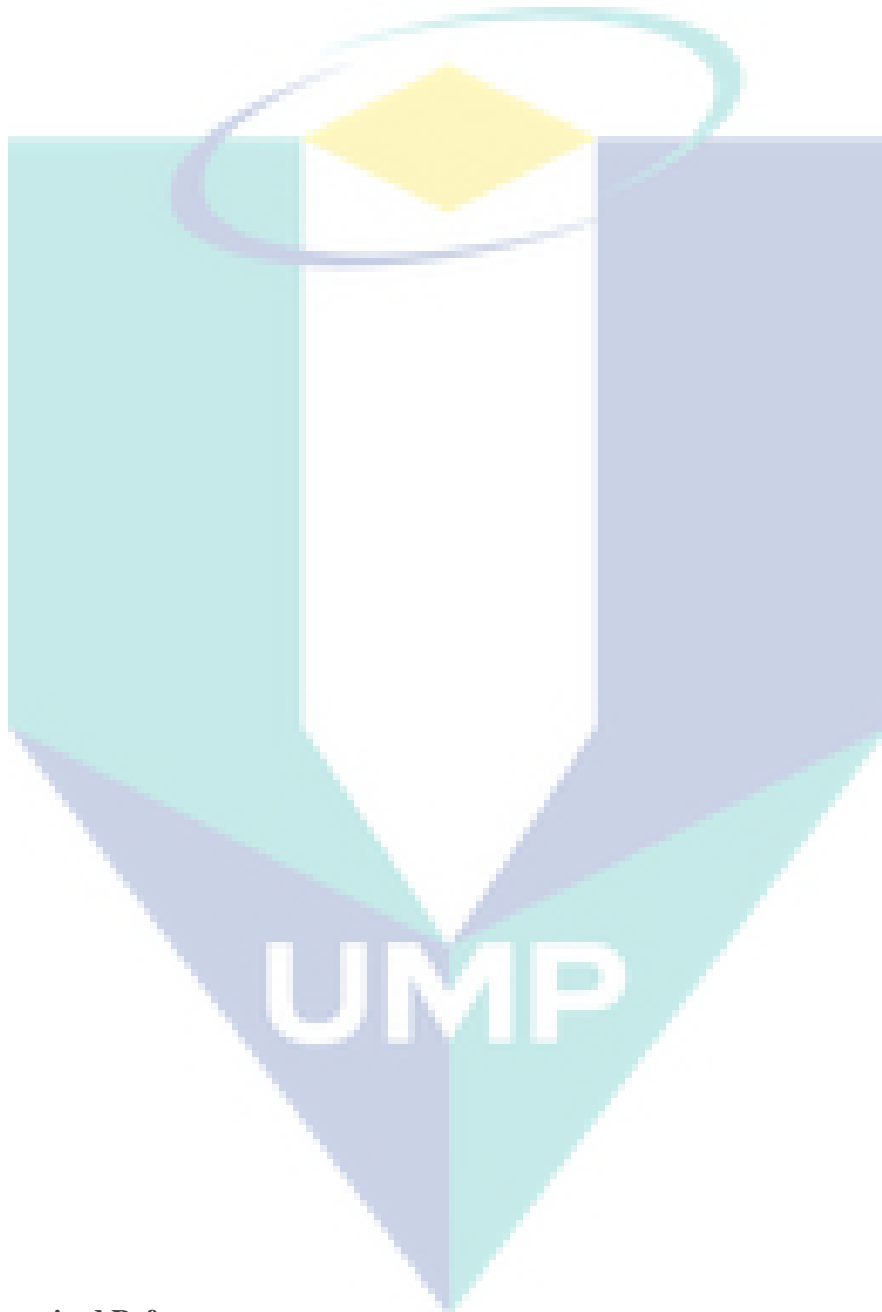
APPENDIX A
SAMPLE APPENDIX 1

For Appendices Heading use TITLE AT ROMAN PAGES style.



APPENDIX B
SAMPLE APPENDIX 2

For Appendices Heading use TITLE AT ROMAN PAGES style.



Uncategorized References

- Abdullah-Al-Wadud, M., Kabir, M. H., Dewan, M. A. A., & Chae, O. (2007). A Dynamic Histogram Equalization for Image Contrast Enhancement. *IEEE Transactions on Consumer Electronics*, 53(2), 593-600. doi: 10.1109/TCE.2007.381734
- Abhishree, T. M., Latha, J., Manikantan, K., & Ramachandran, S. (2015). Face Recognition Using Gabor Filter Based Feature Extraction with Anisotropic Diffusion as a Pre-

- processing Technique. *Procedia Computer Science*, 45, 312-321. doi: <https://doi.org/10.1016/j.procs.2015.03.149>
- Ahmad, J., Javed, F., & Hayat, M. (2017). Intelligent computational model for classification of sub-Golgi protein using oversampling and fisher feature selection methods. *Artificial Intelligence in Medicine*, 78, 14-22. doi: <https://doi.org/10.1016/j.artmed.2017.05.001>
- Ahmed, H. O. A., & Nandi, A. K. (2017, 23-25 Aug. 2017). *Multiple measurement vector compressive sampling and fisher score feature selection for fault classification of roller bearings*. Paper presented at the 2017 22nd International Conference on Digital Signal Processing (DSP).
- Akcay, O., & Avsar, O. (2017). *THE EFFECT OF IMAGE ENHANCEMENT METHODS DURING FEATURE DETECTION AND MATCHING OF THERMAL IMAGES* (Vol. XLII-1/W1).
- Aksu, D., Üstebay, S., Aydin, M. A., & Atmaca, T. (2018). *Intrusion detection with comparative analysis of supervised learning techniques and fisher score feature selection algorithm*. Paper presented at the International Symposium on Computer and Information Sciences.
- Albrecht, P. F., Appiarius, J. C., McCoy, R. M., Owen, E. L., & Sharma, D. K. (1986). Assessment of the Reliability of Motors in Utility Applications - Updated. *Energy Conversion, IEEE Transactions on, EC-1*(1), 39-46. doi: 10.1109/TEC.1986.4765668
- Alelyani, S., Tang, J., & Liu, H. (2018). Feature selection for clustering: A review *Data Clustering* (pp. 29-60): Chapman and Hall/CRC.
- Alkhudhairy, F., Al-Johany, S. S., Naseem, M., Bin-Shuwaish, M., & Vohra, F. (2020). Dentin bond strength of bioactive cement in comparison to conventional resin cement when photosensitized with Er, Cr: YSGG Laser. *Pakistan Journal of Medical Sciences*, 36(2), 85.
- Aruna Devi B., P. R. M. (2019). Performance Evaluation of MRI Pancreas Image Classification Using Artificial Neural Network (ANN) *Smart Intelligent Computing and Applications, Smart Innovation, Systems and Technologies, vol 104*, pp 671-681. doi: 10.1007/978-981-13-1921-1_65
- B. Hizarci, R. C. Ü., H. Ozturk, Z. Kırıl. (2019). Vibration Region Analysis for Condition Monitoring of Gearboxes Using Image Processing and Neural Networks. *Experimental Techniques*, pp 1-17. doi: s40799-019-00329-9
- Bahbishi, N., Mzain, W., Badeeb, B., & Nassar, H. M. (2020). Color Stability and Micro-Hardness of Bulk-Fill Composite Materials after Exposure to Common Beverages. *Materials*, 13(3), 787.
- Banerjee, A., Tiwari, A., Vico, J., & Wester, C. (2008, 1-3 April 2008). *Motor Protection Principles*. Paper presented at the 2008 61st Annual Conference for Protective Relay Engineers.
- Bhasin, V., Bedi, P., & Singhal, A. (2014, 24-27 Sept. 2014). *Feature selection for steganalysis based on modified Stochastic Diffusion Search using Fisher score*. Paper presented at the 2014 International Conference on Advances in Computing, Communications and Informatics (ICACCI).
- Bhattacharya, A., & Goswami, R. T. (2017). *Comparative analysis of different feature ranking techniques in data mining-based android malware detection*. Paper presented at the Proceedings of the 5th International Conference on Frontiers in Intelligent Computing: Theory and Applications.
- Bighnaraj Panda, M. M., Bidyadhar Rout. (2018). Classification of Electrical Home Appliances Based on Harmonic Analysis Using ANN. *Progress in Advanced Computing and Intelligent Engineering, vol 714*, pp 273-280.
- Blake, A., & Isard, M. (2012). *Active contours: the application of techniques from graphics, vision, control theory and statistics to visual tracking of shapes in motion*: Springer Science & Business Media.
- Bonnett, A. H. (1992). *Cause and analysis of bearing failures in electrical motors*. Paper presented at the Petroleum and Chemical Industry Conference, 1992, Record of Conference Papers., Industry Applications Society 39th Annual.

- Bonnett, A. H. (1993, 21-25 June 1993). *Cause and analysis of anti-friction bearing failures in AC induction motors*. Paper presented at the Conference Record of 1993 Annual Pulp and Paper Industry Technical Conference.
- Bortoni, E. C., Siniscalchi, R. T., & Jardini, J. A. (2010, 25-29 July 2010). *Hydro generator efficiency assessment using infrared thermal imaging techniques*. Paper presented at the Power and Energy Society General Meeting, 2010 IEEE.
- Cetingul, M. P., & Herman, C. (2008, 14-17 May 2008). *Identification of skin lesions from the transient thermal response using infrared imaging technique*. Paper presented at the Biomedical Imaging: From Nano to Macro, 2008. ISBI 2008. 5th IEEE International Symposium on.
- . Chapter 3 - Machinery Component Failure Analysis. (1999). In H. P. Bloch & F. K. Geitner (Eds.), *Practical Machinery Management for Process Plants* (Vol. 2, pp. 79-256): Gulf Professional Publishing.
- Chen, C. (2003) "*Computer image processing technology and algorithms*. Beijing: Tsinghua University Press.
- Cherrington, M., Thabtah, F., Lu, J., & Xu, Q. (2019). *Feature Selection: Filter Methods Performance Challenges*. Paper presented at the 2019 International Conference on Computer and Information Sciences (ICCIS).
- Chung, M., Lee, J., Chung, J. W., & Shin, Y.-G. (2018). Accurate liver vessel segmentation via active contour model with dense vessel candidates. *Computer Methods and Programs in Biomedicine*, 166, 61-75. doi: <https://doi.org/10.1016/j.cmpb.2018.10.010>
- da Silva, E. A. B., & Mendonça, G. V. (2005). 4 - Digital Image Processing. In W.-K. Chen (Ed.), *The Electrical Engineering Handbook* (pp. 891-910). Burlington: Academic Press.
- Desai, M. B., Patel, S., & Prajapati, B. (2016). ANOVA and fisher criterion based feature selection for lower dimensional universal image Steganalysis. *International Journal of Image Processing (IJIP)*, 10(3), 145-160.
- Duberstein, C. A., Matzner, S., Cullinan, V. I., Virden, D. J., Meyer, J., Laboratory, P. N. N., & Energy, U. S. D. o. (2012). *Automated Thermal Image Processing for Detection and Classification of Birds and Bats: FY2012 Annual Report : Offshore Wind Technology Assessment*: Pacific Northwest National Laboratory.
- El-Farrash, R. A., El Shimy, M. S., El-Sakka, A. S., Ahmed, M. G., & Abdel-Moez, D. G. (2019). Efficacy and safety of oral paracetamol versus oral ibuprofen for closure of patent ductus arteriosus in preterm infants: a randomized controlled trial. *The Journal of Maternal-Fetal & Neonatal Medicine*, 32(21), 3647-3654.
- Eviatar, H., & Somorjai, R. L. (1996). A fast, simple active contour algorithm for biomedical images. *Pattern Recognition Letters*, 17(9), 969-974.
- Fang, L., Wang, X., & Wang, L. (2020). Multi-modal medical image segmentation based on vector-valued active contour models. *Information Sciences*, 513, 504-518. doi: <https://doi.org/10.1016/j.ins.2019.10.051>
- Gaja, H., & Liou, F. (2018). Defect classification of laser metal deposition using logistic regression and artificial neural networks for pattern recognition. *The International Journal of Advanced Manufacturing Technology*, 94. doi: 10.1007/s00170-017-0878-9
- Garg, V. K., & Bansal, R. (2015). *Comparison of neural network back propagation algorithms for early detection of sleep disorders*. Paper presented at the 2015 International Conference on Advances in Computer Engineering and Applications.
- Gertheiss, J. (2014). ANOVA for Factors With Ordered Levels. *Journal of Agricultural, Biological, and Environmental Statistics*, 19(2), 258-277. doi: 10.1007/s13253-014-0170-5
- Glowacz, A., & Glowacz, Z. (2017). Diagnosis of the three-phase induction motor using thermal imaging. *Infrared Physics & Technology*, 81, 7-16. doi: <https://doi.org/10.1016/j.infrared.2016.12.003>

- Gonzalez-Cordoba, J. L., Osornio-Rios, R. A., Granados-Lieberman, D., Romero-Troncoso, R. D. J., & Valtierra-Rodriguez, M. (2017). Correlation Model Between Voltage Unbalance and Mechanical Overload Based on Thermal Effect at the Induction Motor Stator. *IEEE transactions on energy conversion*, 32(4), 1602-1610. doi: 10.1109/TEC.2017.2706194
- Gonzalez-Cordoba, J. L., Osornio-Rios, R. A., Granados-Lieberman, D., Romero-Troncoso, R. D. J., & Valtierra-Rodriguez, M. (2018). Thermal-Impact-Based Protection of Induction Motors Under Voltage Unbalance Conditions. *IEEE transactions on energy conversion*, 33(4), 1748-1756. doi: 10.1109/TEC.2018.2834487
- Gu, Q., Li, Z., & Han, J. (2012a). Generalized Fisher Score for Feature Selection. *Proceedings of the 27th Conference on Uncertainty in Artificial Intelligence, UAI 2011*.
- Gu, Q., Li, Z., & Han, J. (2012b). Generalized fisher score for feature selection. *arXiv preprint arXiv:1202.3725*.
- Hafez, S. F., Selim, M. M., & Zayed, H. H. (2015). 2d face recognition system based on selected gabor filters and linear discriminant analysis lda. *arXiv preprint arXiv:1503.03741*.
- Han, B., Han, Y., Gao, X., & Zhang, L. (2019). Boundary constraint factor embedded localizing active contour model for medical image segmentation. *Journal of Ambient Intelligence and Humanized Computing*, 10(10), 3853-3862.
- Hashemian, H. M. (2011). State-of-the-Art Predictive Maintenance Techniques. *IEEE Transactions on Instrumentation and Measurement*, 60(1), 226-236. doi: 10.1109/TIM.2010.2047662
- Hemalatha, R., Thamizhvani, T., Dhivya, A. J. A., Joseph, J. E., Babu, B., & Chandrasekaran, R. (2018). Active contour based segmentation techniques for medical image analysis. *Medical and Biological Image Analysis*, 17.
- Hjorth, J. U. (2017). *Computer intensive statistical methods: Validation, model selection, and bootstrap*: Routledge.
- Huang, D., Yang, J., Zhou, D., & Litak, G. (2019). Novel Adaptive Search Method for Bearing Fault Frequency Using Stochastic Resonance Quantified by Amplitude-Domain Index. *IEEE Transactions on Instrumentation and Measurement*, 1-13. doi: 10.1109/TIM.2019.2890933
- IEEE Recommended Practice for the Design of Reliable Industrial and Commercial Power Systems. (1988). *ANSI/IEEE Std 493-1980*, 3. doi: 10.1109/IEEESTD.1988.119231
- Information Guide for General Purpose Industrial AC Small and Medium Squirrel-Cage Induction Motor Standards. (2014).
- Islam, A. K. M. T., Jeong, B.-S., Bari, A. T. M. G., Lim, C.-G., & Jeon, S.-H. (2015). MapReduce based parallel gene selection method. *Applied Intelligence*, 42(2), 147-156. doi: 10.1007/s10489-014-0561-x
- Jadin, M. S., Ghazali, K. H., & Taib, S. (2014, 28-30 Nov. 2014). *Detecting ROIs in the thermal image of electrical installations*. Paper presented at the 2014 IEEE International Conference on Control System, Computing and Engineering (ICCSCE 2014).
- Jadin, M. S., Ghazali, K. H., Taib, S., & Huda, N. (2012, 23-25 Nov. 2012). *Finding ROIs in infrared image of electrical installation for qualitative thermal condition evaluation*. Paper presented at the 2012 IEEE International Conference on Control System, Computing and Engineering.
- Jain, T., Meenu, M., & Sardana, H. (2019). Automated Recognition of Mechanical Parts with Machine Vision System. *Journal of Experimental & Applied Mechanics*, 9(3), 1-6.
- Janssens, O., Loccufer, M., & Hoecke, S. V. (2019). Thermal Imaging and Vibration-Based Multisensor Fault Detection for Rotating Machinery. *IEEE Transactions on Industrial Informatics*, 15(1), 434-444. doi: 10.1109/TII.2018.2873175
- Janssens, O., Schulz, R., Slavkovikj, V., Stockman, K., Loccufer, M., Van de Walle, R., & Van Hoecke, S. (2015). Thermal image based fault diagnosis for rotating machinery. *Infrared Physics & Technology*, 73, 78-87. doi: <http://dx.doi.org/10.1016/j.infrared.2015.09.004>

- Ji, Z., Wang, J., Su, Y., Song, Z., & Xing, S. (2013). Balance between object and background: Object-enhanced features for scene image classification. *Neurocomputing*, 120, 15-23. doi: <https://doi.org/10.1016/j.neucom.2012.02.054>
- Jia, Z., Liu, Z., Vong, C., & Pecht, M. (2019). A Rotating Machinery Fault Diagnosis Method Based on Feature Learning of Thermal Images. *IEEE Access*, 7, 12348-12359. doi: 10.1109/ACCESS.2019.2893331
- Jiang, G., & Wang, W. (2017). Error estimation based on variance analysis of k-fold cross-validation. *Pattern Recognition*, 69, 94-106. doi: <https://doi.org/10.1016/j.patcog.2017.03.025>
- Jung, Y., & Hu, J. (2015). AK-fold averaging cross-validation procedure. *Journal of nonparametric statistics*, 27(2), 167-179.
- Kamaruddin, S., Sunard, K., Ghazali, H., & Hamid, R. *Canned Pineapple Grading Using Pixel Color Extraction*. Paper presented at the Proc. The International Conference on Artificial Intelligence in Computer Science and ICT (AICS 2013).
- Kamble, L. V., Pangavhane, D. R., & Singh, T. P. (2015). Neural network optimization by comparing the performances of the training functions -Prediction of heat transfer from horizontal tube immersed in gas-solid fluidized bed. *International Journal of Heat and Mass Transfer*, 83, 337-344. doi: <https://doi.org/10.1016/j.ijheatmasstransfer.2014.11.085>
- Karim, H., Niakan, S. R., & Safdari, R. (2018). Comparison of Neural Network Training Algorithms for Classification of Heart Diseases.
- Karmakar, S. (2016). *Induction Motor Fault Diagnosis, Power Systems*. Science+Business Media Singapore: Springer.
- Karvelis, P., Georgoulas, G., Stylios, C. D., Tsoumas, I. P., Antonino-Daviu, J. A., Picazo Rodenas, M. J., & Climente-Alarcon, V. (2014, Oct. 29 2014-Nov. 1 2014). *An automated thermographic image segmentation method for induction motor fault diagnosis*. Paper presented at the Industrial Electronics Society, IECON 2014 - 40th Annual Conference of the IEEE.
- Kass, M., Witkin, A., & Terzopoulos, D. (1988). Snakes: Active contour models. *International Journal of Computer Vision*, 1(4), 321-331.
- Kazerouni, A. M. (2009). Design and analysis of gauge R&R studies: Making decisions based on ANOVA method. *World Academy of Science, Engineering and Technology*, 52, 31-35.
- Kohavi, R. (2016). *A study of cross-validation and bootstrap for accuracy estimation and model selection*. 1995. Paper presented at the Proceedings of the Fourteenth International Joint Conference on Artificial Intelligence. Morgan Kaufmann.
- Lassoued, H., & Ketata, R. (2018). *ECG multi-class classification using neural network as machine learning model*. Paper presented at the 2018 International Conference on Advanced Systems and Electric Technologies (IC_ASET).
- Li, W., Mao, K., Zhang, H., & Chai, T. (2010). *Selection of Gabor filters for improved texture feature extraction*.
- Liu, C.-L., Koga, M., & Fujisawa, H. (2005). *Gabor feature extraction for character recognition: comparison with gradient feature*. Paper presented at the Eighth International Conference on Document Analysis and Recognition (ICDAR'05).
- M, V. P., & Ushakumari, S. (2011, 22-24 Sept. 2011). *Incipient fault detection and diagnosis of induction motor using fuzzy logic*. Paper presented at the 2011 IEEE Recent Advances in Intelligent Computational Systems.
- M.Peltola. (2002). Slip of ac induction motors and how to minimize it.
- Ma, F., Zhu, X., Wang, C., Liu, H., & Jing, X.-Y. (2019). Multi-orientation and multi-scale features discriminant learning for palmprint recognition. *Neurocomputing*, 348, 169-178. doi: <https://doi.org/10.1016/j.neucom.2018.06.086>
- Marzook, H., Razek, A. A., Yousef, E., & Attia, A. (2020). Intra-articular injection of a mixture of hyaluronic acid and corticosteroid versus arthrocentesis in TMJ internal derangement. *Journal of stomatology, oral and maxillofacial surgery*, 121(1), 30-34.

- Medeiros, A. G., Guimarães, M. T., Peixoto, S. A., Santos, L. d. O., da Silva Barros, A. C., Rebouças, E. d. S., . . . Rebouças Filho, P. P. (2019). A new fast morphological geodesic active contour method for lung CT image segmentation. *Measurement*, *148*, 106687. doi: <https://doi.org/10.1016/j.measurement.2019.05.078>
- Mehala, N. (October 2010). *Condition Monitoring and Fault Diagnosis of Induction Motor using Motor Current Signature Analysis*. (Ph.D. Thesis), Electrical Engineering Department, NIT Kurukshetra.
- Mike Eby, E. P., Stefanie Kure, Joe Knisley, Mike Holt, Russ LeBlanc, Steven J. Owen. (2011). The Highs and Lows of Motor Voltage. *Electrical Construction & Maintenance (EC&M) Magazine*.
- Mohammed, M. A., Al-Khateeb, B., Rashid, A. N., Ibrahim, D. A., Abd Ghani, M. K., & Mostafa, S. A. (2018). Neural network and multi-fractal dimension features for breast cancer classification from ultrasound images. *Computers & Electrical Engineering*, *70*, 871-882. doi: <https://doi.org/10.1016/j.compeleceng.2018.01.033>
- Nandi, S., Toliyat, H. A., & Li, X. (2005). Condition Monitoring and Fault Diagnosis of Electrical Motors—A Review. *IEEE transactions on energy conversion*, *20*(4), 719-729. doi: 10.1109/TEC.2005.847955
- Nithila, E. E., & Kumar, S. S. (2019). Segmentation of lung from CT using various active contour models. *Biomedical Signal Processing and Control*, *47*, 57-62. doi: <https://doi.org/10.1016/j.bspc.2018.08.008>
- Ojaghi, M., Sabouri, M., & Faiz, J. (2014). *Diagnosis methods for stator winding faults in three-phase squirrel-cage induction motors* (Vol. 24).
- Osornio-Rios, R. A., Antonino-Daviu, J. A., & Romero-Troncoso, R. d. J. (2019). Recent Industrial Applications of Infrared Thermography: A Review. *IEEE Transactions on Industrial Informatics*, *15*(2), 615-625. doi: 10.1109/TII.2018.2884738
- Panda Suchishree, D. K., Mishra Debahuti., (2018). Survey on gene selection methodologies based on filter, wrapper, embedded and hybrid approaches. *Indian Journal of Public Health Research & Development*, *9*(11), 2224-2234. doi: 10.5958/0976-5506.2018.01779.5
- Qiao, X., Bao, J., Zeng, L., Zou, J., & Li, D. (2017). An automatic active contour method for sea cucumber segmentation in natural underwater environments. *Computers and Electronics in Agriculture*, *135*, 134-142.
- Raith, S., Vogel, E. P., Anees, N., Keul, C., Güth, J.-F., Edelhoff, D., & Fischer, H. (2017). Artificial Neural Networks as a powerful numerical tool to classify specific features of a tooth based on 3D scan data. *Computers in Biology and Medicine*, *80*, 65-76. doi: <https://doi.org/10.1016/j.compbimed.2016.11.013>
- Resendiz-Ochoa, E., Osornio-Rios, R. A., Benitez-Rangel, J. P., Hernandez, L. A. M., & Romero-Troncoso, R. d. J. (2017, 29 Aug.-1 Sept. 2017). *Segmentation in thermography images for bearing defect analysis in induction motors*. Paper presented at the 2017 IEEE 11th International Symposium on Diagnostics for Electrical Machines, Power Electronics and Drives (SDEMPED).
- Resendiz-Ochoa, E., Osornio-Rios, R. A., Benitez-Rangel, J. P., Romero-Troncoso, R. D. J., & Morales-Hernandez, L. A. (2018). Induction Motor Failure Analysis: An Automatic Methodology Based on Infrared Imaging. *IEEE Access*, *6*, 76993-77003. doi: 10.1109/ACCESS.2018.2883988
- Rodriguez-Galiano, V. F., Luque-Espinar, J. A., Chica-Olmo, M., & Mendes, M. P. (2018). Feature selection approaches for predictive modelling of groundwater nitrate pollution: An evaluation of filters, embedded and wrapper methods. *Science of The Total Environment*, *624*, 661-672. doi: <https://doi.org/10.1016/j.scitotenv.2017.12.152>
- Roffo, G., & Melzi, S. (2016). Online feature selection for visual tracking.
- Rolf Hopple, e. A. E. (2007). *Motor Bearings, not just a piece of meta*. Paper presented at the IEEE-IAS/PCA Cement Industry Conference, Embassy Suites Airport Convention Center North Charleston, SC.
- Rowlett, M. (2019). 3-Phase, Induction-Type, Electric Motors for Pump Drive.

- Russell Wanhill, S. B., Loris Molent. (2019). P&W 125B Engine Bearing (1994): 2-Stage Exponential FCG Analysis (20 February ed., pp. 49-53): Springer, Dordrecht.
- Sánchez, R.-V., Lucero, P., Macancela, J.-C., Cerrada, M., Cabrera, D., & Vásquez, R. (2018). *Gear Crack Level Classification by Using KNN and Time-Domain Features from Acoustic Emission Signals Under Different Motor Speeds and Loads*. Paper presented at the 2018 International Conference on Sensing, Diagnostics, Prognostics, and Control (SDPC).
- Saqlain, S. M., Sher, M., Shah, F. A., Khan, I., Ashraf, M. U., Awais, M., & Ghani, A. (2019). Fisher score and Matthews correlation coefficient-based feature subset selection for heart disease diagnosis using support vector machines. *Knowledge and Information Systems*, 58(1), 139-167.
- Schatz, M. W. (1971). Overload Protection of Motors---Four Common Questions. *IEEE Transactions on Industry and General Applications*, IGA-7(2), 196-207. doi: 10.1109/TIGA.1971.4181285
- Schoen, R. R., Habetler, T. G., Kamran, F., & Bartfield, R. G. (1995). Motor bearing damage detection using stator current monitoring. *IEEE Transactions on Industry Applications*, 31(6), 1274-1279. doi: 10.1109/28.475697
- Schoen, R. R., Habetler, T. G., Kamran, F., & Bartheld, R. G. (1994, 2-6 Oct. 1994). *Motor bearing damage detection using stator current monitoring*. Paper presented at the Proceedings of 1994 IEEE Industry Applications Society Annual Meeting.
- Sengupta, S. K. C. M. (2016). *Induction Motor and Faults - Approach through Current Signature Analysis*: Springer.
- Sharma, S., Krishna, C. R., & Sahay, S. K. (2019). Detection of advanced malware by machine learning techniques *Soft Computing: Theories and Applications* (pp. 333-342): Springer.
- Shen, L., & Bai, L. (2006). MutualBoost learning for selecting Gabor features for face recognition. *Pattern Recognition Letters*, 27(15), 1758-1767.
- Siddique, A., Yadava, G. S., & Singh, B. (2005). A review of stator fault monitoring techniques of induction motors. *IEEE transactions on energy conversion*, 20(1), 106-114. doi: 10.1109/TEC.2004.837304
- Siddiqui, K. M., Sahay, K., & Giri, V. K. (2015, 19-20 March 2015). *Modelling and detection of bearing fault in SPWM inverter fed squirrel cage induction motor drives*. Paper presented at the 2015 International Conference on Circuits, Power and Computing Technologies [ICCPCT-2015].
- Simsek, S., & Uslu, S. (2020). Determination of a diesel engine operating parameters powered with canola, safflower and waste vegetable oil based biodiesel combination using response surface methodology (RSM). *Fuel*, 270, 117496. doi: <https://doi.org/10.1016/j.fuel.2020.117496>
- Singh, G., Anil Kumar, T. C., & Naikan, V. N. A. (2016). Induction motor inter turn fault detection using infrared thermographic analysis. *Infrared Physics & Technology*, 77, 277-282. doi: <https://doi.org/10.1016/j.infrared.2016.06.010>
- Song, Q., Jiang, H., & Liu, J. (2017). Feature selection based on FDA and F-score for multi-class classification. *Expert Systems with Applications*, 81, 22-27. doi: <https://doi.org/10.1016/j.eswa.2017.02.049>
- Stańczyk, U. (2015). Feature evaluation by filter, wrapper, and embedded approaches *Feature Selection for Data and Pattern Recognition* (pp. 29-44): Springer.
- Štruc, V., & Pavešić, N. (2010a). The complete gabor-fisher classifier for robust face recognition. *EURASIP Journal on Advances in Signal Processing*, 2010, 1-26.
- Štruc, V., & Pavešić, N. (2010b). From Gabor Magnitude to Gabor Phase Features: Tackling the Problem of Face Recognition under Severe Illumination Changes. *Rijeka: Face recognition. Inteh*, 215-238.
- Suganthi, S. S. R., S. J Med Syst. (2014). Analysis of Breast Thermograms Using Gabor Wavelet Anisotropy Index. *Journal of Medical Systems*. doi: 10.1007/s10916-014-0101-6

- Sun, L., Zhang, X.-Y., Qian, Y.-H., Xu, J.-C., Zhang, S.-G., & Tian, Y. (2019). Joint neighborhood entropy-based gene selection method with fisher score for tumor classification. *Applied Intelligence*, 49(4), 1245-1259.
- Taheri-Garavand, A., Ahmadi, H., Omid, M., Mohtasebi, S. S., Mollazade, K., Russell Smith, A. J., & Carlomagno, G. M. (2015). An intelligent approach for cooling radiator fault diagnosis based on infrared thermal image processing technique. *Applied Thermal Engineering*, 87, 434-443. doi: <https://doi.org/10.1016/j.applthermaleng.2015.05.038>
- Thangaswamy, S. S., Kadarkarai, R., & Thangaswamy, S. R. R. (2013). Developing an efficient technique for satellite image denoising and resolution enhancement for improving classification accuracy. *Journal of Electronic Imaging*, 22(1), 013013.
- Tharwat, A. (2018). Classification assessment methods. *Applied Computing and Informatics*. doi: <https://doi.org/10.1016/j.aci.2018.08.003>
- Thomson, W. T., & Fenger, M. (2001). Current signature analysis to detect induction motor faults. *IEEE Industry Applications Magazine*, 7(4), 26-34. doi: 10.1109/2943.930988
- Tian, F., Li, H., Tian, S., Yang, J., Shao, J., & Tian, C. (2020). Psychological symptoms of ordinary Chinese citizens based on SCL-90 during the level I emergency response to COVID-19. *Psychiatry Research*, 112992.
- Vamsidhar, E., PhaniKumar, D. V. V. S., & Gunna Kishore, D. (2016). Application of Fisher Score and mRMR Techniques for Feature Selection in Compressed Medical Images. *International Journal of Engineering and Technology*, 7, 2109-2121.
- Vencl, A., & Rac, A. (2014). Diesel engine crankshaft journal bearings failures: Case study. *Engineering Failure Analysis*, 44, 217-228. doi: <https://doi.org/10.1016/j.engfailanal.2014.05.014>
- Verma, J. (2013). One-Way ANOVA: Comparing means of more than two samples *Data analysis in management with SPSS software* (pp. 221-254): Springer.
- Vinay, N. A., Vinay, H. C., & Narendra, T. V. (2014, 8-10 Jan. 2014). *An Active Contour Method for MR Image Segmentation of Anterior Cruciate Ligament (ACL)*. Paper presented at the 2014 Fifth International Conference on Signal and Image Processing.
- Vora, S., & Yang, H. (2017, 18-20 July 2017). *A comprehensive study of eleven feature selection algorithms and their impact on text classification*. Paper presented at the 2017 Computing Conference.
- Williams, D. J., & Shah, M. (1992). A Fast algorithm for active contours and curvature estimation. *CVGIP: Image Understanding*, 55(1), 14-26. doi: [https://doi.org/10.1016/1049-9660\(92\)90003-L](https://doi.org/10.1016/1049-9660(92)90003-L)
- Żbikowski, K. (2015). Using Volume Weighted Support Vector Machines with walk forward testing and feature selection for the purpose of creating stock trading strategy. *Expert Systems with Applications*, 42(4), 1797-1805. doi: <https://doi.org/10.1016/j.eswa.2014.10.001>
- Zhang, T., & Lu, B.-L. (2010). *Selecting Optimal Orientations of Gabor Wavelet Filters for Facial Image Analysis* (Vol. 6134).
- Zhang, Y., Zhou, Y., Zhang, D., & Song, W. (2019). A Stroke Risk Detection: Improving Hybrid Feature Selection Method. *Journal of medical Internet research*, 21(4), e12437.
- Zimmermann, M., Valcanaia, A., Neiva, G., Mehl, A., & Fasbinder, D. (2019). Three - Dimensional Digital Evaluation of the Fit of Endocrowns Fabricated from Different CAD/CAM Materials. *Journal of Prosthodontics*, 28(2), e504-e509.
- Zin, A., Hawari, K., & Khamisan, N. (2016). Early Detection of Spots High Water Saturation for Landslide Prediction Using Thermal Imaging Analysis. *International Journal of Environmental Science and Development*, 7(1), 41.